ROLLING CONTACT ORTHOPAEDIC JOINT DESIGN

by

Alexander Henry Slocum, Jr.

S.M., Mechanical Engineering, Massachusetts Institute of Technology, 2010
S.B., Mechanical Engineering, Massachusetts Institute of Technology, 2008

Submitted to the Department of Mechanical Engineering
in Partial Fulfillment of the Requirements for the Degree of
Doctor of Philosophy in Mechanical Engineering at the

MASSACHUSETTS INSTITUTE OF TECHNOLOGY

February 2013

Author:_____
Alexander H. Slocum, Jr.
Department of Mechanical Engineering
January 11, 2013

Certified by:_____
Prof. Kripa K. Varanasi
Associate Professor of Mechanical Engineering
Thesis Supervisor and Committee Chair

Accepted by:_____
David E. Hardt
Professor of Mechanical Engineering
Chairman, Department Committee on Graduate Students

ROLLING CONTACT ORTHOPAEDIC JOINT DESIGN

by

Alexander Henry Slocum, Jr.

Submitted to the Department of Mechanical Engineering
on January 11th, 2013 in Partial Fulfillment of the
Requirements for the Degree of Doctor of Philosophy in
Mechanical Engineering

Abstract

Arthroplasty, the practice of rebuilding diseased biological joints using engineering materials, is often used to treat severe arthritis of the knee and hip. Prosthetic joints have been created in a "biomimetic" manner to reconstruct the shape of the biological joint. We are at a disadvantage, however, in that metals and polymers used to replace bone and articular cartilage often wear out too soon, leading to significant morbidity. This thesis explores the use of kinetic-mimicry, instead of bio-mimicry, to design prosthetic rolling contact joints, including knee braces, limb prosthetics, and joint prostheses, with the intent of reducing morbidity and complications associated with joint/tissue failure.

A deterministic approach to joint design is taken to elucidating six functional requirements for a prosthetic tibiofemoral joint based on anatomical observations of human knee kinetics and kinematics. Current prostheses have a high slide/roll ratio, resulting in unnecessary wear. A rolling contact joint, however, has a negligible slide/roll ratio; rolling contact prostheses would therefore be more efficient. A well-established four-bar linkage knee model, in a sagittal plane that encapsulates with the knee's flexion/extension degree of freedom, is used to link human anatomy to the shape of rolling cam surfaces. The first embodiment of the design is a flexure coupling-based joint for knee braces. Failure mode analysis, followed by cyclic failure testing, has shown that the prototype joint is extremely robust and withstood half a million cycles during the first round of tests.

Lubrication in the joint is also considered: micro- and nano-textured porous coatings are investigated for their potential to support the formation of favorable lubrication regimes. Hydrodynamic lubrication is optimal, as two surfaces are separated by a fluid gap, thus mitigating wear. Preliminary results have shown that shear stress is reduced by more than 60% when a coating is combined with a shear thinning lubricant like synovial fluid. These coatings could be incorporated into existing joint prostheses to help mitigate wear in current technology. This thesis seeks to describe improvements to the design of prosthetic joints, both existing and future, with the intent of increasing the overall quality of care delivered to the patient.

Thesis Supervisor: Kripa K. Varanasi
Title: Doherty Associate Professor of Mechanical Engineering

Doctoral Thesis Committee

Thesis Supervisor and Committee Chair: Kripa K. Varanasi, PhD
Doherty Associate Professor of Mechanical Engineering
Massachusetts Institute of Technology

Martin L. Culpepper, PhD
Associate Professor of Mechanical Engineering
Massachusetts Institute of Technology

Douglas P. Hart, PhD
Professor of Mechanical Engineering
Massachusetts Institute of Technology

Just Herder, PhD
Associate Professor of Mechanical and Biomechanical Engineering
TU Delft, The Netherlands

This work is dedicated to
Bubsi, Marianna, Pat and John

Through this their memory lives on!

ACKNOWLEDGEMENTS

Table of Contents

List of Tables

List of Figures

16

This page intentionally
left blank[1]

---

[1] Except now it is no longer blank

CHAPTER

1

INTRODUCTION

(Why do I like to design machines?) "It is the pitting of one's brain against bits of iron, metals, and crystals and making them do what you want them to do. When you are successful that is all the reward you want." – Albert A. Michelson

The focus of this work is the design of rolling element mechanisms for use in articulating joint prostheses and the evaluation of new fracture fixation devices using a rolling contact testing instrument motivated by the joint prosthesis work. Different methods of achieving the necessary kinetics and kinematics required to accurately support and mimic joint motion are investigated, with a foundation based on the last four decades of research related to improving knee prostheses. In theory, a rolling contact knee joint could allow a diseased biological joint to be replaced with a prosthetic that benefits from all of the advantages of rolling contact: reduced sliding, increased resistance to wear, and improved load transfer, leading to an increase in joint lifetime and improved patient outcomes.

It is not a simple task, however, to design, build, and test a new replacement joint, particularly without the resources of a large corporate entity. The intent of this work is thus not to try to re-define the standard of care, but to investigate what a rolling contact prosthetic joint would look like and begin laying the groundwork for development of such a device. This work has several limitations, for example due to the complexity of knee motion only a flexion/extension degree of freedom (DOF) in a sagittal plane is considered in the present model. Synthesis of the joint, however, is rooted in an understanding of knee biomechanics, and is one of the important contributions of this thesis.

The joint design presented herein is, on the other hand, intended to be an immediate improvement to currently available knee braces, as the performance of a rolling contact knee brace is relatively easier to validate. It is the author's intention that the reader engages the scientific method when reading this work; asking the question "What if…?", and then working to validate a hypothesis through analysis and experimentation has often led to some very illuminating results.[2] If just one person comes away inspired with a new idea that leads to an improvements to the delivery of patient care, this work can be considered a success.

1.1   MOTIVATION

The motivation for this research first came from a short, five-minute conversation between the author and Professor Just Herder at Delft University of Technology in Delft, Netherlands in January 2008. It centered on a small mechanism called a flexure coupling, a toy-model of which was on Professor Herder's desk. A solid model of a flexure coupling can be seen in Figure 1.1a.

---

[2] The light bulb is a good example

This sparked the question: "What if we were to try to design a total knee replacement, based on this mechanism, from first principles?" Figure 1.1b shows an image from a conceptual development meeting with Professor Herder a few months later at the 2008 ASME Design of Medical Devices Conference. It would still be at least two years before the idea really began to take root.
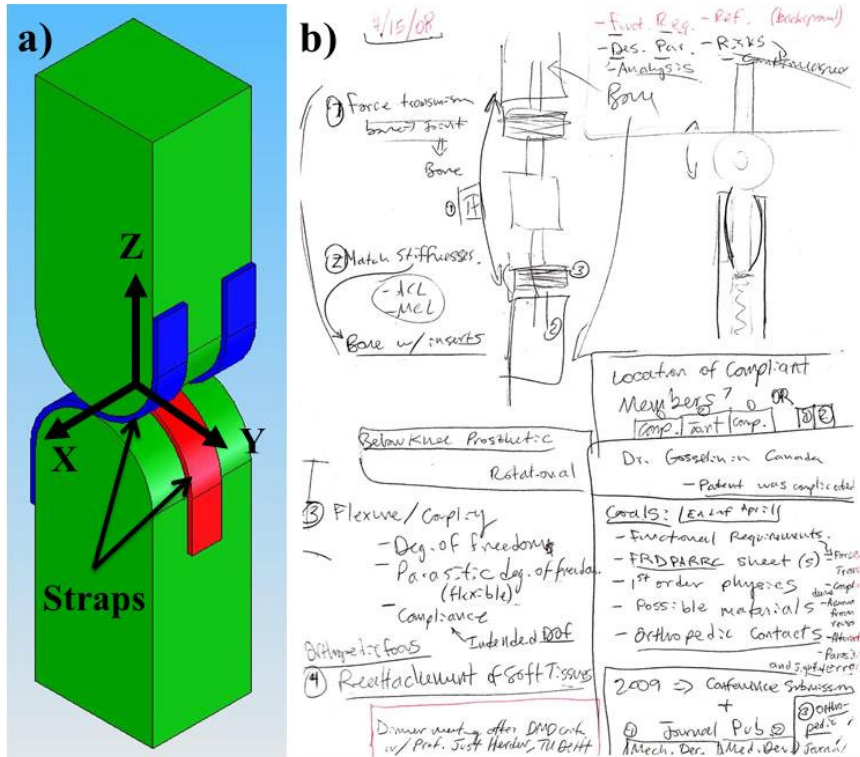
Figure 1.1: (a) Conceptual SolidWorks™ solid model of a flexure coupling; (b) conceptual sketches of the rolling contact knee prosthesis design.

Furthermore, a good design engineer knows that sometimes it is quite all right to be a little weird and go in a direction that not many others, perhaps no one, have gone before. One example of this is the Dual Left Ventricular Assist Device (LVAD) heart prosthesis that was recently developed at the Texas Heart Institute, and is seen in Figure 1.2. The purpose of an LVAD is to work in parallel with the left ventricle of the heart to pump blood out to the body; they are

currently used in cases where a patient's heart is failing (such as congestive heart failure or

dilated cardiomyopathy). In the Dual LVAD heart prosthesis, two LVADs are placed in series

with the pulmonary and systemic circulations, and thus are fully capable of continuously

pumping blood through the body.

Figure 1.2: A dual LVAD heart prosthesis [1].

It was previously thought that the body required pulsatile flow to ensure that blood was

adequately "massaged" deep into the tissues, but with the LVAD blood flow is continuous. Dr.

Billy Cohn, one of the developers of the prosthesis, said, "42 years after the first prosthetic heart,

it's time to look past bio-mimicry. Wings that flap didn't help mankind fly; so why must a

substitute heart beat like a natural one? Mother nature did the best she could" [1]. At the time of

this writing, trials in humans have commenced on the dual LVAD artificial heart. Experiences

like this one lend themselves to the motivation for exploring alternative solutions to creating

knee prostheses.

Current limitations to total knee arthroplasty stem, at least in part, from the fact that the technology is biomimetic: a metal femoral component is used to re-create the geometry of the distal femur, and a polyethylene bearing is used as a substitute for the meniscus and proximal tibia geometry. Mother Nature has had quite a few years to develop articulating joints with a coefficient of friction approaching 0.005 [2, p.12]; it is a testament to human ingenuity and those who have come before that the technology available today lasts as long as it does. There still remains, however, that nagging question of "What if one were to take everything that is known now about knee biomechanics and TKA, and start designing a prosthetic joint from the ground up, with input from precision engineering, nanotechnology, tribology, and rheology?"

Finally, there is an opportunity to improve upon the design of knee braces, which are often prescribed to patients with osteoarthritis, or after surgical repair of trauma to a joint, to improve an individual's confidence in the joint and help slow the progression of disease [3-5]. Also, the prevalence of degenerative changes like osteoarthritis increases significantly with increasing age [6]. These joints are limited in that the ubiquitous double-hinge design does not adequately mimic knee flexion-extension biomechanics. The lifetime of current joints is about fifteen to twenty years, so patients who require a new joint and are greater than twenty years away from normal life expectancy (generally those under the age of fifty-five) have a high probability of requiring revision surgery. Such procedures have a high rate of complications and can lead to significant morbidity. Use of a rolling-contact knee brace that exactly mimics the primary degree of freedom of the knee, could better support the motion of a damaged knee and help

patients live well enough without pain until they reach an age at which subsequent knee replacement would last for the remainder of their life.

1.2   TOTAL KNEE ARTHROPLASTY

Total Knee Arthroplasty (TKA), is one of the most common orthopaedic procedures in the United States today, and in terms of efficacy is also one of the most efficient and effective treatments for disease. *Arthroplasty* is from the Greek words *arthron*, referring to a joint, limb, or articulation, and *plassein*, meaning to form, mold, or forge [7]. Thus, total knee arthroplasty is the practice of forging a new articulating joint from different materials. Figure 1.3a shows a sketch of the anatomy of the human knee, and Figure 1.3b shows a schematic depicting a modern total knee replacement.
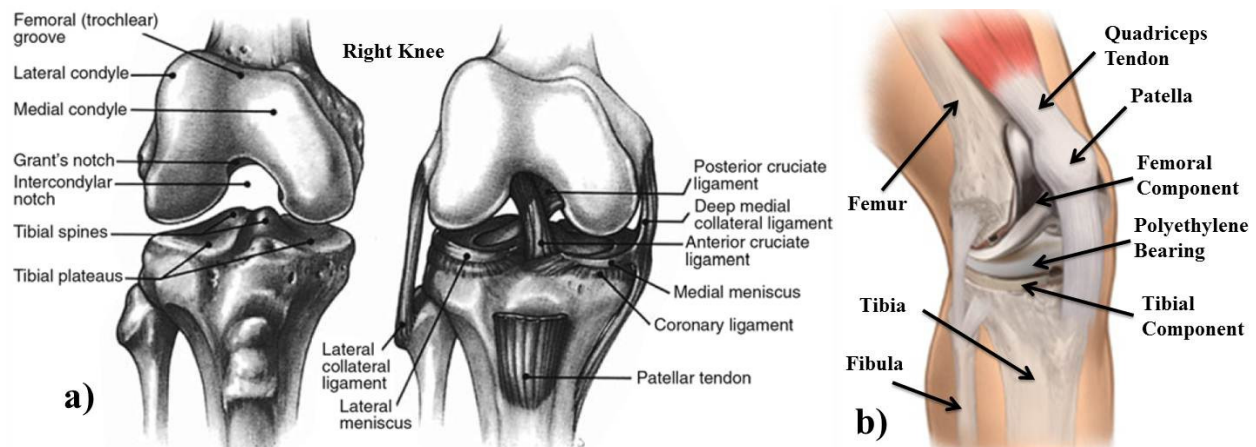
Figure 1.3: (a) Knee anatomy [8]; (b) modern total knee replacement schematic [9].

The first total knee replacement was performed by Ferguson in 1861[3] on a patient who had suffered a traumatic knee injury, including excision of the diseased joint and replacement with a "false joint". The patient was able to regain motion, "attend to her household duties… could

---

[3] Later that same year, the Massachusetts Institute of Technology was founded by W. B. Rogers in Boston, MA.

easily stand on the leg, and could run upstairs or jump off a chair as if she had had no disease and no operation" [10]. This and other milestones in the history of TKA are shown in Figure 1.4.

Timeline of Total Knee Replacement
(1861 – Present)
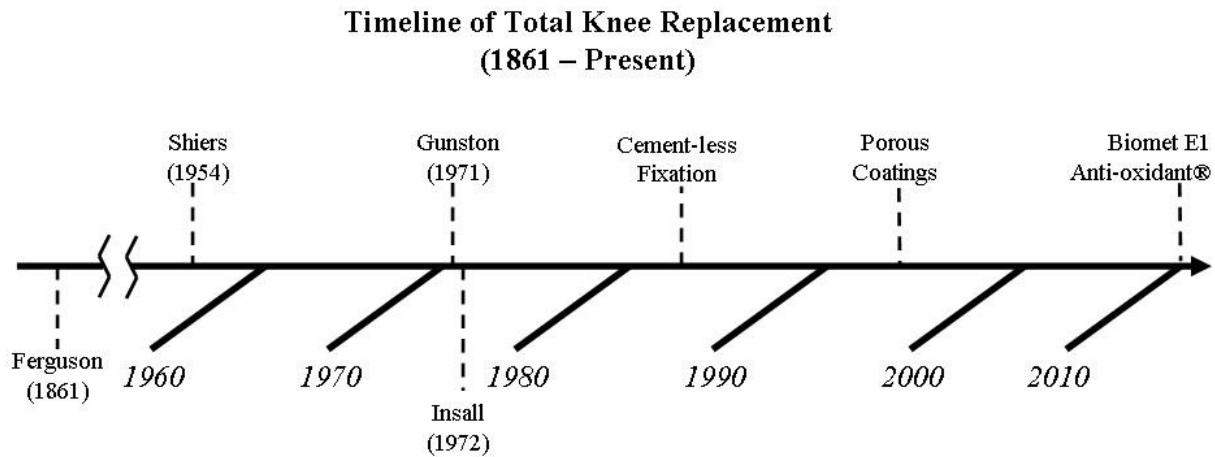
Figure 1.4: A brief timeline of the history of total knee arthroplasty.

In 1953, almost a century later, L. G. P. Shiers introduced his hinged joint for knee arthroplasty [11], which can be seen in Figure 1.5. His work on seventeen patients, who presented with some form of degenerative arthritis in one or both knees, resulted in eight successful operations (47% success) with an average follow-up time of forty-six months. In seven of the seventeen cases, the joint failed at the root of the femoral or tibial post and had to be replaced, of which five were subsequently successful. Only one patient was able to endure both the original knee operation and revision of the joint with a new replacement joint after five years [12]. From a mechanical perspective, the presence of stress concentrations at the interface between both the femoral and tibial stems, as well as the hinge body, is causative of the high incidence of failure at the locations reported.
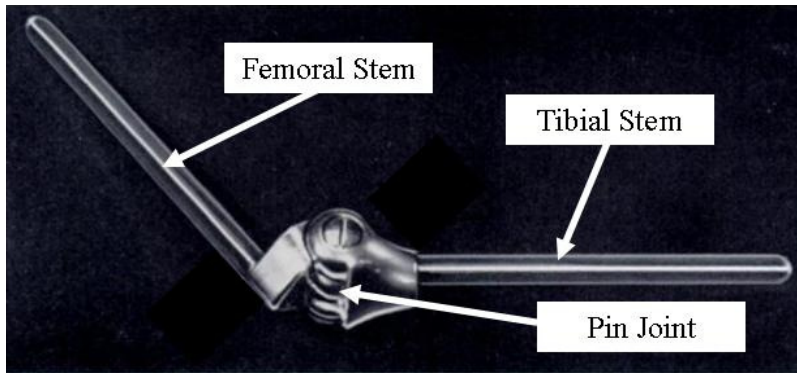
Figure 1.5: Shiers' hinge joint prosthesis [11, 12].

Prior to Shiers, the "broad base of the operation remained the same" from 1914 until 1953; during this time period, physicians utilized a wide array of materials in knee joint arthroplasty, varying from circumcised pigs' bladders [13], to sheets of nylon [14]. In that time span, 896 documented arthroplasty procedures were performed with a success rate of 46% [12]. In 1971 Gunston introduced the concept of a unicondylar (replace one condyle at a time) metal-on-plastic knee replacement [15], wherein the metal surface was affixed to the distal femur and the plastic bearing surface affixed to the proximal tibia. This basic configuration of artificial knee joints has persisted for the past forty years. The similarities between Gunston's original metal-on-polymer design and the "state-of-the-art" metal-on-polymer implants available today from companies like DePuy, Smith & Nephew, and Zimmer are readily apparent to the casual observer, as the significant advances in materials selection and geometrical contouring are not as readily apparent. Figure 1.6 juxtaposes Gunston's original design (left) with an example of the state-of-the-art in knee replacement technology, the Vanguard® total knee available from Biomet, Inc.
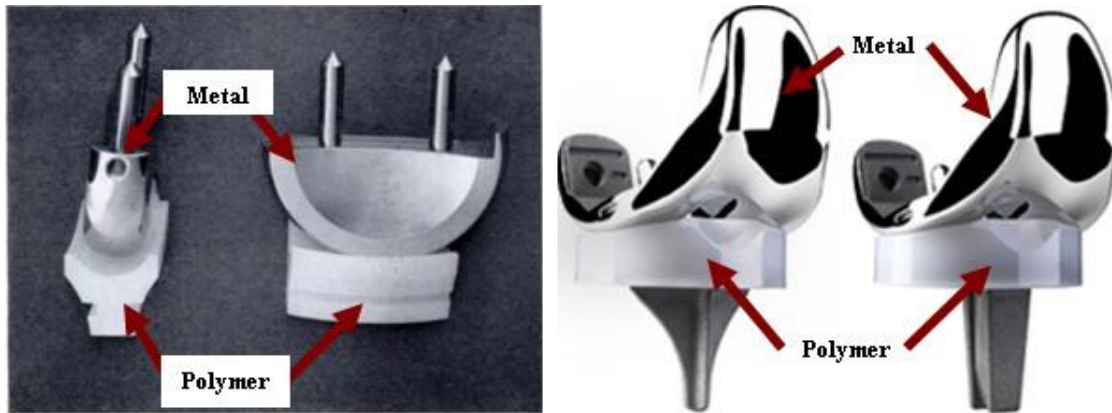
Figure 1.6: Left: Gunston's metal-on-polymer prosthetic implant [15]; right: An example of a metal-on-polymer total knee replacement available from Biomet, Inc. [16].

The similarities between two technologies separated by four decades of research are the result of both scientific and economic factors. Metal-on-polymer TKA is an efficient and effective method of joint arthorplasty that, once approved by the U.S. Food and Drug Administration (FDA) and accepted by the scientific community, became the "state-of-the-art" and a focus of the majority of research efforts directed at optimizing and improving implant function. Evidence of some drawbacks to this iterative approach to designing joints were highlighted in a recent (at the time of this writing) New York Times article describing the short-lived, troubled life of a new implant, the DePuy A. S. R. hip replacement system. Due to the high cost of developing new types of joints, manufacturers are able to obtain approval for "critical implants [which] can be sold without [rigorous] testing if a device, like an artificial hip, resembles an implant already approved and used on patients." [17]. Thus, one of the major reasons that TKA systems have not changed significantly over the years is because it makes more economic sense to optimize existing design than to try to gain approval for a drastically different and new approach. From an engineer's standpoint, however, given the depth of knowledge regarding knee biomechanics

which has been accumulated over the past forty years of optimization, there could now be a better option with significantly greater long-term efficacy.

TKA, in general considered to be an extraordinary success [18], is necessary in the event of damage to the articular cartilage, meniscus, or other soft tissues in the human knee joint, whether from trauma, genetic disease such as rheumatoid arthritis, or other factors. Knee function is provided primarily by the soft tissues in the joint, shown in Figure 1.7a and b; thus, injury to these structures will have the greatest impact on joint stability and treatment selection [19].
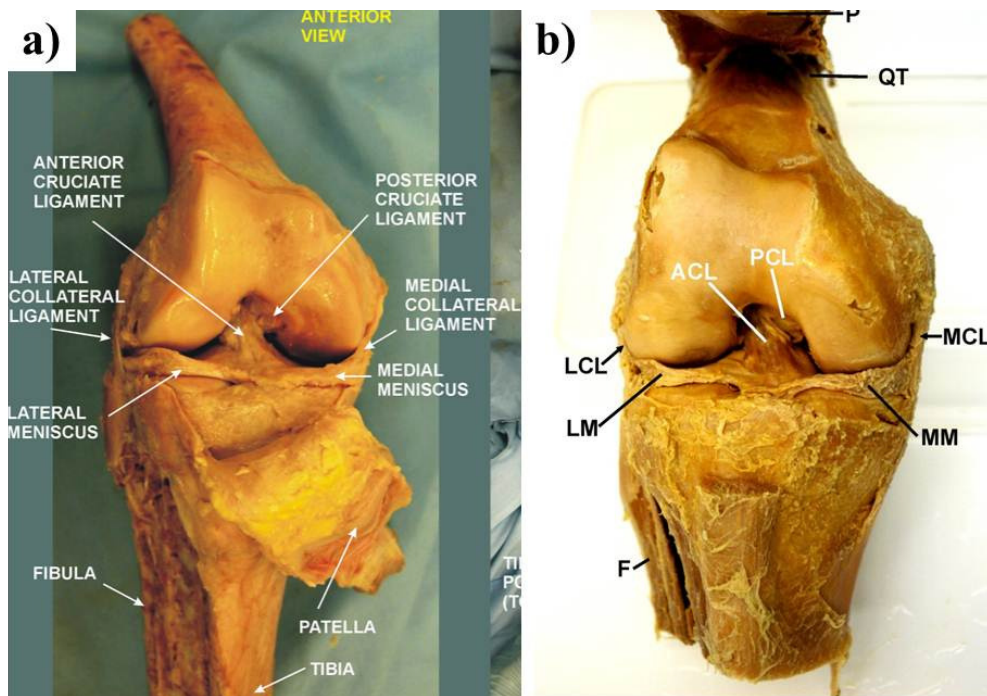
Figure 1.7: (a) and (b) are gross anatomical prosections of human knees, illustrating the relative size and location of soft tissue structures [20, 21].

Articular cartilage is avascular and natural regeneration or repair does not occur; conversely, when a bone is broken, it will heal and new tissue will grow to replace the damaged tissue. Figure 1.8a shows what damaged articular cartilage looks like in cases of degenerative

osteoarthritis; replacement of the damaged tissue with metal and polymer prosthesis components can bee seen in Figure 1.8b.
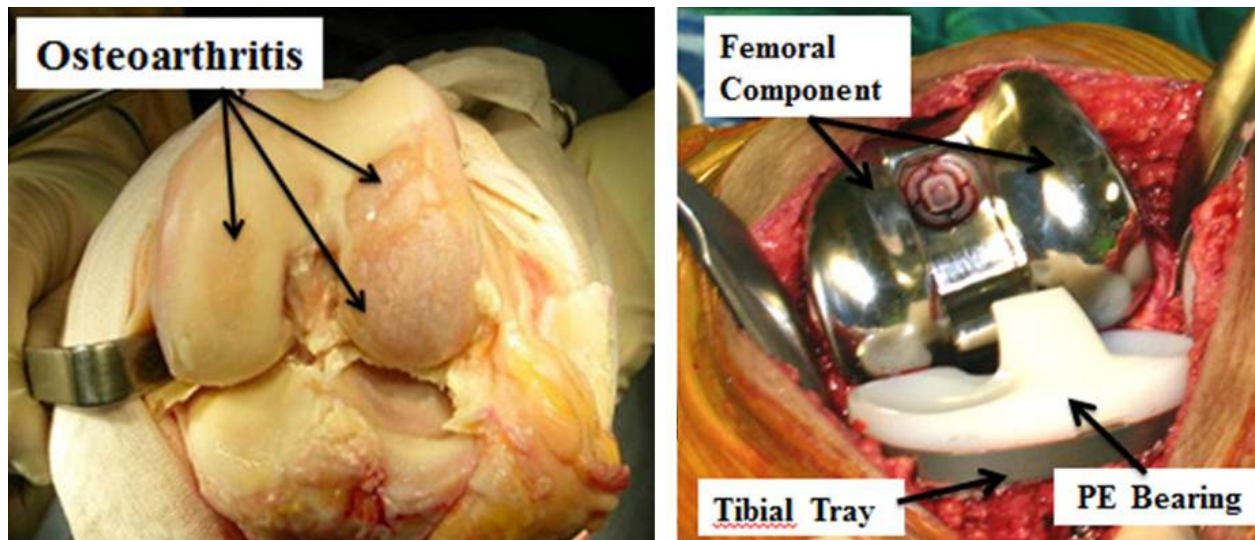
Figure 1.8: (a) damaged articular cartilage in osteoarthritis [22]; (b) subsequent removal of damaged cartilage and replacement with metal and polymer prosthesis components [23]

Knee replacement in an adult over the age of sixty-five generally results in the replacement lasting the lifetime of the patient. Due to several factors, including more active lifestyles and an increase in the weight of the general population, TKA is being performed more frequently in patients aged under the age of sixty-five. More than 350,000 primary TKA procedures and 29,000 revision procedures were performed in the United States in 2002 [24], the most recent year for which data was available. This represents a tripling of the rate at which TKA procedures were performed just twelve years earlier in 1990 [25].

The durability of current implants is such that over increasing lifetimes, the side effects of long-term implantation eventually force the revision of artificial joints. Concerns associated with implant loosening and the potential need for multiple revisions generally discourages the

widespread use of TKA in patients less than fifty years old [26]. According to the most recent projections, the annual incidence of TKA is predicted to increase over 670%, to 3.48 million procedures per year by 2030 [27]. Longer-term implantation, as well as increases in the total number of implants, will require both significant improvements to existing implant technology as well as methods of integrating the implant into the surrounding anatomy in order to reduce the risks of complications such as periprosthetic osteolysis [8].

1.3 INSTITUTIONAL CONTRIBUTIONS

This thesis would not have been possible without those who have come before the author, many of whom have gone on to other exciting work.[4] Reading their theses and papers has provided guidance and inspiration, and also helped to create neural connections and provoke thought processes that otherwise would not have happened. Direct input from the late Professor Robert Mann would have been invaluable; work by him and his students over several decades made significant advancement in clinical and biological applications of engineering to joint design and musculoskeletal biomechanics [28-31].

Work by Seering [32, 33] described contributions from the cruciate and collateral ligaments in supporting a load, and will be used in further work to add additional degrees of freedom to the existing joint. Work by Fijan, also a student of Prof. Mann's, helped the author of this thesis to develop a better understanding of the 3-D kinematics of the normal human knee [34], which led to a hypothesis that a simple matrix model of the knee could be generated to represent range of motion (ROM) and stiffness (C) in all 6 DOFs. This model could then be combined with a

---

[4] *"If I have seen further it is because I have stood on the shoulders of giants'"*– Isaac Newton

synthesis method like Freedom and Constraint Topology [35] to generate a flexural mechanism with the same kinetic and kinematic characteristics as a healthy knee joint.

Recent work in the Bioengineering Laboratory at MGH[5] has also helped guide this thesis work. A study of knee biomechanics using fluoroscopes to assess flexion after TKA [36] illustrated the depth of knowledge surrounding the knee joint that has been acquired, and will be useful in future work. Varadarajan's research [37] supported the development of an understanding of joint mechanics and how they can influence the design of new prostheses. Other work by Most and colleagues, first in developing a 6-DOF robotic test system to evaluate TKA biomechanics [38], and next investigating the mechanics of TKA at high flexion angles [39], was of great influence in the creation of functional requirements for a rolling contact prosthesis presented in Chapter 5.

1.4   THESIS CONTRIBUTIONS

The contributions of this thesis are rooted in the application of machine design principles to medical challenges, wherein machine elements can be brought to bear against limitations of current biomedical technology, with the ultimate goal being to develop new bio-machines to help improve patient care. These contributions are found in Chapters 3-6, while Chapters 1, 2 and 7 serve as the foundation off of which the others are based. Chapters 2 and 7 also provide an introduction to general orthopaedic medicine and biomechanics as they relate to this work. This thesis is focused on a mechanism called a rolling element joint, of which the flexure coupling is a sub-type, as it is applied to problems in fracture fixation and repair, and the design of prostheses

---

[5]http://www.massgeneral.org/ortho/research/researchlab.aspx?id=1479; Director: Dr. Gouan Li, PhD.

for articulating joints. Additionally, lubrication, friction, and wear of joint prostheses can thus be considered from the point of view of rolling element bearing design.

The first contribution of this thesis came from the author's involvement in the development of an adjustable bone plate. During evaluation of mechanical characteristics of the new plate, conventional methods of testing bone plates were not able to properly characterize the new design [40]. A deterministic analysis of bone plate testing methods showed that current practices would have to be modified to accommodate the new technology [41]. Following this, the design and manufacture of a new testing method allowed for characterization of adjustable bone plate designs and comparison with existing technology using rolling element joints to simulate fractures [42].

Next, a rolling contact prosthesis design is achieved using deterministic analyses of knee biomechanics, combined with input from principles of good machine design. General functional requirements for a knee joint are also defined to illustrate the results of the deterministic process. The next step was to analyze the system by looking at optimal configurations for load transmission between two elements of a joint for load transmission. Following this, kinetics of the human knee in a sagittal (2-dimensional) plane is integrated into the mechanism, and rolling cam surfaces are contoured to ensure that their relative motion is equivalent to the rotation/translation seen in the flexion and extension of a human knee joint. A case study of metallic rolling contact joints manufactured out of stainless steel for use in knee braces is also presented, demonstrating its ability to withstand several hundred thousand cycles. The kinetics of this new joint represent a significant biomechanical improvement over current brace designs.

It has been shown that knee biomechanics can be used to deterministically design a better knee brace; at the time of this writing, a grant application for a clinical trial to evaluate the latest prototype has been submitted.

Another contribution of this thesis is demonstrating that shear-thinning fluids, when combined with a micro-scale porous coating, can significantly reduce shear stresses in a lubricated contact. This was shown through investigating potential improvements at the different implant surfaces: the implant-implant interface, where lubrication and wear govern material lifetimes, and the implant-bone interface, where integration of native bone into the structure of the implant is essential for long-term viability of the prosthesis. The implant-implant interface is the primary focus of this research, as the author's skill in a wet lab, as well as the required resources, limited the amount of cell culture work that could be performed.

It is hypothesized that improvements to lubrication can be achieved through encapsulation of synovial fluid, supporting protein-mediated boundary layer formation, through application of a micro-scale hydrophilic coating onto implant materials. Boundary layer formation is well documented to be supported by adsorption of hydrophilic proteins; increased friction leads to protein denaturation and exposure of hydrophobic moieties of those proteins, which then adsorb onto hydrophobic surfaces (i.e. the polymer) and disrupt flow in the boundary layer. Encapsulation could help to prevent hydrophobic proteins from adsorbing onto surfaces, and will also help to mitigate both increases in friction as well as dry contact between the two implant surfaces [43, 44, 45].

Next, growth and proliferation of osteoblasts, which are the principle drivers of bone formation, are investigated on micro-scale porous titanium coatings fabricated using alkaline etch and anodization processes. Osteoblast growth, proliferation, and adhesion have been well-documented to be improved by titanium micro- and nano-structures, often with complicated hydroxy-apatite (HA) based coatings. Also, currently used coatings are generally "sprayed" onto the surface of an implant, for example Trabecular Metal available from Zimmer (Zimmer, Inc., Warsaw, IN). Alkaline etching results in a coating that is fabricated directly into the surface, integrated into the bulk structure of the solid. These have not yet been evaluated, when formed on orthopaedic-grade titanium for their efficacy in supporting cell growth and proliferation, and the results of preliminary studies are described.

1.5   THESIS ORGANIZATION

1.5.1   CHAPTER 1 – INTRODUCTION

Chapter 1 gives a description of the motivations for this work, as well as giving a brief overview of the history of total knee arthroplasty. It also provides a concise explanation of the contributions of this thesis, with brief descriptions of the contents of each chapter.

1.5.2   CHAPTER 2 – MUSCULOSKELETAL PATHOPHYSIOLOGY

Chapter 2 gives a brief introduction to the musculoskeletal system, starting with a gross anatomical view, then descending to the cellular level. The biochemical basis of some important aspects of regulation and growth are also discussed to provide a foundation for understanding the interaction of implant materials and the adjacent human tissues. I am grateful to Dr. Mary

Bouxsein and Dr. Maragaret Seton, instructors for the January 2011 HST Course Musculoskeletal Pathophysiology, for graciously allowing me to take the class while studying for my doctoral qualifying exams. I drew much inspiration from what I learned there, and during my first year of medical school, while writing Chapter 2 [46].

1.5.3   CHAPTER 3 – DETERMINISTIC JOINT DESIGN

Chapter 3 presents a deterministic method for designing rolling element joints for biomedical applications. Different types of joints found in the musculoskeletal system are discussed, and prosthetic mechanical substitutes are evaluated. The chapter ends with a case study in using a deterministic design process to synthesize a rolling element joint for evaluating the performance of a new deformable bone plate for mandible fracture repair [41, 42].

1.5.4   CHAPTER 4 – JOINT DURABILITY

Chapter 4 is an exercise in fatigue, fracture, and lifecycle analysis for a theoretical rolling contact joint. Classical fatigue analysis of crack nucleation and propagation in the straps from Figure 1 is presented, as well as their ability to resist high cycle fatigue. Materials selection for a rolling contact joint is also discussed from the point of view of Hertzian contact stresses, and the Buckingham Load Stress factor is used to predict the lifetime of the rolling elements.

1.5.5   CHAPTER 5 – DESIGN OF ROLLING CONTACT JOINT PROSTHESES

Chapter 5 illustrates the use of a deterministic analysis of knee kinematics and biomechanics to develop a set of functional requirements (FRs) for an articulating joint prosthesis. These FRs are

used to generate concepts with different types of joints, including a flexure coupling. From this, a knee brace was constructed which imitated the same roll-back motion seen in a healthy human knee. Knee biomechanics can be actively applied to prostheses design to develop a better joint for knee braces, fixators for treating dislocations, and also prosthetic limbs, in addition to implants for total knee arthroplasty. A rolling contact knee brace could help reduce pain, improve support, provide additional stability and support rehabilitation by better matching the biomechanics of the knee than the dual-hinge designs in use today.

1.5.6   CHAPTER 6 – NANO-ENGINEERED SURFACE COATINGS

Chapter 6 is focused on nanoengineered coatings, investigated for their ability to improve the performance of implants at two key interfaces: the bone/implant interface and the implant/implant interface. The implant/implant interface is the primary site of lubrication, friction, and wear in joint prostheses, and its ability to withstand stress and support loads are critical to determining an implant's success. The bone/implant interface is critical to the long-term success of the implant as integration of the surrounding bone can help prevent stress shielding and subsequent periprosthetic bone loss. Nano-structured coatings for osseo-integration are also discussed and the results of a brief foray into cell culture are described.

1.5.7   CHAPTER 7 – CONCLUSIONS AND FUTURE WORK

Chapter 7 presents final thoughts and a summary of potential future work that could be pursued, for example clinical evaluation of the performance of the knee brace as compared to current technology. Also, this chapter deals with clinical aspects of Total Knee Replacement (TKA),

such as indications and complications, as well as use of knee braces in patients who are candidates for TKA. Specifically, aseptic loosening, metal ion allergies, and polyethylene wear are discussed and additional resources for background reading provided. Finally, limitations of the current joint are discussed, and suggestions are made for what further research must address in order to create rolling-contact total knee prostheses.

1.6   REFERENCES

[1] "Next: Skipping a Beat", National Geographic Magazine, Dec. 2011:30.
[2] Bartel, D. L., Davy, D. T., Keaveny, T. M., "Orthopaedic Biomechanics", (2006), Pearson Prentice Hall, Upper Saddle River, NJ.
[3] Briggs, K. K., *et al.*"Improvement in Quality of Life with Use of an Unloader Knee Brace in Active Patients with OA: A Prospective Cohort Study". Journal of Knee Surgery, 2012; **25**(05): pp. 417-422.
[4] Brandsson, S., *et al.* "Is a knee brace advantageous after anterior cruciate ligament surgery?" Scandinavian Journal of Medicine and Science in Sports, Vol. **11**;2, pp. 110-114, April 2001.
[5] Stanley, C. J., Creighton, A., Gross, M. T., Garret, W. E., "Effects of a knee extension constraint brace on lower extremity movements after ACL reconstruction". Clin Orthop Relat Res (2011) **469**:1774-1780.
[6] Felson, D. T., et al. "The prevalence of knee osteoarthritis in the elderly. The Framingham Osteoarthritis Study". Arthritis and Rheumatism, Vol. **30**, Iss. 8, pp. 914-918, August 1987.
[7] The Free Dictionary – Medical Dictionary. Online URL: http://medical-dictionary.thefreedictionary.com/
[8] Revel, P. A., Ed., "Joint Replacement Technology", (2008), Woodhead Publishing, Ltd., Cambridge, UK.
[9] Orthopaedic Surgery India, Kerala, India. Online URL: http://www.orthopaedic-surgery-india.com/primary-knee-joint-replacement.html
[10] Ferguson, M., "Excision of the Knee-Joint – Recovery with a False Joint and Useful Limb". Medical Times & Gazette, 1861; **1**:601.
[11] Shiers, L. G. P., "Arthroplasty of the Knee: Preliminary Report of a New Method". Journal of Bone and Joint Surgery, November 1954, Vol. **36B**:4, pp. 553-560.
[12] Shiers, L. G. P., "Arthroplasty of the Knee: Interim Report of a New Method". Journal of Bone and Joint Surgery, February1960, Vol. **42B**:1, pp. 31-39.
[13] Baer, W. S., "Arthroplasty with the Aid of Animal Membrane". American Journal of Orthopaedic Surgery, 1918, **16**:1.
[14] Kuhns, J. G., Potter, T. A., "Nylon Arthroplasty of the Knee Joint in Chronic Arthritis". Surgery, Gynecology and Obstetrics, 1950, **91**:351.
[15] Gunston, F. H., "Polycentric Knee Arthroplasty: Prosthetic Simulation of Normal Knee Movement". The Journal of Bone and Joint Surgery, May 1971, Vol. **53B**:2, pp. 272-277.
[16] Vanguard® Total Knee Replacement System, Biomet, Inc., Online URL: http://www.biomet.at/at-corporate/news/vanguard-monobloc.

[17] Meier, B., "The Implants Loophole". The New York Times, Business Day, December 16, 2010. URL: http://www.nytimes.com/2010/12/17/business/17hip.html?pagewanted=1&_r=1.

[18] Einhorn, T. A., O'Keefe, R. J., Buckwalter, J. A., "Orthopaedic Basic Science: Foundations of Clinical Practice", 3rd Ed. (2007), AAOS, Rosemont, IL.

[19] Wiesel, S. W., Delahay, J. N., "Essentials of Orthopaedic Surgery", 4th Ed. (2010), Springer, New York, NY.

[20] Gadha, R., Summer Dissection Course, JCESOM, 2009.

[21] Zill, S. N., Gross Anatomy and Embryology, Course Materials, JCESOM, 2011-2012.

[22] Image Source: http://24.media.tumblr.com/tumblr_m9pt90Yw6o1rupesho2_400.jpg.

[23] Knee Surgery India, Chennai, India. Online URL: http://www.kneeindia.com/knee-replacement-surgery-guide/.

[24] Mohamed, N. N., Barrett, J., Katz, J. N., Baron, J. A., Wright, J., Losina, E., "Epidemiology of Total Knee Replacement in the United States Medicare Population". Journal of Bone and Joint Surgery, June 2005, Vol. **87A**:6, pp. 1222-1228.

[25] Diduch, D. R., Insall, J. N., Scott, W. N., Scuderi, G. R., Font-Rodriguez, D., " Total Knee Replacement in Young, Active patients. Long-Term Follow-up and Functional Outcome". Journal of Bone and Joint Surgery, April 1997, Vol. 79**A**:4, pp. 575-582.

[26] Kurtz, S., Mowat, F., Ong, K., Chan, N., Lau, E., Halpern, M., "Prevalence of Primary and Revision Total Hip and Knee Arthroplasty in the United States from 1990 Through 2002". Journal of Bone and Joint Surgery, July 2005, Vol. **87A**:7, pp. 1487-1496.

[27] Kurtz, S., Ong, K., Lau, E., Mowat, F., Halpern, M., "Projections of Primary and Revision Hip and Knee Arthroplasty in the United States from 2005 to 2030". Journal of Bone and Joint Surgery, April 2007, Vol. **89A**:4, pp. 780-785.

[28] Carlson, C. E. (1967). *Measurement of Pressure Distribution in the Human Hip Joint*. SM Thesis, MIT.

[29] Flowers, W. C. (1972). *A Man-Interactive Simulator System for Above-Knee Prosthetics Studies*. PhD Thesis, MIT.

[30] Hardt, D. E. (1978). *A Minimum Energy Solution for Muscle Force Control During Walking*. PhD Thesis, MIT.

[31] Hogan, N. E. (1977). *Myoelectric Prosthesis Control: Optimal Estimation Applied to E.M.G. and the Cybernetic Considerations for its use in a Man-Machine Interface*. PhD Thesis, MIT.

[32] Piziali, R. L., Seering, W. P., Nagel, D. A., Schurman, D. J., "The Function of the Primary Ligaments of the Knee in Anterior-Posterior and Medial-Lateral Motions". J Biomechanics, Vol. **13**, pp. 777-784.

[33] Seering, W. P., Piziali, R. L., Nagel, D. A., Schurman, D. J., "The Function of the Primary Ligaments of the Knee in Varus-Valgus and Axial Rotation". J Biomechanics, Vol. **13**, pp. 785-794.

[34] Fijan, R. S. (1990). *A Three-Dimensional Mathematical Model of the Human Knee Joint*. PhD Thesis, MIT.

[35] Hopkins, J. B. (2010). *Design of Flexure-Based Motion Stages for Mechantronic Systems via Freedom, Actuation and Constraint Topologies (FACT)*. PhD Thesis, MIT.

[36] Suggs, J. F. (2007). *Investigation of In-vivo Total Knee Arthroplasty Biomechanics Using a Dual Fluoroscopic Imaging System*. ScD Thesis, MIT.

[37] Varadarajan, K. M. (2010). *In Vivo Knee Biomechanics and Implications for Total Knee Arthroplasty Implant Design*. PhD Thesis, MIT.

[38] Most, E. (2000). *Development of a 6-DOF Robotic Test System for Studying the Biomechanics of Total Knee Replacement*. SM Thesis, MIT.

[39] Most, E. (2004). *The Biomechanics of Knees at High Flexion Angles Before and After Total Knee Arthroplasty*. ScD Thesis, MIT.

[40] Cervantes, T. M. (2011). *Design of a Bone Plate for Mandible Fracture Fixation.* SB Thesis, MIT.

[41**]** Slocum, Jr., A. H.**,** Cervantes, T. M., Seldin, E. B., Varanasi, K. K., "Analysis and Design of Rolling-Contact Joints for Evaluating Bone Plate Performance". Medical Engineering & Physics, Vol. **34**, pp. 1009-1018, 2012.

[42] Cervantes, T. M., Slocum, Jr., A. H., Seldin, E. B., "Design and Experimental Evaluation of Adjustable Bone Plates for Mandibular Fracture Fixation", Journal of Biomechanics, Vol. **45**:1, pp. 172-178, 2012.

[43] J. D. Smith, R. Dhiman, S. Anand, E. R. Garduno, R. E. Cohen, G. H. McKinley, K. K. Varanasi, "Droplet Mobility on Lubricant-Impregnated Surfaces". *Soft Matter (Accepted)*.

[44] S. Anand, A. T. Paxson, R. Dhiman, J. D. Smith, K. K. Varanasi, "Enhanced Condensation on Lubricant-Impregnated Nanotextured Surfaces". *ACS Nano*, 2012 6 (11), pp. 10122-10129.

[45] Roba, M., Naka, M., Gautier, E., Spencer, N. D., Crockett, R., "The Adsorption and Lubrication Behavior of Synovial Fluid Proteins and Glycoproteins on the Bearing-Surface Materials of Hip Replacements". Biomaterials, **30**:2072-2078, 2009.

[46] Bouxsein, M., Seton, M., HST.021 Class Materials, January/IAP 2011, Harvard Medical School.

*This page intentionally
left blank*

CHAPTER

2

THE MUSCULOSKELETAL SYSTEM

"Medicine's silent teachers have entrusted to us their most private and valuable mortal possession, so that in death they can teach us, and that we may help the living." – Unknown

2.1   INTRODUCTION

In order to design prosthetics that interact with and support the human body, an understanding of the underlying principles that govern its function must be obtained. This Chapter presents a very brief introduction to both the gross and microscopic anatomy and function of the musculoskeletal system, including joints, bone, muscle, and connective tissue. There are a plethora of texts already devoted to these and related topics; some of which are drawn upon heavily in the construction of this Chapter, and should be consulted for further details [1-4].

The primary difference between mechanical and biological joints is that most biological joints are statically indeterminate systems. Unlike man-made mechanical joints, which are designed based on physical models, one cannot consider the kinematics of a biological mechanism without

knowledge of the loads acting upon it or the forces being transmitted between two pieces of opposing articular cartilage [1]. This makes for a particularly unique challenge in modeling these structures; assumptions must often be made so that engineering models can be applied to predict the performance of biological joints.

When referring to aspects of the human anatomy, it is also important to consider use of appropriate terminology related to the location of different structures. This is done in reference to what is called the "anatomical position," a diagram of which can be seen on the left side of Figure 2.1. In a right-handed coordinate system, the X-axis would be pointing out from an individual's navel, the Y-axis would be directed orthogonally to the person's left, and the Z-axis would point out of the top of their head. This is illustrated on the right hand side of Figure 2.1.
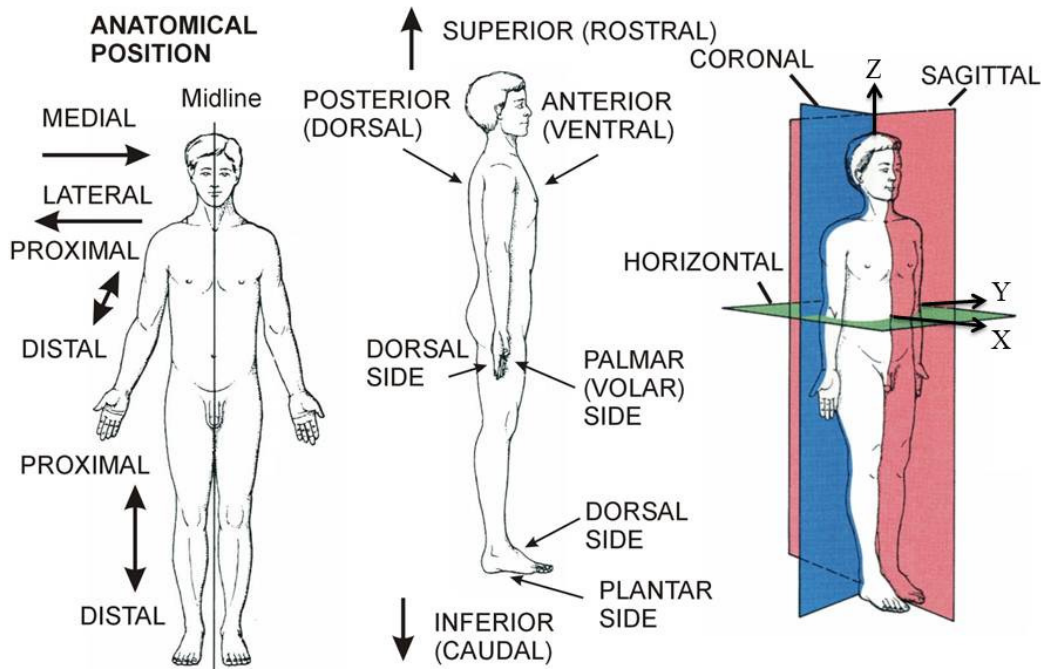
Figure 2.1: Anatomical position, showing the orientation of coronal, sagittal, and transverse planes, as well as proximal, distal, medial, and lateral directions [5]

Anatomical position is defined as a person standing erect and relaxed with hands at their sides and palms facing forward, and having three important reference planes: sagittal, coronal, and transverse. A sagittal plane bisects the body (contains the X- and Z- axes), such that on each side there are still one hand and one foot. The coronal plane is oriented vertically and is orthogonal to the sagittal plane, and can be thought of as a crown worn on the head (there is a "C" in both Coronal and Crown; contains the Y- and Z- axes). Finally, a transverse plane is horizontal and located orthogonal to the sagittal plane; this is the view most commonly used to visualize the body's structures with imaging modalities like CT or MRI (contains the X and Y axes).

Three sections address different levels of detail in the musculoskeletal system; Section 2.2 briefly outlines musculoskeletal development and describes some basic functional properties. Section 2.3 outlines the macrostructure, and gives gross anatomical examples of each tissue type (bone, ligaments, muscle, etc.). Section 2.4 describes the macrostructure of various tissues, and also presents a very brief discussion of certain aspects of the physiology of the musculoskeletal system, while Section 2.5 focuses on related pathologies.[6] These are important because observations of the body at the macro-scale are often the direct result of micro-scale pathology; understanding this link is critical to both the design of biomechanical systems as well as the delivery of effective patient care.

2.2   MUSCULOSKELETAL SYSTEM

The musculoskeletal system consists of all the bone, muscle, tendons, ligaments, synovium, and other components that enable motion, provide support and protection for vital organs, and allow

---

[6] Pathology is defined as the precise study and diagnosis of disease; as a noun it refers to the presence of disease.

a person to interact with their surroundings and maintain homeostasis. The system as a whole is derived from mesoderm, one of the three germ cell layers found in human embryos (along with endoderm and ectoderm). Endoderm forms many structures found inside the body, and also forms the lining of some body cavities. Ectoderm forms the skin, and also is the origin of the central nervous system. Separation of the germ cell layers is summarized in Figure 2.2

.
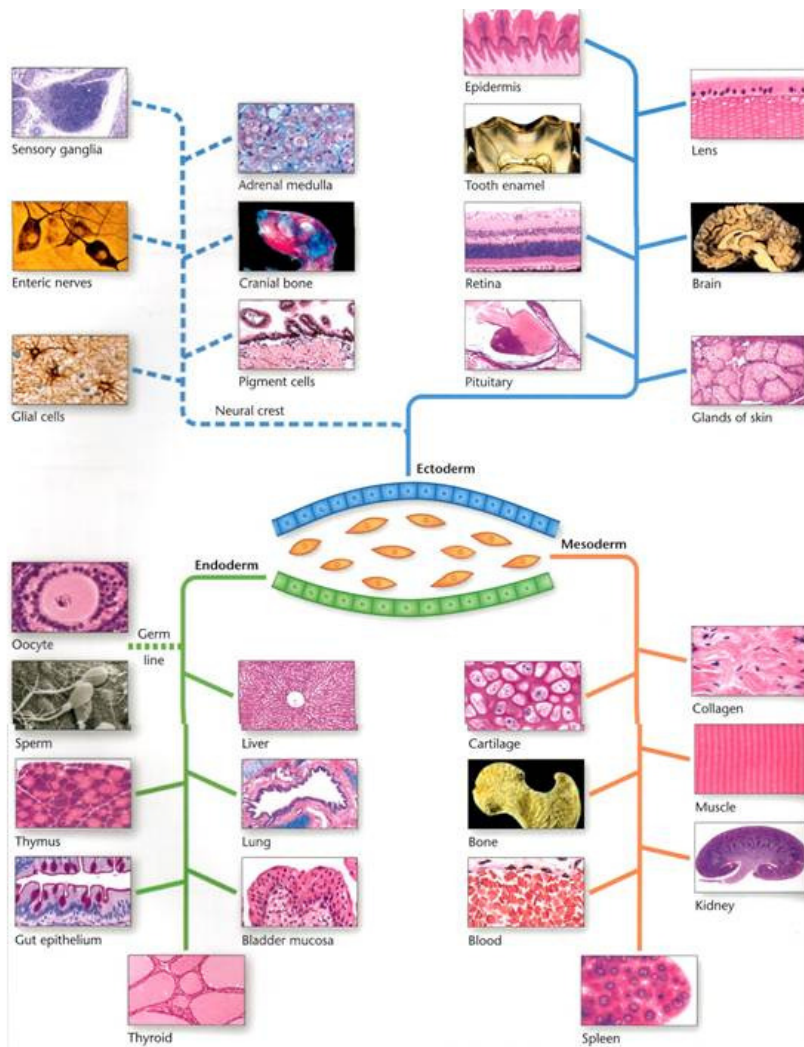
Figure 2.2: Differentiation of the germ cell layers [4].

Mesoderm further differentiates into mesothelium, mesenchyme, and other embryological tissue; mesothelium forms muscles and mesenchyme forms connective tissue, including bones and cartilage. Overall, the functions of the musculoskeletal system can be grouped into four categories [1] including (1) hematopoesis, (2) mineral storage, (3) protection of the vital organs, and (4) support and motion.

One of the most intriguing aspects of bone is that it can respond to an applied load; this principle has been described empirically as Wolff's Law: Bone will preferentially grow in such a way as to resist an applied load [6, 7]. On the microscopic level, transmembrane proteins within osteoblasts sense small amounts of strain in the bone; these induce positive changes in cellular physiology that lead to increased formation of new bone [8]. Wolff's Law is part of the motivation for preventative treatments for those at risk of developing osteoporosis (i.e., post-menopausal women). It also provides a potential explanation for the loss of periprosthetic bone seen in recipients of artificial joints.

2.3 MACROSTRUCTURE

An introduction to gross anatomy is the start of a top-down approach to learning about the musculoskeletal system, including bone, muscle, cartilage, tendons, and ligaments. Bone forms the support structure from which the rest of an individual's soft tissues derive their shape, and also provides protection for the vital organs. Muscle is found throughout the human body, in everything from blood vessels, to the lungs, and the gastrointestinal and reproductive tracts. Cartilage allows formation of a joint between two solid pieces of bone, and tendons and

ligaments allow for transmission of forces across joints. Examples of each type of tissue are shown in Figure 2.3.
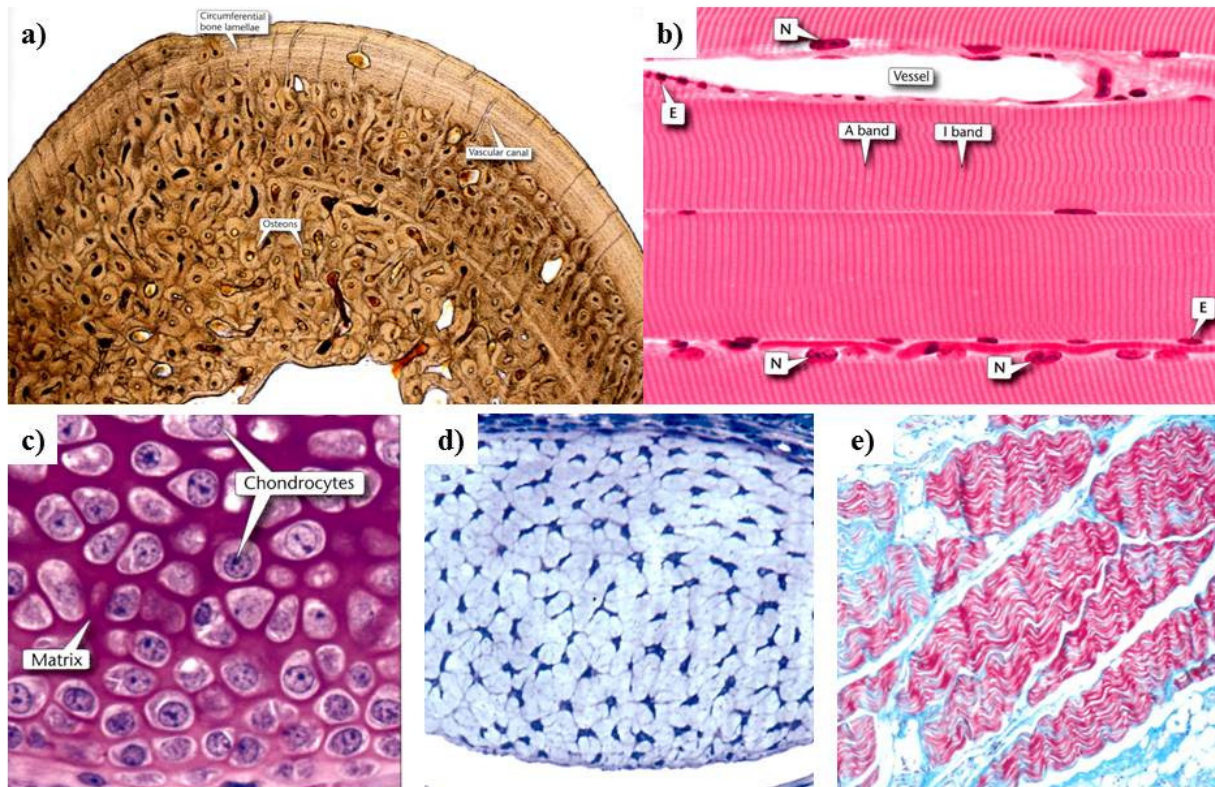
Figure 2.3: Examples of (a) Bone, (b) Muscle, (c) Cartilage, (d) Tendon, (e) ligament [4].

2.3.1 BONES

The human body contains 210 bones,[7] generally organized into three groups: long bones, short bones, and flat bones. Examples of long bones are the femur (the longest bone in the body) in the leg, and the humerus in the upper arm; these bones are defined as having a large aspect ratio. Short bones are found in the ankle and wrist, and generally have aspect ratios around 1. Flat bones can be found in the skull, the sternum, and the pelvis, and also make up the transverse and spinous processes of vertebrae. The pelvis is often also called the innominate bone as it is a

---

[7] 206 bones, plus two sesamoid bones under the head of the first metatarsal in each foot

fusion of three separate bones: the pubis, the ischium, and the ilium. Figure 2.4a—d show examples of different types of bones found in the body.
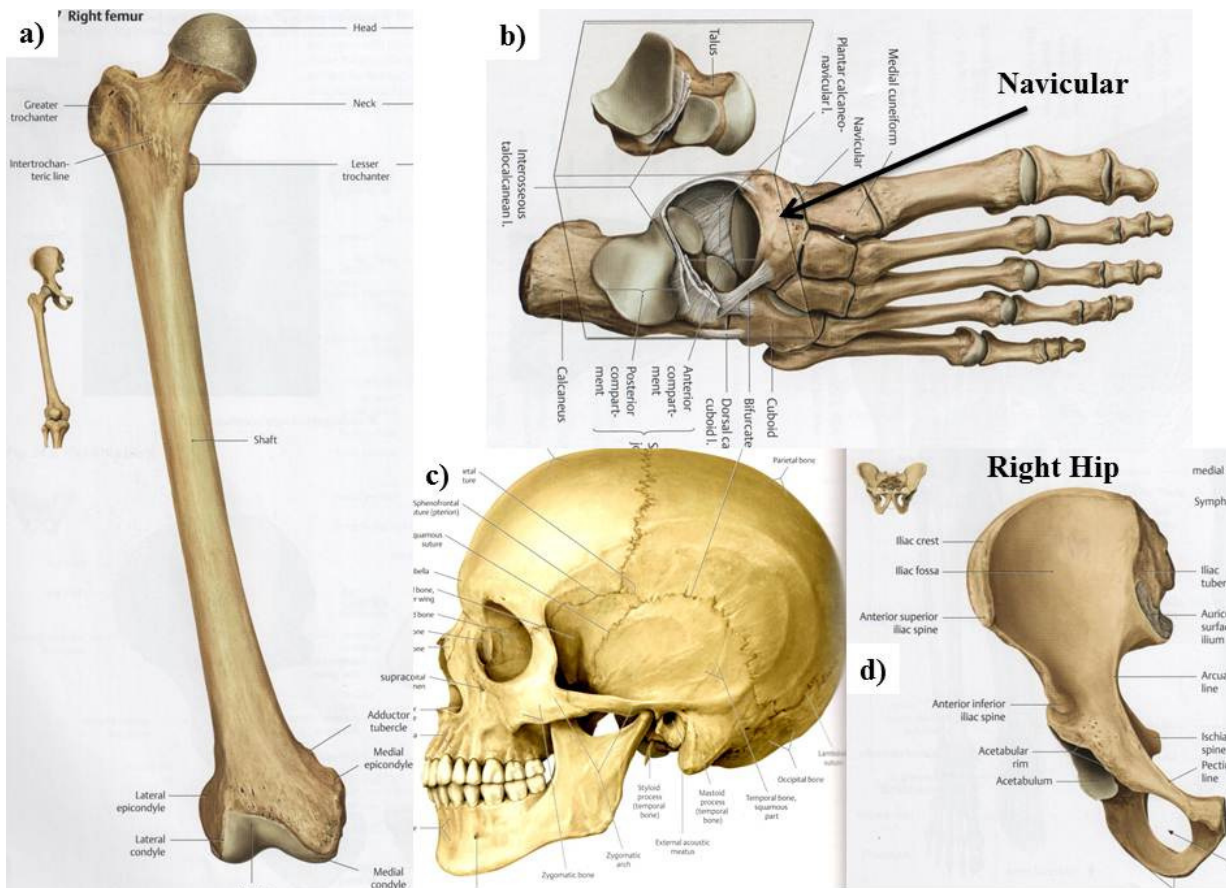
Figure 2.4: Types of bones in the body, including (a) long bones like the femur, (b) short bones like the navicular in the foot, (c) flat bones of the skull, and (d) the right half of the innominate bone (pelvis) [3].

Most bones in the body have an outer layer of dense tissue referred to as cortical bone, and an inner section of less dense, sponge-like tissue referred to as cancellous or trabecular bone. Marrow, principally found adjacent to trabeculae in the internal structure of a bone, is the principle site of hematopoiesis (growth of blood cells) which, in an adult, only occurs in the axial skeleton.

In the long bones, there are three primary segments: the diaphysis, metaphysis, and epiphysis. The epiphysis, at the end of the bone, contains the growth plate, which is closer to the metaphysis than the end of the bone; long bones have articular cartilage covering their ends that serves to form joints like the hip, shoulder, knee, or elbow. A schematic of segments of these areas can be seen in Figure 2.5 [9]. The diaphysis is the middle segment, which is made up of mostly cortical bone and is penetrated by a medullary artery that supplies nutrients to osteocytes, osteoblasts, and other cells in the bone. The metaphysis and epiphysis are mostly made up of trabecular bone covered by a thin layer of cortical bone. It should be noted that the ends of the long bones are larger in area, making them well suited to transmit high body weight forces.
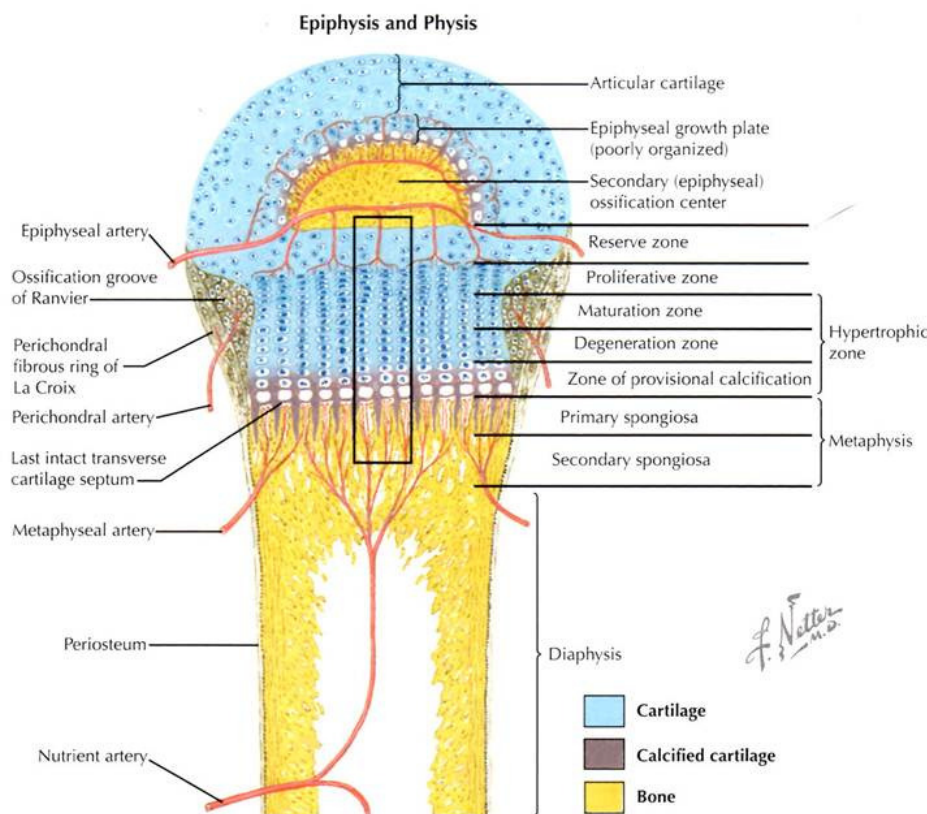
Figure 2.5: A sketch showing structures which make up the long bones, including the diaphysis, metaphysis, and epiphysis [9].

The macrostructure of bones is directly influenced by their microstructure, as described previously in the discussion of Wolff's Law. The stresses placed on a piece of bone will determine the resultant shape of the solid structures, as observed in Figure 2.6a, which shows a cross-section through the proximal part of a human femur. Figure 2.6b is a cross-section through the proximal tibia, illustrating how the ends of the long bones have increased horizontal cross-sectional areas and larger amounts of trabecular bone, ideal for distributing forces transmitted across the joint.
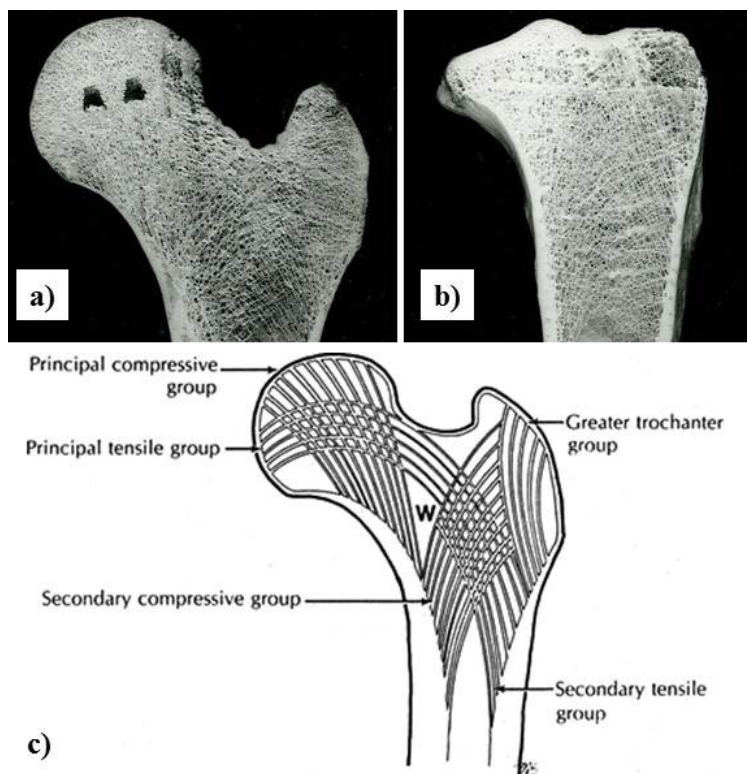
Figure 2.6: Cross-section through the proximal part of (a) the human femur and (b) the human tibia [10] and (c) a sketch showing the organization of primary trabecular fibers [6, 7].

The major orientations of trabeculae in the human femur are seen in the sketch at the bottom of Figure 2.6. This illustrates how stresses associated with supporting the body weight, like those transmitted through the innominate bone to the hip joint and down the femur, are resisted by the major orientation of trabeculae fibers as required by Wolff's law.

2.3.2   MUSCLE

There are three different types of muscule: skeletal, smooth, and cardiac. Examples of each can be seen in Figure 2.7. They are similar in their function, but all are different in their physiology and response to hormones and chemical signals. Because it is difficult to visualize smooth muscle in gross specimens, a histological section of the wall of a large, muscular artery is presented.
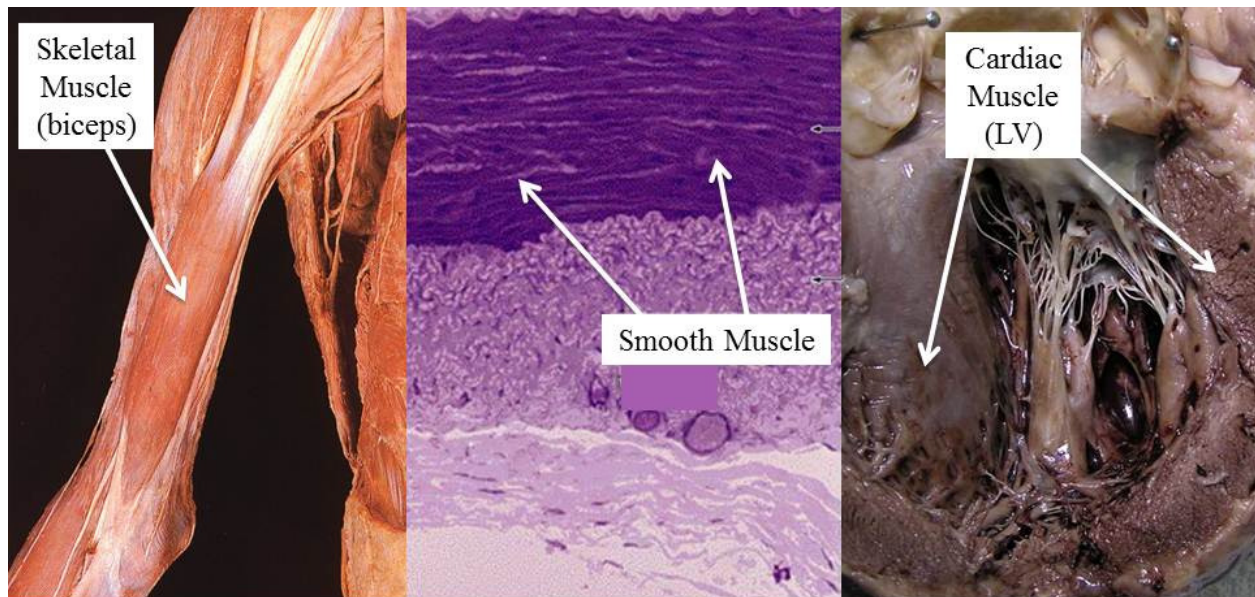
Figure 2.7: Skeletal muscle in the biceps (left), smooth muscle in an artery (middle), and cardiac muscle (right) [11].

Here, the focus is on skeletal muscle function; a detailed discussion and comparison of skeletal, smooth, and cardiac muscle as well as their physiology is outside the scope of this work. From here on, the word "muscle" will be used to refer to skeletal-type muscle. In general, a muscle can be characterized by four features: origins, insertions, actions, and innervations. More specifically, an origin is generally considered to be the more proximal attachment of the muscle to the skeleton, and an insertion the more distal attachment. The action of a muscle is based on which joint it affects; for example, one action of the biceps muscle is to flex the elbow joint (decrease the angle between the forearm and the humerus).

Some muscles also have multiple origins and insertions. Groups of fibers are organized into specific muscles, even if they share a common function, based on distinct patterns of innervation by nerves. An example of this is the quadriceps muscle in the thigh, which has four heads (hence the "quad"): rectus femoris, vastus medialis, vastus lateralis, and vastus intermedius. Each muscle group works with the others in concert to extend the leg,[8] but each is innervated by a separate fiber of the femoral nerve, and can be stimulated separately from the others.

2.3.3 JOINTS

In the human body, different joint types enable various motions, falling into two structural categories: fibrous and cartilaginous (articulating). Articulating joints are found in the fingers (interphalangeal joints), spine (between superior and inferior spinous processes of vertebrae), and the knee, and generally permit larger ranges of motion than fibrous joints. The bony surfaces

---

[8] Anatomically, the leg refers to the tissues below the knee, while "lower extremity" refers to the entire limb.

in each case are covered with articular cartilage and the joint is surrounded by a synovial membrane that produces synovial fluid which lubricates and bathes the joint.

An example of a fibrous joint is the pubic symphisis, at the anterior portion of the pelvis, formed by fusion of the left and right pubic bones created by a piece of tough, fibrous cartilage (fibro-cartilage). There are also fibrous joints between the twelve costal cartilages and the sternum (six costal cartilages on each side), and between the surfaces of each vertebral body, which in themselves are covered with articular cartilage. Examples of fibrous and cartilaginous joints can be found in Figure 2.8.
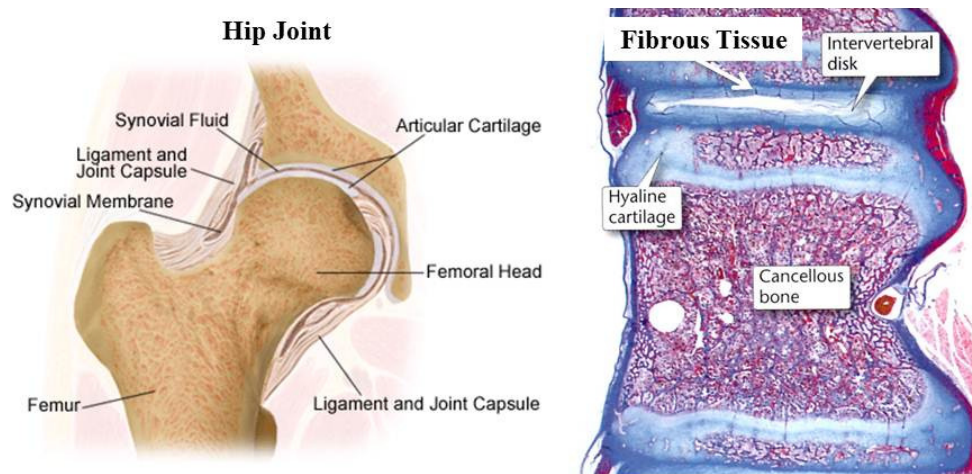
Figure 2.8: The hip, an articulating cartilaginous joint (left)[9]; one of the fibrous joints in the spine, found between each vertebral body and formed by an intervertebral disk made of fibro-cartilage (right) [4].

There are twelve major joints found in the extremities where each limb meets the torso (shoulder or hip), at the mid-portion of the limb (elbow or knee), and where the limb meets the hand or

---

[9] Image source: http://www.jacksonvilleorthopaedicsurgeon.com/total-hip-replacement.php (downloaded: 12/29/2012).

foot (wrist or ankle). The skull sits on synovial joints formed by the occipital bone and the first and second cervical vertebrae; each vertebra of the spinal column also has a synovial joint with vertebrae above and below. Of all the joints in the human body, it is those of the limbs which are generally affected by degenerative changes and are candidates for prostheses, i.e. the hip, knee, shoulder, wrist, etc.

The development of prostheses for certain joints has followed the demand for the joints that most often wear out, i.e., the hip and the knee. The hip is a ball-and-socket joint and so lends itself rather nicely to bio-mimicry with engineering materials. The knee joint however, has motions that are far more complex owing to its two polycentric, differently-sized condyles (the medial condyle being larger than the lateral). Other joints in the body, such as the shoulder, ankle, elbow, and wrist, are often replaced using prosthesis in cases where severe rheumatoid or osteo-arthritis has damaged the joint to the point at which there is significantly reduced range of motion. Here, prostheses can be used to restore function to an otherwise healthy individual. Section 3.2.1 contains a more detailed discussion of the different types of joints found in the human body and what types of prostheses are used to replace them.

2.3.4 TENDONS AND LIGAMENTS

Two common examples of these connective tissue structures are the Anterior Cruciate Ligament (ACL) and the Achilles tendon. The former is well-known for its propensity to tear, which can subsequently led to the development of arthritis of the knee, while the latter is the largest tendon in the body, as it must be able to support the body's entire weight and propel the foot forward during walking. These soft-tissue structures hold the musculoskeletal system together: Tendons

connect muscle to bone0020and ligaments connect bone to bone. Images of different soft tissue structures can be seen in Figure 2.9.
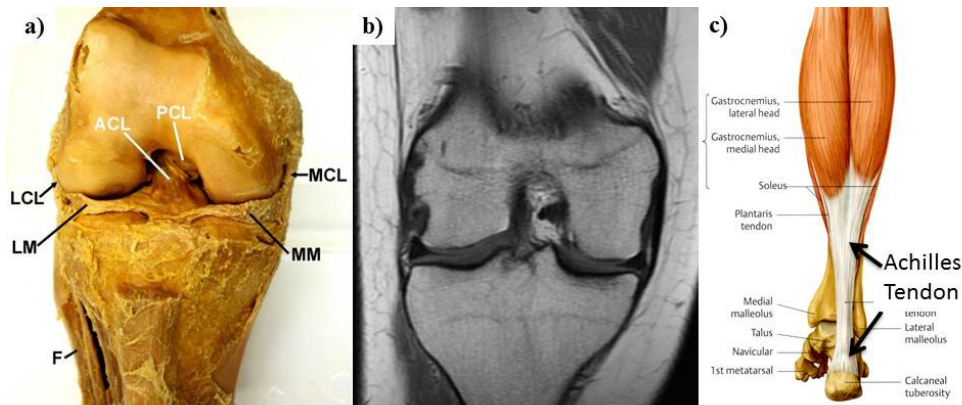
Figure 2.9: (a) The cruciate ligaments, including the ACL and PCL [5]; (b) one image from a CT scan of a torn ACL [5]; (c) an Achilles tendon from a cadaver [3].

2.4   MICRO-STRUCTURE

The physical properties of each of the tissues that make up the musculoskeletal system are defined by their microstructure, which also leads to differences between each tissue that are apparent at the macro-scale. Histological examination of tissues can be used to understand the physiological basis for their function, and how they influence homeostasis. For example, observation of the microstructure of muscle would show that striations are made up of an overlapping actin/myosin meshwork, which gives skeletal muscle the ability to pull with substantial force compared to similarly sized man-made actuators. Collagen and connective tissue are covered first, then cartilage, bone, muscle, and ligaments and tendons.

2.4.1   COLLAGEN

Collagen makes up multiple different tissues within the musculoskeletal system. The most abundant types of collagen include types I–IV, and type VII, all of which are listed in Table 2.1,

with the primary structures in which they are found. The amino acid glycine is found every third residue, and is important in the creation of hydrogen bonds to allow for formation of the triple helix.

Table 2.1: Summary of collagen types and their respective uses within the body [4].

Collage	Forms Structures	Fibrillar	Source
Type I	Tendons; Ligaments; Bone	Yes	Fibroblasts, Osteoblasts, Odontoblasts, Adipocytes
Type II	Cartilage	Yes	Chondroblasts
Type III	Reticular structure of organs	Yes	Fibroblasts, Adipocytes, Schwann cells, Muscle cells
Type IV	Lamina Densa	No	Fibroblasts, Muscle cells, Adipocytes, Schwann cells
Type VII	Anchors Lamina Densa to Reticular fibers	No	Fibroblasts, Muscle cells, Adipocytes, Schwann cells

Each collagen molecule is composed of three polypeptide chains (called α-chains) in a right-handed triple helix, hydrogen bonded together. The enzyme peptidase cleaves the ends of the α-chains in the triple helix to form the final collagen molecule. The collagen fibrils are linked together in an overlapping pattern, illustrated in Figure 2.10.
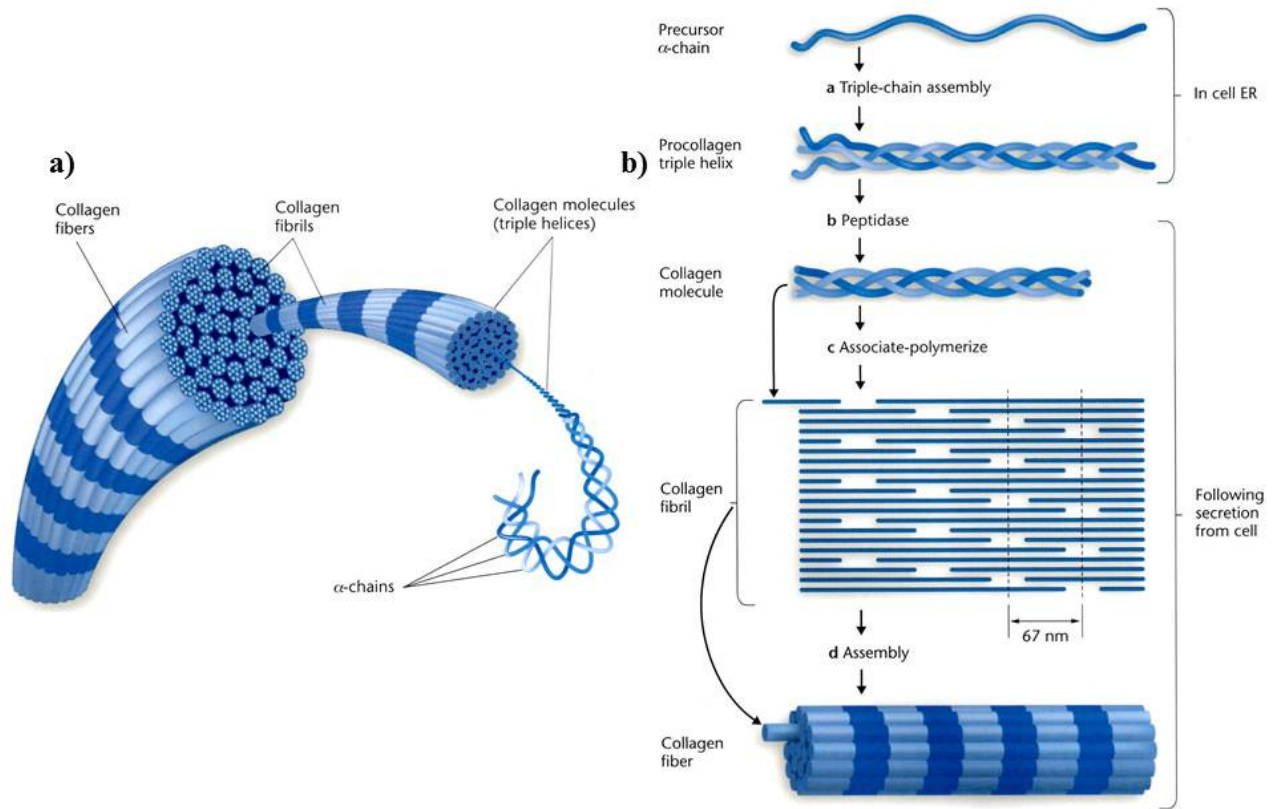
Figure 2.10: Schematic of (a) the orientation of collagen α-chains in fibers, and (b) collagen assembly, starting with the precursor α-chain, and ending with a collagen fiber [4].

On a side note, Vitamin C is an important component involved in the synthesis of collagen and is one reason that individuals who develop scurvy often have bleeding gums; the high rate of turnover in the oral mucosa leads to bleeding as new connective tissue cannot easily be synthesized. Thus, Vitamin C is an essential nutrient for maintenance of connective tissue. Additional information on collagen synthesis and the different tissues it helps to create can be found in a pathology text like Robbins and Coltran [12, pp. 437-438].

2.4.2   CARTILAGE

Cartilage, made from Type II collagen, provides both strength and flexibility to structures in the human body, and also enables highly efficient articulation of joint surfaces. Cartilage is also present as an intermediate during the growth of bone, as it atrophies and then undergoes mineralization both during embryological developing of the skeleton, and during the fracture healing process. During the growth of new cartilage, chondroblasts, differentiated from mesenchymal stem cells, sequester themselves in lacunae (small pockets where the cells reside) by secreting cartilage matrix proteins (Type II collagen, chondtroitin sulfate, keratin sulfate, and hyaluronic glycosaminoglycans – GAGs). Figure 2.11 shows an image of hyaline cartilage in the initial growth phase, with chondrocytes sequestering themselves in lacunae. Newly formed chondrocytes are flat and found near the periphery, which blends with a superficial fibrous layer on the right side of the image.
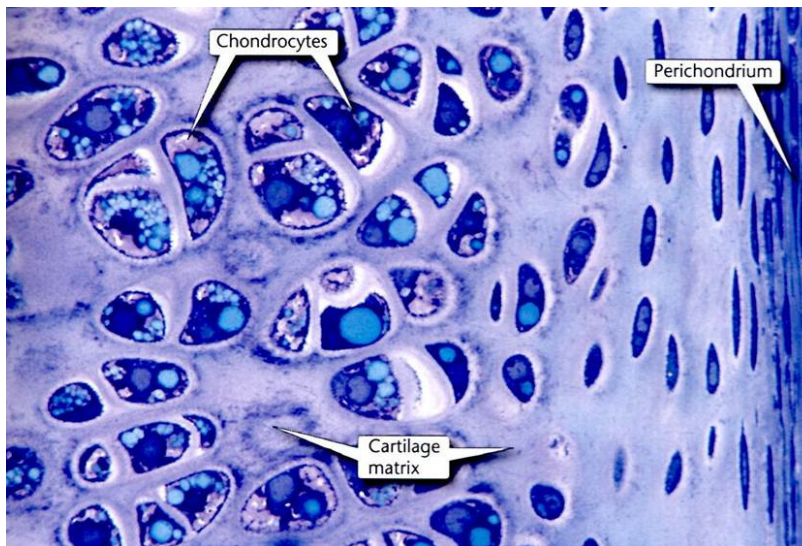
Figure 2.11: Growth of hyaline cartilage showing chondrocytes in lacunae (left side), and the fibrous perichondrium (right side) [4].

Continued expansion of the tissue occurs through either interstitial or appositional growth; interstitial describes the formation of new chondroblasts in the center of the tissue, and appositional refers to new chondroblast growth at the periphery. One chondroblast will divide to form two daughter chondroblasts. Once the growth is complete, minor injury can be accommodated by growth of new chondroblasts from chondrogenic cells in the perichondrium; extensive damage leads to differentiation of mesenchymal cells into fibroblasts and formation of a fibrous scar. Cartilage is found in joints (articular cartilage), the ear and nose, the rib cage, and as fibrocartilage in certain joints (i.e. the pubic symphisis). Figure 2.12 shows a cross section of articular cartilage with calcified areas and the subchondral bone.
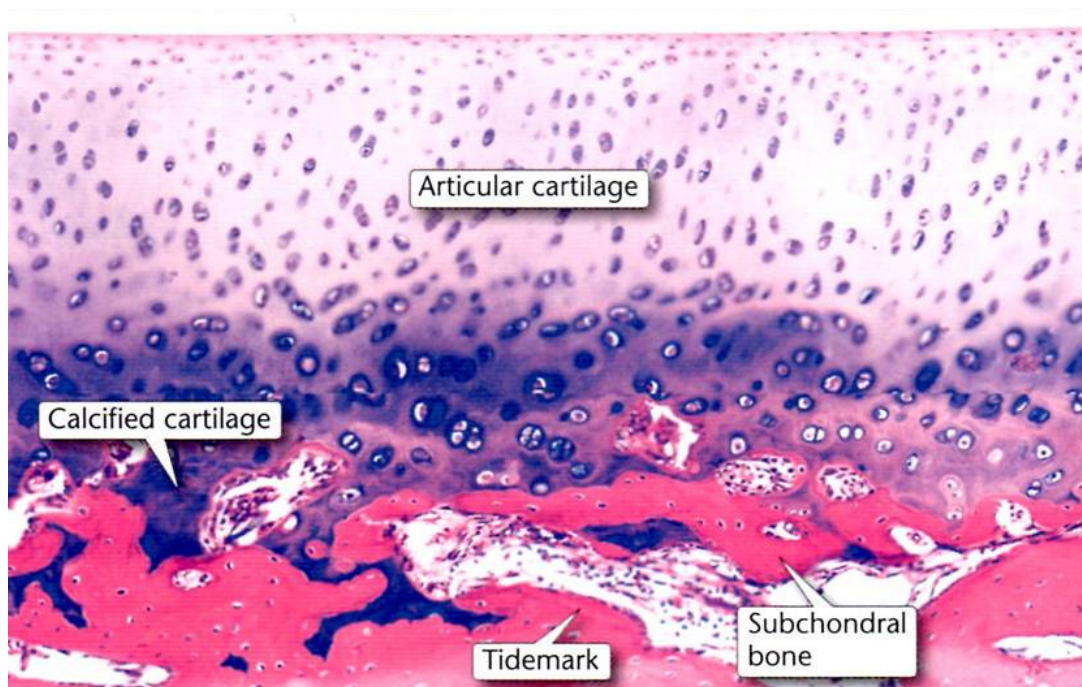
Figure 2.12: Articular cartilage, showing periosteal chondrocytes and underlying bone [4].

2.4.3 BONE

Bone serves as a functional support for soft tissues, is the site of proliferation for a majority of the cellular components of the immune system, and is also the principal location for storage of

minerals like calcium and phosphate in the body. The two principal cell types involved in the formation and degradation of bone are osteoblasts and osteoclasts, which can be seen in Figure 2.13; osteocytes are senescent osteoblasts that reside in lacunae and maintain mature bone. Figure 2.14 shows a sketch of the different types of cells found in bone, including osteoblasts, osteoclasts, and osteocytes. The distinction between osteoblasts and osteoclasts is important as it forms the basis for several pathologies related to implant failure (e.g. periprosthetic osteolysis, osteoporosis) and age-related bone loss (osteoporosis).
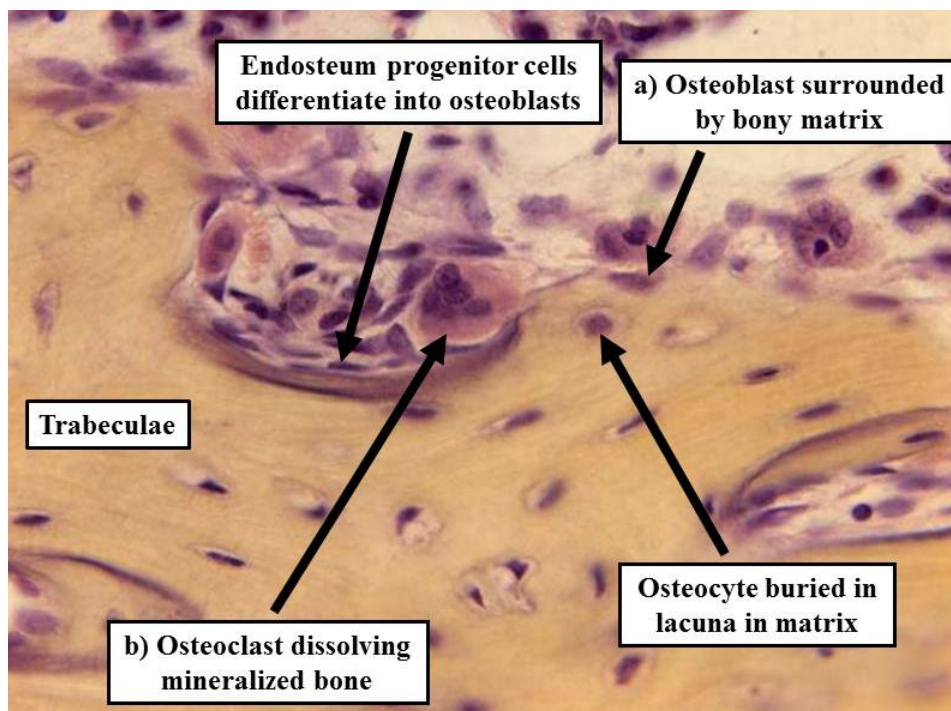
Figure 2.13: Images of (a) osteoblasts and (b) osteoclasts in trabecular (cancellous) bone [13].
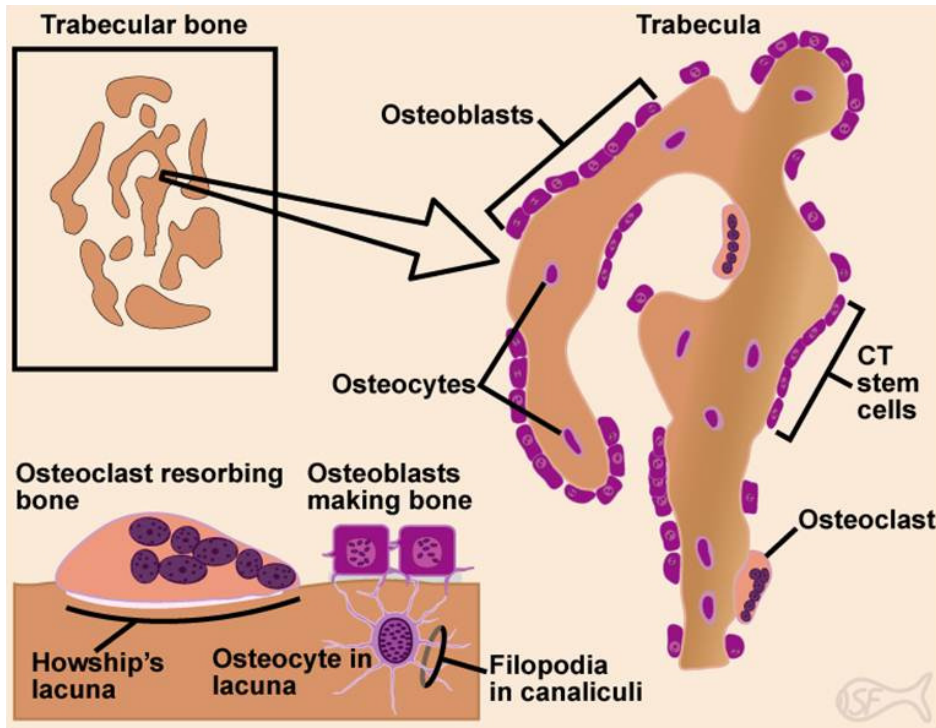
Figure 2.14: Schematic showing trabecular bone, osteoclasts, osteoblasts, and osteocytes and their various functions [13, 14].

Bone growth (ossification) in the fetus occurs via two methods: intramembranous and endochondral, illustrated in Figure 2.15. In the primary ossification center, new bone is found at the center of the image, and hyaline cartilage and the zone of hypertrophying chondrocytes is found at the periphery. Endochondral ossification in the image on the right shows the diaphysis (center) separating the two future epiphyseal areas currently formed by hyaline cartilage [4].
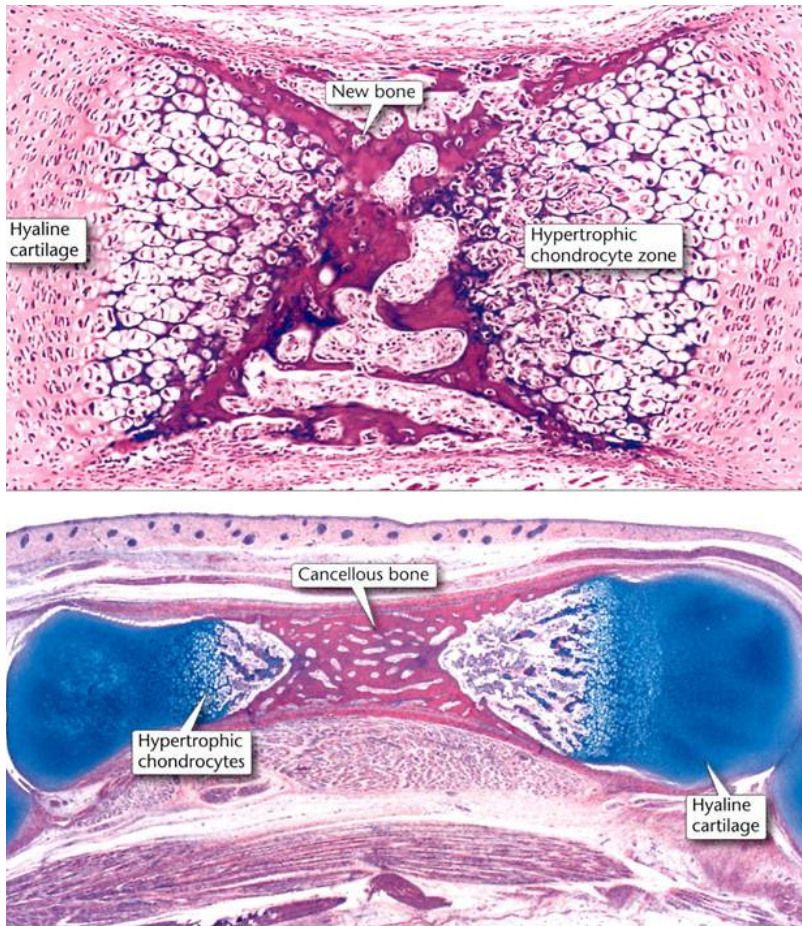
Figure 2.15: Images of a primary ossification center (top) and endochondral ossification (bottom) [4].

Intramembranous ossification involves a thin sheet of mesenchymal tissue that eventually forms flat bones, like those of the skull. Osteoblasts, derived from mesenchymal cells, secrete osteoid (bone matrix proteins) and form lacunae. The mesenchymal cells, however, are initially surrounded by GAGS and randomly oriented collagen fibrils, which will later give the "woven" appearance to immature or "woven" bone. Osteoid calcifies into tiny spicules ("spicule" meaning needle-like) which expand to form trabeculae, and then grow appositionally through the addition of more bone by osteoblasts. As the trabeculae grow, the network of spicules can encircle blood

vessels and form immature (woven) primary bone. Periosteum, "peri-" meaning "outer" and "osteum" referring to bone, is a fibrous sheet created by the outermost layer of cells of the original mesenchymal sheet, which form fibroblasts, and then go on to create the fibrous perisoteum.

Endochondral ossification, like that seen in the bottom image in Figure 2.15 forms the long and short bones. The outline of the bone is created by hyaline cartilage formation within a mesenchymal layer. Formation of a periosteal bony collar surrounding the hyaline cartilage is the first indication that the structure will convert to bone; the outer cellular layer of the hyaline cartilage structure is converted from perichondrium to periosteum, which forms osteoblasts. This is followed by the subsequent laying-down of the bony collar and enables the next step of bone formation. Cartilage relies on diffusion for nutrients, and as the bony collar forms, diffusion is cut off. The chondrocytes will eventually hypertrophy and die, and the cartilage matrix calcifies.

Blood vessels of the periosteum then pierce its surface and invade the parenchyma, enabling osteoprogenitor cells to follow suit and colonize the calcified cartilage matrix. Osteoprogenitor cells then differentiate into osteoblasts and secrete osteoid, which calcifies and forms immature (woven) bone. Over time the woven bone is remodeled by osteoblasts and osteoclasts to form compact (mature) bone. Cartilage remains at either end of the bone, both in the epiphyseal (growth) plate (hyaline cartilage) separating the diaphysis and epiphysis, and as hyaline (articular) cartilage enabling relative motion between opposing bone ends.

Fully developed bone has a hierarchical structure, shown in the histological slide of cortical and trabecular bone seen in Figure 2.16. The major functional unit of cortical bone is the osteon, a cylinder of bone with a central opening referred to as a haversian canal through which blood vessels can grow. Osteoblasts and osteoclasts work in opposition of one another to create the haversian canals. Both macrophages and osteoclasts are derived from macrophage progenitor cells, descended from pro-monoblasts differentiated from bone marrow stem cells. This common cellular ancestor means that forces acting on osteoclasts invariably will have some influence on macrophages, and vice versa, ultimately influencing the macro-structure of bone. Empirical observations of periprosthetic bone loss in joint replacement have linked the death of macrophages, due to ingestion of micro-scale particles from implant components, to up-regulation of osteoclast activity leading to increased bone resorption (osteolysis) near the implant (periprosthetic).
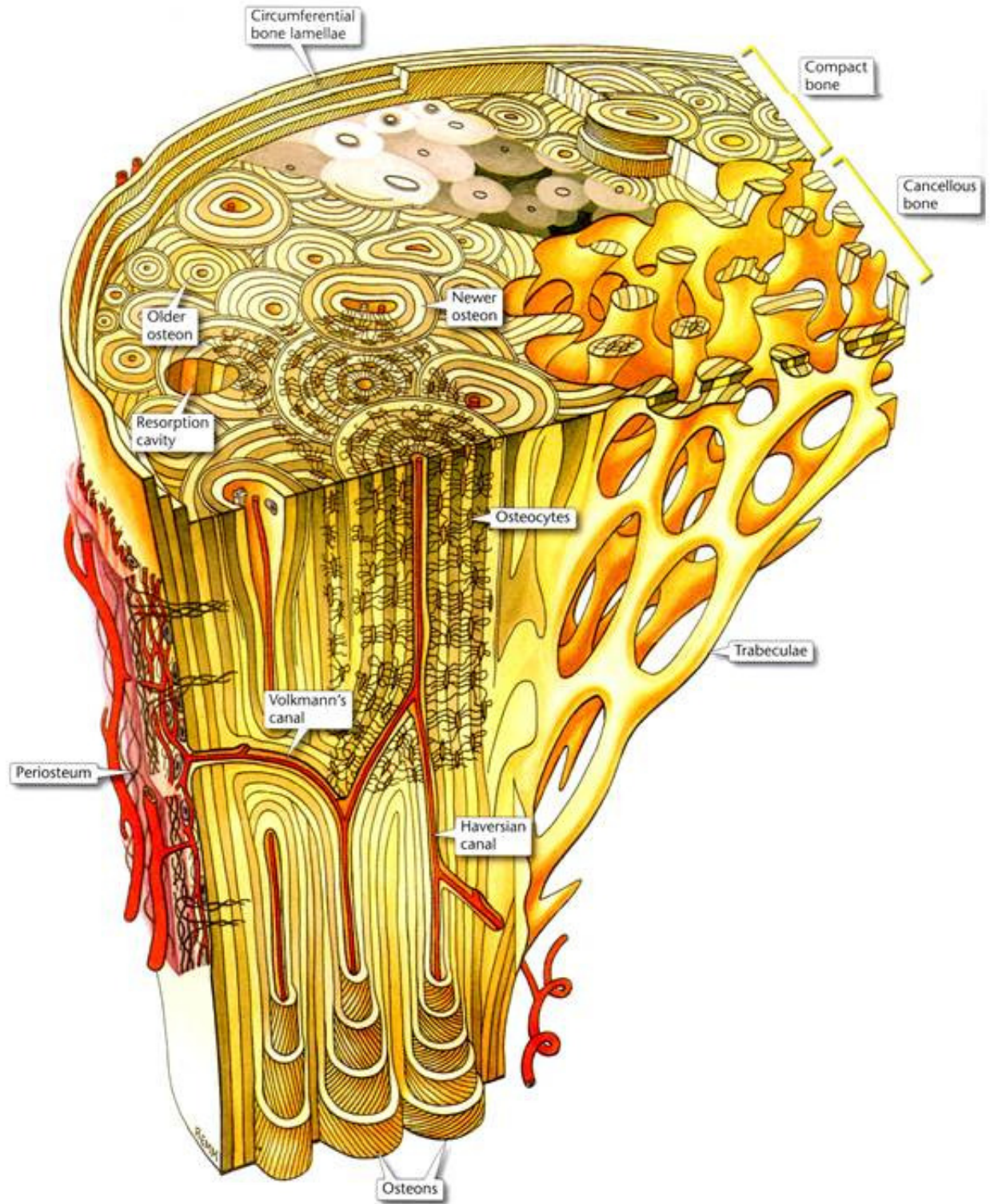
Figure 2.16: Images showing the hierarchical structure of (a) cortial (compact) bone and (b) trabecular (cancellous) bone [4].

Osteons and haversian canals are formed by the opposing actions of osteoblasts and osteoclasts in what is referred to as a "cutting cone," an example of which can be seen in Figure 2.17. Osteoclasts are found at the front of the tear-drop-shaped cutting cone and dissolve bone by secreting acids that break down the mineral matrix, which is resorbed and recycled to become a source of calcium, or to make new bone. Osteoblasts cover the inner surface of the cutting cone behind the osteoclasts, and secrete compounds that eventually mineralize and form new bone. A cutting cone will progress at a rate of a few millimeters per every few weeks, resulting in a person's entire skeleton being remodeled every few years.
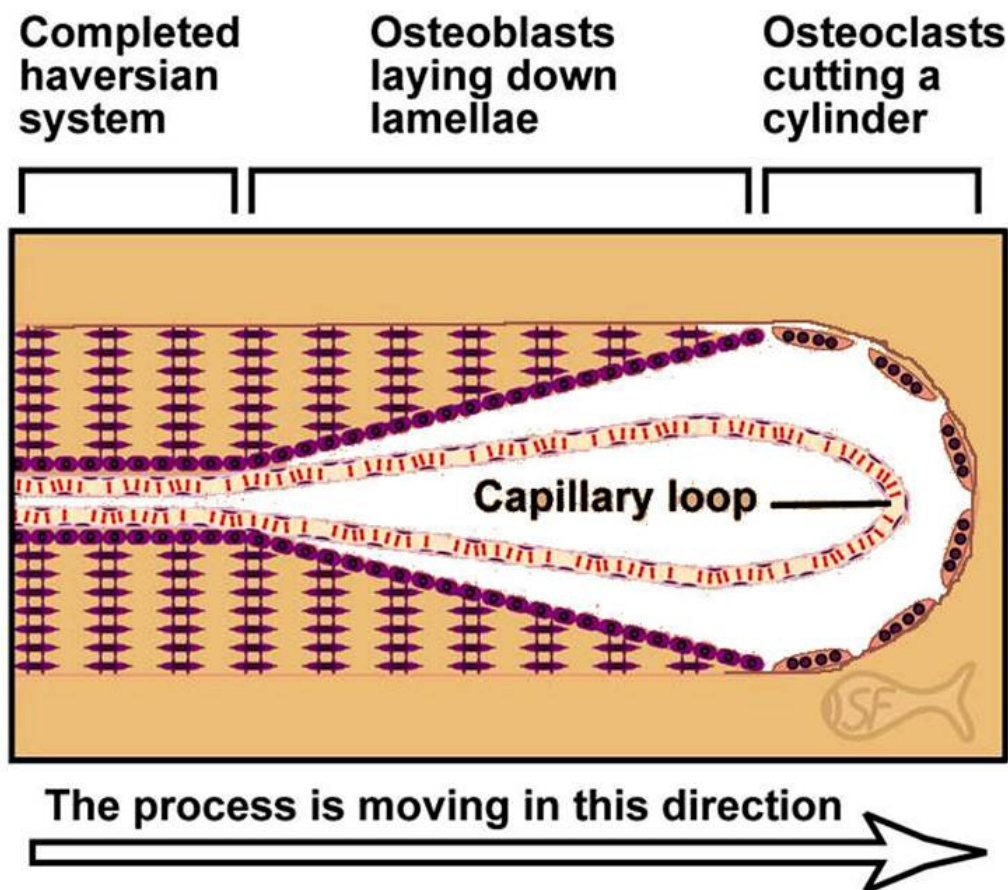
Figure 2.17: A cutting cone, which results in the formation of new haversian canals [13, 14].

2.4.4 MUSCLE

There are three different types of muscle: skeletal, cardiac, and smooth. They are classified based on their histological characteristics as well as their functions; examples of each are shown in Figure 2.18. Skeletal muscle can be identified by the presence of abundant striations, formed by contractile filaments that overlap inside the cytoplasm of each individual muscle cell [4, 13-14]. Also, all of the muscle fibers and myocytes (muscle cells) are generally oriented in the same direction as seen in the section in Figure 2.18a. Cardiac muscle is also striated, but is differentiated from skeletal muscle by the presence of intercalated disks, seen in Figure 2.18b. Smooth muscle, in Figure 2.18c, has neither striations nor intercalated disks.
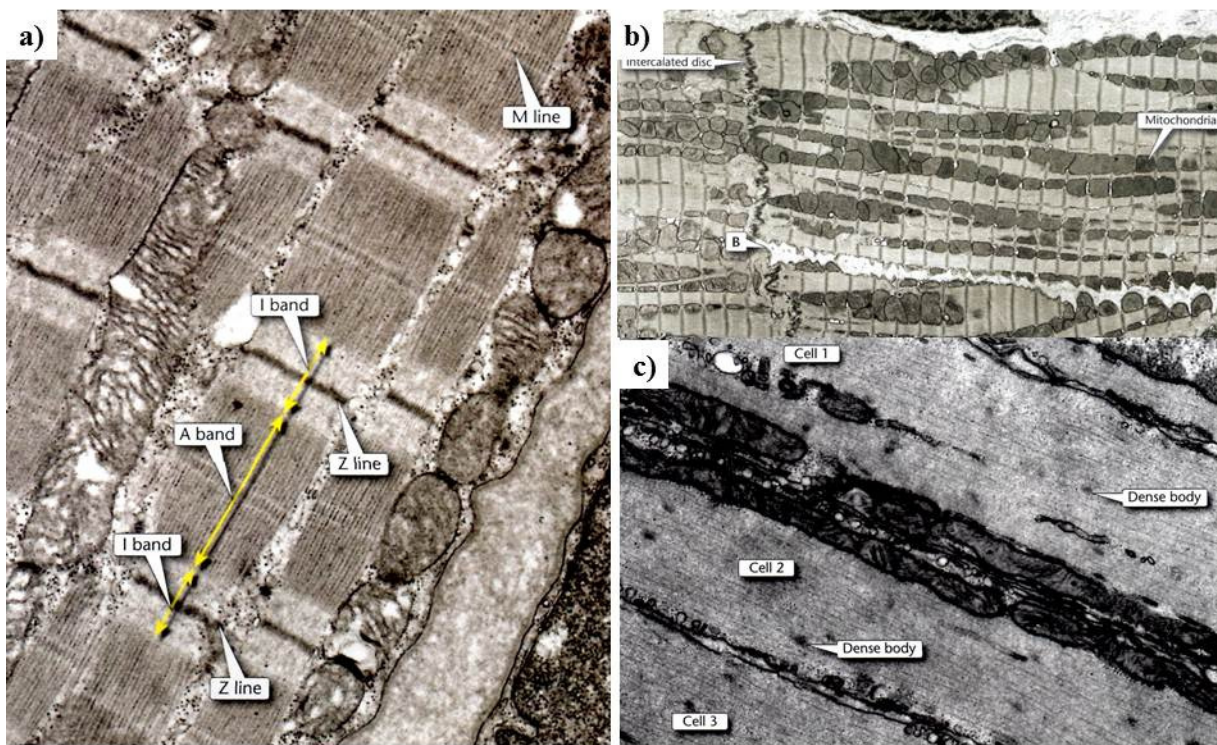
Figure 2.18: Histological preparations of (a) skeletal muscle, (b) cardiac muscle, and (c) smooth muscle, with characteristic features of each labeled [4].

Figure 2.19 shows a schematic of the organization of skeletal muscle, starting with the macro structure, all the way down to the molecular structure with myosin, actin, and troponin molecules making up the myosin/actin crosslinking.
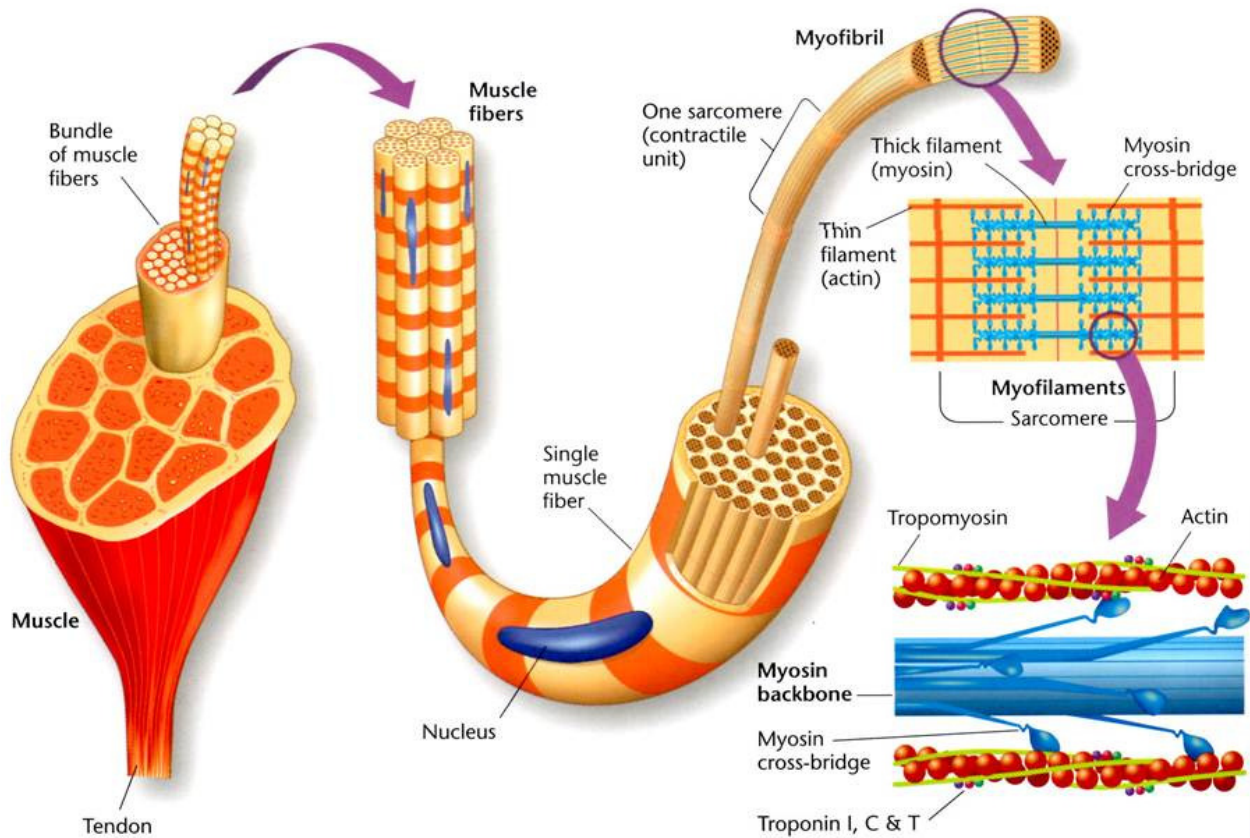
Figure 2.19: The structure of skeletal muscle, with bundles of muscle fibers, a single muscle fiber with a nucleus, down to the sarcomere and the myosin/actin crosslinking [4].

The striations seen in skeletal muscle come from the basic contractile unit of a muscle fiber, the sarcomere, which is made up primarily of actin and myosin filaments. Actin filaments are anchored to the Z line, a backbone of actin that runs orthogonally to the longitudinal axis of the fiber; a sarcomere is defined as the space between two Z lines. Figure 2.20 shows a microscopic view of the sarcomere, with the Z lines, M lines, A band, and I band. The M line is where thick myosin filaments are anchored, and is in the middle of the dark A band, which is the location of

myosin filaments. The I band is the location of thin actin filaments that have not yet overlapped with myosin, and is thus lighter than the A band. Excessive stretching is resisted by the intermediate filament protein desmin, which connects adjacent sarcomeres.
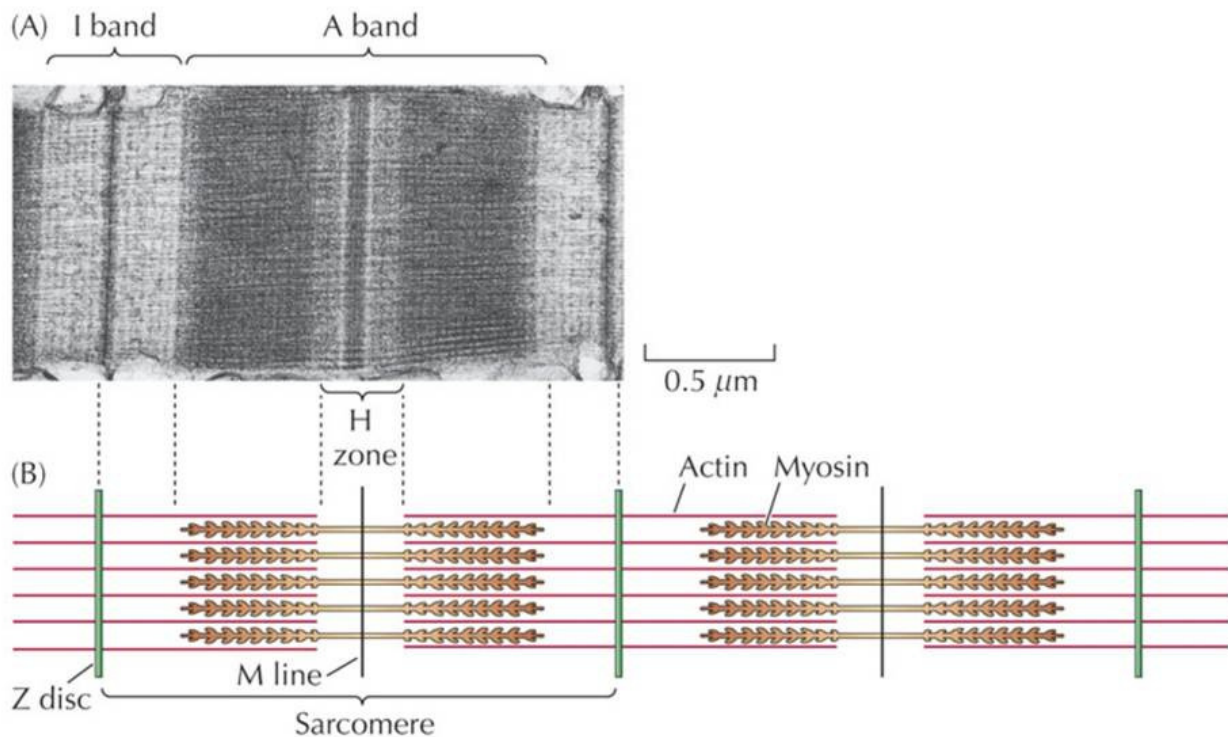
Figure 2.20: A histological section showing a sarcomere, the basic contractile unit of skeletal muscle [15].

Cardiac muscle has striations, but is also characteristically different from skeletal muscle in that it contains what are called intercalated disks, shown in Figure 2.18b. These are where cardiac muscle cells are joined by inter-cellular gap junctions such that a depolarization of one cell allows stimulation of subsequent myocytes without requiring an additional nerve impulse.

Intercalated disks, along with purkinje fibers[10], ensure that cardiac muscle cells contract in relative unison. Finally, smooth muscle does not have striations, and is often observed to have a stochastic arrangement of cells, as seen in Figure 2.18c. In-depth discussions of the differences among the three types of muscle can be found in [4], and many more images of their structure can be found in [4, pp. 137-160].

2.4.5 TENDONS & LIGAMENTS

Tendons and ligaments are arrangements of dense connective tissue, allowing the structures to withstand substantial amounts of tensile force. Tendons are either composed of regular or irregular connective tissue. In regular connective tissue, the fibers are generally organized in one direction like a rope, whereas irregular connective tissue has a more stochastic three-dimensional orientation of fibers, somewhat like a net. Figure 2.21a-b shows a histological slide of dense regular connective tissue found in a tendon, and the enthesis, where the tendon inserts onto a bone. Tendons that are made of dense irregular connective tissue, which usually attach muscle to bone, can support many muscle fibers pulling in different directions and so must be relatively isotropic. The achille's tendon is one of the most well-known structures in the human body, for its involvement in the death of the structure's namesake.

---

[10] Highly-conductive modified cardiac muscle cells that help electrical signals spread rapidly through the ventricles.
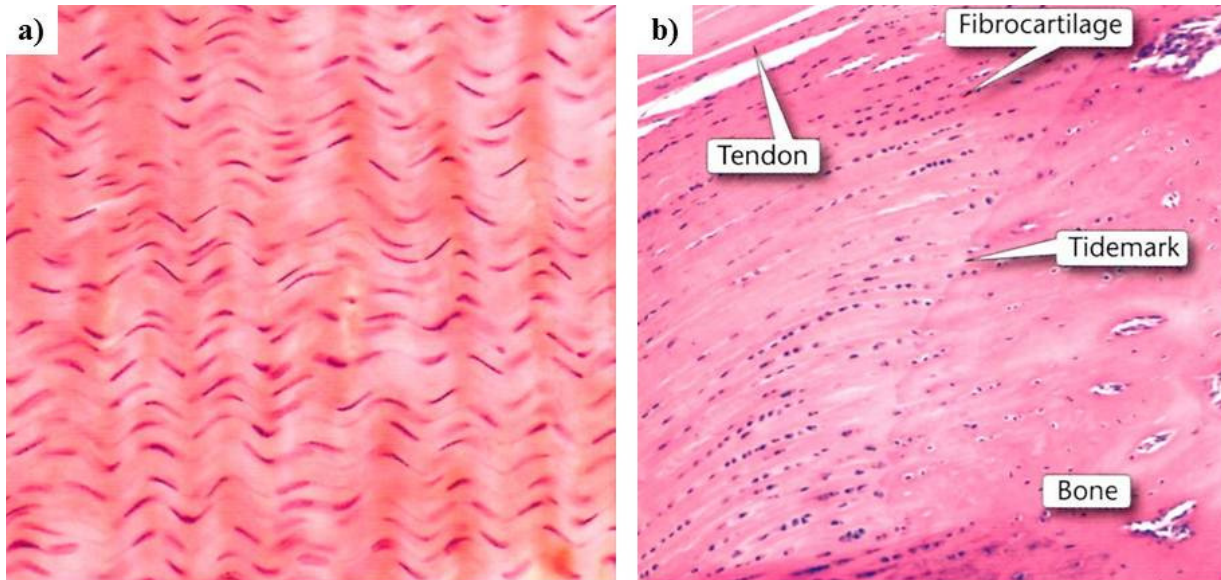
Figure 2.21: (a) Dense regular connective tissue of a tendon; (b) fibrocartilage and the enthesis, where a tendon or ligament attaches muscle to bone [4].

Ligaments are made up of dense regular connective tissue, as they connect two pieces of bone together and so usually resist loads applied nominally in a single direction. Examples of ligaments are the anterior and posterior cruciate ligaments, which resist subluxation forces in the knee joint and, with the lateral and medial collateral ligaments, hold the cartilaginous knee joint together. Ligaments also generally have a higher content of elastic fibers, as it would not make sense for a muscle to contract and have to take up slack in an elastic tendon when trying to run away from a saber-tooth tiger. Because ligaments provide more structural support, having some degree of elasticity decreases the chance that they will tear under adverse motions, i.e. a high stiffness ACL would probably be more prone to tearing. Figure 2.22 shows images of the elastic fibers in a ligament, and a section of a ligament with multiple collagen bundles making up its structure.
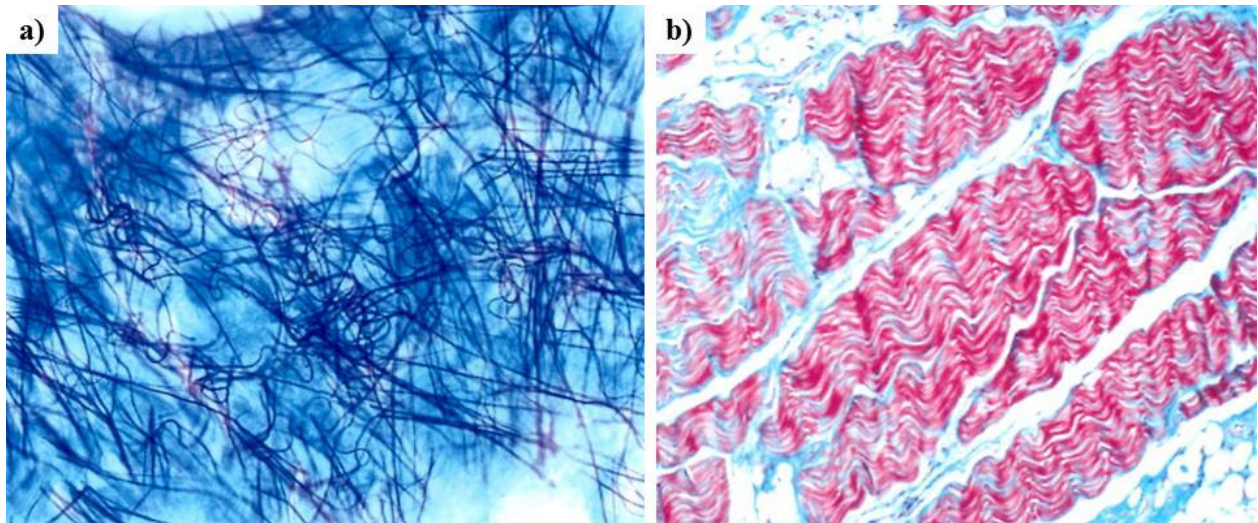
Figure 2.22: Images of the microstructure of ligaments showing (a) elastic fibers (the dark blue lines) in the extracellular matrix of a ligament that have relaxed with fixing and staining of the tissue sample; (b) wavy collagen fibers in a ligament (red) surrounded by connective tissue and elastin (blue/white non-staining) [4].

2.5   PATHOPHYSIOLOGY

Pathophysiology of the musculoskeletal system is often the result of biochemical imbalances in cellular function resulting in defects in cartilage formation (marfan's syndrome, osteogenesis Imperfecta), nerve signal conduction impairments (myasthenia gravis), joint integrity problems (arthritis, ankylosing spondylitis), loss of bone structure (osteoporosis), and various other ailments. Most of these will be discussed here only briefly; multiple resources are available for far more detailed coverage of musculoskeletal pathophysiology [2, 6, 9; 12, Ch. 22].

2.5.1   CARTILAGE FORMATION

Biochemical defects in the formation of cartilage lead to diseases of the connective tissues like marfan's and ehlers-danlos syndromes, and conditions like osteogenesis imperfecta, where the

bones are weak and brittle. In marfan's syndrome, a defect in the gene for fibrillin leads to formation of altered fibrillin molecules. A patient with marfan's is typically tall and lanky, with long fingers and is also commonly double-jointed. Because the defect is of elastic connective tissue that is also found in the circulatory system (i.e. the aorta), these patients are at increased risk for developing aneurysms, dissections, and other complications because the integrity of their vessel's walls are more easily compromised. An excellent discussion of marfan's syndrome can be found in Chapter 3 of Robbins and Coltran: Pathologic Basis of Disease [12, pp. 94-98].

2.5.2   *CONDUCTION ABNORMALITIES*

These types of diseases are often neurological, but have a direct impact on the musculoskeletal system, the innervation of which by nerves enables induction of contractions. As described earlier, groups of muscle fibers are innervated by individual nerve fibers, and in diseases like myasthenia gravis, antibodies affect receptors at the neuromuscular junction. This results in impaired stimulation of muscle fibers, manifesting as weakness and loss of function [12, pp. 1275-76].

2.5.3   *JOINT INTEGRITY*

Diseases affecting the integrity of joints include osteoarthritis, rheumatoid arthritis, and ankylosing spondylitis. Osteoarthritis is a degenerative disease associated with the process of aging, and has also been observed to have a high chance of developing in a young person with a joint subjected to trauma (like an ACL tear) [16, 17]. Rheumatoid arthritis is an immune system-related disease that leads to progressive degeneration of joints, causing significant morbidity associated with loss of function.

2.5.4   BONE STRUCTURE

Diseases of the structure of bone can occur as developmental or metabolic disorders, or as disorders in the formation of Type I collagen (the precursor of bone). Osteogenesis imperfecta (OI), osteoporosis, paget's disease, rickets (seen in children) or osteomalacia (seen in adults), and Vitamin D deficiency all affect the strength of the composite tissue, resulting in weak, fragile bones that are prone to fractures. Also, the long bones of children with Rickets are bowed as they are unable to properly support the increasing weight of the growing individual. While these conditions all have similar effects on the patient, they range from congenital defects (such as OI), to age-associated diseases (like osteoporosis) to the result of changes in metabolic function (as in Paget's).

OI occurs when there is a defect in the formation of Type I collagen, which serves as a precursor to bone formation (and is mineralized during the formation of bone); one of the prototypical signs observed in a patient with OI is blue sclera (the normally white part of the eye surrounding the iris). This is because the sclera has Type I collagen in it, and is thinner due to the defective collagen that allows the underlying vasculature to show through, giving it a bluish hue.

Osteoporosis results from a dis-equilibrium in the formation and degradation of bone. These two opposing processes are well-balanced in most individuals, leading to normal physiological turnover of the bones every few years and the formation of subsequent layers of haversian systems. As described in Section 2.4.3, osteoblasts and osteoclasts drive each of these opposing processes (formation and degradation, respectively), so factors which influence the function of

either cell type can tip the balance in favor of one or the other process. In post-menopausal women, lower levels of estrogen lead to a dis-inhibition of osteoclast activity, causing increased rates of bone resorption. Wolff's Law has some influence on bone homeostasis as well, as patients can develop osteoporosis after significant periods of inactivity or bed rest. Further, it can also be caused by low-mineral states as it is synonymous with low bone mineral density.

2.5.5   BIOMECHANICS

The study of the kinetics and kinematics of the musculoskeletal system is a very diverse field, ranging from static analysis of bones for things like fracture fixation [18], to dynamic walking models of the lower limbs used for developing bipedal robots and limp prostheses [19, 20]. The Journal of Biomechanics [21] and the journal Clinical Biomechanics [22] are two excellent sources of the latest in advanced research in the field and should be consulted for further study. Also, Chapters 3—6 of this thesis all have a foundation rooted in some aspect of this field.

2.6   REMARKS

The human musculoskeletal system is the ultimate machine, capable of self-repair, with the ability to remodel and also generate immense forces due to the high power density of muscle. As an engineer with aspirations of designing mechanical prostheses to interact with this system, one is humbled by its complexity but also inspired by its beauty. As with any other endeavor, the design engineer must develop a detailed understanding of the systems with which they are working, as often inspiration for ideas can be found through study of new concepts. An example of this is the ideas presented in Chapter 6, related to enabling the body's natural lubricants to better function in a joint through coating its surfaces with micro- and nano-structures.

Another example is the modification of existing machine elements so that their kinetics exactly match the kinematic motion of existing biological joints. Here, the mechanical joints which are modified are readily at the disposal of a design engineer, and it is known how to make them very durable.

2.7   REFERENCES

[1] Bartel, D. L., Davy, D. T., Keaveny, T. M., "Orthopaedic Biomechanics". Pearson Prentice Hall, Upper Saddle River, NJ, 2006.

[2] Brinkmann, P., Frobin, W., Leivseth, G., "Musculoskeletal Biomechanics" 1st Ed. (2002), Thieme Medical Publishers, New York, NY.

[3] Gilroy, A. M., MacPherson, B. R., Ross, L. M., Eds., "Atlas of Anatomy", 1st Ed. (2008), Thieme Medical Publishers, New York, NY.

[4] Kerr, J. B., "Functional Histology", 2nd Ed. (2010), Mosby Elsevier, New York, NY.

[5] Zill, S. N., Gross Anatomy and Embryology, Course Materials, JCESOM, 2011-2012.

[6] Bucholz, R. W., Heckman J. D., Court-Brown, C. M., Tornetta, P., "Rockwood and Green's Fractures in Adults", 7th Ed. (2009), Lippincott Williams & Wilkins, Philadelphia, PA.

[7] Skedros, J. G., Baucom, S. L., "Mathematical Analysis of Trabecular 'Trajectories' in Apparent Trajectorial Structures: The Unfortunate Historical Emphasis on the Human Proximal Femur". Journal of Theoretical Biology, Vol. **244**:1, January 2007, pp. 15-45.

[8] Majeska, R. J., "Cell Biology of Bone", In: Cowin, S. C., editor. Bone Mechanics Handbook, 2nd Ed., CRC Press, 2001, pp.1-24.

[9] Thompson, J. C., "Netter's Concise Orthopaedic Anatomy", 2nd Ed. (2010), Saunders Elsevier, Philadelphia, PA.

[10] Gibson, L. J., 3.595 – Mechanics of Porous Materials, Course Material, MIT, Spring 2011.

[11] Berk, M., Gross Anatomy and Embryology, Course Material, JCESOM, 2011-2012.

[12] Kumar, V., Abbas, A. K., Fausto, N., Aster, J. C., "Robbins and Cotran Pathologic Basis of Disease", 8th Ed. (2010), Saunders Elsevier, Philadelphia, PA.

[13] Berk, M., Microanatomy and Ultrastructure, Course Material, JCESOM, 2011-2012.

[14] Fish, S., Gross Anatomy and Embryology, Course Material, JCESOM, 2011-2012.

[15] Cooper, G. M., Hausman, R. E., "The Cell: A Molecular Approach", 5th Ed. (2009), Sinauer Associates, Inc., Sunderland, MA.

[16] Lohmander, L. S., Ostenberg, A., Englund, M., Roos, H., "High Prevalence of Knee Osteoarthritis, Pain, and Functional Limitations in Female Soccer Players Twelve Years after Anterior Cruciate Ligament Injury". Arthritis & Rheumatism, 2004, Vol. **50**:10, pp. 3145-3152.

[17] Chaudhari, A. M., Briant, P. L., Bevill, S. L., Koo, S., Andriacchi, T. P., "Knee Kinematics, Cartilage Morphology, and Osteoarthritis after ACL Injury". Medicine and Science in Sports and Exercise, 2008, **40**(2):215-222.

[18] Cervantes, T. M., Slocum, Jr., A. H., Seldin, E. B., "Design and Experimental Evaluation of Adjustable Bone Plates for Mandibular Fracture Fixation", Journal of Biomechanics, Vol. **45**:1, pp. 172-178, 2012.

[19] Endo, K., Herr, H., "Human Walking Model Predicts Joint Mechanics, Electromyography and Mechanical Economy". IEEE/RSJ International Conference on Intelligent Robots and Systems, 2009, pp. 4663-4668.

[20] Endo, K., and Herr, H., "A Model of Muscle-Tendon Function in Human Walking". IEEE International Conference on Robotics and Automation, 2009, pp. 1909-1915.

[21] The Journal of Biomechanics, Elsevier, Online URL: http://www.jbiomech.com/home.

[22] Clinical Biomechanics, Elsevier, Online URL: http://www.clinbiomech.com/.

CHAPTER

3

DETERMINISTIC JOINT DESIGN

"You can only obtain it with blood, sweat, tears, and design" – Alexander H. Slocum

Deterministic design is the practice of synthesizing a machine based on a set of requirements describing the functions (functional requirements) which the mechanism must be able to perform [1, 2]. It helps a design engineer remove any bias towards any particular concept or idea; isolating and identifying the functional requirements is often the first step in developing a new mechanism or machine. Axiomatic-based design is a similar method for designing machines and utilizes several axioms to guide the definition of a machine's functional requirements[11] [3]. In this chapter, aspects of rolling element joint design are discussed, including the kinetics, kinematics, and dynamics of simple concepts related to rolling mechanisms. Then, a case study in joint design for a biomechanical application is presented for a machine used to evaluate bone plates for fracture fixation [4, 5]

---

[11] An axiom is defined as "a fundamental truth that is always observed to be valid, and for which there are no counterexamples or exceptions" [3].

3.1 INTRODUCTION

Joint are used to add degrees of freedom (DOFs) to a machine in order to satisfy the functional requirements of a specific application. They can be used to transmit force, torque, or motion, and also to construct mechanisms with known kinetics like linkages. There are many different types of joints, sketches of which can be seen in Figure 3.1 and which also lists the degrees of freedom of each [6]. It is important to note that not all types of joints permit motion, for example rigidly joining two pieces of material by bolting, welding, or otherwise fixing them together creates a rigid joint [7].
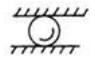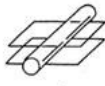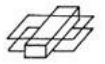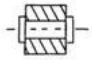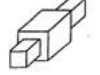
Degree of freedom (f)	Rotational	Translational	Schematic of element pair	Comments
5	3	2		sphere between parallel planes or concentric spheres, or coaxial cylinders
4	3	1		ball in cylinder
4	2	2		cylinder between parallel planes
3	3	0		ball joint (S)
3	2	1		sphere in slotted cylinder
3	1	2		plane joint (E)
2	2	0		slotted sphere
2	2	0		torus
2	1	1		cylindrical joint (C)
2	1	1		roller in slot
1	1	0		turning pair (R) or pin joint
1	0	1		sliding pair (P)

Figure 3.1: Sketches of different types of moving, uncoupled joints [6].

To the benefit of a design engineer working on prostheses for the human body, models of mechanical joints have already been extensively studied in the laboratory setting, and the dynamics and mechanics of each are well-known [7, 8]. It is no small challenge, however, to figure out how to relate loads and motions found in the human body to those experienced in the laboratory. Examples of joints found in existing machines can be seen in Figure 3.2
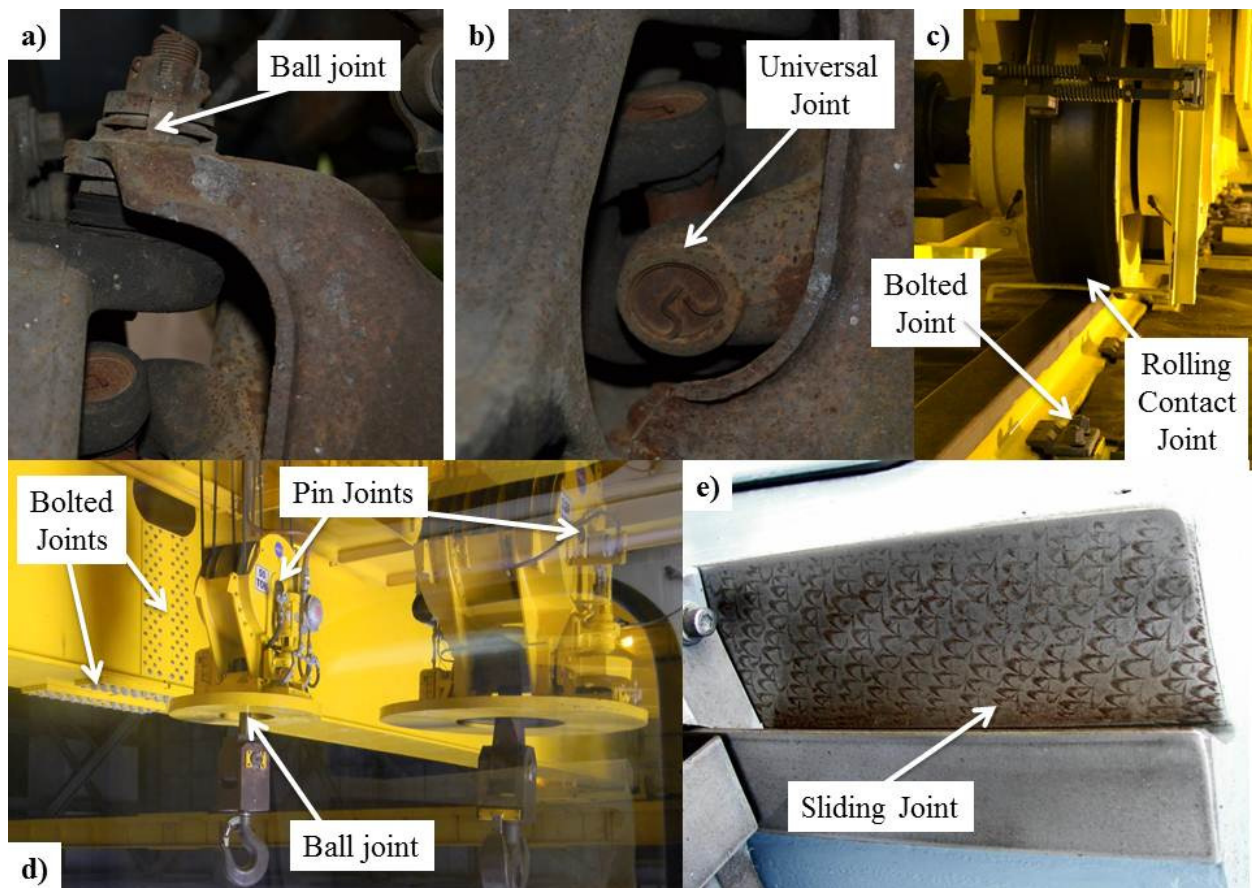
Figure 3.2: Examples of different types of mechanical joints: (a) a ball joint from the front axle of an automobile[12]; (b) a universal joint connecting the wheel to the driveshaft[2]; (c) one of the train wheels and railroad track, a rolling contact joint, supporting the crane in (d) [9, 10]; (d) the 325 ton main hoist and 50 ton backup hoist, used to stack the Saturn V and Space Shuttle

---

[12] Images of the from axle of author's Ford F-250.

components in the Vehicle Assembly Building at NASA, both of which use pin joints [9, 10]; and e) a sliding dovetail joint from a vertical milling machine.

Rolling Contact Joints (RCJs), or Rolling Link Mechanisms (RLMs) as described by Montierth [11], have unique characteristics that make them well-suited for certain biomedical or biomechanical systems where other types of joints are inadequate. A rolling contact joint is defined as "a system of constraints that allows a link to roll without slip over another link" [12]. While they increase a mechanism's overall kinematic complexity, RCJs provide several benefits over other types of joints. These include decoupled motions, increased Range of Motion (ROM), compactness, potentially low friction, and local transmission ratios [12]. Design rules call for a compressive force and a constraining system to keep convex-convex joints in constant contact; these can be through the use of flexural straps, cables, linkages, or as will be shown a test specimen held in each link using set screws.

Furthermore, high force applications of RCJs are limited by Hertzian contact stresses [11] and lubrication is essential for the success of these mechanisms in systems sensitive to particulate wear debris. Rolling joints are also subject to wear by multiple different modes, including slip which can lead to fretting and spalling of the material surface which can be studied in the laboratory under controlled conditions [13]. Different modes of failure in rolling contact have been studied and written about extensively [14], and more in-depth discussions of rolling contact failure modes can be found in texts relating to rolling bearing design [15, 16]. Rolling contact joint configurations, including convex/concave surfaces and convex/convex surfaces, will be

evaluated and compared to one another with the intent of selecting one type of interface that will be used in the prosthetic rolling contact knee joint.

3.2   DETERMINISTIC ANALYSIS

There are several factors which must be considered when designing a mechanical joint, including the desired ROM, load capacity, lifetime, constraint mechanisms, materials selection for durability and environmental compatibility, and overall joint stability. Each of these will be discussed, and then a case study will be presented on designing a mechanism for testing a new adjustable bone plate [5]. Use of a deterministic process allows the design engineer to objectively evaluate each concept for its utility in satisfying the functional requirements of a given application.

3.2.1   TYPES OF BIOLOGICAL JOINTS

Joints in the human body can be classified by both structure and function, relating to the tissues that make up the joint or the degree of motion which it enables, respectively. A joint that permits almost no relative motion, or a "fixed" joint, is referred to as a *syntharthrosis*, an *amphiarthrosis* if there is a moderate amount of relative motion, and if the joint enables a large range of motion it is called a *diarthrosis*, or *diarthrodial* joint. Examples of each can be seen in Figure 3.3, including the pterion in the skull (a syntharthrosis), the pubic symphisis (an amphiarthrosis) and the knee (a diarthrosis). Amphiarthroses often are called "cartilaginous", and diarthroses referred to as "synovial" joints.
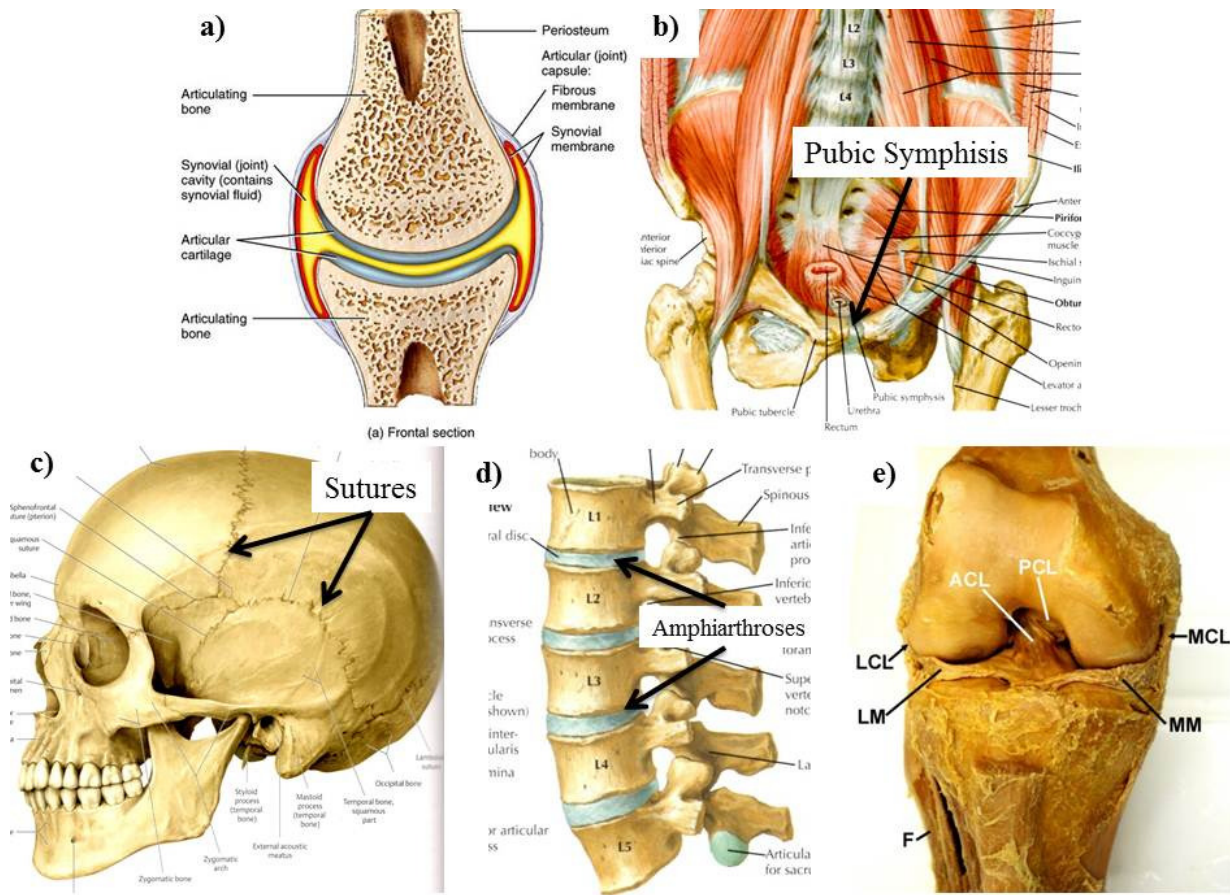
Figure 3.3: Examples of different classes of joints: (a) schematic of a synovial joint[13]; (b) the fibro-cartilageouns pubic symphisis [17]; syntharthroses in the skull where the skull bones fuse (forming sutures) [18]; (d) amphiarthroses in the spine between vertebrae and disks [17]; (e) the knee, a diarthrosis [19].

Different joints in the body can be approximated by mechanical joints. For example, the hip is a ball-and-socket joint, held together by ligaments and tendons, and actuated by muscles like the gemelli and gluteus maximus. An interphalangeal joint (in the finger) is a hinge or pin joint with relatively simple two-dimensional motion. The knee is an example of a hingle-like joint that has

---

additional DOFs, which increase the complexity of its kinetics and kinematics. Use of a deterministic approach to bioprosthetic joint design begins with isolating the major degrees of freedom for each joint, and choosing a simple mechanical joint that enables the maximum number of degrees of freedom.
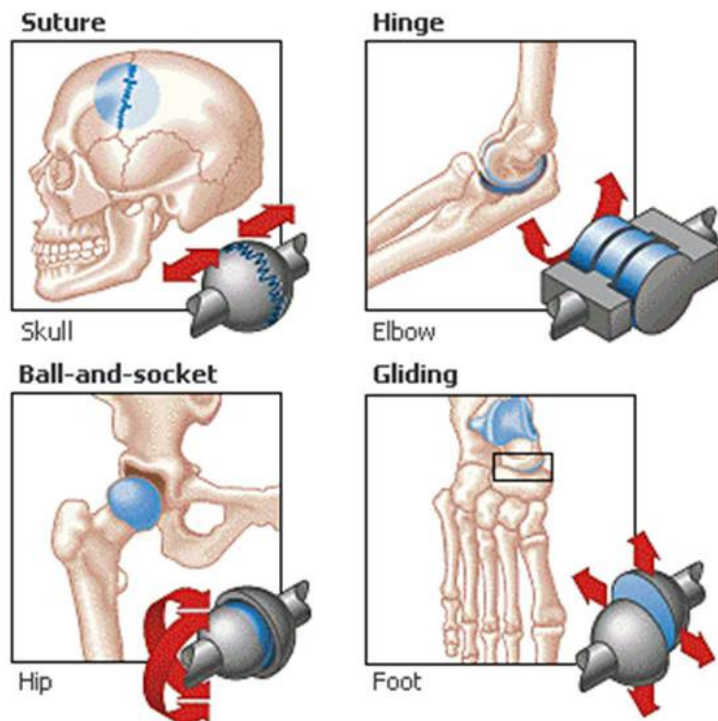
Figure 3.4: Different types of biological joints represented as mechanical structures [20].

Most biological joints have multiple degrees of freedom and operate via coupled motions because of the nature of the tissues defining their constraints. The tibio-femoral joint, otherwise known as the knee, is the focus of this thesis and a prime example of coupled motions. One functional requirement (FR) for a biological joint is for it to have a large range of motion for movement. This FR competes with size limitations driven by energy requirements. Therefore, the knee joint developed (in multiple animals, including humans) to be a complicated superposition of rolling, sliding, axial rotation, and translation. The major degree of freedom of

the knee joint is flexion/extension in a two-dimensional sagittal plane; additional degrees of freedom involve rotation about the long bones that make up the leg. This results in motions of the joint being coupled, i.e. the center of rotation will move antero-posteriorly while the limb flexes, so translation is coupled to rotation. Several mechanical joints with coupled motions are seen in Figure 3.5, most notably the cam pair with 2 degrees of freedom: Translation coupled to rotation.
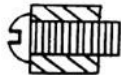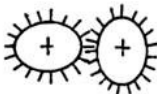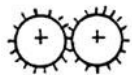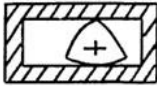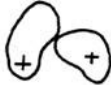
Degree of freedom (f)	Kinematic element	Comments	Degree of freedom (f)	Kinematic element	Comments
1		helical pair (H)	2		noncircular gear pair
1		circular slider in circular slot	1		constant-breadth cam
2		gear pair (G)	2		constant-breadth cam
2		cam pair			

Figure 3.5: Machine elements with coupled motions [6].

Other smaller motions in biological joints result from deformation of soft tissue structures like ligaments and, in the case of a knee, the meniscus. Small motions resulting from deformations in soft tissue in the knee are also dependent on the loads placed on the joint, adding to the complexity of its kinetics [21, 22]. In these cases assumptions must be made to select the major DOFs of a joint, i.e. rotation/translation in the knee, sliding/rotation in the elbow, and multi-axis rotation in the hip, and then an appropriate mechanical structure modified to match the kinetics of the biological joint.

3.3   KINETICS AND KINEMATICS OF ROLLING CONTACT

The two elements of a rolling link mechanism can have different shapes, whether they both are cylindrical, elliptical, or are a combination of both. For two equally sized elliptical rolling elements, diagonally opposite foci can be connected by a rigid link of constant length equal to the major axis of the ellipse [11]. This is analogous to the way two cylindrical elements can be connected by a single rigid length equal to the sum of the radii of each element. The fact that the foci of each element can be connected with a rigid link means that a four-bar linkage can be used to approximate their motion, with the intersection of the rigid links coincident with the point of contact of the two rolling elements. Here, the power of rolling contact is first seen: Motion of the instant center of rotation of a linkage defines the path the point of contact between two cam surfaces should follow such that those cams are able to replace the linkage in a mechanism.

One way to think about relative motion of cam surfaces is in terms of *polodes*. A "*polode*" simply refers to one of the solid bodies under consideration. In the case of a rolling contact joint there will be two polodes: One fixed and one moving. An "*envelope*" refers to the path over which one curve will roll, so for cams A and B in, in rolling contact, cam B is the envelope for cam A, and cam A is the envelop for B as seen in Figure 3.6 [23, pp. 65]. For more detail on fixed and moving polodes, and other ways to model mechanism motion, the reader should consult a text on the kinetics of mechanisms, for example Section 2.2 in Dijksman's "Motion Geometry of Mechanisms" [23, pp. 53, 65].
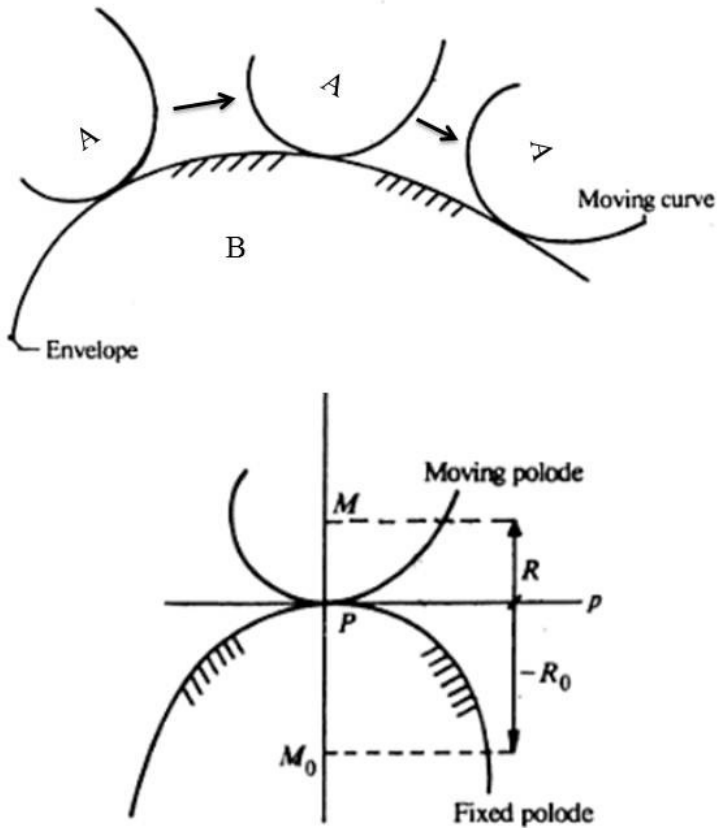
Figure 3.6: Tangential rolling motion of one cam over another (top); sketch of fixed (*M*) and moving polodes (*M_o*) of two cam surfaces, tangent at *P* (modified from [23]).

In the case of a knee joint, the femur and the tibia (meniscus) are moving and fixed curves, respectively; the moving curve rolls and slides over and about the fixed curve, making the meniscus the envelope for the femur. While the envelope, however, is normally defined based on rolling and sliding motion between two curves, for rolling contact (where sliding is expected to be near zero) the envelope can be defined as stated above. In Chapter 5, it will be shown how a four-bar linkage mechanism can be used to find the shapes of the fixed and moving polodes of a rolling-contact joint mimicking the two-dimensional biomechanics of the human knee joint.

In the human body, articulation is a combination of rolling and sliding, enabled by articular cartilage. The motion of elliptical rolling elements is almost equally complex, being a combination of rotation and translation. It is this aspect of rolling link motion that makes these types of mechanisms uniquely suited to replace articulating joints. There is an excellent discussion of relative motion in rolling element joints by Montierth and Howell [11].

3.4   MECHANICS OF ROLLING CONTACT

Contact mechanics are especially important to consider when designing a mechanism to serve a specific function, for example modifying an existing machine element like a rolling contact joint to mimic the motion of a knee [6, 24]. There are two critical degrees of constraint required to ensure proper function of a rolling contact joint [11]. The first is a no-slip condition between the two link surfaces; this ensures low-friction rolling motion, and reduces the risk of fretting, spalling, pitting or sub-surface wear inherent to rolling and sliding contact mechanisms [25, pp.315-16]. The second constraint is that of normal contact between the links, the behavior of which is determined mostly by Hertz contact theory [1, 2, 25]. It should be noted that these two constraints are coupled; the risk of fretting or spalling increases if contact is lost and then made again between links, while high contact stresses can also damage the contact area and increase the risk and rate of both surface and sub-surface wear in the mechanism.

When evaluating different configurations for contact, flat-on-flat is the null condition, where the radius of curvature is infinite and hertz contact stress goes to zero. Round-on-flat is another example, along with both round-on-round cases: Convex-convex and convex-concave. Kinematic analysis defines the useful range of motion for each, and modifications to the kinetics

enable modeling of certain joints, i.e. concave-convex is representative of a natural knee joint. Table 3.1 shows the four cases of rolling element mechanisms and gives the relative slide/roll ratios of each as well as joints for which they could be used to replace.

Table 3.1: The four types of rolling contact joints, including the null condition.				
Configuration	*Flat on flat*	*Convex on flat*	*Convex on Convex*	*Convex on Concave*
Slide/roll ratio	Infinite	Moderate	Low	High
Prostheses	None	Shoulder, wrist	Finger, knee	Shoulder, wrist, knee, hip

3.4.1 CONTACT MECHANICS

Considering the mechanics associated with contact between two links or surfaces is critical when designing a rolling-contact joint. The mechanism relies on rolling contact to function, and methods of constraint [11] are never infinitely stiff, yielding the potential for small amounts of sliding contact. To design a mate between two machine elements in such a configuration requires knowledge of the elastic yield strength, fracture toughness, fatigue strength, and most importantly surface strength of the components. Additionally, there are factors that contribute to surface wear in RCJs which must be considered in order to ensure a sound joint; these factors include [25]:

1. Hertz contact stresses

2. Number of cycles

3. Surface finish

4. Hardness

5. Degree of Lubrication

6. Temperature

3.4.2 HERTZ CONTACT

Analysis of the contact stresses in a rolling element mechanism are critical to the success of the mechanism; because they are often very high over a small area, Hertz contact stresses can be the origination site for crack propagation, spalling, fretting, and other wear mechanisms [2]. Hertz contact stresses are linked to the joint material's hardness, which in turn influences its elastic modulus, and in turn the size of the contact area and magnitude of contact stress. The RCJ here can be modeled as a special case of the standard Hertz contact equations. Two cylinders in line contact with each other, as in Figure 3.7a, develop a contact patch of width *2b* and length *l*, as in Figure 3.7b, when a load *F* is applied [25].
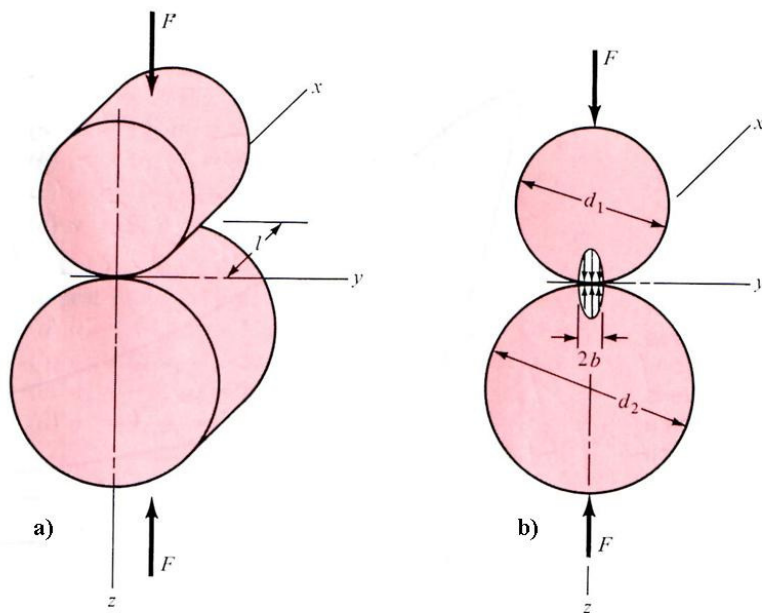
Figure 3.7: (a) two cylinders in line contact; (b) contact patch formation under load [25].

The half-width *b* is defined by Equation 3.1; it is a function of the poisson ratio *v*, Young's modulus *E*, cylinder radii d_1 and d_2, applied load *F*, and contact width *l*. The maximum contact pressure is given by Equation 3.2. It is important to note that the principle failure mode in Hertz

contact is shear, as the highest stress associated with Hertz contact are sub-surface shear stresses which can lead to crack generation, spalling, and other types of wear [2].

$$b = \sqrt{\frac{2F}{\pi l} \frac{(1-v_1^2)/E_1 + (1-v_2^2)/E_2}{1/d_1 + 1/d_2}} \text{ Eq. (3.1)}$$

$$p_{max} = \frac{2F}{\pi b l} \text{ Eq. (3.2)}$$

3.4.3   BUCKINGHAM LOAD STRESS FACTOR

While Hertz contact can result in stresses well above the yield strength of a material, fatigue does not require the stress state of the material to exceed the elastic limit. Also, component fatigue can still contribute significantly to wear in the mechanism. Fatigue can be controlled for during the design process by using the surface strength S_C, given by Equation 3.3, to determine the contact pressure which will cause yielding after a given number of cycles; w is used instead of l for the contact length in this instance.

$$S_C = \frac{2F}{\pi b w} \text{ Eq. (3.3)}$$

It is important to note that surface strength S_C is identical to the Hertz contact pressure p_{max}. Use of the load-stress factor developed by Buckingham [25] provides insight into the limitations of the current embodiment. It is derived using Equations 4 and 6 for cylinders in line contact, and is given by Equation 3.4.

$$K_1 = 2.857 S_C^2 \left(\frac{1}{E_1} + \frac{1}{E_2} \right) \text{ Eq. (3.4)}$$

The design equation which will ensure surface fatigue failure does not occur until after 10^8 cycles is given by Equation 3.5.

$$K_1 = \frac{F}{w}\left(\frac{1}{r_1} + \frac{1}{r_2}\right) \textbf{Eq. (3.5)}$$

3.5   CASE STUDY: ROLLING CONTACT JOINTS FOR FRACTURE FIXATION

This case study is adapted from an article by the author and colleagues, which described the design of a dynamic testing machine for evaluation of the mechanical performance of bone plates used in mandibular fracture fixation [4]. Figure 3.8a shows an image of the machine, and Figure 3.8b shows an image of a new bone plate design [1]. Bone plates are one of the most effective methods of repairing mandible fractures [26]. They are applied using bone screws and require surgical exposure of the fracture site. Initial fracture alignment is critical to prevent malocclusion, or misalignment of teeth after healing. Malocclusions as small as 5 microns can be functionally disruptive and cause significant patient morbidity; also, they cannot be objectively assessed by physicians via bite paper or X-ray [27]. A new bone plate design gives surgeons direct control over fracture alignment by deforming of a compliant structure to correct for observed misalignment after the application of bone screws [5, 28].
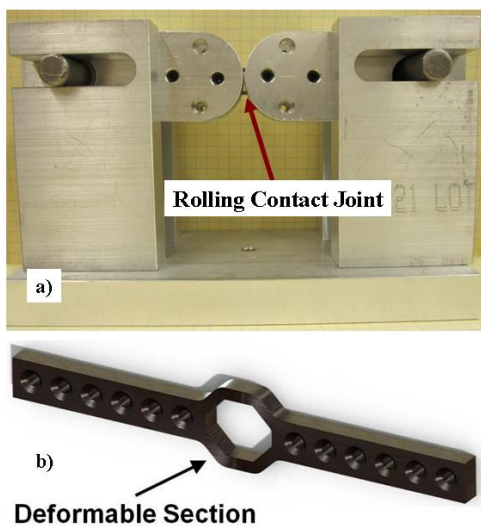
Figure 3.8: (a) rolling-contact joint testing apparatus; (b) adjustable bone plate [1].

Rolling Contact Joints (RCJs), or Rolling Link Mechanisms (RLMs) as described by Montierth [11], have unique kinematics that make them well-suited for certain biomedical/biomechanical systems where other types of joints are inadequate. A rolling contact joint is defined as "a system of constraints that allows a link to roll without slip over another link" [12]. While they increase a mechanism's overall kinematic complexity, RCJs provide several benefits over other types of joints including: decoupled motions, increased Range of Motion (ROM), compactness, potentially low friction, and local transmission ratios [12]. Design rules call for a compressive force and a constraining system necessary to keep convex-convex joints in constant contact, as used in the present mechanism. High force applications of RCJs are limited, however, by Hertzian contact stresses [11].

A Rolling Contact Joint can be used to accurately simulate bending loads normally experienced by bone plates used to join fractured mandible segments. Loads can be applied directly to the plate, analogous to *in vivo* loading conditions. Oftentimes during the healing process bone plates are subject to substantial loading prior to formation of a bony union [29]. Line contact between the convex rolling surfaces is used as a simplification of bone fragments meshing together. In order for this new plate to be adopted by oral & maxillofacial surgeons, the stiffness of the plate must equal or exceed that of existing plates. The structure, considered a "one-use" compliant mechanism, is deformed by the surgeon after the plate has been affixed in order to improve fracture alignment. Because of this, it is important to evaluate the bone plate after it has been subjected to clinically relevant deformations to ensure that they will not affect mechanism efficiency.

3.5.1 DYNAMIC TESTING MACHINE

Figure 3.9 shows the machine on the laboratory bench, with a coordinate system used to define error motions in the machine. It is oriented so that e_x is colinear with the line contact between the two mounting arms, e_y is aligned with the direction of translation of the pin/slider joints, and e_z is normal to the plane containing the bone plate's neutral axis for this bending configuration. To determine the stiffness of each interface an applied load of 400 N, equal to the measured peak male bite force, was assumed to be placed on the machine.
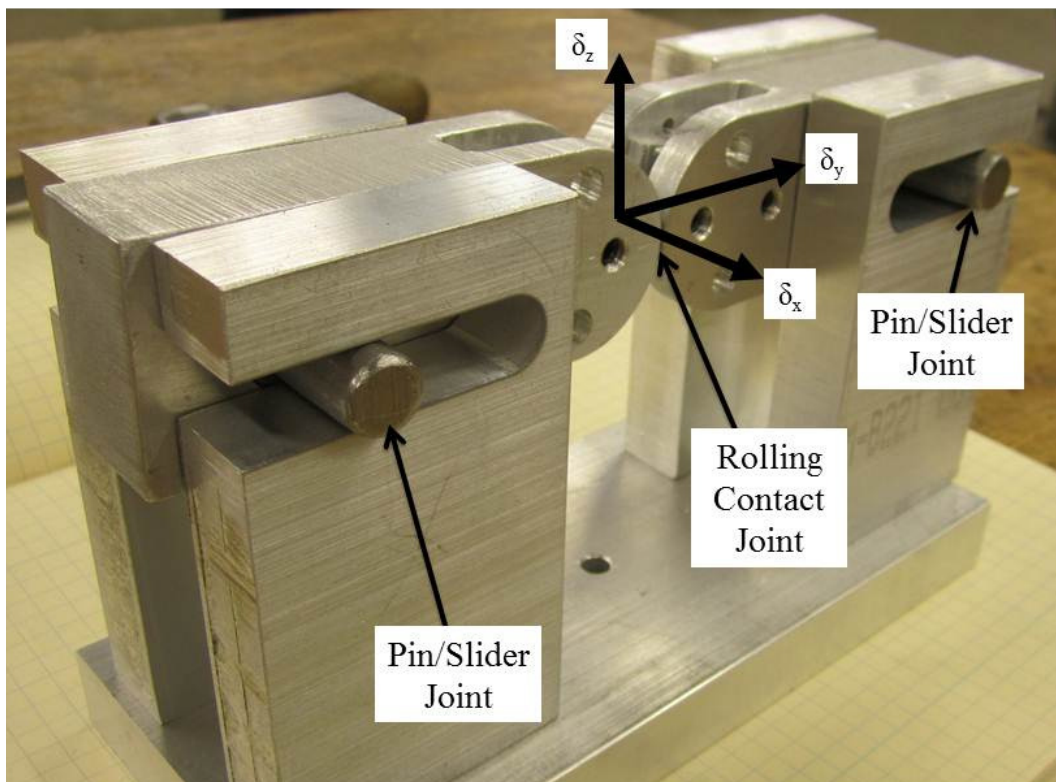
Figure 3.9: Instrument for testing adjustable bone plates, with coordinate system shown.

Equations 3.1 and 3.2 can be used to model the machine as a cylinder on a plane surface by making one of the diameters infinite (round-on-flat condition). Using an applied load F equal to

the maximum measured masseter muscle force of 400N, the maximum pressure in the rolling

contact joint can be calculated to be 176 Pa, and that for the pin/slider joint (with four contact

points) would be 278 Pa. The rolling contact joint is made of a 6061-T6 aluminum alloy, and the

pin/slider joint used a 316 stainless pin sliding on a machined Aluminum 6061-T6 surface. It is

assumed that a compressive force of 400N applied by an Instron® (Instron, Norwood,

Massachusetts) results in an equal compressive force within the rolling contact joint.

The analysis shows that neither the rolling contact joint, nor the pin/slider joint will yield under

an applied load of 400N (90lb-f). Testing will be performed on individual bone plates at a slow

rate of deformation, suggesting that the machine will be inherently low-cycle. In this instance,

however, consideration of the resistance of the mechanism to wear is important as contact forces

developed during evaluation of a bone plate can still result in fatigue.

Figure 3.10 shows the mechanism used to fixture bone plates to the mounting arms. The slot in

the mounting arm used to fixture the bone plate was milled using a 1.58mm (1/16in) endmill,

from a single piece of Aluminum 6061-T6 that had been waterjet cut to form the rolling link

surface. A feed rate of 6.35mm/min (0.25in/min) and cuts of 0.5mm (0.020in) were used to

ensure a good surface finish. To fixture the bone plate in the mounting arms, 8-32 set screws

with a seating torque of 2.26 Nm (20lb-in) were used, resulting in a holding power of 1712.6N

(385 lb-f) [28]. Tapped, counter-bored holes for support screws were made to apply a pre-load

and prevent loosening of the set-screws.
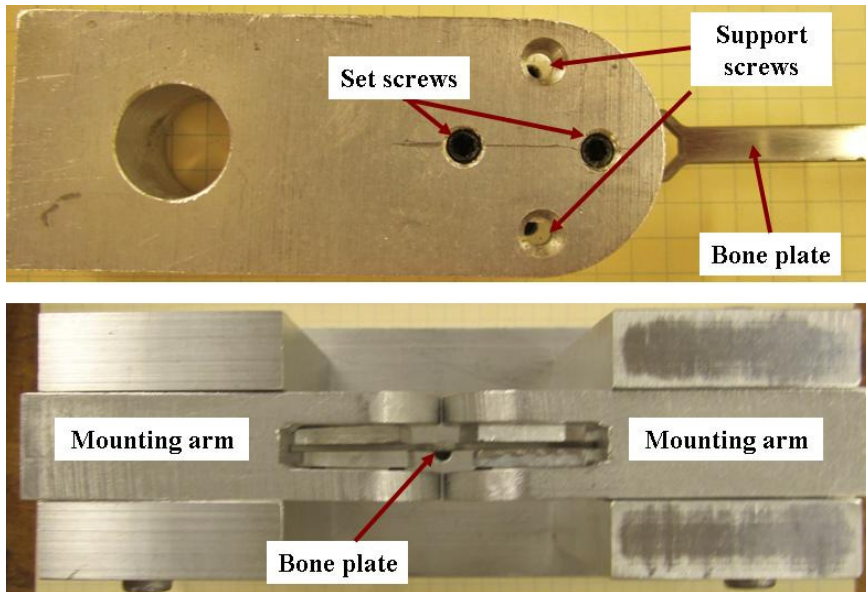
Figure 3.10: Constraint mechanism with front and top views of the bone plate fixture utilizing shims and set screws.

3.5.2 BUCKINGHAM LOAD STRESS ANALYSIS

The surface strength of the rolling contact joint used in this instrument is 176MPa, and 139MPa for the pin/slider joint. The value for the pin/slider contact is found assuming equal distribution of load among the four contact regions, with two contact regions per shaft, and is used in Equation 3.4. Using Equation 3.5, for this machine r_1 is defined to be equal to r_2, and the minimum radius is 0.012m (0.47in). For the pin/slider joint r_1 is considered to be infinite, so the minimum radius for r_2 is 0.025m (0.98in). As contact radii used in this machine are greater than these values, the fatigue life of the machine can be assumed to be on the order of 10^8 cycles [25].

3.5.3 ERROR ANALYSIS

The most critical module of the machine is its ability to isolate the behavior of any given plate, whether deformed or un-deformed. Misalignments in the mounting arms or method of plate

fixation during application of a test load could lead to development of parasitic forces and moments, which in turn would affect the accuracy and repeatability of the test. As illustrated in the schematic shown in Figure 3.11, loads are applied at the centerline of the bone plate to minimize parasitic torques.
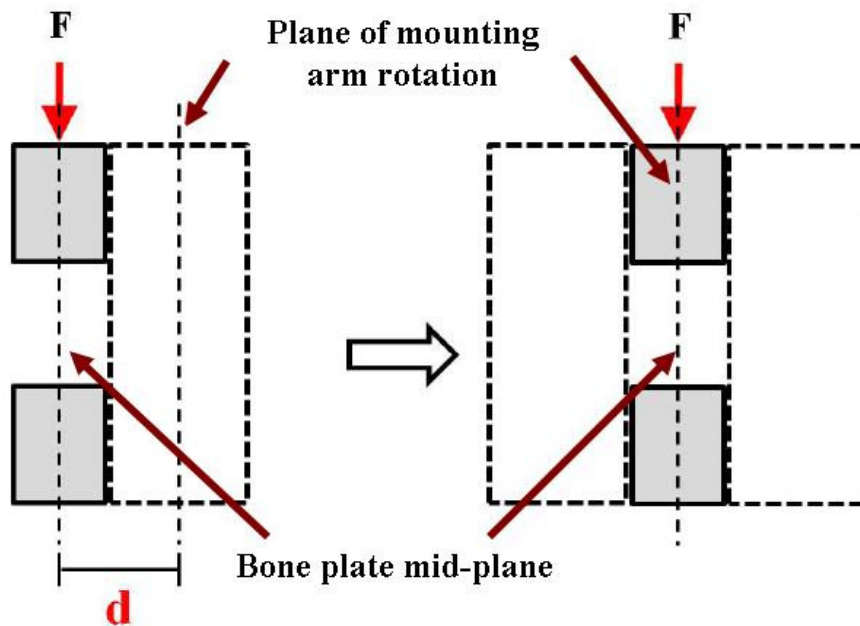
Figure 3.11: schematic diagram showing method of avoiding parasitic moments in the mounting configuration [28].

The initial concept [4, 5] proposed that the bone plate be mounted to the face of the RCJ links, which would have resulted in a parasitic moment M_p, given by Equation 3.6. To avoid this adverse loading, the centerline of the bone plate should be in the same plane as the centerline of the mounting arm. Shims of equal size, placed on either side of the plate, allow the use of set-screws to provide flexibility to fixture the plate in different configurations.

$$M_p = F \times d \quad \textbf{Eq. (3.6)}$$

To determine the number of supports, consider the possibility of misalignment occurring at the interface between the mounting arm shaft and the slotted support, illustrated by Figure 3.12a. Each mounting arm has two needle bearings press-fit into precision-cut holes. If the slot height is greater than the shaft diameter, then adverse loading conditions illustrated by Figure 3.12b can result. There is also a length requirement for the slot based on the diameter of the shaft, as defined by St. Venant [2].

Bearing block cross section   **Bone plate cross section**
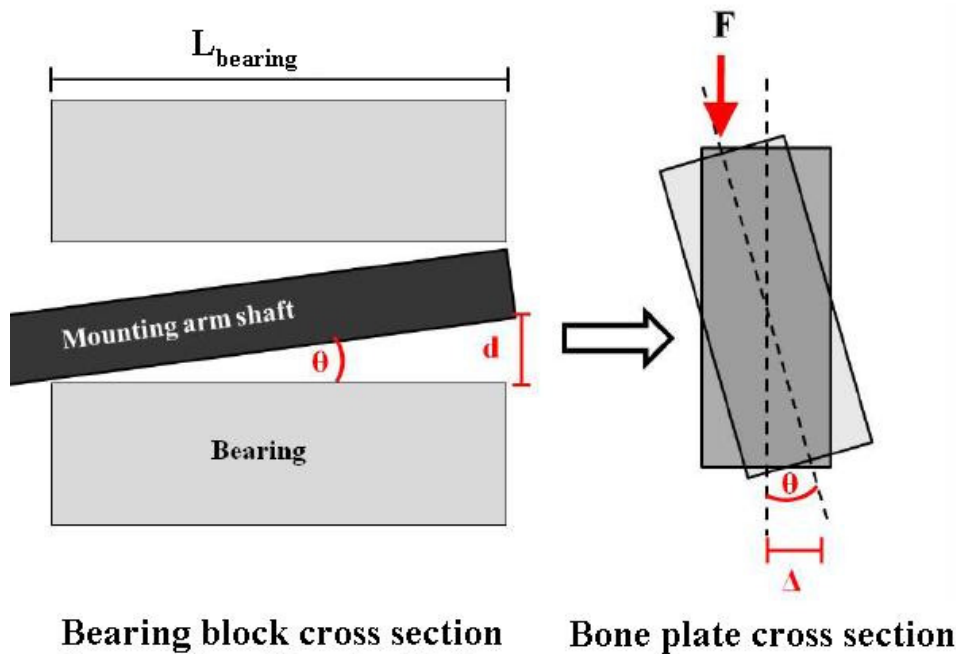
Figure 3.12: Schematic of shaft misalignment supporting the bone plate mounting arm [28].

This is also used to define y-axis rotational error motions. This would cause the bone plate to be offset from the point of load application, resulting in misalignment during loading with potential to damage the machine. Using the small angle approximation, and assuming bearing constraint length L_b to be 50.47mm (1.987in), Equation 3.7 yields the tolerance δ_s [28].

$$\sin(\theta) \approx \theta$$

$$\sin(\theta) = \frac{\delta_s}{L_b}$$

$$\sin(\theta) = \frac{2\delta_s}{h_{plate}}$$

$$\frac{2\delta_s}{h_{plate}} \le 0.01$$

$$\sin\left(\frac{\delta_s}{L_b}\right) \le 0.01$$

$$\delta_s \le 0.01\, L_b \quad \textbf{Eq. (3.7)}$$

The machining tolerance for the pin/slider slot is $\delta_s \le 0.49$mm (0.0197in) to maintain an offset less than 1% of bone plate height (which is easily attainable). Furthermore, two supports are used instead of a single slot to further reduce misalignment. Alignment of the bone plate in the mounting arms is also important. Parasitic forces are generated if the plate were not aligned with the plane in which the arms rotate. Figure 5c illustrates the condition where the bone plate tilts in the mounting arms. The height of the mounting arms is not listed because the drawing is not to scale.
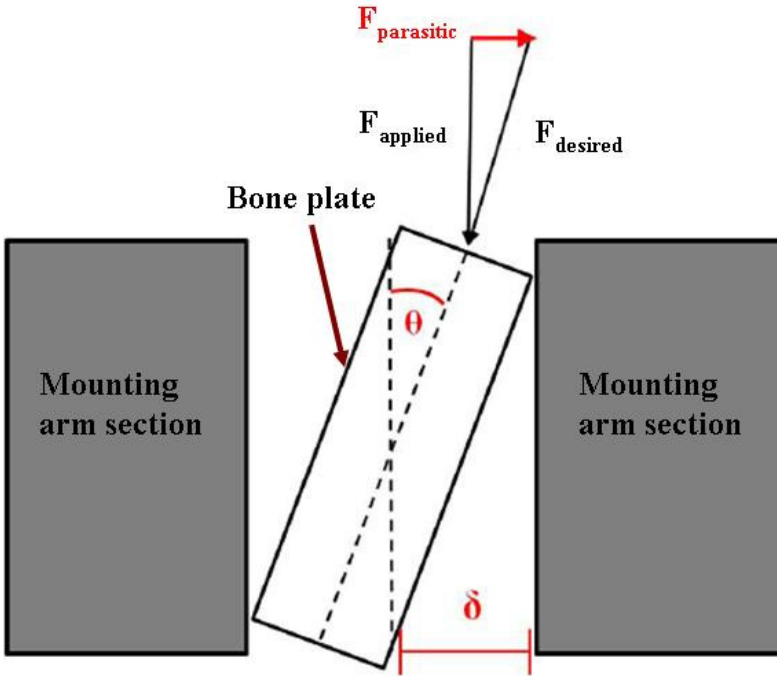
Figure 3.13: Schematic of variables for tolerance analysis of the mounting arms [28].

This is also used to analyze error motions in the $\mathbf{e_x}$ direction, discussed later in the error budget. Equation 3.8 shows that the mounting arm slot must be machined with a tolerance $\delta_m \leq 0.0635$mm (0.0025in) to ensure parasitic forces less than 1% of the applied load F, given plate width w=12.7mm (0.5in).

$$\sin(\theta) = \frac{2\delta_m}{w}$$

$$\sin(\theta) = \frac{F_{par}}{F_{applied}}$$

$$\frac{F_{par}}{F_{applied}} \leq 0.01$$

$$\sin\left(\frac{2\delta_m}{w}\right) \leq 0.01$$

$$\delta_m \leq \arcsin(0.01)\frac{w}{2} = 0.0635 \qquad \textbf{Eq. (3.8)}$$

It should be noted that there are only 3 intended degrees of freedom for the machine: vertical translation of the joint contact line δ_z, rotation about the joint interface θ_x, and translation of the pin/slider δ_y. These are defined based on the coordinate system given in Figure 3.9.

Rotation about the y-axis is allowed due to machining tolerances. The stiffness of the other rotational and translational degrees of freedom are assumed to be infinite in keeping with the functional requirements of the machine. An error budget for the machine is shown in Table 3.2,. The required accuracy for translation in the $\mathbf{e_y}$ and $\mathbf{e_z}$ directions is assumed to be 5 microns as it is approximately the minimum maloclusion which can be functional disruptive; this is also well within the resolution of the Instron test machine used to apply loads.

Table 3.2: Dynamic testing machine error budget [4].				
Direction	**Accuracy**	**Repeatability**	**Expected Stiffness**	**Interface**
δ_x	32μm	+/-32 μm	n/a	n/a
δ_y	5μm	+/-2.5μm	36 N/μm	Horizontal pin/slider
δ_z	5μm	+/-2.5μm	1960N/μm	Vertical pin/slider
θ_x	6.6μrad	+/- 3.3μrad	0.46Nm/μrad	Rolling contact joint
θ_y	4.35μrad	+/-9.7μrad	n/a	n/a
θ_z	n/a	n/a	n/a	n/a

The highest measured bone plate stiffness was 709.22 N/mm, which translates to a bending stiffness of 4.12e-3 Nm/μrad; this is two orders of magnitude smaller than the predicted rotational stiffness in the θ_x direction of 0.46 Nm/μrad for the rolling contact joint under an

applied load of 400N. Thus, bone plate deformation will occur before any significant deformations are induced the machine. Furthermore, the total vertical stiffness of the four pin/slider joints, as determined by hertz contact theory, is 1960N/μm. Hooke's law can be used to determine the required horizontal stiffness of the interface: if a steel/aluminum coefficient of friction of 0.45 is used, a frictional force F_f of 180N results from an applied load F of 400N. Assuming a required positional accuracy of x=5μm, the horizontal stiffness k can be determined by $k=F_f/x$, and is equal to 36N/μm. The vertical and horizontal stiffness' of the pin/slider joint are 1.96e6N/mm, and 3.6e4N/mm, respectively, as compared to 7.06e2N/mm for the stiffest bone plate [4, 5].

3.5.4   EXPERIMENTAL RESULTS

Experiments were performed at room temperature or approximately 72°F; the behavior of the materials tested and the joint material do not change significantly between this and 98.6°F. The mounting arms were fabricated using an Omax® waterjet with a Tilt-A-Jet™ to eliminate draft angle. Wetted 400-grit sandpaper was then gently applied to the convex surfaces of the links to improve surface finish. The pin-slider joints were milled as a single slot in 19.05mm (3/4in) thick Aluminum 6061-T6 plate, and then halved to create a pair of supports with equal height and consistent tolerance.

Performance of the bone plate was evaluated using the dynamic testing machine described previously. Testing bone plates of differing geometries while keeping the material properties constant will give insight into the performance of the new bone plate relative to those currently used by surgeons. Bending stiffness and force to failure will be the metrics used to evaluate

relative performance of the bone plates. Bending stiffness is a standard of measurement specified in ASTM-F382, and is calculated by finding the slope of the linear elastic region of the force-displacement curve [5]. Plates with different geometries will have different bending stiffness; therefore this parameter can be used to compare performance between different bone plate embodiments. Force to failure will be measured by increasing the load until the plate fails. This has been measured in the literature [30, 31] and will enable further comparison between new and existing plates. Figure 3.14 shows results of two different tests.
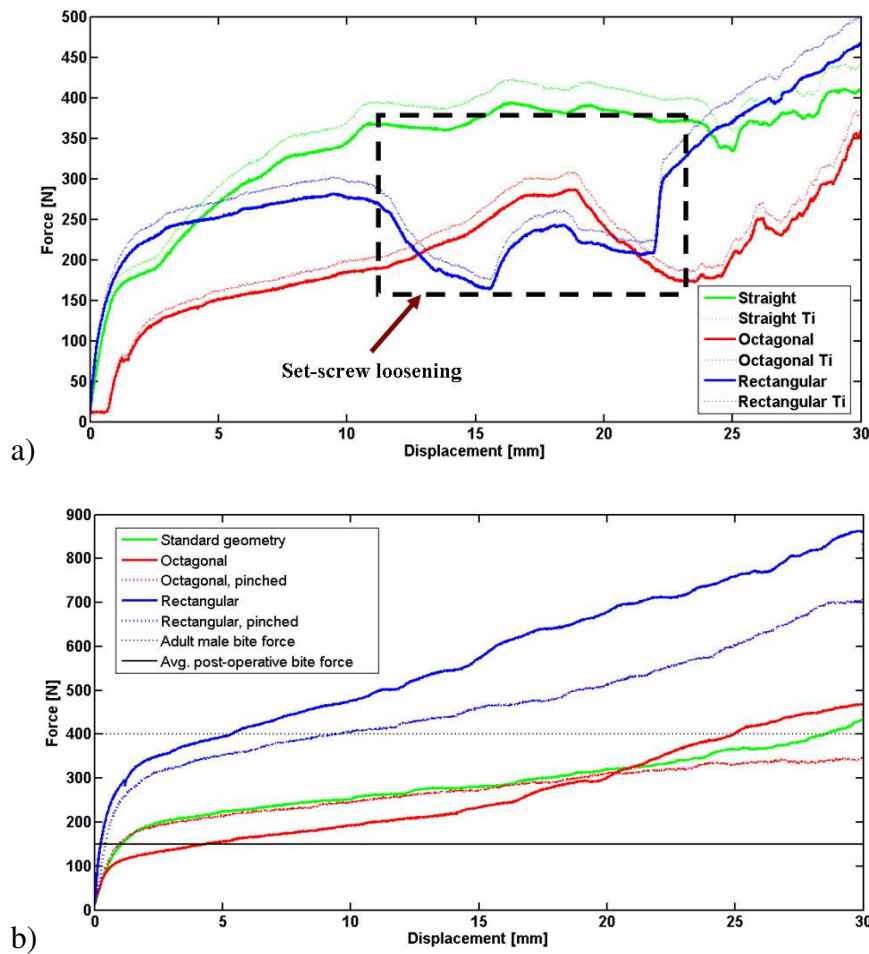
Figure 3.14: a) data showing plate slippage due to inadequate set-screw preload; b) successful test up to 30mm of vertical displacement.

Maintaining the minimum set screw torque is imperative for obtaining relevant data. Figure 3.14a shows results for a configuration in which the minimum torque was not achieved. This caused slipping at the plate/shim interface. The coefficient of kinetic friction is less than the coefficient of static friction, so a sharp decrease in force is observed. Any results with evidence of slipping must be discarded. Next, the standard bone plate geometry is used to establish a baseline so that results can be scaled to account for material difference, and compared to existing data for conventional bone plates. Figure 3.14b shows force vs. displacement data for 5 different bone plate configurations, as well as landmarks for peak masseter bite force and average post-operative bite force [5]

Figure 3.19 shows before and after images of standard as well as deformed and un-deformed adjustable bone plates; stiffness values are shown for each bone plate tested in the machine. The rectangular adjustable bone plate had the highest stiffness in its un-deformed state, and still the highest stiffness after deformation, of all bone plates tested. Further studies involving animals or human clinical trials most likely would use this plate. Stiffness was calculated as specified in the ASTM and ISO testing standards for testing bone plate [5].

Before Testing	After Testing	Stiffness
Standard		176.32 N/mm
Octagonal		174.22 N/mm
Octagonal, pinched		227.58 N/mm
Rectangular		709.22 N/mm
Rectangular, pinched		323.38 N/mm

Figure 3.15: Deformed and un-deformed bone plates, with measured stiffness values, before and after experimental evaluation in the dynamic testing machine [5].

3.6   REMARKS

Rolling contact joints present inherent advantages over other types of joints, specifically for biomechanical and biomedical applications. The kinematics of rolling contact joints can be directly controlled by contouring the surfaces of the links, and degrees of freedom can be added or removed by the addition of flexures, compliant members, or cables. Joints with relatively complicated motions such as the elbow or knee, as well as the behavior of fractures under certain loading conditions, can be simulated using rolling contact joints. The contact and constraint requirements [11] also present a unique opportunity for integrated degrees of constraint and compliance. Flexures designed to constrain two links to rolling contact can also have integrated compliant structures allowing for small rotations, much the same way ligaments of a knee joint allow for the same motions but constrain the joint to articulate.

In terms of designing new tools for fracture fixation, the kinetics and kinematics of multiple-link rolling contact mechanisms can be accurately modeled [11, 12, 25]. Additionally, machines can be designed to simulate loading conditions more accurately even in more complex fractures that result in multiple bone fragments, or which span a joint. Here, a rolling-contact joint is used in a testing machine to simulate *in vivo* loading conditions more accurately than current standards for bone plate testing. It has allowed for validation of a prototype adjustable bone plate for reducing the incidence of malocclusion. Because this machine is limited to in-plane deformations, further improvements to the apparatus will be focused on enabling the evaluation of bone plates subjected to multi-plane deformations.

Furthermore, usability studies are currently being conducted to determine the limits of deformation of the adjustable segment and also to measure forces required to achieve various deformations. These studies involve plating a synthetic mandible fixtured in a jig with pre-determined misalignments, and then deforming the plate until the segments are re-aligned. The deformation of the plate in 6 degrees of freedom is tracking with before and after scans taken with a volumetric CT machine. A patent application has been filed at the time of this writing, for which the author is listed as a co-inventor [32].

3.7   REFERENCES

[1] Slocum, A. H., "Precision Machine Design'" (1992), Prentice Hall, Englewood Cliffs, NJ.
[2] Slocum, A. H., 2008, *FUNdaMENTALS of Design*, Topic 3 – *FUNdaMENTAL* Principles, Online URL: http://pergatory.mit.edu/resources/FUNdaMENTALS.html.
[3] Lee, D. G., Suh, N. P., "Axiomatic Design and Fabrication of Composite Structures" (2005), Oxford University Press, New York, NY.

[4] Slocum, Jr., A. H., Cervantes, T. M., Seldin, E. B., Varanasi, K. K., "Analysis and Design of Rolling-Contact Joints for Evaluating Bone Plate Performance". Medical Engineering & Physics, July 23rd, 2012.

[5] Cervantes, T. M., Slocum, Jr., A. H., Seldin, E. B., "Design and Experimental Evaluation of Adjustable Bone Plates for Mandibular Fracture Fixation". Journal of Biomechanics (2011), Published online October 31, 2011. DOI:10.1016/j.jbiomech.2011.09.010.

[6] Freudenstein, F., Maki, E. R., "The creation of mechanisms according to kinematic structure and function". Environment and Planning B, 1979, Vol. **6**, pp. 375-391.

[7] Slocum, A. H., 2008, *FUNdaMENTALS of Design*, Topic 9 – *Structural Connections & Interfaces*, Online URL: http://pergatory.mit.edu/resources/FUNdaMENTALS.html.

[8] Williams, J. H., "Fundamentals of Applied Dynamics", 1st Ed (2006), John Wiley and Sons, Hoboken, NJ.

[9] Personal Communication, General Jerald D. Stubbs, USAF Retired, Chief Counsel, Office of the Chief Counsel, NASA John F. Kennedy Space Center, July 2012.

[10] National Aeronatucis and Space Administration, Kennedy Space Center, Vehicle Assembly Building, Cape Canaveral Air Force Station, Cape Canaveral, Florida.

[11] Montierth, J. R., Todd, R. H., Howell, L. L., "Analysis of Elliptical Rolling Contact Joints in Compression". ASME Journal of Mechanical Design, March 2011, **133**:3, pp. 1-10.

[12] Collins, C. L., "Kinematics of Robot Fingers with Circular Rolling Contact Joints". Journal of Robotic Systems, **20**:6 (2003), pp. 285-296. DOI:10.002/rob.10087.

[13] Yamada, T., "Rolling Wear Characteristics of Annealed Carbon Steels under Dry Contact Conditions", Wear, **51** (1978), pp.279-288.

[14] Tallian, T. E., "On Competing Failure Modes in Rolling Contact", ASLE Transactions (1967), **10**:4, pp.418-439.

[15] Harris, T. A., Kotzalas, M. N., "Essential Concepts of Bearing Technology", 5th Ed. (2007), CRC Press, Taylor and Francis Group, Boca Raton, FL.

[16] Harris, T. A., Kotzalas, M. N., "Advanced Concepts of Bearing Technology", 5th Ed. (2007), CRC Press, Taylor and Francis Group, Boca Raton, FL.

[17] Thompson, J. C., "Netter's Concise Orthopaedic Anatomy", 2nd Ed. (2010), Saunders Elsevier, Philadelphia, PA.

[18] Gilroy, A. M., MacPherson, B. R., Ross, L. M., Eds., "Atlas of Anatomy", 1st Ed. (2008), Thieme Medical Publishers, New York, NY.

[19] Zill, S. N., Gross Anatomy and Embryology, Course Materials, JCESOM, 2011-2012.

[20] Taghizadeh, K., Bastanfoard, M., "The Anatomy of a Human Body, a Model to Design Smart High Building". Science and Technology, **2**(1):8-14, 2012.

[21] Piziali, R. L., Seering, W. P., Nagel, D. A., Schurman, D. J., "The Function of the Primary Ligaments of the Knee in Anterior-Posterior and Medial-Lateral Motions". J Biomechanics, Vol. **13**, pp. 777-784.

[22] Seering, W. P., Piziali, R. L., Nagel, D. A., Schurman, D. J., "The Function of the Primary Ligaments of the Knee in Varus-Valgus and Axial Rotation". J Biomechanics, Vol. **13**, pp. 785-794.

[23] Dijksman, E. A., "Motion Geometry of Mechanisms", Cambridge University Press, New York, NY, 1976.

[24] Freudenstein, F., Woo, L. S., "Kinematics of the Human Knee Joint". Bulletin of Mathematical Biophysics, 1969, Vol. **31**, pp. 215-232.

[25] Shigley, J. E., Mischke, C. R., Mechanical Engineering Design, 5th ed., McGraw Hill, Inc., New York, 1989, pp. 73-74, 315-16.

[26] Fox, A. J., Kellman, R. M., "Mandibular Angle Fractures: Two-Miniplate Fixation and Complications". Archives of Facial Plastic Surgery, **5**:464-469, 2003.

[27] Cory Resnick, MD. Personal Communication, January 2011.

[28] Cervantes, T. M. (2011). *Design of an Adjustable Bone Plate for Mandibular Fracture Fixation*. SB Thesis, MIT.

[29] Bartel, D. L., Davy, D. T., Keaveny, T. M., 'Orthopaedic Biomechanics: Mechanics and Design in Musculoskeletal Systems'. Pearson Prentice Hall, Inc., Upper Saddle River, NJ, 2006, pp.272-282.

[30] Jain, S., Simmons, O., Hanemann, M., Baratta, R., Guerra, A., Metzinger, S., "Comparison of Tensile Strength of Resorbable Plating Systems Used in Monocortical Mandible Angle Osteotomy Repair". Archives of Facial Plastic Surgery, **8**:390-395, 2006.

[31] Karoglan, M., Shutz, K., Schieferstein, H., Horch, H., Neff, A., "Development of a static and dynamic simulator for osteosyntheses of the mandible". Technology and Health Care, **14**:449-455, 2006.

[32] Seldin, E and Slocum Jr., A. H., "Systems and Methods for an In Vivo Adjustable Bone Plate". US Provision Patent Application, 61/317,884, January 2010.

*This page intentionally
left blank*

CHAPTER

4

JOINT DURABILITY & MATERIALS SELECTION

"Nothing's ever built to last, but that doesn't mean it's not worth building" – Unkown

4.1   INTRODUCTION

The rolling surfaces of a prototype rolling contact knee joint, seen in Figure 4.1a were synthesized based on knee anatomy, through the use of a four-bar linkage model of simplified knee biomechanics (flexion/extension) [1]. There are significant advantages to using rolling contact when constructing a prosthetic joint made from engineering materials. In this chapter, four candidate materials are evaluated for their potential use in rolling contact prostheses. Possible failure modes are also assessed, including fatigue and fracture analysis of the constraints and rolling surfaces. Also presented are methods of evaluating the flexural constraints using a repetitive motion machine to subject the joint to several hundred thousand cycles.
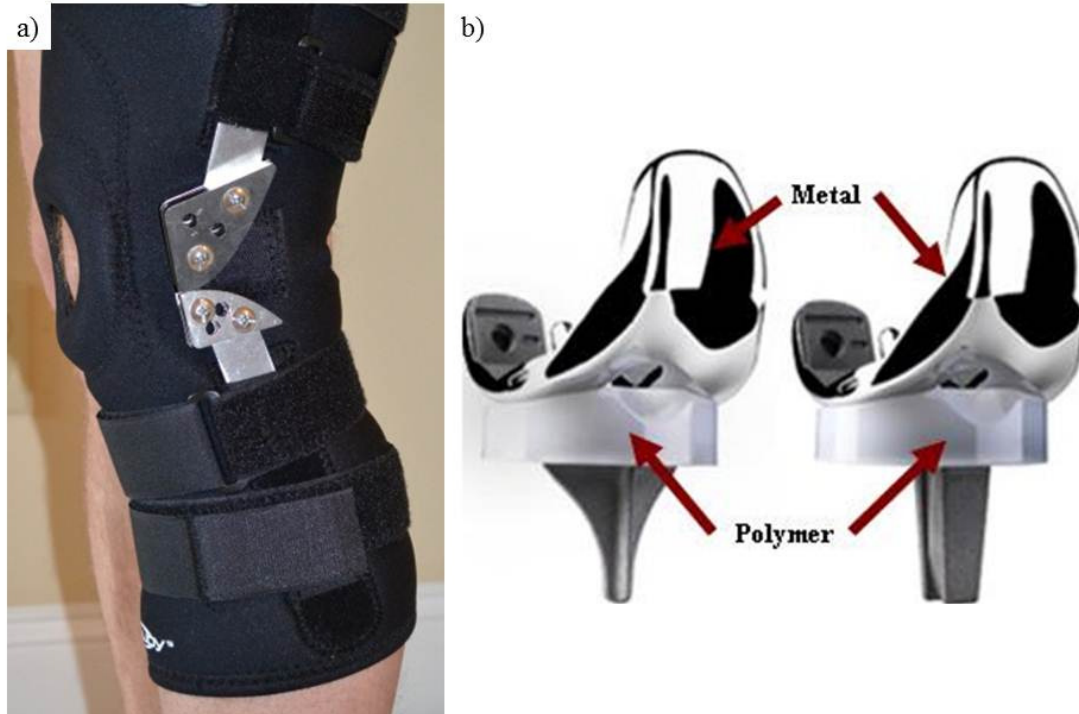
Figure 4.1: a) Prototype rolling contact joint [1]; b) metal-on-polymer total knee prosthesis (Biomet, Inc., Warsaw, IA) [2].

Conventional knee replacement utilizes a biomimetic arrangement of metal on polymer, in an attempt to re-create the geometry of the articulating surfaces present in a healthy joint. An example of a biomimetic joint, shown in Figure 1b, replaces the distal femur with a metallic femoral component (often a Cobalt Chrome alloy), articulating on an Ultra-High Molecular Weight Poly-Ethylene (UHMWPE) bearing surface affixed to a metallic (Titanium, Cobalt Chrome or stainless steel alloy) tibial tray which replaces the proximal tibia.

The prototype joint seen in Figure 4.1a uses a convex/convex arrangement with three constraints, based on the mechanism of a flexure coupling. Current prostheses based on sliding contact joints that directly emulate the biological knee joint are very successful at reducing or even eliminating

pain in patients with degenerative joint diseases. As such must be acknowledged in any work attempting to suggest an alternative design. They have a limited lifetime, however, because they cannot take full advantage of biomechanical mechanisms such as mimicking the interaction of synovial fluid with cartilage; this motivates the search for an improved synthetic joint.

As discussed here, a potential key to improving joint lifetime is replacing sliding with rolling contact. In high performance machines rolling element joints yield the longest lifetimes. Figure 4.2a—b shows sketches from patents for rolling contact prosthesis for (a) inter-phalangeal joints and (b) a knee joint [3, 4]. A sketch model of a rolling contact flexure-coupling knee joint is shown in Figure 4.2c. This concept was the basis for synthesizing the rolling contact joint seen in Figure 1a, based on the first-order flexion/extension degree of freedom (DOF) in a healthy knee. A four-bar linkage model of knee biomechanics is used to link knee biomechanics to the shape of the flexure coupling surfaces [1, 5]. The concept utilizes two anterior-posterior (AP) straps, and one posterior-anterior (PA) strap to both constrain the joint and prevent subluxation of the femoral or tibial components relative to one another when the joint is flexed under load.
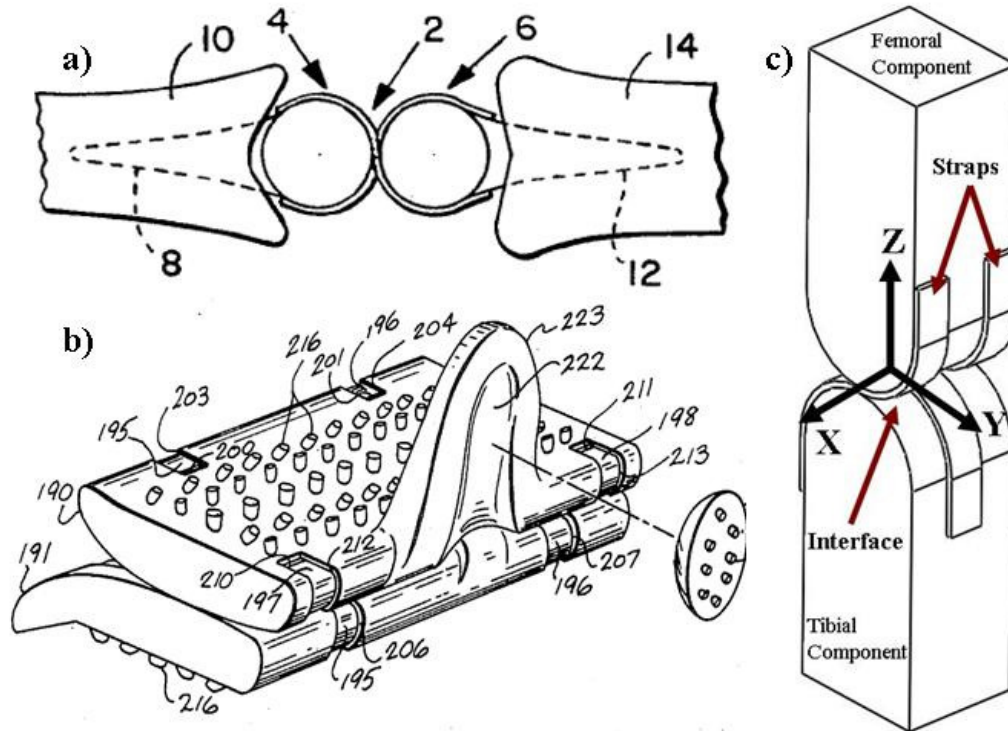
Figure 4.2: Images of flexure couplings proposed for use in prosthetic inter-phalangeal (a) and knee joints (b) [3, 4]; concept sketch of a flexure coupling prosthesis (c).

Herein, it will be shown that conventional orthopaedic materials can be used in a rolling contact prosthetic joint to improve contact mechanics, which will lead to reduced wear and improved joint lifetime. Loading conditions on the straps are analyzed using methods developed to model stresses in steel reinforced concrete, providing a deterministic basis for placing the straps in a "trochlear-like" groove to eliminate compressive stresses on the straps. Fracture in the straps is also analyzed to determine the minimum crack length to ensure a lifetime equivalent to current prostheses. Contact stresses and fatigue in the bulk surfaces of the joint are assessed using Hertz Contact theory and Buckingham's Load Stress Factor. Table 4.1 provides a list of symbols for this chapter.

Table 4.1: Chapter 4 Nomenclature	
Symbol	**Description**
C_d	Cycles per day
C_y	Cycles per year
C_{15}	Steps over a 15-year period
C_{30}	Steps over a 30-year period
ε_x	Bending (engineering) strain in a curved beam
ρ	Radius of curvature
σ	Stress
y	Height of a fiber relative to the neutral axis
NA	Neutral axis
E	Young's modulus
υ	Poisson ratio
r_{femur}	Distance from femoral head contact to tibiofemoral center of rotation
r_f	Radius of femoral component at point of contact
$r_{contact}$	Distance between P and point of contact
P	Intersection of femoral and tibial axes
F_{BW}	Force due to body weight
F_c	Reaction force at tibio-femoral contact point
X_o	Origin of a strap (X=1, 2, 3)
X_i	Insertion point of a strap (X=1, 2, 3)
p_o	Hertz contact pressure
a_o	Area of contact patch
R	Radius of contact patch

4.2   MATERIALS SELECTION

Selecting proper materials is critical to the lifetime of high performance mechanisms [6]. Knee braces, and even more so total knee replacements, are subjected to hundreds of thousands of cycles. The mechanism by which polymer debris is formed suggests a fracture failure mode in the surface of the UHMWPE due to this high cycle loading [7, 8]. Polymer fracture can lead to saturation of the joint capsule with particles ranging in size from a few nanometers to tens of microns [7]. The immune response to these particles can lead to osteolysis, and subsequent aseptic loosening, presenting a barrier to patients receiving implants at younger ages and who are very active [9]

The first step in the process for selecting material for an artificial joint is to determine the number of cycles it must undergo during its useful lifetime. It is assumed that a patient receiving a prosthetic knee joint will continue to perform Activities of Daily Living (ADL), so a daily load of about 5000 cycles will be placed on the joint, leading to 1.83 million cycles per year, and 27.4 million cycles over the lifetime of an implant that lasts 15 years. A knee brace worn for just 6 hours a day would then be subject to nearly half a million cycles each year. These calculations are summarized in T

Table 4.2: Estimation of total cycles a joint is subjected to during ADL.

Parameter	Value	Symbol
Daily cycles	5000	C_d
Yearly cycles	1,825,000	C_y
Cycles over 15 years	27,400,000	C_{15}
Cycles over 30 years	54,800,000	C_{30}

In a rolling contact joint using straps as constraints, there must be an upper limit to strap dimensions due to the fact they must deform as the joint flexes. A high degree of flexion is one of the functional requirements of the joint, and thus a constraint should be placed on the maximum achievable stress state in the straps. Figure 4.3 shows a sketch of a beam in bending [10].
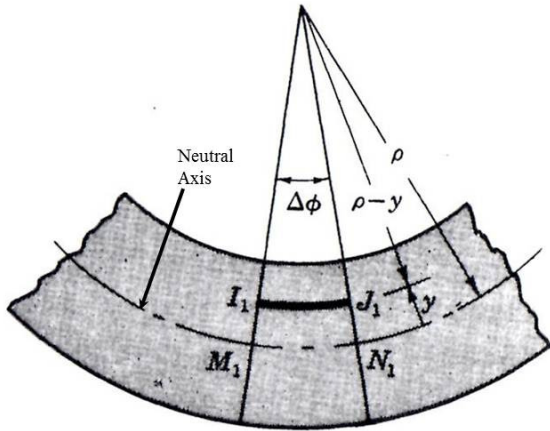
Figure 4.3: Beam bending schematic used to derive elasticity conditions for joint straps [10].

Plastic yielding through bending reduces the overall strength of a constraint and rapidly precipitates failure. Equation 4.1 shows the relationship between strain in the strap as a function of thickness and radius of curvature, and Equation 4.2 gives the resulting stress in the strap as a function of thickness y [10, pp.420-421]. These can be used to define an upper limit to the thickness of a strap based on the radius of the joint components; elasticity, at least in bending, can be defined to exist.

$$\varepsilon_x = -\frac{y}{\rho} \qquad \textbf{Eq. (4.1)}$$

$$\sigma = E\varepsilon_x = -\frac{Ey}{\rho} \qquad \textbf{Eq. (4.2)}$$

Because the strap is very long, depending on the radius of curvature a condition of plane stress or plane strain could exist. Once the geometry of the joint is defined, the state of stress in the strap can be determined using both conditions and the larger of the two used to define the constraint on thickness. These define an upper limit to the thickness of the strap as a function of the radius of curvature of the prostheses' rolling surfaces (ρ). The elasticity requirement thus comes from the fact that the bending stress resulting from the strap forming around the radius of curvature of the cam surfaces must not exceed the yield stress of the material. Next, a coordinate system must be established, which can be difficult as there are multiple conventions for coordinate systems here.

A Femoral Coordinate System (FCS) generally assumes that the leg[14] will move, while the body remains fixed as happens during leg swing while walking; a Tibial Coordinate System (TCS) assumes that the foot is "planted" and the rest of the body moves as in the next step taken during walking. The FCS and TCS are illustrated in Figure 4.4, as well as the fact that at a high flexion angle, the instant center of the joint P is in front of the joint. To determine the loads to which a joint is subjected, and the resulting strap load (they are providing constraint), they must first be applied to a more proximal joint. For example, a load must be transmitted through the hip in order to reach the knee; in a deep squat this will be amplified by the length of the femur, and this must be taken into account to ensure an accurate representation of joint loading during ADL.

---

[14] The anatomical definition of the leg are those structures distal to the tibiofemoral joint
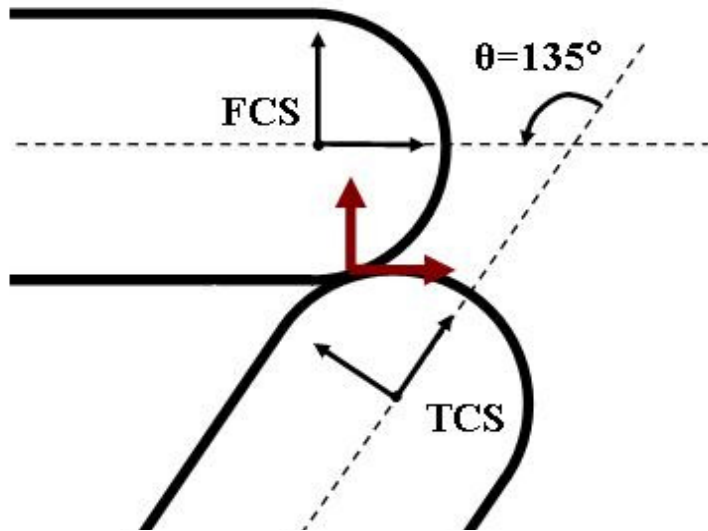
Figure 4.4: Schematic showing femoral (FCS) and tibial coordinate systems (TCS) in a sketch model of a rolling contact prosthesis.

For the case of a knee joint, the body weight is transmitted through the hip to the femur. Here, a prosthetic knee joint is assumed as this type of joint will see more load than a knee brace. Figure 4.5 shows a free body diagram of joint loading for a prosthetic knee in flexion to ~120 °.The joints of an average human being weighing 80kg are subject to contact forces as high as eight times body weight [11]; in the figure, the force F_c is on the order of 3000-4000N. Table 4.1 should be consulted for explanations of symbols in the figure.

Figure 4.5: Free-body diagram of forces due to squatting, in a rolling contact joint.

This model can also be used to determine the tensile loads in the straps. In the figure, the labels

"1" and "2" indicate the origins (subscript "o") and insertions (subscript "i") of two different

straps. There are three straps in a flexure coupling; 1 represents the path of the 1 inner strap, and

2 represents the path taken by the outer two straps. Subluxation of the femoral component (FCS)

to the left of the tibial component (TCS) is resisted by the straps connecting between points 2_o

and 2_i. Equation 4.3 shows the equilibrium condition for determining strap load based on action

of the body weight force, F_{BW}.

$$F_T = F_{BW}\left(\frac{r_{femur}}{r_{contact}}\right) \text{ Eq. (4.3)}$$

The equation assumes that only one strap is supporting the load, so that results are applicable to

both opposing sets of straps in the flexure coupling. For a body weight force on the joint of

3500N, the pure tensile stress in the strap will be proportional to the cross-section area of the

strap. This stress can be estimated using a representative strap; assuming the width of a human

knee joint is around 75-100 mm, three straps in a flexure-coupling based prosthesis will each

have a width of around 30 mm. The thickness of the strap is then determined by the modulus and yield stress of the material. A design problem is now apparent, in which bending stresses (proportional to thickness) and tensile stresses (inversely proportional to thickness) are working against one another, providing a band-pass filter with which to isolate acceptable strap thicknesses for a joint.

4.2.1. HERTZ CONTACT STRESSES

Rolling surfaces are subjected to contact stresses proportional to the equivalent modulus of the material pairing, as well as the radius of curvature [12, 13, 14]. Equation 4.4 gives the contact patch half-width, and Equation 4.5 gives the contact pressure.

$$b = \sqrt{\frac{2F}{\pi l} \frac{(1-v_1^2)/E_1 + (1-v_2^2)/E_2}{1/d_1 + 1/d_2}} \quad \textbf{Eq. (4.4)}$$

$$p_{max} = \frac{2F}{\pi bl} \quad \textbf{Eq. (4.5)}$$

If orthopaedic materials are used to fabricate a rolling contact joint, peak contact stresses will result under the greatest applied load, which during ADL can be up to 8x an individual's bodyweight. Table 4. **3** gives the relevant material properties for common materials used in orthopaedic applications including titanium, stainless steel, ultra-high-molecular-weight polyethylene (UHMWPE), and cobalt-chrome. The surgical metals described in the table are all used in engineering applications for high-performance, long-lasting machine elements which are often subjected to extreme environments and loading conditions.

Table 4. 3: Properties of four common Orthopaedic materials [15].					
Material	**ρ (kg/m³)**	**N**	**σ_y (MPa)**	**E (GPa)**	**K_{IC} (MPa-m$^{1/2}$)**
Ti6Al4V	4400	0.34	960	110	75
CoCrMo	8500	0.30	1200	220	20
SS316	8000	0.28	600	200	225
UHMWPE	0.939	0.46	24	1.2	X

These incredibly high joint loads are often experienced when a patient stands up un-assisted (i.e. no help from the arms) from a seated position. A flexed rolling contact joint in a 75kg individual subjected to a high degree of flexion will result in 3600 N being transmitted between the joint surfaces. Table 4.4 shows hertz contact stresses for different material combinations in this representative joint, and can be considered "relative stresses" as they will all change in proportion to component geometry.

Table 4.4: Hertz contact stresses (MPa) for different orthopaedic material combinations.				
Femoral Component	Ti6Al4V	CoCrMo	SS316	UHMWPE
Tibial Component				
Ti6Al4V	23.87	27.44	26.92	3.71
CoCrMo	27.44	33.29	32.38	3.72
SS316	26.92	32.38	31.54	3.72
UHMWPE	3.71	3.72	3.72	2.64

Estimated Hertz stress in joints of different material combinations suggests that the optimal material for a prosthetic metal on metal joint would be Titanium, and if a metal and polymer

were used then Titanium again would be the choice. We can look at models for lifetime of other machine elements subjected to high cyclic loads, such as rolling element bearings.

4.3 FATIGUE OF JOINT SURFACES

This section focuses on surface wear and fatigue as a result of contact forces in a prosthetic joint which can occur in both the surfaces of the joint due to contact stresses (two-body wear) and in the straps due to both tensile and bending stresses caused by loading of the joint in flexion. If particles are generated from components then three-body wear can occur. Types of wear often seen in rolling element mechanisms are shown in Figure 4.6. A text on rolling element bearing technology should be consulted for further discussion of wear types and mechanisms [16-17].
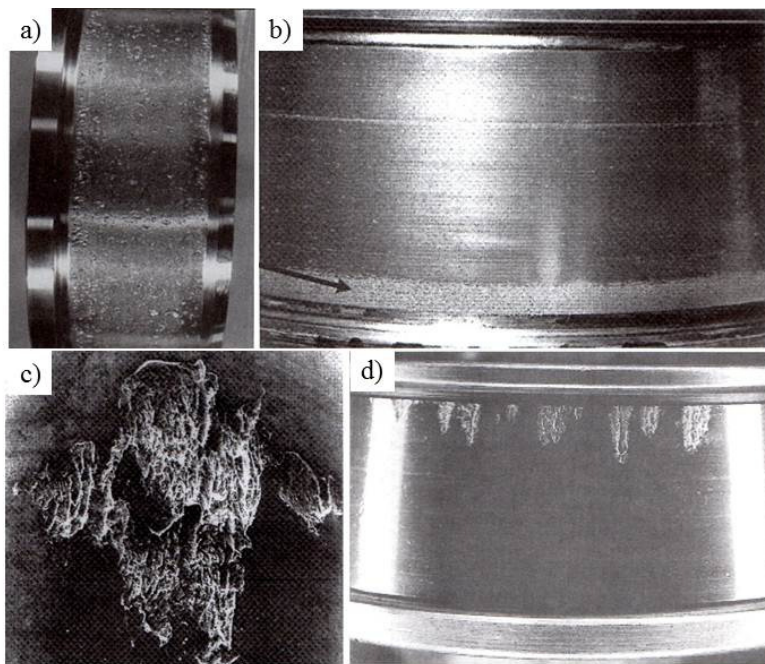
Figure 4.6: Different types of wear seen in rolling contact, including: (a) surface-initiated fatigue, (b) smearing, (c) surface fatigue spalling, and (d) edge wear due to sub-surface initiated fatigue spalls [17].

According to Talian [17, 18], a worn surface appears, to the naked eye, as "featureless, matte, and nondirectional". The original marks formed during the manufacturing process are worn away. This often occurs in mild wear, and signs of other wear mechanisms like fretting and micropitting are not present; as such mild wear is not a mode of bearing failure by itself, but more serious forms of wear like smearing, galling, and fatigue can rapidly lead to failure of rolling elements [17].

Finally, rolling surfaces in a prosthetic joint will continually be subjected to high compressive loads in static situations, such as the heel strike in walking, or even when a person is standing still. These types of loading conditions, even in a well-lubricated joint, could lead to brinnelling. Brinnelling is defined as "plastic deformation caused by sudden impact [as in walking] during [motion], or by heavy loading while [stationary]" [17]; it can be seen in Figure 4.7.
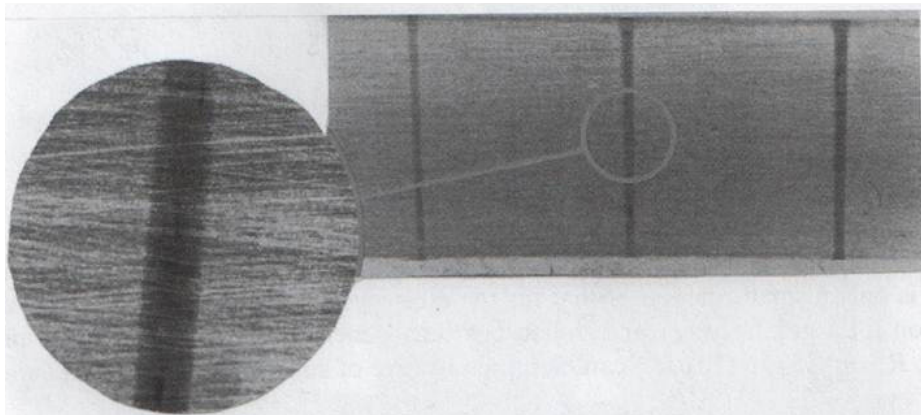
Figure 4.7: Brinnelling on the raceway of a tapered roller bearing[15] [17].

A method of linking contact stresses to fatigue and wear rates in a rolling element joint would be effective in helping to predict the useful lifetime of a mated pair in rolling contact.

---

[15] Image from [17] Courtesy of Timken, Online URL: http://www.timken.com/en-us/Pages/Home.aspx.

4.3.1. BUCKINGHAM LOAD-STRESS FACTOR

As described in Chapter 3, Section 3.4.3, an advantage of utilizing rolling contact for a prosthetic joint is that methods of modeling fatigue life in high-performance rolling-element bearings are now applicable. Fatigue yielding does not require the stress state of the material to exceed the elastic limit, can lead to significant wear in the mechanism, and as such must be assessed. Buckingham's load stress factor K_1, given by Equations 4.6a and 4.6b, uses the surface strength of an interface S_C (the contact pressure which will cause yielding after a given number of cycles) to estimate the minimum radius of curvature, of the components in contact, to ensure a fatigue life of at least 10^8 cycles (compared with current joint lifetimes of $\sim 10^7$ cycles) [12]. If both radii are known, then K_1 determined by Equation 4.6b must be less than the K_1 Equation 4.6a to ensure that failure by fatigue will not occur.

$$K_1 = 2.857\, S_C^2 \left(\frac{1}{E_1} + \frac{1}{E_2} \right) \quad \textbf{Eq. (4.6a)}$$

$$K_1 = \frac{F}{w} \left(\frac{1}{r_1} + \frac{1}{r_2} \right) \quad \textbf{Eq. (4.6b)}$$

Buckingham's equations are normally used to predict lifetimes for rolling element bearings often subjected to high radial loads and operating in extreme environments [12]. This concept was developed based on Buckingham's work with a machine for testing a standard rolling contact pair during his investigations of wear in gear teeth.

4.3.2. STATIC SLIP ANALYSIS

Kinematic analysis of slip will enable a deterministic comparison of the conventional joint configuration, which uses a biomimetic arrangement of a convex metal femoral component on a

concave polymer, with the convex-convex arrangement of a flexure coupling. Figure 4.8 illustrates this comparison, with a free body diagram of each arrangement also shown; Section 5.3.1 contains a more in-depth discussion. The slip angle γ is lower in the convex-convex arrangement.
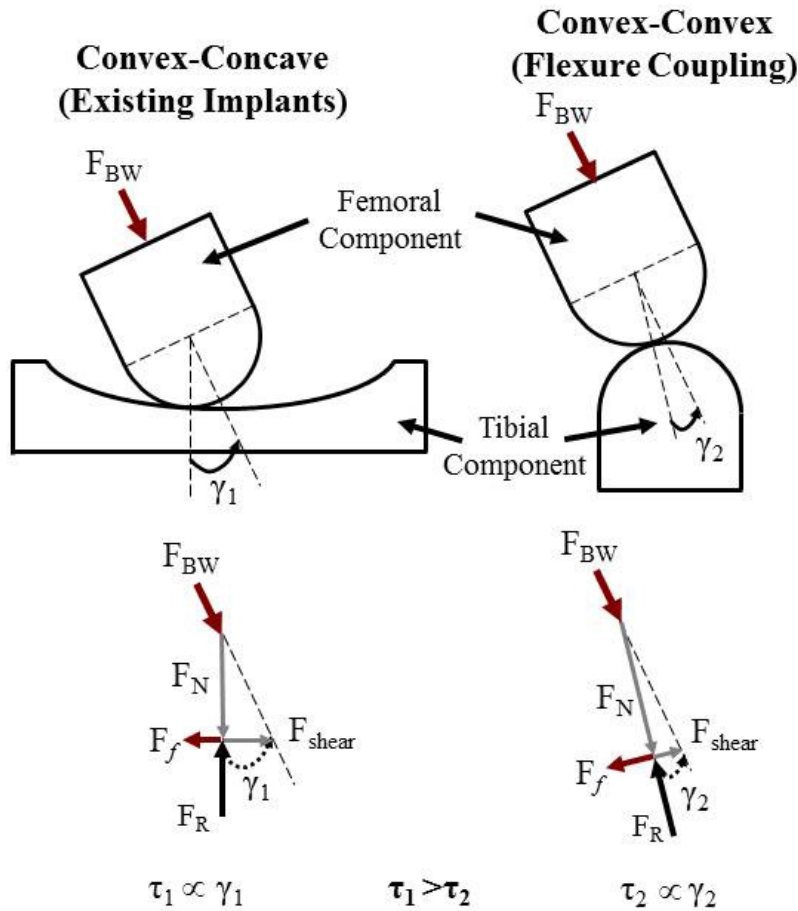
Figure 4.8: Comparison of conventional joint configuration (convex-concave) with the rolling contact arrangement in a flexure coupling (convex-convex).

From the free body diagram, the normal force on the joint is $F_N = F_{BW}\cos(\gamma)$, and an equal and opposite reaction force, $F_R = -F_N$, is generated in the lower component. The resulting friction force, $F_f = \mu F_R$, is the product of the coefficient of friction and the reaction force. Also, the shear

component of the body weight force is $F_{shear} = F_{BW}\sin(\gamma)$. To prevent slip, there must either be a high coefficient of friction in the joint (which is highly unadvisable), or the shear force must be low. Thus, the static condition for no slip is when $F_f > F_{shear}$. The convex-convex arrangement has a smaller shear angle γ_2, a greater $F_f = \mu F_{BW}\cos(\gamma_2)$, but also F_{shear} is now a much smaller component, and so overall is less likely to slip than the convex-concave configuration. Stability will be provided by soft fabrics in a knee brace, or soft tissues in the body for joint replacement.

4.3.3. SLIP BETWEEN ROLLING SURFACES

Slip is inherent to all rolling elements due to changes in loads, direction of motion, and other factors. It is dependent on the pre-load holding two rolling surfaces in contact, and is often the cause of fretting fatigue, defined as "accelerated surface damage occurring at the interface between contacting materials subjected to small oscillatory movements" [19]. It has been shown that hertz stress induces wear in contacts, especially those subjected to high numbers of cycles, and observations of increases in wear after certain numbers of cycles suggest that fatigue plays a role [20].

Slip can lead to fretting and wear in joint surfaces, so the degree of slip reduction achieved through the use of a rolling contact joint constrained by straps that do not possess infinite stiffness (the requirement for pure rolling) should be compared to slip in current joints. This enables quantification of the potential degree of improvement by utilizing a rolling contact joint. Table 4.5 summarizes compares slip in a rolling contact joint to that in a conventional prosthesis. Hooke's law ($\delta = F/k$) can be used wherein the stiffness of a constraint k (the tensile stiffness of one strap) defines the ultimate slip length δ when loaded with a force F.

Table 4.5: Comparing total lifetime slip in rolling contact and conventional joints.

Rolling Contact Joint Slip			Conventional Joint Slip		
Parameter	**Value**	**Units**	**Parameter**	**Value**	**Units**
Strap Material	Ti6Al4V	-	Condyle Radius	0.025	m
Yield Strength	180	MPa	Flexion Angle	100	Deg
Modulus	900	GPa	Arc Length	0.043	m
Strap Width	0.006	m	-		
Strap Thickness	0.0001	m	-	-	-
Strap Length	0.04	m	-	-	-
Strap Stiffness	1.35E+7	N/m	-	-	-
Load	3600	N	-	-	-
Load per side	1800	N	-	-	-
Slip Length (δ)	**0.00027**	m	Slide Length	**0.043**	m
Daily Use	5000	Cycles	Daily Use	5,000	Cycles
Daily Slip	1.33	m	Daily Slip	218.17	m
Yearly slip	486.67	m	Annual Slip	79,630.64	m
Est. Lifetime	20	years	Est. Lifetime	20	years
Lifetime slip	**9733.33**	m	Lifetime Slip	**1,592,612.94**	m
Reduction	**99.39%**	-	Reduction	**0%**	-

The resultant "deflection" in the rolling contact joint is the maximum allowable slip given the stiffness of a single strap (not counting traction or friction forces, which also resist slip, or multiple straps). It should be noted that if a load of 1800N were placed on it, the strap would

yield plastically; this is half of the total body weight force of 3600N because there are two knee joints. Overall, a reduction in the total slip over the lifetime of the joint is estimated to be greater than 99%, which is important if the joint is to retain functionality for 20 years or more.

4.4   STRAP FRACTURE AND FATIGUE

The straps constraining the two rolling elements can fail by multiple ways, including tensile, bending, fatigue, and brittle and elastic fracture. Tensile and bending were addressed in Section 4.2. Fatigue and fracture in the strap will now be discussed. Brittle strap fracture is first analyzed using a macroscopic fracture criterion for globally brittle fracture [6, 21]. The brittle fracture analysis in Section 4.4.1 links a material's critical stress intensity factor K_{IC} with a mode I stress intensity factor K_I. Elastic fracture, discussed in Section 4.4.2, also utilizes the same stress intensity factor K_{IC}, but allows a design engineer to evaluate yielding due to crack propagation, ultimately leading to strap failure.

4.4.1. BRITTLE FRACTURE

 "Globally brittle fracture is characterized by little or no macroscopically detectable inelastic deformation" [21], and is dependent on the presence of cracks that are either found in the material initially or develop during use. As a result, it is not based on observable deformation in the strap. Because of this, the risk of brittle fracture is of particular importance to evaluate in high-cycle, high-load applications including aircraft components and prosthetic joints. Equations 4.7 and 4.8 give expressions for the critical stress of failure, and critical crack size, respectively.

$$\sigma_f = \frac{K_{IC}}{\sqrt{\pi a}} \text{ Eq. (4.7)}$$

$$a_c = \frac{1}{\pi}\left(\frac{K_{IC}}{\sigma^\infty}\right)^2 \text{ Eq. (4.8)}$$

Figure 4.9 shows a plot of fracture stress due to a crack, versus the length of the crack, found using Equation 4.7. The yield strength for Grade 5 Ti6Al4V is shown in the figure as the horizontal line (900 MPa). To find the critical crack size, this value is used in Equation 4.8 to find the critical crack size, which is labeled in the figure (a_{crit} = 2.31 mm).
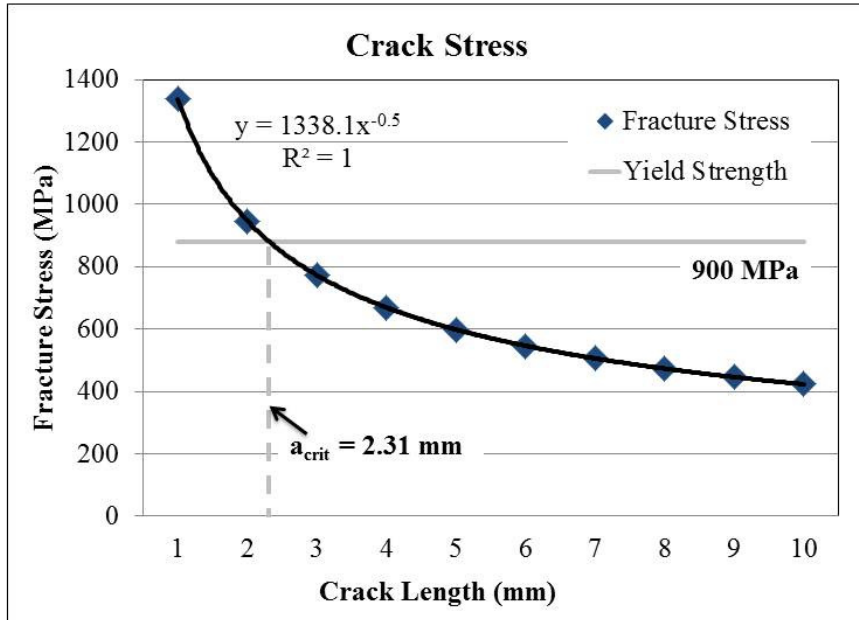
Figure 4.9: Plot showing decrease in stress around a crack; the yield stress of Grade 5 titanium and the critical crack size are also labeled in the figure.

4.4.2. CRACK PROPAGATION

For dynamic loads, a traction stress σ_{tt} can be defined in the strap as the reaction force F_c, which can be as large as 8x the patient's body weight [11], divided by the area of the contact patch a_o, as given in Equation 4.9. This stress is resultant from the strap preventing subluxation of the joint components relative to one another as the patient stands.

$$\sigma_{tt} = \frac{F_C}{a_o} \quad \textbf{Eq. (4.9)}$$

128

Here, an analogy can be made to pre-stressed steel beams used to reinforce concrete structures, a schematic diagram of which is shown in Figure 4.10a. When the structure deforms, the steel beam experiences tangential and normal forces due to interaction with the surrounding structure [22], much in the same way that the straps in this joint used to constrain the prosthesis could interact with the tibial and femoral components.
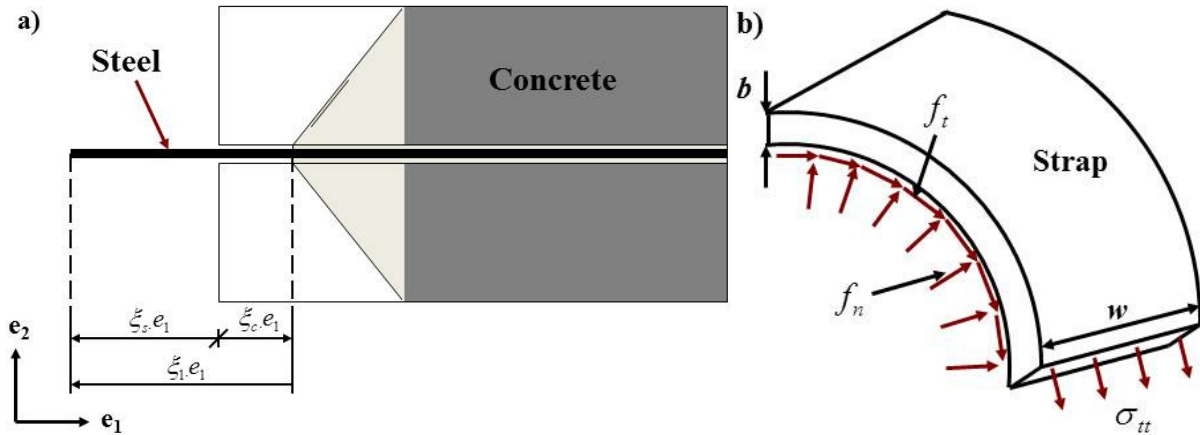
Figure 4.10: (a) schematic of stress states in steel-reinforce concrete, adapted from [22]; (b) parasitic forces resultant on a bent strap (width w, thickness b) under compression.

In order to properly predict the mode, whether fracture or fatigue, by which a strap is most likely to fail during dynamic loading (e.g. while walking, or cycling the joint), superposition of "parasitic" forces induced by this interfacial phenomena must be considered. When the strap forces have been determined, the fracture energy can be calculated and the most likely mode of failure, given a set of loading conditions, can subsequently be predicted. The schematic shown in Figure 4.10b illustrates the parasitic loads on a bent strap.

Equations 4.10a and 4.10b give an approximate relationship between the traction stress in the strap, and the tangential force and normal forces experienced by the strap. Table 4.6 summarizes

the calculation of the tensile and tangential stress on the strap as it is deformed, stretched and bent over the rounded surface of the implant. It should be noted that the normal force equation is similar to that for the tensile stress in the wall of a thin-walled pressure vessel.

$$f_t = \sigma_{tt} b \quad \textbf{Eq. (4.10a)}$$

$$f_n = Y/\rho \quad \textbf{Eq. (4.10b)}$$

Table 4.6: Calculating forces in the joint when flexed and loaded.

Parameter	Value	Units	Symbol
Strap width	10	mm	W
Body weight	80	kg	BW
Force body weight	800	N	F_{BW}
Contact Force	8000	N	F_c
Contact Area	6.1e-5	m^2	A_c
Contact Stress	131.5	MPa	P
Tangential force	**13.1**	MN/m	f_t
Normal force	**6.5**	MN/m	f_n

A strap force Y is then equal to the product of the traction stress σ_{tt}, as given in Equations 4.10a and b, and can be approximated as an equivalent to contact stress. The cross-sectional area of the strap A, starting with Equation 4.11a, can then be linked to the strap force Y, as in Equation 4.11b.

$$\frac{dY}{ds} + f_t = 0 \quad \textbf{Eq. (4.11a)}$$

$$\frac{dY}{\rho(s)} + f_n = 0; \; f_t = -f_n \tan(\varphi)$$

$$\frac{dY}{ds} + \frac{1}{\rho(s)} \tan(\varphi) ds = 0$$

$$\int \frac{dY}{Y(s)} = -\int_0^l \frac{1}{\rho(s)} \tan(\varphi) ds; \; \sigma(s) = \frac{Y(s)}{A}$$

$$\int \frac{dY}{Y(s)} = -\int_0^l \frac{1}{\rho(s)} \tan(\varphi) ds; \; \sigma(s) = \frac{Y(s)}{A} \quad \textbf{Eq. (4.11b)}$$

Subsequently, this relationship can be expanded to show that the potential energy stored in the strap prior to fracture is a function of the total length of the strap l_0, the Young's modulus E of the material, and the cross-sectional area A, as shown in Equation 4.12. The "length condition" here provides an upper limit on the length of the strap allowed to be in compression.

$$\varepsilon_{pot}^- = \frac{1}{2} \int \frac{Y^2(s)}{EA} ds = \frac{1}{2} EA \varepsilon_s^2 l_0 \quad \textbf{Eq. (4.12)}$$

Finally, this can be related to the fracture energy release rate G, as the difference in the potential energy stored in the strap prior to fracture (Equation 4.13a) and the potential energy remaining in the strap after fracture occurs, as seen in Equation 4.13b.

$$G = \varepsilon_{pot}^- - \varepsilon_{pot}^+; \; \varepsilon_{pot}^+ = 0 \quad \textbf{Eq. (4.13a)}$$

$$G = \frac{1}{2} E \varepsilon_s^2 l_0 \quad \textbf{Eq. (4.13b)}$$

Once a value for G has been determined an approximation of Irwin's Formula, seen in Equation 4.14, can be used to estimate the stress intensity factor for the strap. This relates parasitic tangential and normal forces to the resulting stress intensity surrounding a crack.

$$K_I = \sqrt{EG} \quad \textbf{Eq. (4.14)}$$

Equation 4.14 can be used in concert with the Paris-Erdogan law [15, p.114], as in Equation 4.15, to predict the number of cycles to yield a given material; ΔK_I is the change in stress intensity.

$$\frac{d\overline{a}}{dN} = c\left(\frac{\Delta K_I}{K_{IC}}\right)^n \qquad \textbf{Eq. (4.15)}$$

The number of cycles required to reach fatigue failure in the strap is given by Equation 4.16 as a function of the change in stress intensity in the strap based on the strap force Y.

$$\Delta K_I = \Delta\sigma Y\sqrt{\pi a}$$

$$\int_0^{N_f} dN = \int_{a_i}^{a_c} \frac{d\overline{a}}{c\left(\Delta K_I/K_{IC}\right)^n}$$

$$\int_0^{N_f} dN = \int_{a_i}^{a_c} \frac{d\overline{a}}{c\left(\Delta\sigma_{tt}Y\sqrt{\pi a}/K_{IC}\right)^n}$$

$$N_f = \left(\frac{2}{2-n}\right)\left(\frac{a_f^{(2-n/2)} - a_i^{(2-n/2)}}{C\left(\Delta\sigma_{tt}Y\sqrt{\pi}/K_{IC}\right)^n}\right) \quad \textbf{Eq. (4.16)}$$

The cycles to yield also depends on the critical stress intensity factor of the material, and the initial and final crack sizes. Constraints on the geometry of the implant, such as the maximum thickness and length of the strap, can then be incorporated into functional requirements to aid in the design of the joint.

Now, the fracture energy, stress intensity, and number of cycles to fatigue a strap can be determined, given a certain strap geometry and size. In the case of a strap subjected to a traction stress of 131.5 MPa resulting from a patient with 80kg body weight standing up, the resulting stress intensity in the strap with a crack of approximately 0.1 mm in size, given by Equation 4.17, is 2.3 MPa-m$^{1/2}$.

$$K_I = \sqrt{EG} \quad \textbf{Eq. (4.17)}$$

132

Table 4.7 summarizes the results of the fracture calculations. This is an order of magnitude less than the critical stress intensity for Titanium, which depending on grade, is between 44 and 66 MPa-m$^{1/2}$.

Table 4.7: Summary of fracture analysis.			
Parameter	**Value**	**Units**	**Symbol**
Stress	131.5	MPa	σ_{tt}
Crack length	0.1	mm	a
Ti modulus	100	GPa	E
Ti Fracture Energy	54.3	J/m^2	G_{Ti}
Stress Intensity	2.3	MPa-m$^{-1/2}$	K_{IC}
Ti Stress Intensity	75	MPa-m$^{-1/2}$	K_{Ti}
Fracture?	**NO**	-	-

Furthermore, using the critical stress intensity for Titanium of 75 MPa-m$^{1/2}$ it can be shown that the critical crack size is 7mm. Seven millimeters is used as the final crack length for the Paris-Erdogan calculation, and values for c and n are also assumed. The minimum stress intensity is approximately zero (under relaxed conditions) and the resulting fatigue life of the strap, from Equation 4.16, is several orders of magnitude larger than the necessary lifetime, as outlined in Table 4.8. The strap in this configuration would have essentially infinite fatigue life as the mean stress is less than half of the yield stress.

Table 4.8: Summary of fatigue analysis.			
Parameter	**Value**	**Units**	**Symbol**
Initial crack length	0.1	mm	a_o
Critical crack size	7	mm	a_{crit}
Scaling constant	0.9	n/a	C
Exponential,	2	n/a	N
Min. Stress Intensity	0	MPa-m$^{-1/2}$	K_{min}
Peak Stress Intensity	2.3	MPa-m$^{-1/2}$	K_{max}
Fatigue?	**NO**	-	-

Failure mechanisms observed in existing implants are by fracture of the polymer bearing surface [23]. The present work suggests that a rolling contact loading condition could result in a significant increase in the overall lifetime of the joint. It has been shown that a prototype rolling contact joint can achieve the required ROM utilized by a patient during ADL [1]. As mentioned previously, during a design review [24] of this analysis it was suggested that the straps could be moved into a groove in the middle of the implant to reduce traction stresses, and this configuration can be seen in Figure 4.11. This configuration will be used during the design of a rolling contact prosthesis presented in Chapter 5.
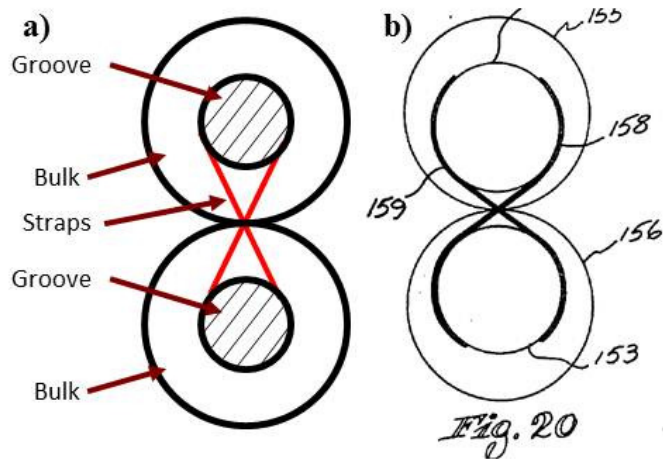
Figure 4.11: (a) rolling-contact prosthesis concept, the bulk supports weight, and the straps enable constraint; (b) shows a sketch from [4] illustrating an identical configuration.

4.5   MECHANICAL TESTING

Total knee prostheses are subjected to the full weight of the body during locomotion, and as such evaluating the durability of a rolling contact prosthesis should involve similar loading conditions. An example of a testing machine for a biomimetic prosthesis is seen in Figure 4.12. In the case of a rolling contact joint for a knee brace, compressive loads are significantly reduced, and here are estimated to be around 10% of total body weight on each side. A brace worn by an 80kg individual is estimated to experience 80N of compressive load, so each joint will see around 40N, or around 10 pounds in compression.
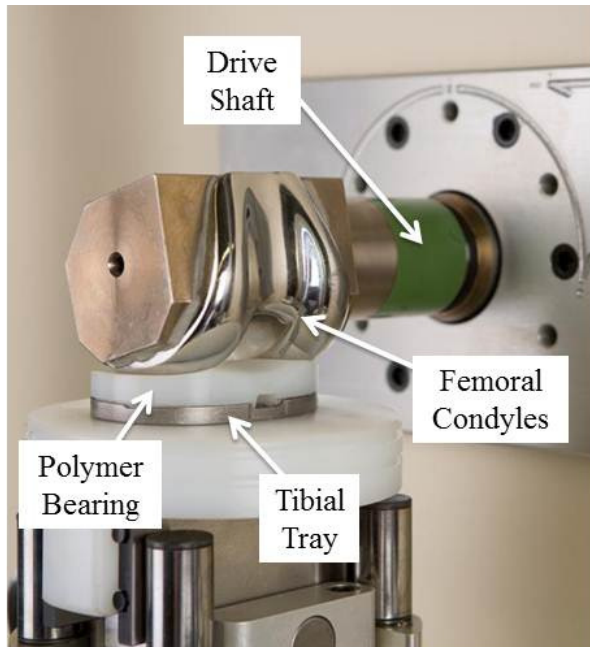
Figure 4.12: A typical testing machine for biomimetic knee prostheses[16].

A testing machine was built using a chain-driven train-wheel mechanism to cyclically load and unload a rolling contact knee brace. The first generation testing machine can be seen in Figure 4.13 with different components labeled. Figure 4.14 shows a close-up view of the prototype joint mounted in the first generation testing machine. The results of durability testing for the rolling contact prosthetic knee joint will be discussed in Chapter 5, Section

---

[16] Image source: http://www.a-tech.ca/series.php?id=879
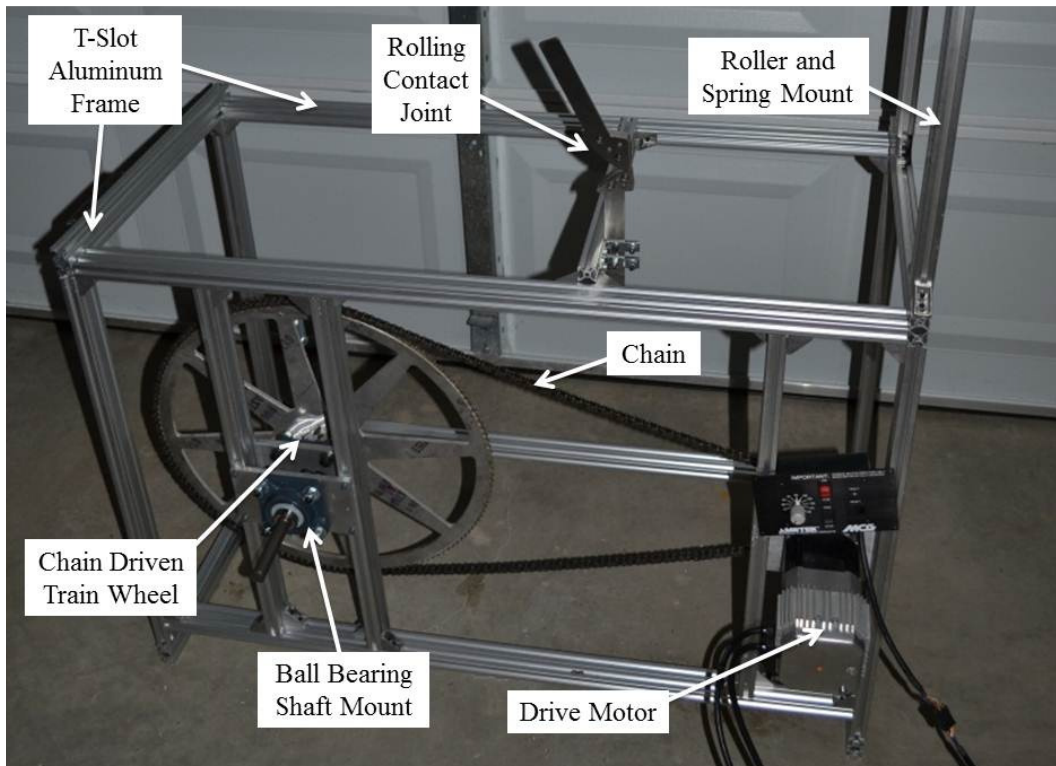
Figure 4.13: Machine for testing the first generation joint for a knee brace.
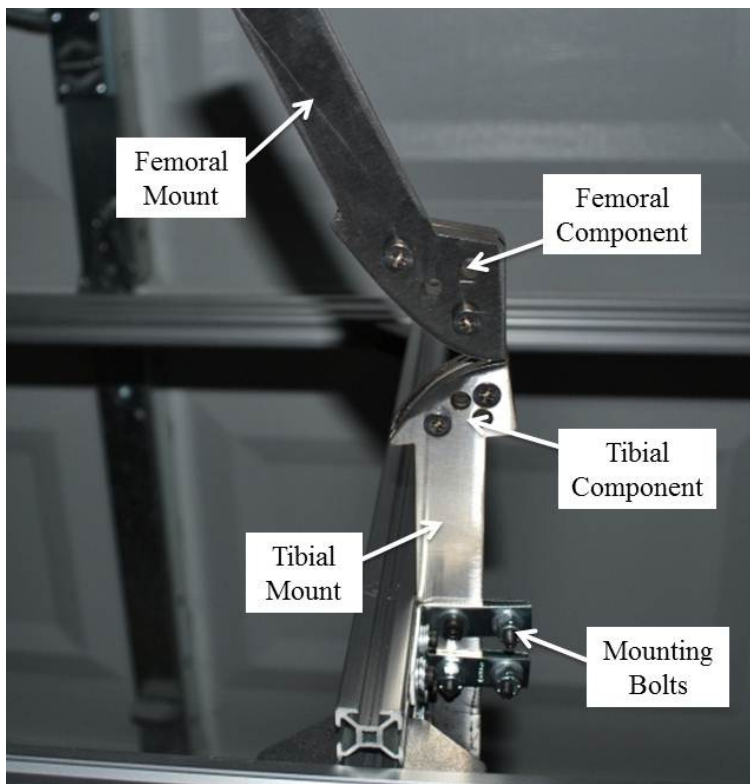
Figure 4.14: Detail view of the 304SS prototype rolling contact joint in the testing machine.

4.6   REMARKS

While fatigue is the most likely failure mode in the current configuration, this can be mitigated by introducing compliant structures into the implant to allow for parasitic motions equivalent to the normal motions in a healthy knee joint [25-27]. Methods of failure for UHMWPE bearing components used in existing implants include sub-surface de-lamination at a critical depth of about 1 mm (made worse by oxidation of the polymer) [28]. Additional failure methods include the micro-fracture of surface particles [28] and propagation of micro-cracks in the polymer implant [8].

The subsequent release of sub-micron and micron-sized particles can result in osteolysis and loosening of the prosthesis [28]. This can be further instigated by evaluating the propagation of surface cracks orthogonal to the direction of motion, for example mode I fracture under sliding/rotating contact, or mode II crack propagation from sliding contact [29]. By utilizing a well-designed rolling contact joint with adequate lubrication, risk of these failure modes decreases significantly. Further work will include design of a testing machine similar to that created by Dressler et al., seen in Figure 4.15 with various components labeled [30].
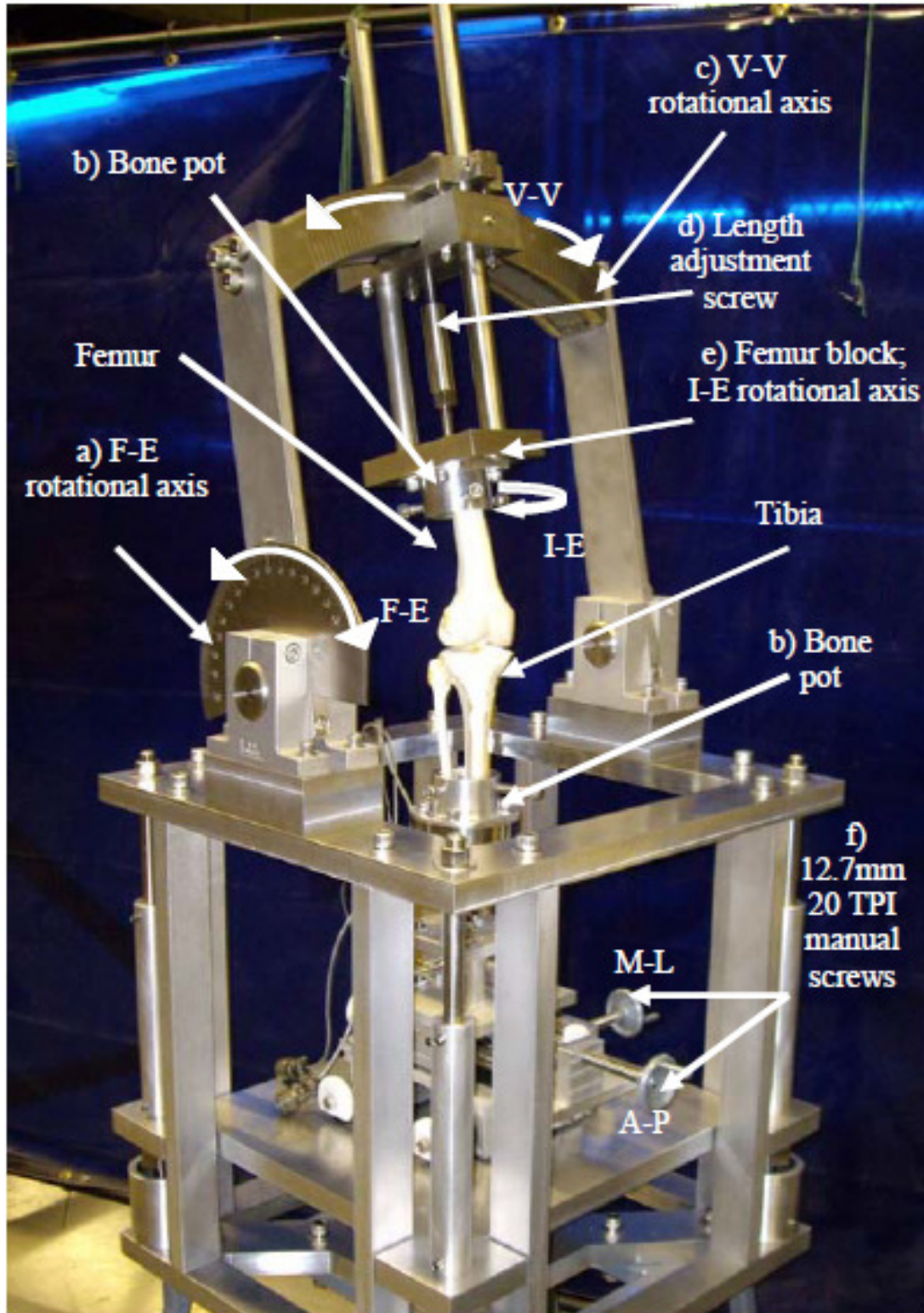
Figure 4.15: Multi-axis testing apparatus for knee joint testing [30].

4.7   REFERENCES

[1] Slocum, Jr., A. H., Herder, J. L., Varanasi, K. K., "Biomechanical Design of Rolling-Contact Knee Joint Prostheses". Presented at the 2012 Annual Meeting of the American Society for Biomechanics, Gainesville, FL, August 15-18, 2012.

[2] Vanguard® Total Knee Replacement System, Biomet, Inc., Warsaw, Indiana. Online URL: http://www.biomet.at/at-corporate/news/vanguard-monobloc.

[3] Bora, Jr., F. W., "Prosthetic Joint", U.S. Patent #4,267,608, 1981.

[4] Hillberry, B.M., Hall, Jr., A.S., "Rolling Contact Prosthetic Knee Joint", U.S. Patent #3,945,053, 1976.

[5] Jeanneau, A., Herder, J., Laliberte, T., Gosselin, C., "A compliant Rolling Contact Joint and its Application in a 3-DOF Planar Parallel Mechanism with Kinematic Analysis", Proc. ASME Design Eng. Tech. Conf., Sept 28 - Oct 2, 2004, Salt Lake City, Utah, DETC2004-57264.

[6] Ashby Materials Selection Book ------------

[7] Utzschneider, S., Paulus, A., Datz, J.-C., Schroeder, C., Sievers, B., Wegener, B., Jansson, V., "Influence of Design and Bearing Material on Polyethylene Wear Particle Generation in Total Knee Replacement". Act Biomaterialia, **5**, 2009, pp.2495-2502.

[8] Wang, A., Sun, D. C., Stark, C., Dumbleton, J. H., "Wear Mechanisms of UHMWPE in Total Joint Replacements". Wear 181-183, 1995, pp. 241-259.

[9] Diduch, D. R., Insall, J. N., Scott, W. N., Scuderi, G. R., Font-Rodriguez, D., "Total Knee Replacement in Young, Active patients. Long-Term Follow-up and Functional Outcome". Journal of Bone and Joint Surgery, April 1997, Vol. 79**A**:4, pp. 575-582.

[10] Crandall, S. C., Dahl, N. C., Lardner, T. J., An Introduction to the Mechanics of Solids, 2nd Ed., McGraw Hill, Inc., New York, 1999.

[11] Mundermann, A., Dyrby, C. O., D'Lima, D. D., Colwell Jr., C. W., Andriacchi, T. P., "In Vivo Knee Loading Characteristics during Activities of Daily Living as Measured by an Instrumented Total Knee Replacement". J Orthop Res **26**:1167-1172, 2008.

[12] Shigley, J. E., Mischke, C. R., Mechanical Engineering Design, 5th ed., McGraw Hill, Inc., New York, 1989, pp. 73-74, 315-16.

[13] Slocum, Jr., A. H., Cervantes, T. M., Seldin, E. B., Varanasi, K. K., "Analysis and Design of Rolling contact Joints for Evaluation of Bone Plates for Fracture Fixation". Submitted to Medical Engineering and Physics, December 2011.

[14] Slocum, A. H., 2008, *FUNdaMENTALS of Design*, Topic 3 – *FUNdaMENTAL* Principles, Online URL: http://pergatory.mit.edu/resources/FUNdaMENTALS.html.

[15] Revel, P. A., Ed., "Joint Replacement Technology" (2008), Woodhead Publishing, Ltd., Cambridge, UK.

[16] Harris, T. A., Kotzalas, M. N., "Essential Concepts of Bearing Technology", 5th Ed. (2007), CRC Press, Taylor and Francis Group, Boca Raton, FL.

[17] Harris, T. A., Kotzalas, M. N., "Advanced Concepts of Bearing Technology", 5th Ed. (2007), CRC Press, Taylor and Francis Group, Boca Raton, FL.

[18] Tallian, T. E., "Rolling Contact Failure Control Through Lubrication". Proceedings of the Institute of Mechanical Engineers, 1967-68, Vol. **182**:3A, pp.205-236.

[19] Elkholy, A. H., "Fretting Fatigue in Elastic Contacts Due to Tangential Micro-Motion". Tribology International, Vol. **29**(4), pp. 265-273, 1996.

[20] Yamada, T., "Rolling Wear Characteristics of Annealed Carbon Steals Under Dry Contact Conditions". Wear, Vol. **52**, pp. 279-288, 1978.

[21] Anand

[22] Ulm, F. J., "Modeling of Pre-setressing of Concrete Structures: A Boundary Condition Problem of Slip at Interface". Proceedings of the International Conference of Computational Modeling of Concrete Structures, Euro-C 1994, Vol. 2, pp. 785-804.

[23] Gomoll, A., Wanich, T., Bellare, A., "J-Integral Fracture Toughness and Tearing Modulus Measurement of Radiation Cross-Linked UHMWPE". J Orthop Res, **20**:1152-1156, 2002.

[24] Graham, M., Slocum, A., Moreno-Sanchez, R., "Teaching High School Students and College Freshman Product Development by Deterministic Design with PREP", ASME J Mech Des, 2007, **129**, pp. 677-681, Special Issue on Design Engineering Education.

[25] Hopkins, J. B., Culpepper, M. L., "Synthesis of Multi–degree of Freedom, Parallel Flexure System Concepts via Freedom and Constraint Topology (FACT) – Part I: Principles". Precision Engineering, Vol. **34**(2), pp. 259-270, April 2010.

[26] Hopkins, J. B., Culpepper, M. L., "Synthesis of Multi–degree of Freedom, Parallel Flexure System Concepts via Freedom and Constraint Topology (FACT) – Part II: Principles". Precision Engineering, Vol. **34**(2), pp. 271-278, April 2010.

[27] Hopkins, J. B., Culpepper, M. L., "Synthesis of Precision Serial Flexure Systems Using Freedom and Constraint Topologies (FACT)". Precision Engineering, Vol. **35**(4), pp. 638-649, October 2011.

[28] Kennedy, F. E., Van Citters, D. W., Collier, J. P., "Tribological Characteristics of Polyetheylene Bearings of Knee Prostheses". Int J Surface Science and Eng, **4**:2, pp.166-174.

[29] Eberhardt, A. W., Kim, B. S., "Stress Intensity Factors for a Vertical Surface Crack in Polyethylene Subject to Rolling and Sliding Contact". ASME Journal of Biomechanical Engineering, December 2008, Vol. **120**, pp. 778-782.

[30] Dressler, J. L., Ng, R. T., Amirfazli, A., Carey, J. P., "Development and Evaluation of a Multi-Axis Biomechanical Testing Apparatus for Knee". Int J Experimental and Computational Biomechanics, Vol. 1, No. 3, 2010.

This page intentionally
left blank

CHAPTER

5

ROLLING CONTACT KNEE JOINT PROSTHESES

"The worst thing I can be is the same as everybody else. I hate that." – Arnold Schwarzenegger

5.1   INTRODUCTION

Durability, fracture, and fatigue in orthopaedic implants directly influences implant lifetime and the morbidity and mortality associated with total knee replacement. The analysis, design, and manufacture of a rolling-contact prosthetic joint that mimics the primary motion of flexion and extension observed in a healthy knee will be described. A prototype joint, shown in Figure 5.1, was laser-cut from 304 Stainless Steel (304SS) and used to create a rolling-contact knee brace; flexural bands in a flexure-coupling type arrangement constrain the joint to rolling motion. This joint design could also be used as an external fixator in the treatment of knee dislocations [1]. Rolling-contact is the most efficient method of load transmission when constrained to non-biological materials (i.e., metals and polymers). While the general concept of a rolling-contact joint prosthesis is not new, as illustrated by its use in interphalangeal joint prostheses [2] and as hypothesized by Hillberry in 1976 [3], a method of achieving similar kinematics as existing

prostheses with an improved mechanical loading configuration has been developed using results of prior studies of knee biomechanics [4-6]. A four-bar linkage model of the knee is used to define the motion of the instant center of rotation of the joint based on a patient's unique anatomy; this can then be used to drive the shaping of the rolling surfaces and synthesis of the joint.
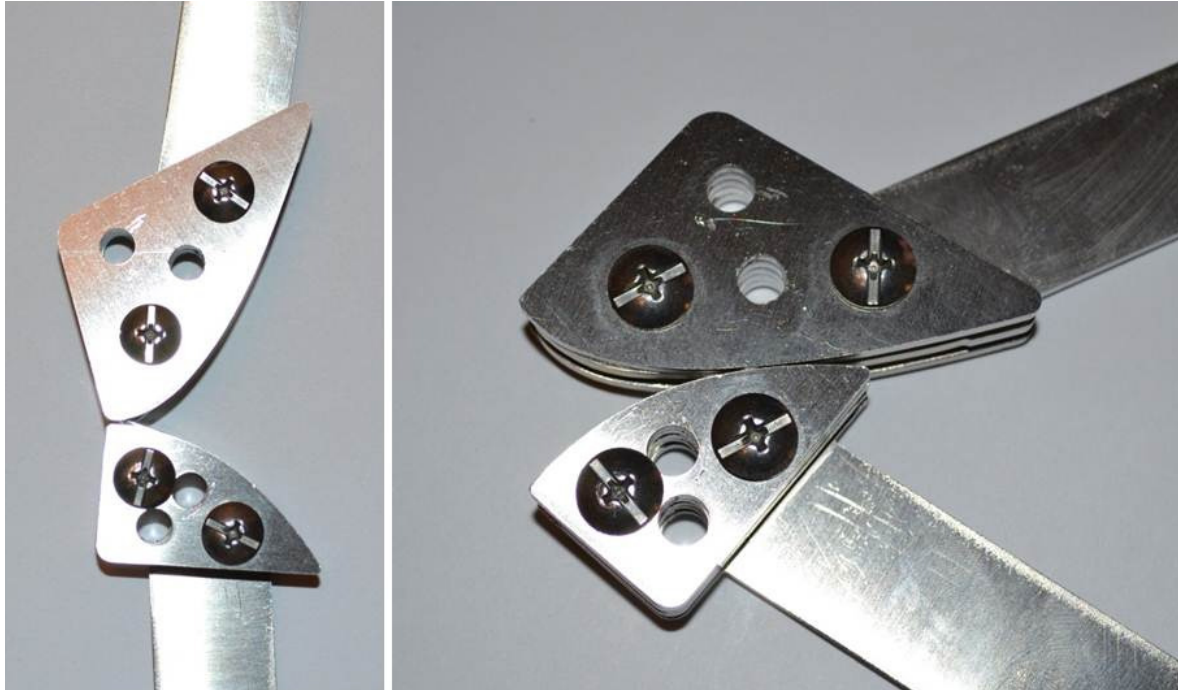
Figure 5.1: A prototype rolling-contact joint, laser cut from 304SS, which accurately mimics knee flexion and extension.

The first documented total knee arthroplasty (TKA) was performed in 1861 at King's College Hospital, London, UK [7]. The next major advance in technology for prosthetic articulating joints was the introduction of Insall's duocondylar prosthesis in the 1970's; the basic biomimetic configuration of a metal/polymer bearing joint persists today [8-10]. TKA it is a very successful procedure, with recently documented success rates of greater than 90% being observed in a study of several million joint replacements performed over a period of 12 years [11]. Furthermore,

TKA's use has increased from 129,000 to 381,000 cases per year between 1990 and 2002, and the total number performed annually in the US is expected to reach 3.4 million by 2030 [12].

As Gunston wrote in 1971, "biomechanical study and cadaveric experience" are necessary to validate the design of new prosthetic joints [9]. Through these practices, a wealth of knowledge has been catalogued regarding the biomechanics, kinematics, and kinetics of the tibiofemoral and patellofemoral joints as well as the soft tissues supporting knee motion, the anatomy of which is illustrated in Figure 5.2. This has allowed for significant improvements to performance, most dramatically in the last decade with the onset of cross-linked UHMWPE. Yet, despite these improvements, wear of the polyethylene bearing, whether from fatigue, fracture, or oxidative stresses, still remains the primary cause of implant failure, and often requires revision to replace damaged or worn-out components [13].
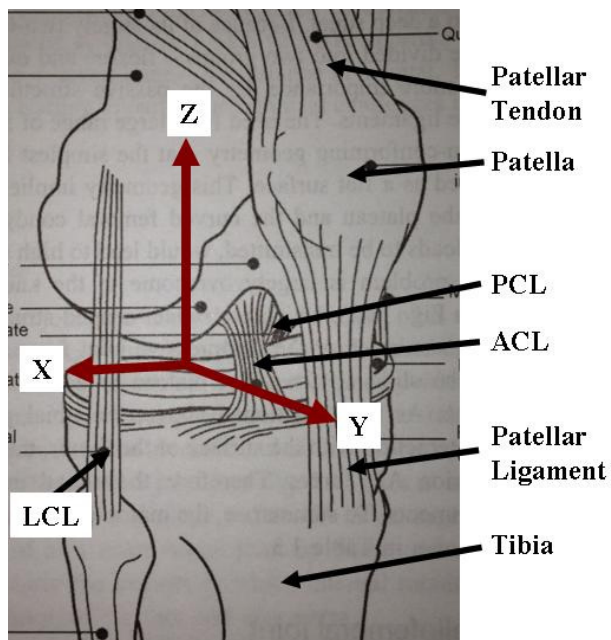
Figure 5.2: human knee joint anatomy with generalized coordinate system [14, p. 17].

A prosthetic knee that lasts twenty years can theoretically be achieved using current technology [15]; Smith and Nephew was recently granted approval by the FDA to market a "30-year knee". This approval was granted based on results from wear simulation studies performed on the VERILAST system (Smith & Nephew, London, UK),which consisted of an oxidized zirconium femoral component and cross-linked polyethylene bearing surface [16, 17]. It should be noted, however, that the reported lifetime of these prosthetic knees are based on simulated wear; failure of total knee prostheses can also be caused by other factors like infection, aseptic loosening, or yielding of periprosthetic bone [18, 19]. As patients are receiving implants at younger ages, however, and staying more active later in life, improvements to not just joint materials, but also the overall design of the joint, must be made to achieve significant increases in joint lifetimes beyond the 20 year mark [14, 20].

The results of research focused on improving the performance of technology for total knee replacement will be used to drive the synthesis of a simple planar rolling contact joint. This joint is based on the concept of a flexure coupling [21]**, using flexural bands to constrain relative motion of the surfaces, and will serve as a proof-of-concept for the development of future joints with additional degrees of freedom (DOFs). Here, the design process used to construct a joint with two DOFs for use outside of the body in a knee brace is described. Also, while the present joint is suitable for use outside of the body, additional degrees of freedom must be added before it can be considered appropriate as an implantable joint.

5.2 DETERMINISTIC ANALYSIS

It is well known that flexion/extension is the primary degree of freedom (DOF) of the tibiofemoral joint. Articulation is enabled by articular cartilage on the proximal and distal ends of the tibia and femur, respectively. A fibrous meniscus affixed to the tibia results in a concave surface on the tibia, leading to increased joint stability; articulation of the surfaces (coupled rolling/sliding motion) allows for a large range of motion (ROM) to be achieved in a compact volume. The healthy knee joint has a convex-concave configuration, where the femur is convex and the tibia/meniscus forms the concave portion. Soft tissues in the joint, namely the cruciate (ACL and PCL) and collateral ligaments (LCL and MCL), provide further constraint during motion and loading of the joint, making the knee an impressive feat of precision biological engineering. These structures were illustrated in Figure 2.

Current total knee prostheses have a biomimetic design that generally possesses a UHMWPE bearing surface, which is supported by a tibial tray that is usually made of Titanium, Cobalt Chrome, or Stainless Steel alloys [14, pp. 81-104]. A modern total knee prosthesis can be seen in Figure 5.3, as well as an A/P radiograph of a patient with bilateral prosthetic joints. Development of these implants has followed an iterative model guided in part by increasingly more invasive studies of knee biomechanics. These tests have ranged from non-invasive mechanical assessment and mathematical models [5, 6, 22] to experimental apparatuses like multi-DOF robotically-driven cadaver knee simulators or fluoroscopic imaging systems allowing measurement of knee biomechanics in human subjects [23-26]. Making further improvements to current technology will require first proving that the technology can work outside of body, as in the case of a rolling-contact knee brace.
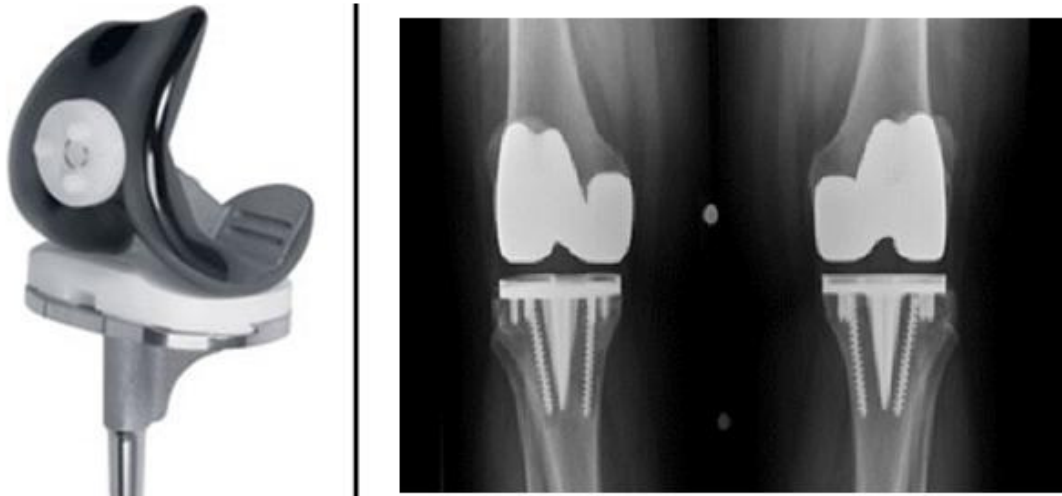
Figure 5.3: Smith & Nephew's Genesis II total knee replacement (left) [17]; radiograph of bilateral total knee replacements (right) [27].

5.2.1 FUNCTIONAL REQUIREMENTS

Deterministic analysis of the joint shown in Figure 2, coupled with a literature review of tibiofemoral joint biomechanics yielded six functional requirements (FRs) for rolling-contact knee prostheses, as seen in Table 1. Assumptions were made to enable simplification of the problem to the knee's primary flexion/extension degree of freedom. Once this initial concept is evaluated and demonstrated to be durable enough to withstand millions of cycles, additional degrees of freedom can be added. These additional degrees of freedom are conventionally referred to, when considering a flexural system, as "parasitic error motions" [28; 29, pp. 521-538]. Adding them in a deterministic manner to a rolling-contact design in order to match a normal knee's additional degrees of freedom would ensure that the rolling contact joint mimics all of the natural knee motions. It would also help mitigate bone loss that has been observed to be often associated with over-constrained prostheses.

Table 5.1: Functional Requirements (FRs) for a rolling contact knee joint prosthesis.
1. Range of articulation: +5° extension and >-120° flexion
2. Lifetime: 30M+ cycle
3. A/P Translation: 2-5 cm
4. Internal/External Rotation: +15°/-15°
5. Support loads up to 4x body weight (4000 N)
6. Variable stiffness design to allow tuning to patient's biomechanics

First principles and good machine design practices are used, in conjunction with the current body of knowledge relating to knee biomechanics and implant technology, to guide the design of a rolling-contact prosthesis "from the ground up". For example, a joint that utilizes a method of load transmission which reduces fracture or fatigue of the joint surfaces, yet still enables a large ROM, would not be subject to one of the main failure modes of current implants [30]. A successful prosthesis must maintain a large Range of Motion (ROM) to also adequately support the Activities of Daily Living (ADL). Furthermore, it should be able to withstand tens of millions of cycles, under loads greater than the patient's bodyweight, in order to last the duration of a patient's lifetime. An external joint is presented here which satisfies functional requirements 1 and 3, demonstrating that synthesis of such a joint is possible and setting the stage for further development of 6-DOF rolling contact joints.

5.3   ROLLING CONTACT JOINT DESIGN

Rolling-element bearings would be excellent candidates for achieving large ranges of motion with little resistance in a compact volume with high durability. A revolute (pin) joint, on the other hand, does not lend itself to anatomically accurate knee kinematics. A pin joint was used

for the first knee arthroplasty in 1861 and similar designs were used as prostheses for several knee replacements in the 1960s [7, 31, 32]. The latter joints failed not only due to stress concentrations around non-filleted edges, as shown in Figure 5.4 [31], but also because they did not adequately reproduce knee motion [32]. Additionally, the concept of a rolamite-based knee joint was proposed in 1973 [33], using a single S-shaped band and two cylindrical rollers. The rolamite knee is similar in principle to the design presented here in that they both use flexible bands to constrain two bodies to rolling contact for significantly reduced friction. The rolamite knee, however, is limited to simple linear motion and the use of cylinders, and the patient's weight would be supported by only a single strap. Because the current design uses additional straps it has an inherently greater degree of flexibility and can be expanded to include additional DOFs; the rolamite knee is constrained to 1 DOF. In the present design bulk surfaces support the patient's bodyweight, and their motion is constrained by flexural bands arranged in the configuration of a flexure-coupling.
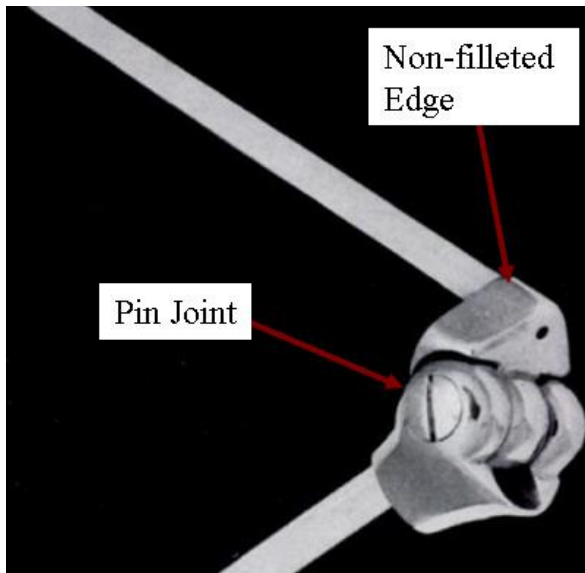
Figure 5.4: Pin-joint knee prostheses introduced in the 1960's by Shiers [30].

5.3.1   STATIC ANALYSIS

Two types of rolling contact are evaluated for their ability to achieve a large ROM and maintain rolling contact, as mentioned previously in Chapter 4. Figure 5.5 shows two types of rolling-contact joints: one a convex-concave configuration (similar to a healthy knee) and the other a convex-convex configuration. To increase the ROM of a convex-concave joint, nature added two polycentric femoral condyles and coated them with articular cartilage. Using two condyles decreases the Hertz contact stress as the load is halved, and also provides further lateral and torsional stability. Cruciate ligaments provide constraint against subluxation (for example, an individual with a damaged ACL would present with a positive drawer sign) and other adverse motions, and other soft tissues (meniscus, MCL, LCL) constrain additional motions. Articular cartilage enables high-efficiency rotation, with a coefficient of friction near zero, coupled with translation (sliding) so that the convex-concave joint can achieve a large ROM [34].
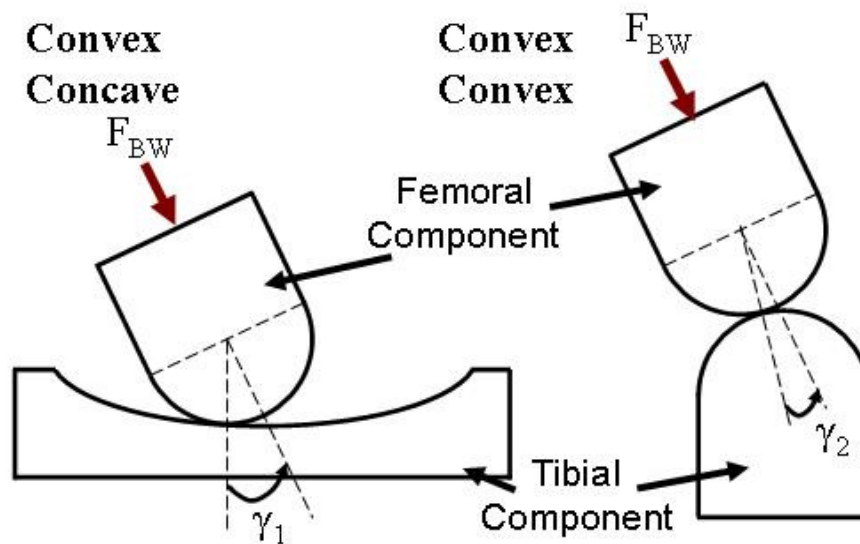
Figure 5.5: Comparison of slip angle γ in a convex/concave joint (biological and current knee prostheses) and a convex/convex rolling-contact knee joint [35].

The coefficient of friction within articulating joints has been measured to be near zero and thus the knee can rotate efficiently about an axis within the polycentric femoral condyle [23, 24, 26]. This motion becomes less efficient if the cartilage is damaged or if it has been replaced by arthroplasty [36]. The convex-convex configuration, however, allows for pure rolling-contact and a large ROM coupled to anterior/posterior translation thus satisfying FRs 1-3. As illustrated in Figure 5.5, there is a shear force generated in a prosthesis using the convex/concave configuration as articular cartilage is no longer present to lubricate the joint surfaces. This force is also larger than a similar force generated in the convex/convex arrangement. Equation 5.1 shows that the shear force is proportional to the shear angle γ according to:

$$F_{shear} = F_{BW} \sin(\gamma_1) \quad \textbf{Eq. (5.1)}$$

Shear angle, as discussed in Chapter 4, Section4.3.2, is the angle between the line of action of a load transmitted through the femoral component and a line drawn between the point of contact and center of rotation. This angle is larger in the convex-concave configuration [34] resulting in a larger shear force on the interface and, as is currently observed, high rates of polyethylene wear. In the convex-convex configuration, shear stresses would be reduced and, because the mechanism would be constrained to rolling contact rather than articulation, theoretical wear rates should be lower.

Figure 5.6 shows a free-body diagram of the forces presented in the different configurations at the point of contact (from Figure 5.5). Not only is the shear force F_{shear} lower in the convex-convex configuration due to decreased shear angle γ_2, but the friction force F_f resisting the action of F_{shear}, generated at the interface, is greater in this configuration due to a larger normal force between the surfaces. F_R is the reaction force on the tibial component, and is equal and opposite

the normal force, F_N. The convex-convex loading condition would improve an implant's resistance to slip and could also lead to reduce wear.
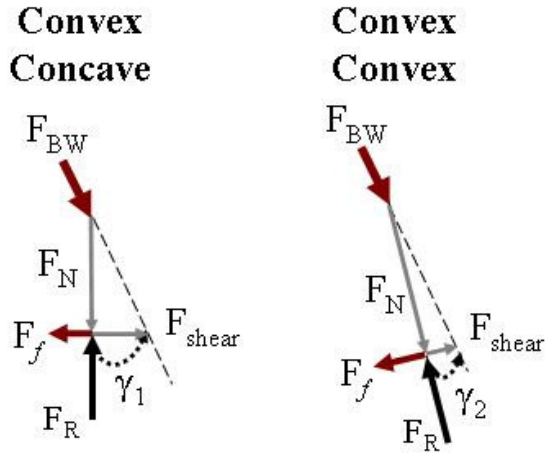
Figure 5.6: Free-body diagram of the loading configurations illustrating shear and friction forces; F_R is the reaction force in the lower component.

The normal force F_N is a function of F_{BW}, given by Equation 5.2. Equation 5.3 gives the friction force F_f as a function of F_{BW} and the static coefficient of friction, μ, between the surfaces in contact. Equation 5.4 gives the slip condition for the rolling contact joint.

$$F_N = F_{BW} \cos(\gamma) \quad \textbf{Eq. (5.2)}$$

$$F_f = \mu F_N \quad \textbf{Eq. (5.3)}$$

$$F_f > F_{BW} \sin(\gamma) \quad \textbf{Eq. (5.4)}$$

This simple model shows that, based on first principles, a convex-convex joint is more mechanically efficient in that it can be constrained to pure rolling and also reduces the chance of slip, which could significantly reduce wear. There are also numerous examples where rolling contact is used as a highly efficient means for achieving relative motion while supporting immense loads. Such examples include rolling-element bearings for paper mills or the wheels of

a locomotive. Hertz contact stresses in the current joint can be considered once the appropriate kinetics have been achieved, as this stress is dependent on the relative radii of the joint radius.

5.4   ROLLING CAM SYNTHESIS

The next step in the design process is to synthesize polycentric (cam) surfaces that will accurately reproduce tibiofemoral flexion and extension. A flexure-coupling (the mechanism behind a Jacob's Ladder) was chosen as the basic morphology of the current joint, as the straps provide well-constrained flexion and extension coupled with antero-posterior translation (analogous to a healthy knee) while maintaining rolling contact throughout the ROM [34, 35]. From a mechanical point of view, rolling contact has inherent advantages over sliding-contact.

Prior art for rolling-contact joints were either not subjected to significant compressive loads, as is the case for interphalangeal joint prostheses [2], or did not match joint motions to the kinematics of the natural joint and thus would not adequately restore normal joint function [3]. Freudenstein and Woo [4] generated curves to describe the motion of the knee joint based off of measurements of paths scribed on the tibia by points fixed to the femur, and vice versa. These curves were consequently described using logarithmic-spiral centrodes to represent the relative tibio-femoral motion, limited to just 92° of flexion. This was one of the first instances in which it was demonstrated that knee motion could be described using rolling surfaces.

Here, a four-bar linkage model [5, 6] in a sagittal plane is used to define constraints on the primary flexion/extension degree of freedom of the joint. What is different about this work is that the motion of the instantaneous center of rotation is used to generate a reference curve, from

154

which two rolling surfaces can be determined and used to create the same motion as the four-bar linkage. The surfaces in rolling-contact will be deterministically constrained to match the motions of the natural joint by tracking the four-bar linkages center of rotation (COR), as shown in Figure 5.7. This can be done in a reliable fashion based on the results of previous work [4, 5, 6] In an abstract sense, imaging of a patient's knee can be used to determine the relative locations of the cruciate ligament origins and insertions; unique surfaces can then be created for that patient without invasive measurement of relative tibio-femoral joint motion.
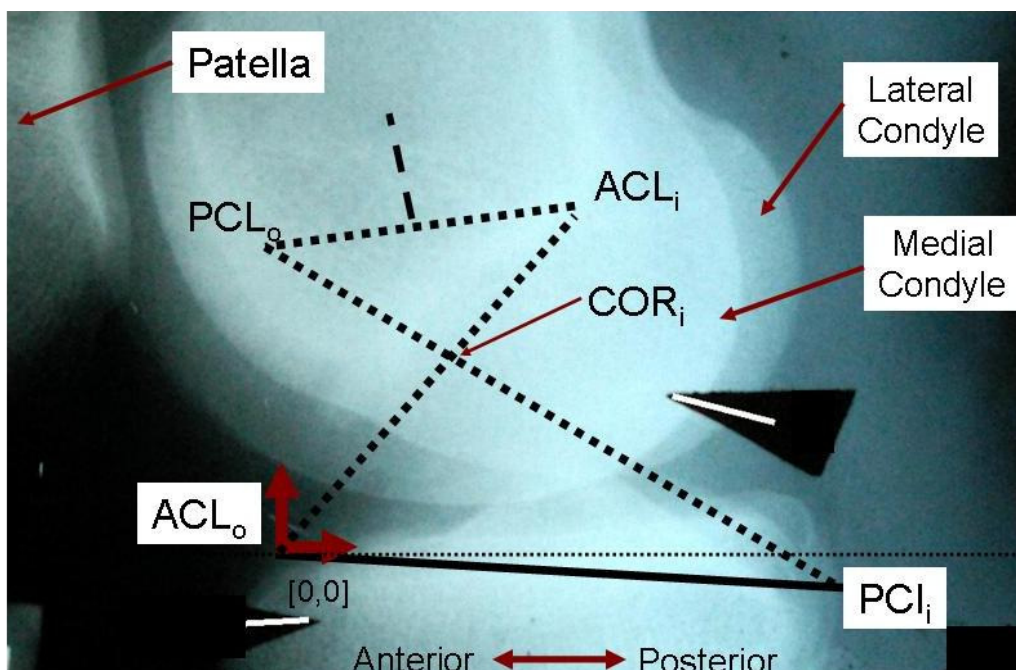
Figure 5.7: Radiograph of a healthy knee with four-bar linkage overlaid showing origins and insertions of the cruciate ligaments [37].

A highly-efficient rolling-contact joint could mimic normal knee kinetics with cam surfaces that maintain contact exactly at the center of rotation of the joint. By definition, rolling-contact inherently minimizes sliding and thus excessive traction stresses and the resulting wear can be mitigated. The origin and insertion coordinates of the ACL and PCL can be mathematically

155

related to vectors drawn between the points in the x, y, and z directions, and thus the center of rotation can be found and traced from total extension ($\theta=0°$) to significant flexion ($\theta>120°$), as illustrated in Figure 5.8a-c. Theta, θ, refers to the abstract angle between the tibia and femur and is not shown in the figure. Total flexion angle is measured between the initial and final direction of the normal vector to the follower link. The subscripts "*o*" and "*i*" refer to origin and insertion, respectively.
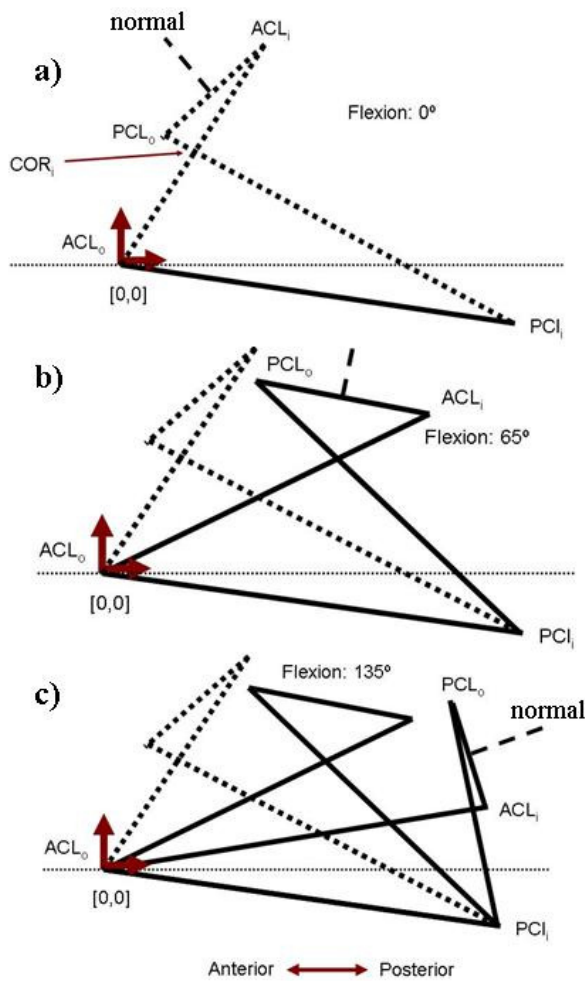
Figure 5.8: Sequence of four bar linkage motion as the knee is moved through 135 degrees of flexion (a-c). The coarse dashed line is the normal to the follower link.

Solving the forward kinematics problem for a four-bar linkage can be used to find the instantaneous center of rotation of the mechanism. Once the motion of the COR is known, it can be used to synthesize a set of cam surfaces which exactly mimic the motion of the knee joint in a sagittal plane. Figure 9 shows a schematic diagram for a four-bar linkage representation of the knee with relevant parameters labeled. The lengths for the ACL and PCL links are calculated using values adapted from previous studies on knee motion [6] and the x and y-coordinates of each point are summarized in Table 2.

Table 5.2: Coordinates for each linkage pivot shown in Figure 5.9 [6].

Pivot	X-Coordinate	Y-Coordinate
A	0	0
B	12.440	32.715
C	7.763	21.973
D	37.300	-5.000
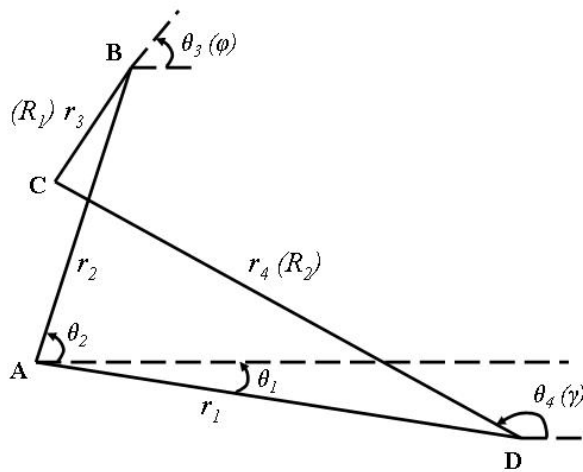
Figure 5.9: Schematic diagram illustrating parameters used to find the motion of the instant center of the coupler link for the four-bar linkage.

Table 5.3**:** Known, unknown, dependent and independent variables in Figure 5.9. lists the independent and dependent variables. The points A, B, C, and D are coordinates of the origin or insertion point of the ACL or PCL; these are used to construct vectors $r_{1\text{-}4}$, and the angles $\theta_{1\text{-}4}$ are between the vector and the horizontal. A closed-loop constraint for the four-bar linkage, the first step in deriving the COR equations of motion, is given in Equation 5.5.

$$r_1 + r_4 = r_2 + r_3 \quad \textbf{Eq. (5.5)}$$

Table 5.3: Known, unknown, dependent and independent variables in Figure 5.9.			
Known	**Dependency**	**Unknown**	**Dependency**
r_1	Independent	θ_3	$f\{r_1, r_2, r_3, r_4, \theta_1, \theta_2\}$
r_2	Independent	θ_4	$f\{r_1, r_2, r_3, r_4, \theta_1, \theta_2, \theta_3\}$
r_3	Independent	B_x	$f\{r_2, \theta_2\}$
r_4	Independent	B_y	$f\{r_2, \theta_2\}$
θ_1	Independent	C_x	$f\{D_x, r_4, \theta_4\}$
θ_2	Independent	C_y	$f\{D_y, r_4, \theta_4\}$

The values of θ_1, r_1, r_2, r_3, and r_4 are constant. The angle between vector **AB** and the horizontal, θ_2, is indexed during the analysis. As **AB** rotates about point A, the follower link **BC** rotates from its initial angle (fully flexed) through an angle of 135° to ensure adequate range of motion of the cam surfaces. This ensures that the joint will fulfill the first functional requirement. Imaginary numbers are introduced in Equation 5.6 to describe the position of each pivot *A-D* with respect to its components in the x- and y-directions in terms of the variables listed in Table 5.3. These imaginary numbers will eventually be used to derive equations for θ_3 and θ_4 as functions of the independent variables.

$$r_1 e^{i\theta_1} + r_4 e^{i\theta_4} = r_2 e^{i\theta_2} + r_3 e^{i\theta_3} \quad \textbf{Eq. (5.6)}$$

Equation 5 can be rearranged and the r_1 and r_2 terms can be grouped into a single imaginary variable z thus allowing for isolation of dependent variables according to Equations 5.7a-b. Equations 5.7c-d are the real (x) and imaginary (y) components of z in terms of r_1, r_2, θ_1, and θ_2.

$$r_1 e^{i\theta_1} - r_2 e^{i\theta_2} = r_3 e^{i\theta_3} - r_4 e^{i\theta_4} \quad \textbf{Eq. (5.7a)}$$

$$z_{1,2}(x,y) = z_{1,3}(x,y) = r_1 e^{i\theta_1} - r_2 e^{i\theta_2} = r_3 e^{i\theta_3} - r_4 e^{i\theta_4}$$

$$z(x,y) = r_3 e^{i\theta_3} - r_4 e^{i\theta_4} \quad \textbf{Eq. (5.7b)}$$

$$x_{1,2} = \mathrm{Re}(z_{1,2}) = r_1 \cos(\theta_1) - r_2 \cos(\theta_2) \quad \textbf{Eq. (5.7c)}$$

$$y_{1,2} = \mathrm{Im}(z_{1,2}) = r_1 \sin(\theta_1) - r_2 \sin(\theta_2) \quad \textbf{Eq. (5.7d)}$$

Four substitutions are now made: $r_3 = R_1$, $r_4 = -R_2$, $\theta_3 = \varphi$, and $\theta_4 = \gamma$. Equation 5.7b will then be expanded and elimination of φ is achieved through use of a trigonometric identity as described below, resulting in Equation 5.8.

$$z(x,y) = r_3 e^{i\theta_3} - r_4 e^{i\theta_4} = R_1 e^{i\phi} + R_2 e^{i\gamma}$$
$$x = \mathrm{Re}(z) = R_1 \cos(\phi) + R_2 \cos(\gamma)$$
$$y = \mathrm{Im}(z) = R_1 \sin(\phi) + R_2 \sin(\gamma)$$
$$\cos(\phi) = \frac{x - R_2 \cos(\gamma)}{R_1}$$
$$\sin(\phi) = \frac{y - R_2 \sin(\gamma)}{R_1}$$
$$\sin^2(\phi) + \cos^2(\phi) = \left(\frac{y - R_2 \sin(\gamma)}{R_1} \right)^2 + \left(\frac{x - R_2 \cos(\gamma)}{R_1} \right)^2 = 1$$

$$y^2 - 2R_2 y \sin(\gamma) + R_2^2 \sin^2(\gamma) + x^2 - 2R_2 x \cos(\gamma) + R_2^2 \cos^2(\gamma) = R_1^2 \quad \textbf{Eq. (5.8)}$$

Equation 8 can be further simplified, resulting in Equation 5.9.

$$x^2 + y^2 - 2R_2 y \sin(\gamma) - 2R_2 x \cos(\gamma) + R_2^2 = R_1^2$$

$$y\sin(\gamma) + x\cos(\gamma) = \frac{x^2 + y^2 + R_2^2 - R_1^2}{2R_2} \quad \textbf{Eq. (5.9)}$$

Using the trigonometric identity in Equation 5.10, an equation for γ as an explicit function of independent variables can be found via substitution of Equation's 7c-d. This expression is given by Equation 5.11.

$$b\sin(x) + a\cos(x) = \sqrt{a^2 + b^2} \, \cos(x - \arctan(b/a)) \quad \textbf{Eq. (5.10)}$$

$$y\sin(\gamma) + x\cos(\gamma) = \sqrt{x^2 + y^2} \, \cos(\gamma - \arctan(y/x)) = \frac{x^2 + y^2 + R_2^2 - R_1^2}{2R_2}$$

$$\gamma = \theta_4 = \arctan\left(\frac{y}{x}\right) \pm \arccos\left(\frac{x^2 + y^2 + R_2^2 - R_1^2}{2R_2\sqrt{x^2 + y^2}}\right) \quad \textbf{Eq. (5.11)}$$

Now that γ can be described in terms of only independent variables, an equation for φ as a function of independent variables and γ (now that γ is known) can be obtained from the derivation of Equation 9; this relationship is provided in Equation 5.12.

$$\phi = \theta_3 = \arctan\left(\frac{y - R_2\sin(\gamma)}{x - R_2\cos(\gamma)}\right) \quad \textbf{Eq. (5.12)}$$

Now that the kinematics of the pivots are known, motion of the COR_i can be described analytically for any given value of the links r_{1-4}, and in turn any values derived from anatomical analysis. The COR of the linkage is the point at which the links r_2 and r_4 intersect, as given by Equation 5.13. Linear equations can be used to describe each segment for all values of θ_2.

$$y_1 = m_1 x_1 + b = m_2 x_2 = y_2 \quad \textbf{Eq. (5.13)}$$

While points A and D are stationary, the slope m_2 of link r_2 is found by taking the tangent of θ_2. Equations 5.7c-d, 5.11, and 5.12 can be used to find the x- and y-coordinates of C (C_x, C_y) at the current value of the flexion angle θ_2. Coordinates C_x and C_y are then used to find the intercept, b, and slope, m_1, of the segment r4. Equation 5.14a gives the x-coordinate of the r_2-r_4 intersection,

and Equation 5.14b gives the y-coordinate. This method allows information about the geometry of an individual's knee to be used to synthesize a unique curve mimicking the motion of that person's joint. Figure 5.10 shows the motion of the instantaneous center of rotation of the four-bar linkage model of a knee.

$$X = x_1 = x_2 = \frac{b}{m_2 - m_1} \quad \textbf{Eq. (5.14a)}$$

$$Y = m_2 X \quad \textbf{Eq. (5.14b)}$$
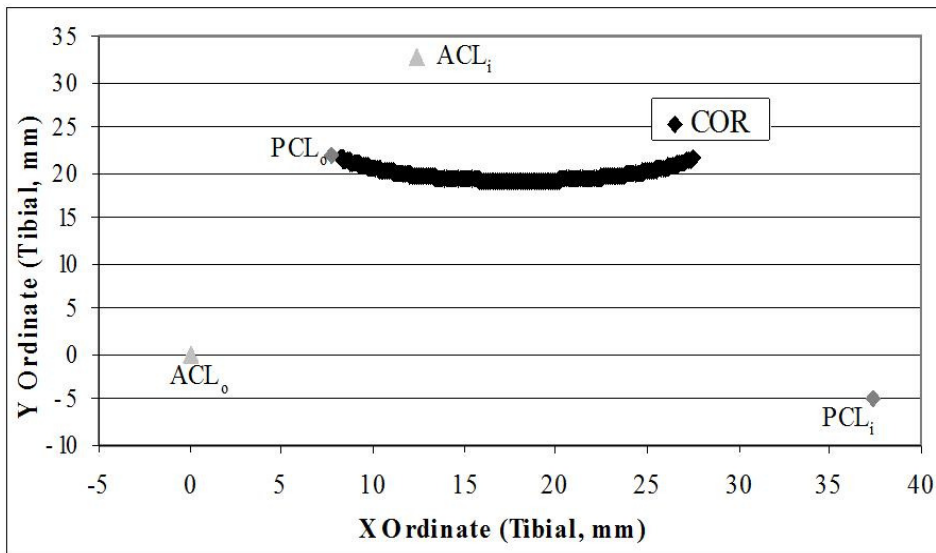
Figure 5.10: Motion of the instantaneous center of rotation of the four-bar linkage constructed from origins and insertions of the ACL and PCL.

5.5   FLEXURE STRAP TOPOGRAPHY

Once the contours of the polycentric surfaces have been obtained to mimic a healthy knee's kinematics, flexure straps or compliant rolling-contact elements [21, 38-40] must be synthesized to guide the desired kinematics. These straps must effectively constrain unwanted DOFs, while allowing the polycentric surfaces to roll along their contours with minimal sliding, satisfying FR5 when the joint is flexed (the top surfaces would tend to slide off of the bottom surface when

the joint is flexed). They must also be durable enough to withstand tens of millions of flexion/extension cycles to satisfy FR2. Two concepts for satisfying these requirements are shown in Figure 5.11. The first concept, shown in Figure 5.11a-b, is constrained by three centrally located flexure straps. The second concept, shown in Figure 5.11c-d, is constrained by four flexure straps which are located along the outer sides of the rolling surfaces. The initially flat straps of either concept must be thin enough such that they will not plastically deform as they are bent along the surfaces of the cams. The widths of these straps may be adjusted such that their opposing spring-back forces will balance and enable highly-efficient flexion.
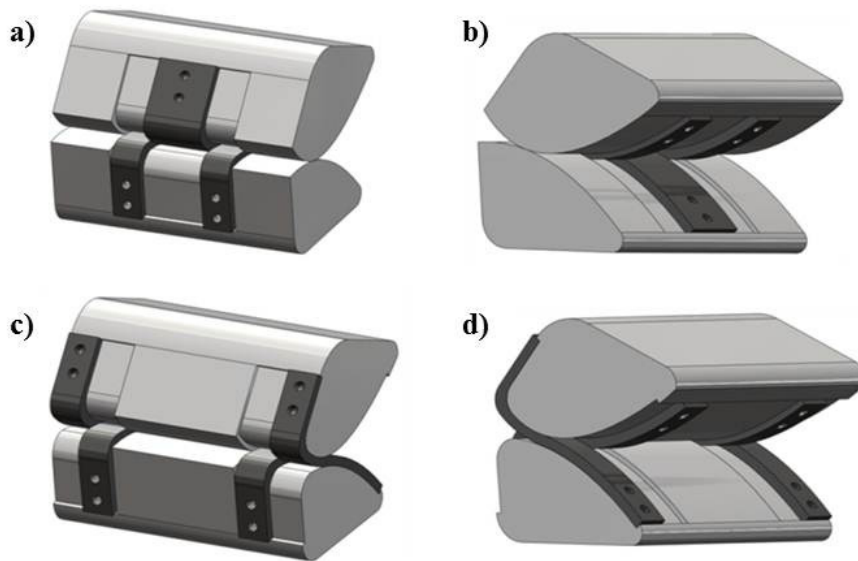
Figure 5.11: Front and back views of flexure straps for two different concepts (a-d).

The straps should be tensioned such that they are always touching one of the two cams. The straps should each be separated by a small amount horizontally, such that they do not rub past each other as they lift up and lay down on the cam surfaces as the cams roll. Except for the location of these small gaps between the straps, there is a single line of contact between the two cams for either concept at every position of the joint. The advantage of the first concept shown

in Figure 5.10a-b is that it only possesses three straps. The advantage of the second concept shown in Figure 5.10c-d is that it is capable of providing greater resistance to unwanted rotational DOFs. The straps' geometry and material properties in either concept, however, can be adjusted to match the compliance in flexion/extension of a healthy knee.

5.6   JOINT MANUFACTURE AND TESTING

Deterministic synthesis of a rolling contact prosthetic tibiofemoral joint using knowledge of the biomechanics of the healthy joint provides significant mechanical advantage over sliding contact joints. A four-bar linkage model of the knee taken in a sagittal plane can be used to find a solution to the forward kinematics problem of the mechanism [5, 6, 28]. Tracking the instantaneous center of rotation (COR) as the intersection of the lines of action for the ACL and PCL, as described analytically above, generates the COR curve in Figure 5.12. This section details the synthesis of cam surfaces, prototyping of the joint using a 3-D printing process (Objet Connex 500[17], Precision Compliant Systems Laboratory, MIT), and the manufacture and testing of two generations of prototype joints.

---

[17]Manufactured by Stratasys, Inc. Online URL: http://objet.com/3d-printers/connex/objet-connex500
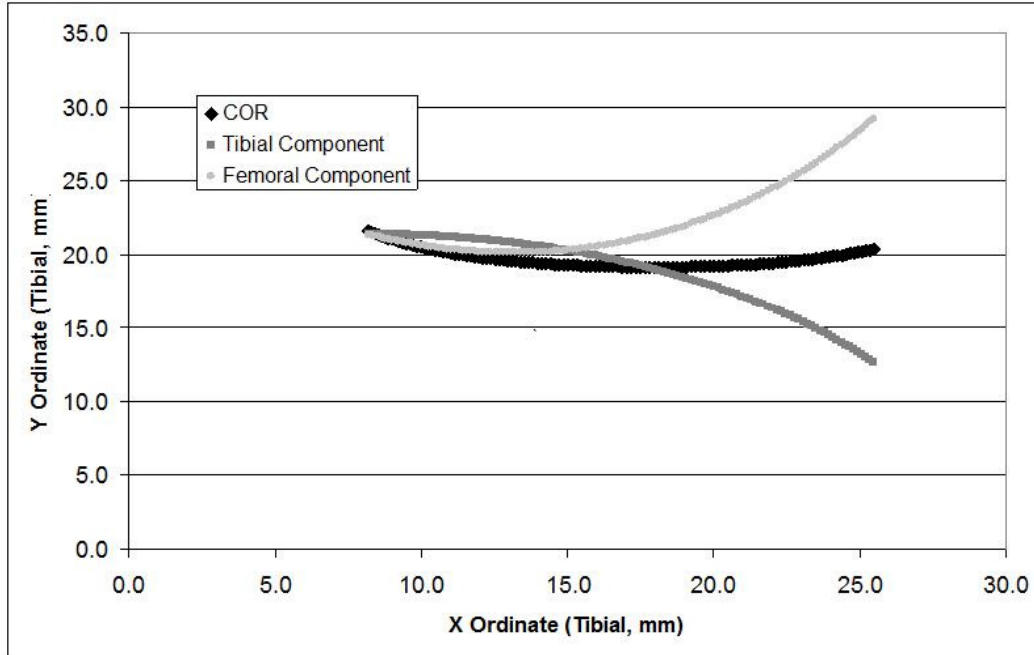
Figure 5.12: Curves defining motion of tibiofemoral joint instant center of rotation, the surface of the tibial component, and the resultant femoral component curve.

Based on the four-bar linkage model, the insertion of the ACL on the anterior proximal tibia serves as the origin of the mechanism. This eliminates the need, at least preliminarily, to select a certain tibial or femoral coordinate system as the knee joint is a statically indeterminate system (i.e., knowing the degree of flexion/extension does not guarantee knowledge of soft tissue loads, and vice versa). The tibial component surface in Figure 5.12 was selected to be a circle that intersects the initial position of the linkage COR, adapted from [6], and is described by Equation 5.15a. This curve can realistically be any shape, and can be chosen in the first stages of joint synthesis.

$$y = \sqrt{x^2 - (x - 8.2028)^2} \text{ **Eq. (5.15a)**}$$

The femoral component surface is found by taking the difference between the COR and tibial component curves. The expression for the femoral component surface, a 3rd order polynomial (R^2=0.999), is given in Equation 5.15b. Fitting a fourth-order polynomial (R^2=0.999) to the COR curve yields an expression for its motion as a function of anterior/posterior position as is given by Equation 5.15c. These curves will be important in the future when joint lubrication is considered to ensure that surface integrity is maintained.

$$y = 0.0009\ x^3 + 0.013\ x^2 - 0.83\ x + 26.718 \quad \textbf{Eq. (5.15b)}$$

$$y = 0.0001\ x^4 - 0.009\ x^3 + 0.2541\ x^2 - 3.3579\ x + 36.375 \quad \textbf{Eq. (5.15c)}$$

As the femoral and tibial components roll relative to one another, the geometric summation of their surfaces yields motion that is mathematically and anatomically equivalent to the primary articulation DOF in a healthy knee joint. The curves in Figure 5.12 were used to create solid models of the femoral and tibial components in SolidWorks™ (Dassault Systems, Waltham, MA), and a prototype was fabricated using a Stereolithography 3-D printing process (American Precision Prototyping, Tulsa, OK). A rolling-contact joint with a ROM of between 120° and 130° is shown in Figure 5.13.
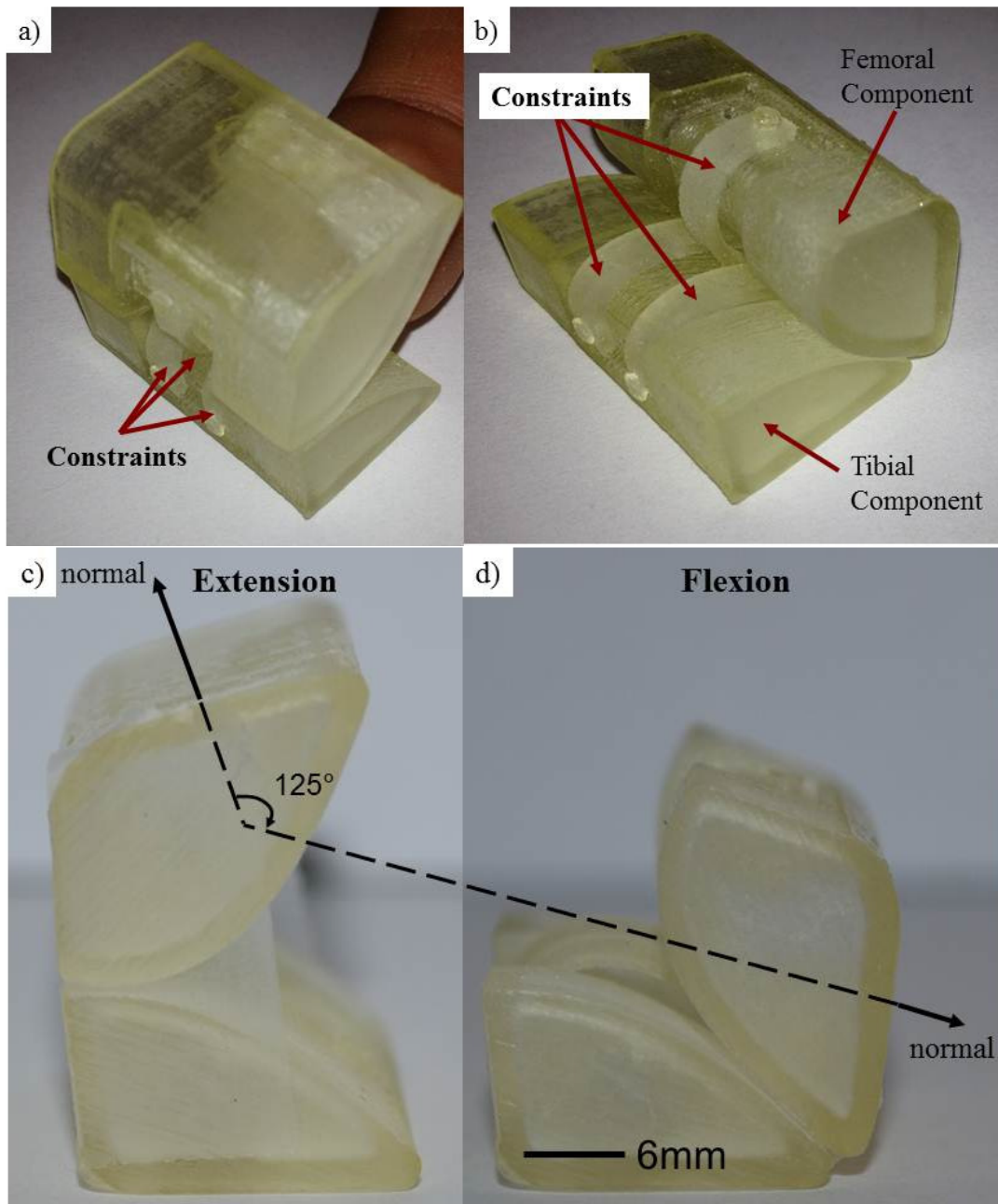
Figure 5.13: (a-b) Isometric view of a 3-D printed prototype joint using curves in Figure 5.12; (c-d) achieving flexion/extension range of greater than 120° via rolling contact.

5.6.1 FIRST-GENERATION PROTOTYPE JOINT

A rolling-contact joint for knee braces was then reduced to practice, based on the prototype in Figure 13. 304 Stainless Steel was chosen for its high yield strength and low cost, and the joint components were fabricated using a laser cutter and 6mm plate [41]. Figure 14a shows an exploded view of the knee brace joint components. Sex bolts are used to maintain a low profile and keep the assembly compressed together, while spring pins are used to maintain alignment. The nature of the laser-cutting process required a gap size of about 0.8mm, which was filled with appropriately sized aluminum shims.
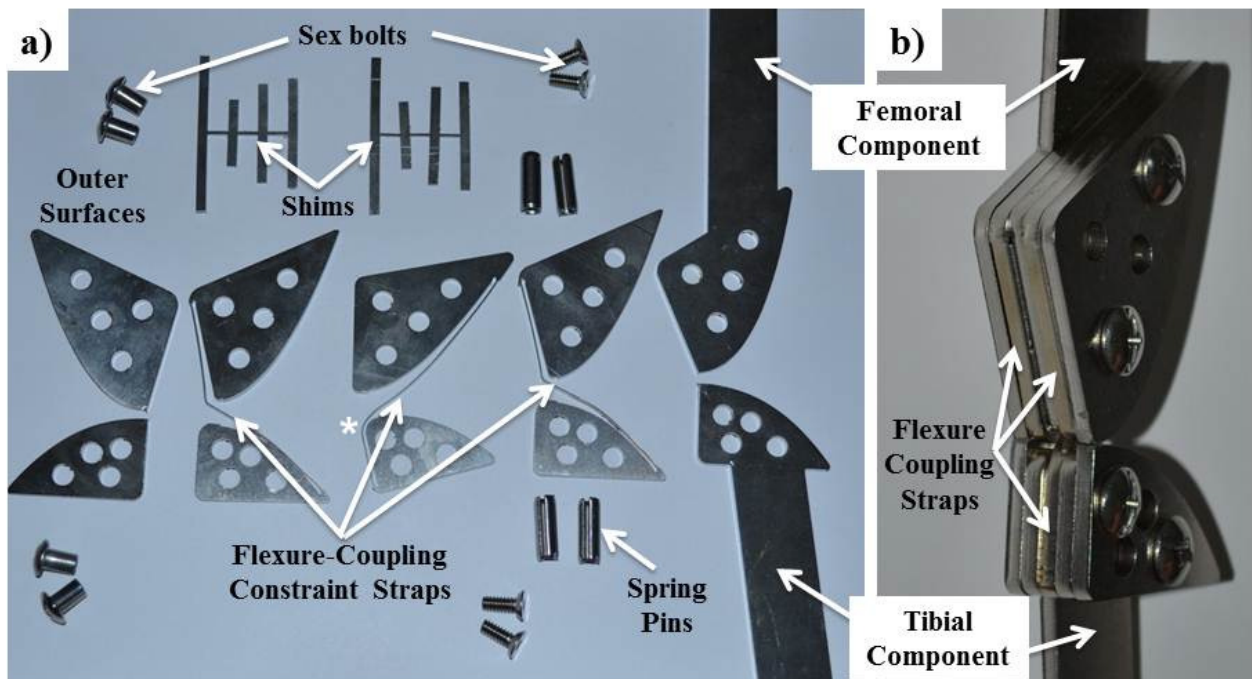
Figure 5.14: (a) Exploded view of components for the stainless steel rolling-contact joint seen in Figure 5.1; (b) Isometric view of the assembled prototype.

Proper flexure coupling constraint requires two straps running anterior-posterior, and one strap posterior-anterior; these three components are slightly smaller in size than the femoral, tibial, and outer surface components labeled in Figure 5.14a. The parts on the left labeled "outer surfaces"

are exact matches to the femoral and tibial components on the right, which are the physical embodiments of the curves in Figure 5.12; together these four components provide rolling support to the joint and are constrained by spring pins. Figure 5.14b shows an isometric view of the assembled joint, with the flexure coupling straps labeled; the mounting arms on the femoral and tibial components are used to attach the joint to the body of the knee brace.

Figure 5.15a and 5.15b show the joint from Figure 14b used in a commercially-available knee brace (Donjoy Playmaker Brace, DJO, LLC, Vista, CA). As demonstrated by author AHS the joint is capable of supporting motion within the normal range as encountered within the activities of daily living. The straps seen in Figure 14a are fabricated in a "pre-bent" configuration to attempt to reduce bending stresses, and the shims are required to enable the degree of constraint provided by the flexures and fill in the gap created during the laser cutting process.

Figure 5.15: Rolling contact knee brace joint in extended (a) and flexed (b) positions.

During the first round of tests with the machine described in Chapter 4, Section 4.5, the joint's integral flexures failed due to a combination of extreme bending stresses and changes in the joint material properties caused by the manufacturing process. Laser cutting melts and vaporizes material while cutting. As such, the aerospace industry avoids the use of laser-cut aluminum components because of deleterious effects on material properties like fatigue strength [42]. While the material used here is stainless steel, the empirical observation of significantly reduced fatigue strength (failure after a very low number of cycles), it is hypothesized that the laser cutting process had similar effects on the stainless steel's material properties. Due to this fact, conventional machining methods were used in the next generation joint, and a new method of constraining the straps had to be designed.

Failure of the prototype joint during testing occurred at the bend in the middle constraint, indicated by the white "*" in Figure 5.14, after just 9:53 minutes. Running at 1 Hz meant that this was after only 593 cycles; the failed strap can be seen in Figure 5.16. The reduced fatigue strength of the steel was likely caused by the fabrication method, which could have caused formation of a heat-affected zone (HAV). The resultant decrease in K_{IC}, combined with the tight radius of the anterior surface of the tibial component led to failure of the strap.

Figure 5.16: Image of failure in the middle strap.

5.6.2   *SECOND-GENERTION PROTOTYPE JOINT*

From a deterministic perspective [29], the risk in this case is low cycle fatigue in the strap due to too tight radii at the anterior portion of the joint.   The countermeasure to this would be to continue the curve and groove anteriorly to increase the radii of curvature into the mounting zone. Further, other materials for the straps are now considered as a new manufacturing process will be used to create the cam surfaces. These materials would include Kevlar, the use of thinner bands, or possibly layered straps[18].

---

[18] Analogous to the use of leaf springs in the suspension of most heavy duty pickup trucks.
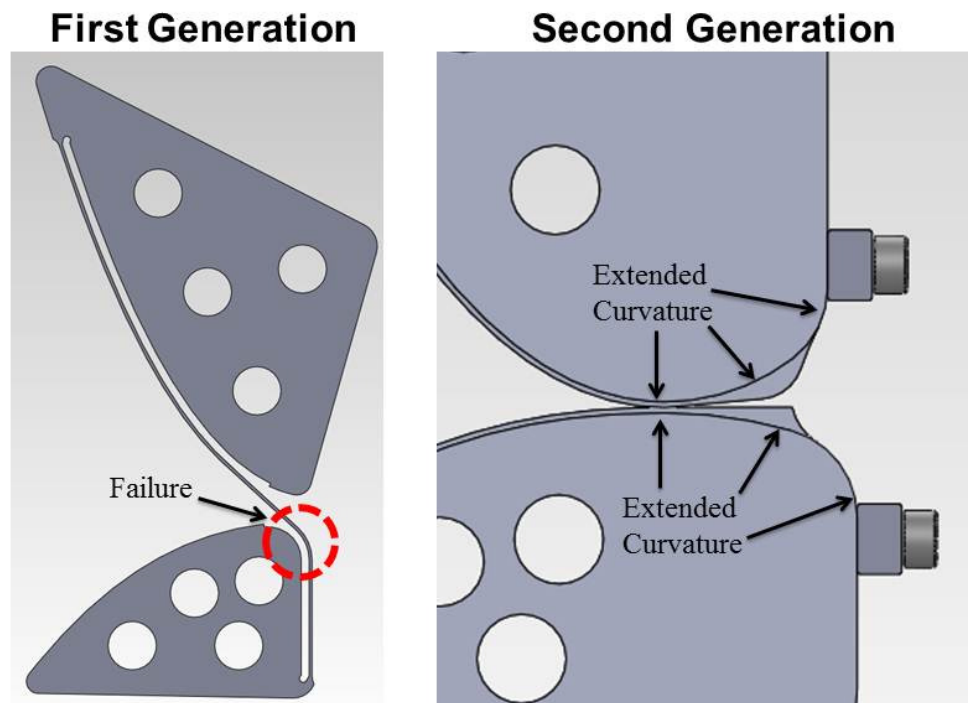
Figure 5.17: Images of the SolidWorks™ models of the first and second generation joints, highlighting the point of failure in the first and increased radius of curvature in the second.

The process of laser cutting straps directly into each component of the multi-layered first generation joint was simple, fast, and enabled a rapid proof of concept for the kinematics. The design and modeling of the straps to ensure proper spacing and placement of shims to close the gaps created by the manufacturing process, however, was very time-consuming (and necessary). During the evaluation of different strap materials, thinner titanium stock (12" x 12" and 0.1mm thick) was sourced for several thousand dollars, far outside the monetary constraints of the current work. Kevlar® string, however, was readily available from McMaster; Kevlar® has already been used in various biomedical applications ranging from hernia repair mesh, sutures, and even as a graft for ACL reconstruction [43]. The second generation rolling contact joint, using Kevlar® string for constraint, is seen in Figure 5.18. The femoral and tibial components

seen on the left side of the figure were manufactured each as one piece on a milling machine, with a groove for the Kevlar® string. To mount the joint in the testing machine, the tabbed femoral and tibial components from the image on the left side of Figure 5.14 were bolted to the solid tibial and femoral components using sex bolts.
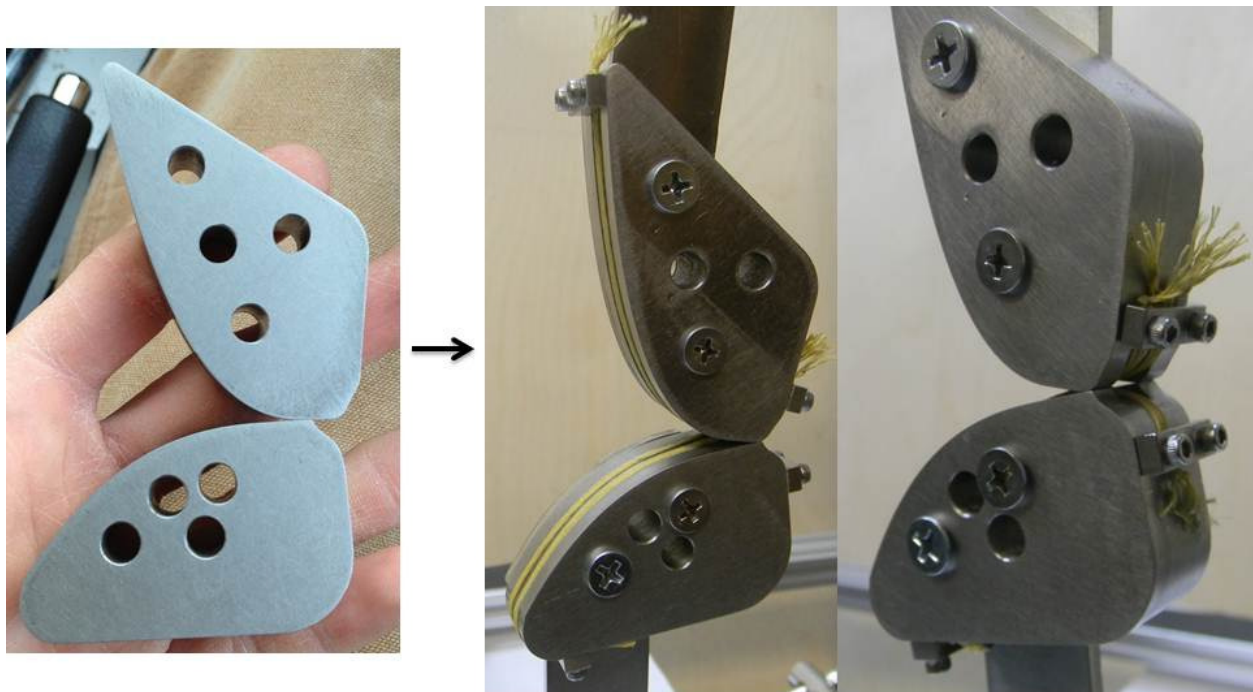
Figure 5.18: (a) Metal components manufactured by Hillside Engineering [44]; (b) posterior and anterior views of the joint assembled using Kevlar string.

Finally, the testing machine was updated, and the train-wheel mechanism was replaced by a lever arm, and larger pulleys were added so that the forces on the femoral side of the joint were more in line. In the previous version of the testing machine described in Chapter 4, Section 4.5, the forces illustrated in Figure 5.19**:** Machine for cyclically flexing and extending the prototype joint in Figure 5.18**:** (a) Metal components manufactured by Hillside Engineering [44]; (b) posterior and anterior views of the joint assembled using Kevlar string., showing the updated machine, were directed in significantly different directions than those shown in the figure. The larger

pulleys used in the updated version brought these two forces more in line, reducing parasitic forces on the joint.
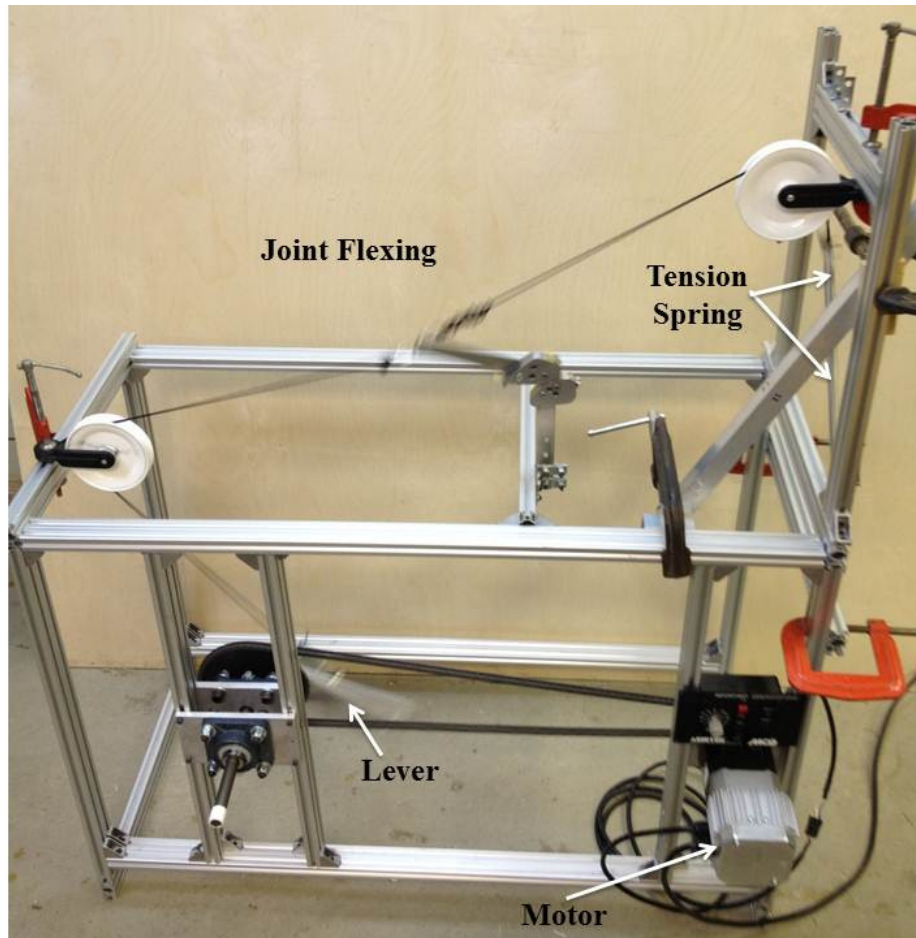
Figure 5.19: Machine for cyclically flexing and extending the prototype joint in Figure 5.18**:** (a) Metal components manufactured by Hillside Engineering [44]; (b) posterior and anterior views of the joint assembled using Kevlar string.

5.6.3   DURABILITY TESTING RESULTS

The second generation joint from Figure 5.18 was placed in the testing machine, and cycling was begun at a rate of 1 cycle per second, which can be visualized in Figure 5.19. The joint was cycled continuously for 119 hours and 30 minutes, at which point there was a 2 hour stoppage

due to a gear that slipped off of the motor shaft. The gear was replaced, re-tightened, and the machine re-started. The joint ran for another 21 hours and 26 minutes before failing catastrophically after almost 500,000 cycles. Images of the timer and the joint, with the cause of failure labeled, can be seen in Figure 5.20. The failed joint was cycled in the machine for no more than 2 hours, as no supervision was present when the joint failed.
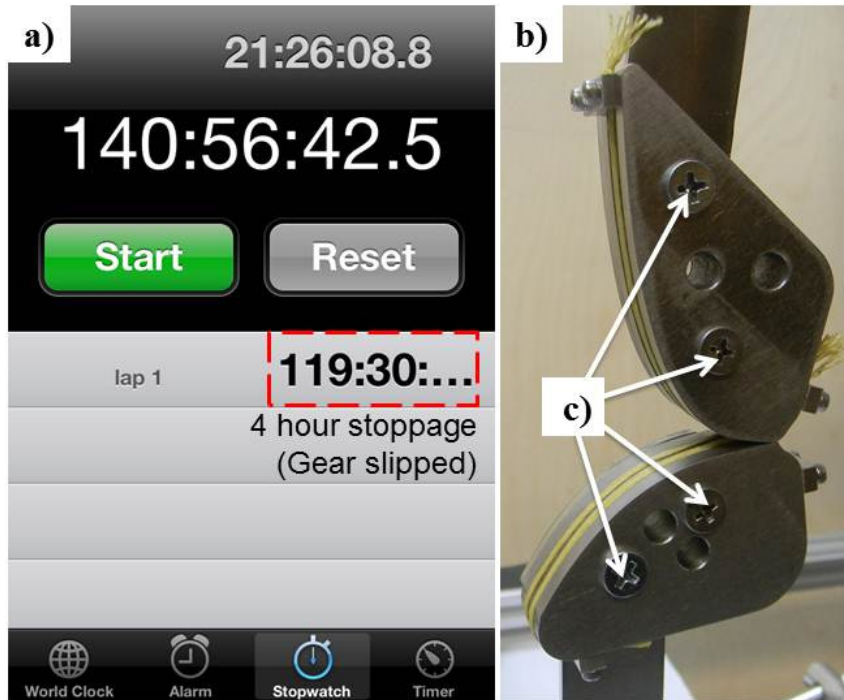
Figure 5.20: (a) timer showing 140 hours and 56 minutes of cycling, minus 4 hours of stoppage and failure amounts to 493,002 cycles; (b) the bolts that loosened, causing failure.

The mechanism for failure was loosening of the sex bolts, labeled as item c in Figure 5.20. After the sex bolts came loose on one component, the tabbed components kept cycling and the Kevlar string caused the femoral and tibial components to continuously slam into one another for an unknown amount of time, but still ran for less than 2 hours. The damage caused by this can be seen in Figure 5.21.

174
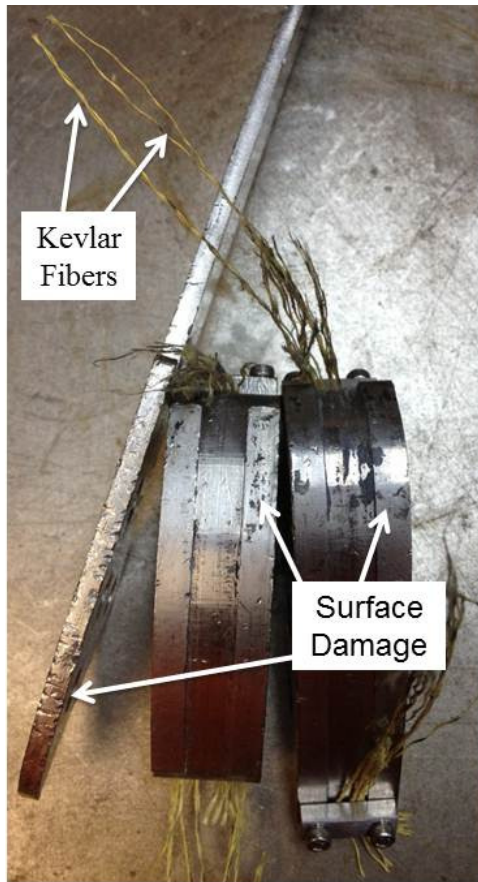
Figure 5.21: Damage to joint surfaces caused by loosening of the sex bolts.

As it stands, the results show that a rolling contact knee brace constructed using Kevlar® straps can withstand at least 500,000 cycles. At the time of writing this thesis, a second round of parts had been ordered from the machine shop. The next round of tests will include a stoppage of cycling for tightening of all bolts, with Loctite used initially on cleaned bolts and threads. This work sets the stage for development of a multi-axis testing machine for additional experiments after other degrees of freedom are added to the present joint.

5.7   REMARKS

There are several factors that must be considered in the design of knee joint prostheses: joint kinematics and kinetics, materials selection, as well as the bio-compatability of materials for implantable joints. Semi-constrained knees, trochlear-groove retaining implants, and uni-compartmental knees have enabled improvements in procedural outcomes and have maintained the morphological similarities between healthy joints and prostheses.

A method of synthesizing rolling surfaces from a four-bar linkage model of a healthy knee has been described. Using this method, a prototype rolling-contact joint with >120° of flexion/extension motion has been fabricated from 304SS and used in a knee brace. This joint demonstrates that a convex-convex configuration can be designed to accurately mimic the primary flexion/extension motion of a healthy knee. These results will enable further development of a 6-DOF joint utilizing flexural straps for constraints, and which has almost identical motions as a healthy knee joint.

A prototype joint has also been synthesized using knowledge of knee biomechanics and kinematic linkage synthesis, and a rolling-contact joint for a knee brace has been reduced to practice and successfully tested. Further analysis and experimentation on this prototype is essential, and will be focused on evaluating the lifetime of the straps and wear on the rolling surfaces through several hundred thousand, or even several million cycles.

One such material, Smith & Nephew's oxidized zirconium femoral components, could mitigate the risks of complications associated with metal ion allergies [16, 17]. Additionally, improvements to joint lubrication also must be investigated for optimizing the performance of this rolling contact joint. Work is currently under way to evaluate different types of coatings in an attempt to ensure that an Elasto-Hydrodynamic Lubrication (EHL) regime is always present in the rolling-contact joint, as boundary or mixed lubrication regimes have been shown to lead to increased wear over other types of lubrication [36].

Matrix decomposition of loads and deflections of constraints (ACL, PCL, MCL, and LCL stresses) and joint anatomy based on finite-element modeling could be used to generate two matrices describing the motions and stiffnesses of a knee in 6-DOF. These matrices can then be used to create a flexural joint with kinetics that better mimic those of a healthy knee joint, as flexion/extension is only the primary degree of freedom [45-47]. In this way, secondary degrees of freedom in the coronal plane (varus/valgus rotation) and around the axis of the femur (medial rotation associated with extension) can be added once this simple model is validated.

5.8   REFERENCES

[1] Marcacci, M., *et al.*, "Articulated External Fixator for Treatment of Complex Knee Dislocation". Clin Orthop Relat Res (2012) **470**:869-876.
[2] Bora, Jr., F. W., "Prosthetic Joint", United States Patent #4,267,608, 1981.
[3] Hillberry, B. M., Hall, Jr., A. S., "Rolling Contact Prosthetic Knee Joint", U.S. Patent #3,945,053, 1976.
[4] Freudenstein, F., Woo, L. S., "Kinematics of the Human Knee Joint". Bulletin of Mathematical Biophysics, Volume 31, pp. 215-232, 1969.
[5] Smidt, G. L., "Biomechanical Analysis of Knee Flexion and Extension". J Biomechanics 1973, Vol. 6, pp.79-92.
[6] Zavatsky, A. B., O'Connor, J. J., "A model of human knee ligaments in the sagittal plane Part 1: response to passive flexion". Proc Instn Mech Engrs 1992, Vol 206, pp. 125-134.
[7] Furguson, W., "Excision of the Knee-Joint – Recovery with a False Joint and a Useful Limb". The Medical Times and Gazzette, 1861, Vol. **1**, p. 601.
[8] Ranawat, C. S., Insall, J., Shine, J., "Duo-Condylar Knee Arthroplasty: Hospital for Special Surgery Design", Clinical Orthopaedics and Related Research, October 1976, Number 120, pp. 76-82.
[9] Gunston, F. H., "Polycentric Knee Arthroplasty: Prosthetic Simulation of Normal Knee Movement", J Bone and Joint Surgery, May 1971, **53B**:2, pp. 272-277.
[10] Insall, J. N., Ranawat, C. S., Aglietti, P., Shine, J., "A Comparison of Four Models of Total Knee Replacement Prostheses". J Bone Joint Surg Am. 1976, **58**:754-765.
[11] Kurtz, S., *et al.*, "Prevalent of Primary and Revision Total Hip and Knee Arthroplasty in the United States From 1990 Through 2002", J Bone Joint Surg Am., 2005, **87**:1487-1497.
[12] Kurtz, S., Ong, K., Lau, E., Mowat, F., Halpern, M., "Projections of Primary and Revision Hip and Knee Arthroplasty in the United States from 2005 to 2030", J Bone Joint Surg Am., 2007, **89**:780-785.
[13] Sharkey, P. F., Hozack, W. J., Rothman, R. H., Shastri, S., Jacoby, S. M., "Why Are Total Knee Arthroplasties Failing Today?". Clinical Orthopaedics and Related Research, 2002, **404**:7-13.

[14] Revel, P. A., Ed., "Joint Replacement Technology", (2008), Woodhead Publishing, Ltd., Cambridge, UK.

[15] Ritter, M. A., Meneghini, R. M., "Twenty-Year Survivorship of Cementless Anatomic Graduated Component Total Knee Arthroplasty", The Journal of Arthroplasty, **25**:4, June 2010, pp. 507-513.

[16] "Smith and Nephew Receives FDA 510k Clearance for a 30-year Knee", PR Newswire, April 22, 2010. Online URL: http://www.prnewswire.com/news-releases/smith--nephew-receives-fda-510k-clearance-for-a-30-year-knee-91815029.html.

[17] Smith & Nephew, London, UK. Online URL: http://global.smith-nephew.com.

[18] Bozic, K. J., *et al.*, "The Epidemiology of Revision Total Knee Arthroplasty in the United States", Clinical Orthopaedics and Related Research, 2010, **468**:45-51.

[19] Mahomed, N. N., *et al.*, "Epidemiology of Total Knee Replacement in the United States Medicare Population", J Bone Joint Surg Am., 2005, **87**:1222-1228.

[20] Beck, M., "Pushing Limits of New Knees", The Wall Street Journal, April 19, 2011. Available Online: http://online.wsj.com/article/SB10001424052748704004004576270844211718806.html.

[21] Jeanneau, A., Herder, J., Laliberte, T., Gosselin, C., "A compliant Rolling Contact Joint and its Application in a 3-DOF Planar Parallel Mechanism with Kinematic Analysis", Proc. ASME Design Eng. Tech. Conf., Sept 28 - Oct 2, 2004, Salt Lake City, Utah, DETC2004-57264.

[22] Fijan, R. S., "A 3-Dimensional Mathematical Model of the Human Knee Joint", PhD Thesis, 1990, Massachusetts Institute of Technology.

[23] Sultan, P. G., Most, E., Schule, S., Li, G., Rubash, H. E., "Optimizing Flexion After Total Knee Arthroplasty", Clinical Orthopaedics and Related Research, 2003, **416**:167-173.

[24] Most, E., *et al.*, "The Kinematics of Fixed- and Mobile-Bearing Total Knee Arthroplasty", Clinical Orthopaedics and Related Research, 2003, **416**:197-207.

[25] Most, E., "Development of a 6-DOF Robotic Test System for Studying the Biomechanics of Total Knee Replacement", SM Thesis, 2000, Massachusetts Institute of Technology.

[26] Suggs, J. F., "Investigation of In-Vivo Total Knee Arthroplasty Biomechanics Using a Dual Fluoroscopic Imaging System", PhD Thesis, 2007, Massachusetts Institute of Technology.

[27] McKee, J., "Finding Better Knee Implant Materials". American Academy of Orthopaedic Surgeons Website, Retrieved on 12/26/2011. URL: http://www.aaos.org/news/aaosnow/aug08/clinical3.asp.

[28] Slocum, FUNdaMENTALS of Design, Topic 10 – Bearings: Flexural Rolling, pp. 30-31. Available online at: http://pergatory.mit.edu/resources/FUNdaMENTALS.html.

[29] Slocum, A. H., Precision Machine Design. Prentice-Hall, New York, 1992.

[30] Wang, A., Sun, D. C., Stark, C., Dumbleton, J. H., "Wear Mechanisms of UHMWPE in Total Joint Replacements", Wear, 1995, Volume 181-183, pp. 241-249.

[31] Shiers, L. G. P., "Arthroplasty of the Knee: Preliminary Report of a New Method", J of Bone and Joint Surg UK, November 1954, **36B**:4, pp. 553-560.

[32] Shiers, L. G. P., "Arthroplasty of the Knee: Interim Report of a New Method", J of Bone and Joint Surg UK, February 1960, **42B**:1, pp. 31-39.

[33] Thornton, A. W., Predecki, P., "Design Considerations in a Rolamite Knee Joint Prosthesis". J Biomed Mater Res Symposium, **4**:419-433, 1973.

[34] Brinckmann, P., Frobin, W., Leivseth, Musculoskeletal Biomechanics, pp. 85-90, Thieme, New York, NY, 2002.

[35] Montierth, J. R., Todd, R. H., Howell, L. L., "Analysis of Elliptical Rolling Contact Joints in Compression". ASME Journal of Mechanical Design, March 2011, **133**:3, pp. 1-10.

[36] Kennedy, F. E., Van Citters, D. W., Collier, J. P., "Tribological Characteristics of Polyethylene Bearings of Knee Prostheses", Int J of Surface Science and Engineering, 2010, **4**:2, pp. 166-174.

[37] Personal Communication with Sasha Zill, PhD, 10/20/2011. Professor, Section of Anatomy, Joan C. Edwards School of Medicine, Marshall University.

[38] Trease, B. P., Moon, Y.-M., and Kota, S., 2005. "Design of large-displacement compliant joints," Journal of Mechanical Design, Transactions of the ASME, 127(4), pp. 788 – 798.

[39] Cannon, J. R., Lusk, C. P., and Howell, L. L. "Compliant rolling-contact element mechanisms," Proceedings of the ASME International Design Engineering Technical Conferences and Computers and Information in Engineering Conference, DETC2005-84073.

[40] Halverson, P.A., Howell, L.L., and Magleby, S.P., 2010, "Tension-Based Multi-stable Compliant Rolling-Contact Elements," Mechanism & Machine Theory 45(2), pp. 147-156.

[41] Dolan's Welding & Steel Fabricating, 118 Venture Street, Johnstown, PA 15909. Online URL: http://www.dolanswelding.com/.

[42] Riveiro, A., Quintero, F., *et al.*, "Laser Cutting Aerospace Aluminum", Industrial Laser Solutions for Manufacturing, March 1, 2008. Online URL: http://www.industrial-lasers.com/articles/print/volume-23/issue-3/features/application-report/laser-cutting-aerospace-aluminum.html.

[43] Andersen, H. N., Amis, A. A., "Review on tension in the natural and reconstructed anterior cruciate ligament". Knee Surg, Sport Traumatol, Arthroscopy (1994), **2**: pp. 192-202.

[44] Hillside Engineering, 10A Rainbow Terrace, Danvers, MA 01923. Online URL: http://www.hillsideeng.com/.

[45] Miller, M. C., Berger, R. A., Petrella, A. J., Karmas, A., Rubash, H. E., "Optimizing Femoral Component Rotation in Total Knee Arthroplasty", Clinical Orthopaedics and Related Research, 2001, **392**:38-45.

[46] Williams, A., Logan, M., "Understanding Tibio-Femoral Motion". The Knee, **11**:2, pp. 81-88, 2004.

[47] Williams, A., Phillips, C., "Functional In Vivo Kinematic Analysis of the Normal Knee". In: Bellemans, J., Ries, M. D., Victor, J., eds. "Total Knee Arthroplasty: A Guide to Get Better Performance". New York: Springer Medizin Verlag, 2005: 32-37.

*This page intentionally
left blank*

CHAPTER

6

NANOENGINEERED SURFACE COATINGS

This chapter focuses on the application of porous coatings at each interface, with the goal of improving implant integration and lubrication; while the focus of this thesis is developing a new rolling-contact knee brace, this work has application to existing technology as well. The primary contribution of this chapter is characterization of improvements to lubricity through application of porous coatings. Results of lubrication studies and characterization of porous coatings from a lubricity standpoint was more in-depth, and these are the primary contribution of this chapter. Investigation of bone growth on porous coatings presented here is very preliminary and restricted to observations of osteoblast proliferation.

6.1   INTRODUCTION

There are two interfaces in all prostheses that are critical to the implant's long-term success: The implant-implant interface and the implant-bone interface. An implant's durability and useful lifetime can be increased by application of porous coatings at two interfaces: to promote

ingrowth of bone, and improve lubrication between implant components in contact. On one hand, characteristics of the implant-bone interfaces determine the degree of bone growth into the coating, influencing the subsequent integrity of a relatively rigid prosthesis-bone joint. On the other hand, lubrication between two opposing surfaces in an implant (the implant-implant interface) directly affects wear in the prosthesis and in turn determines the lifetime of the joint. Lubrication is especially important, based on empirical observation of current joints, as wear of joint components can have a negative effect on the implant/bone interface – i.e. peripsothetic osteolysis.

The importance of lubrication and integration in an implant is illustrated by Figure 6.1a, which shows a severely worn polymer insert from a prosthetic knee joint, and a radiograph highlighting the osteolysis that can result, in Figure 6.1b. The images are representative and are not from the same patient. They highlight the potential morbidity associated with fatigue and fracture of the polymer bearing, and subsequent release of micron and sub-micron scale particles from both the polymer and metallic components. This pathologic process leads to up-regulation of osteoclast activity and greater rates of bone degradation (periprosthetic osteolysis), otherwise known as aseptic loosening[19]. Aseptic loosening is briefly discussed in Chapter 7, Section 7.2.3.

---

[19]It is called aseptic because another common cause of bone resorption is infection or "sepsis"; in the case of **Figure 6.1**b there is no evidence of infection, hence "aseptic" loosening.
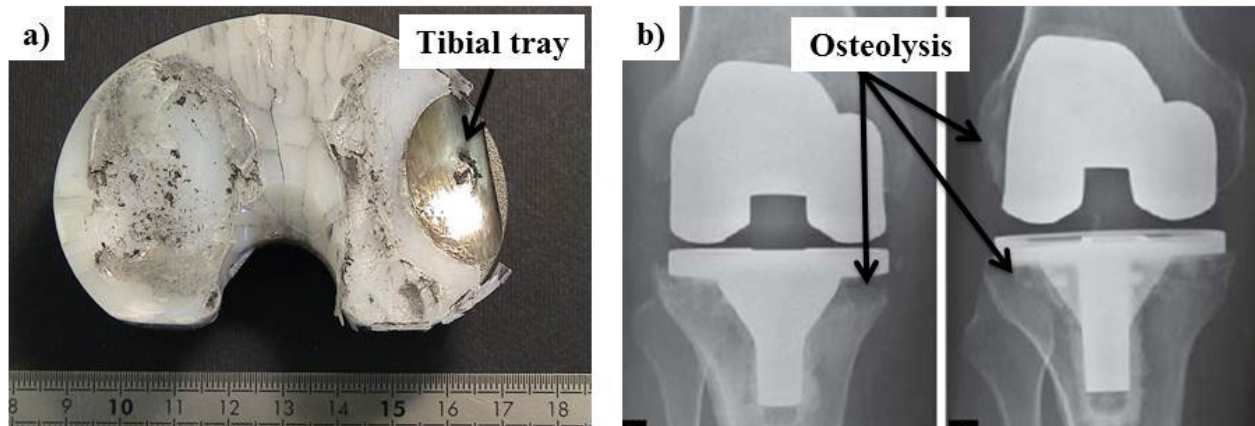
Figure 6.1: (a) a severely damaged polymer insert that has been worn through down to the underlying tibial tray support [1]; (b) radiograph showing periprosthetic osteolysis most likely induced by wear of joint materials and release of particles [2].

A greater degree of integration can slow the progression of bone loss by taking advantage of Wolff's law, and improvements to lubrication between joint surfaces can further slow their rate of wear. Achieving both of these goals can lead to longer-lasting, more durable joints and, ultimately, improved patient outcomes.

6.2   IMPLANT INTEGRATION

Increased bone growth into the implant structure leads to a stronger static joint between the implant and adjacent bone.   Also, some orthopaedic metals like Titanium, are naturally osteogenic for reasons that are currently unknown [3, 4], and as such are utilized to create a majority of existing coatings. Several different types of coatings have been previously pursued for use at the bone-implant interface to try to improve contact between the implant and adjacent bone, the first of which debuted as early as the 1970s [5].   These include plasma spraying, grit

blasting, and treatment with chemicals like acids or alkaline solutions; examples of coatings that have been applied to hip prostheses can be seen in Figure 6.2.
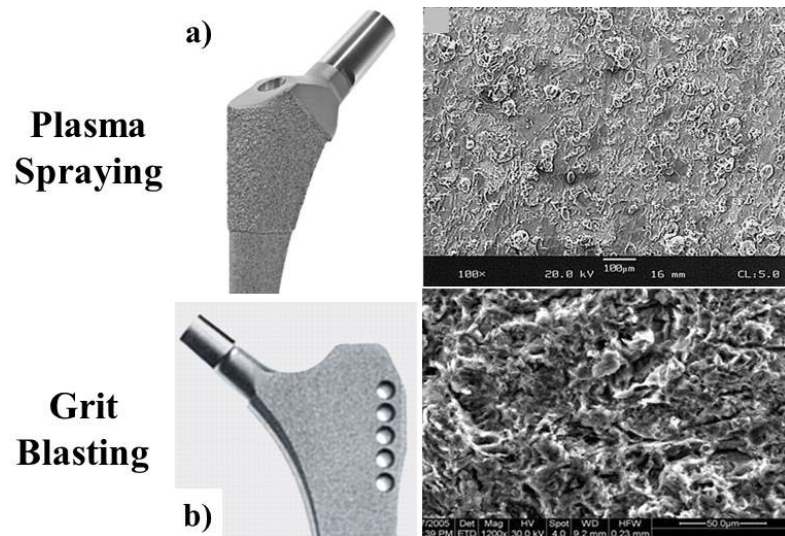
Figure 6.2: Femoral stems treated with (a) plasma spraying [6] and (b) grit blasting [7]. SEM views of the resulting surface structure are also shown [8].

Biological tissue adjacent to the implant is mostly trabecular bone, which has a porosity, otherwise known as relative density, of around 25% [9], and is usually the structure that resists a majority of the load transmitted by the joint components. The hierarchical structure of bone was described in Chapter 2; trabecular bone is the principal type present at the ends of the long bones, which also contain marrow, blood vessels, and other softer tissues that help maintain homeostasis. Wolff's Law applies to this situation in that little to no force is transmitted across areas of the joint where there is little contact or ingrowth of bone, and as such those areas of bone will be resorbed over time. This is most often seen in patients receiving hip implants where stress shielding is most prevalent; areas of bone adjacent to the femoral stem which are not adequately loaded will resorb. In one case of a patient with a prosthetic hip, the bulk of tissue making up the grater trochanter has been reabsorbed and an X-ray of the subject can be seen in

Figure 6.3. Thus, bone loss can be induced by both normal wear of the implant components as well as inadequate distribution of loads from the implant to the trabecular bone support.
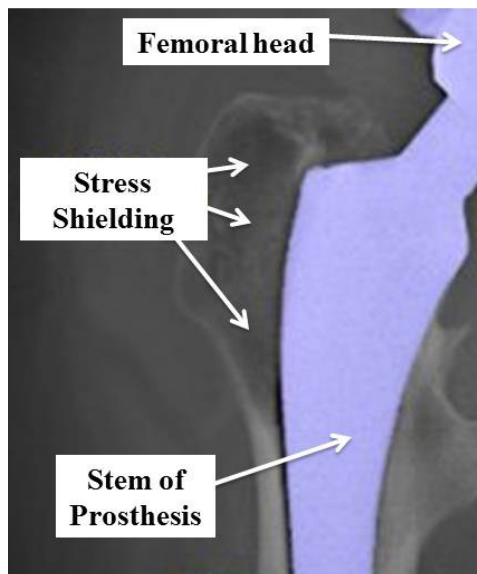
Figure 6.3: Evidence of stress shielding in a hip prosthesis.[20]

There is a dichotomy of sorts present, in that the metallic stem has to be stiff enough to support a patient's body weight, yet compliant enough to adequately distribute the load to adjacent bony tissue to prevent reabsorption. Bone cement, when used in an implant, attempts to mitigate the effects of stress shielding by helping to provide an improved interface between the implant and the surrounding bone. Increasing the area of contact by using the cement helps to distribute load to trabeculae that otherwise would not be loaded by the solid metal stem. When a porous coating is used, sometimes bone cement is not necessary as the metallic foam adequately distribute the load among many contacts, which can also be called "elastic averaging" [10]. Figure 6.4 shows examples of cemented and non-cemented hip prostheses. The asterisk in the left image of the

---

[20] Image source: http://www.radiologyassistant.nl/en/p431c8258e7ac3/hip-total-hip-arthroplasty.html.

figure highlights the radio-lucent polymer bearing, while in the right side image, the radio-lucent gap is blocked because the implant is coated in titanium, which is radio-opaque.
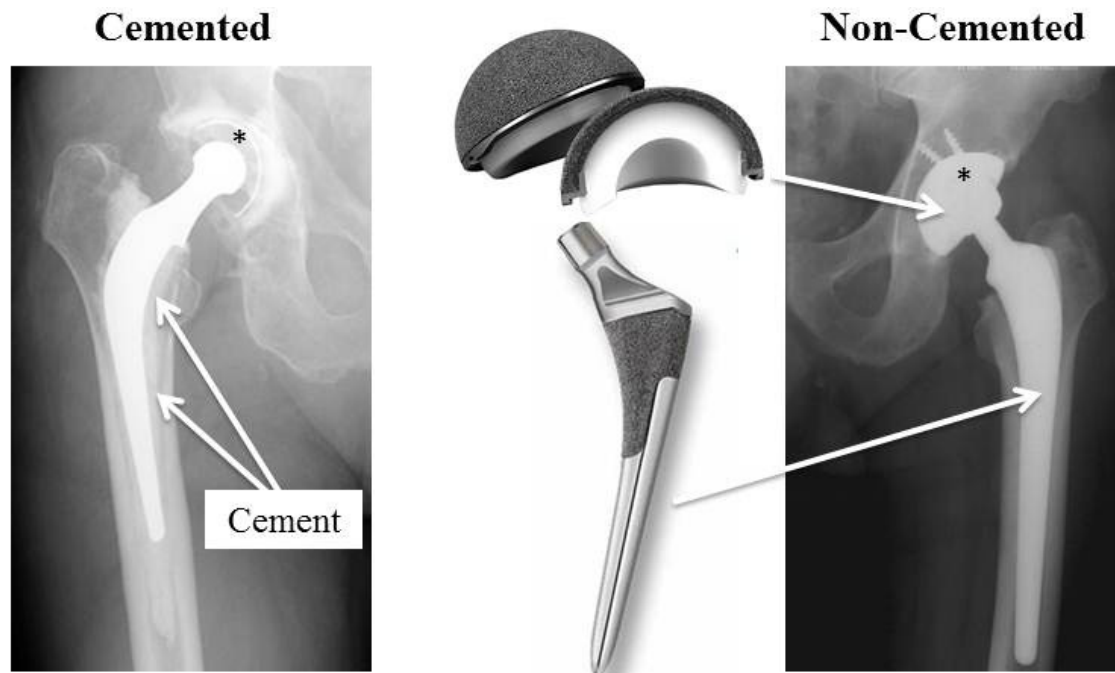
Figure 6.4: Radiographs showing examples of cemented[21] (left) and un-cemented (right) hip prostheses [11]. The asterisk denotes the location of a radio-lucent gap created by the polymer bearing. The middle image shows a hip implant available from Zimmer [12, 13].

As seen in the previous figure, stiff implants result in more focused load transmission, leading to more bone resorption. Recent improvements to porous coatings, for example Trabecular Metal available from Zimmer, have resulted in substantial improvements to bone ingrowth [14] by increasing the contact area between the bone and implant. The porous titanium structures of Trabecular Metal and native trabecular bone have similar porosity, on the order of 250 microns, as illustrated in Figure 6.5. Trabecular metal, however, is fabricated in a similar manner to other

---

[21] Image source: http://www.gentili.net/thr/totalhip.htm

186

porous coatings in that it is applied to the surface of the implant, specifically by a method called vapor deposition [15, 16]. Other processes like sintering have been used to coat implants with beads or particulate of other geometry.
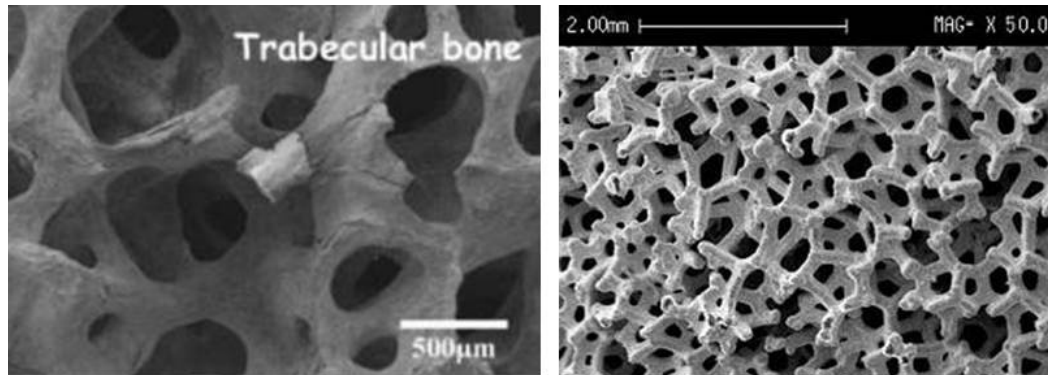
Figure 6.5: (a) SEM of trabecular bone[22]; (b) trabecular metal available from Zimmer [15].

Porous coatings applied to the surfaces of orthopaedic implants are essentially metallic foams that serve to improve load distribution, and as such can be modeled as porous media [9]. From a deterministic standpoint, the goal of the coating is to increase the number of contacts between the implant and the surrounding bone. There must then be deformation of those points which first come into contact to allow others to do the same. Hence, an "elastically averaged" state is ideal, where there are a huge number of compliant contacts, rather than a few focal contacts with higher stresses. An elastically averaged state can be reached if a porous coating is contoured such that the local stiffness of the foam matches that of the closest trabecular structures. Table 6.1 gives examples of methods used to fabricate different types of foams, some of which are often used to create current orthopaedic porous coatings ("orthopaedic foams") [17]. As stated earlier, plasma spraying of titanium or hydroxyapatite onto the smooth surface of an implant is often used to create an orthopaedic foam which encourages bone ingrowth [18]. A plasma-sprayed

---

[22] Image source: http://cbtrr.mst.edu/ (accessed 1/1/2013).

tibial tray, used to anchor the polymer bearing insert of a knee prosthesis, can be seen in Figure 6.6.

Table 6.1: Summary of common methods of manufacturing porous materials [17].

Closed-cell foam		Open-cell foam		
Method	**Pore Distribution**	**Method**	**Homogeneity**	**Grading**
Plasma spraying	Graded	Vapor Deposition	Homogenous	No
Gas Injection	Random	Rapid Prototyping	Homogenous	Yes
Foam Decomposition	Random	Plasma spraying	Non-homogenous	No
		Sintered metal fibers/powders	Non-homogenous	No

Figure 6.6: Biomet Regenerex® tibial tray, with plasma-sprayed titanium foam [19].

While this and other porous coatings, like trabecular metal, are showing significant promise, they are subject to several limitations. Coatings are usually applied to the surface of the implant, creating a seam interface between the coating and the smooth surface of the implant, as illustrated in Figure 6.7**:** Histological section showing the seam present at the interface between the cup of a hip prosthesis and adjacent bone, which has grown into the porous coating [20].. A

sintered bead coating has been applied to the bone side of the acetabular component of a hip prosthesis, with subsequent infiltration of osteoblasts and ingrowth of bone (stained basophilic, or purple). Another co-morbid factor associated with the use of all coatings is the risk of releasing metallic particles into the body. Delamination of the foam coating from the substrate occurs when the resulting joint formed by growth of bone into the coating is stronger than the bond between the coating and the smooth surface of the implant. A stress placed on the implant that exceeds the strength of the bond at the seam labeled in Figure 6.7 increases the risk of the implant shearing off of the coating, leading to catastrophic failure.
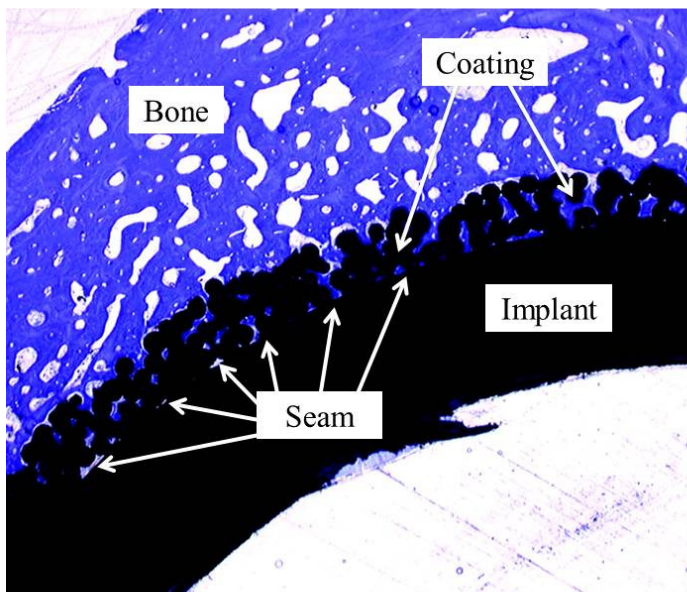
Figure 6.7: Histological section showing the seam present at the interface between the cup of a hip prosthesis and adjacent bone, which has grown into the porous coating [20].

This significant risk then begs the question, "can a porous coating be created such that it is intrinsic to the bulk metallic structure, with a stiffness that is equivalent to or near that of adjacent trabecular bone?" Such a coating, manufactured directly into the surface of the implant as opposed to adhered to the surface, would not have a distinct seam, or shear plane, meaning the

foam would be significantly less likely to fail by shear. Because of its inherent ability to be osteogenic[23], titanium-based porous coatings appear to hold the most promise [3-5].

Different methods of fabricating coatings can now be evaluated to ensure that the resulting material is both bio-active and supportive of progenitor cell differentiation and osteoblast proliferation. Two different processes are considered here: Etching and anodizing. The resulting orthopaedic foams created by etching or anodizing will then be assessed for their ability to support osteoblast growth, as well as characterized to determine their strength and stiffness and porous materials [9]. Etched and anodized titanium coatings are investigated in Grade 5 Titanium (Ti6Al4V), which is often used in orthopaedic implants, as their methods of fabrication are documented, and often involve commercially pure Titanium or Hydroxyapatite (HA) [21-25].

6.2.1 SAMPLE PREPARATION

Twelve 25 mm square coupons were produced from a 6mm thick piece of Grade 5 (Ti6Al4V) titanium bar [26]. They were then polished by Mirror Finish Polishing [27]. Two coupons were selected and then each was individually cleaned in an ultrasonic bath in deionized water, wiped off with acetone, and placed in an individual petri dish. Next, an etching process similar to that described by Tanaka [22] was used to fabricate a nano-scale coating on the surface of one of the coupons. Figure 6.8 shows an image of a virgin, polished coupon and an etched coupon soaked in 29M NaOH at 80°C for 29 hours. Scanning Electron Microscope views of the coatings can be seen in Figure 6.11, Figure 6.19, and Figure 6.20. Anodized coatings have not yet been

---

[23] Osteogenic generally refers to the ability of a substance to stimulate the growth of osteoblasts.

incorporated into this aspect of the work, but will continue when additional resources and funding become available.

Figure 6.8: Images of polished (left) and etched (right) Ti6Al4V coupons.

The etching process creates a surface topology that is intrinsic to the bulk substrate, and therefore does not have the shear plane seen in Figure 6.7. It is intended to be able to load individual bone spicules, which could lead to localized stimulation of osteoblasts and better distribution of joint forces across the implant/bone interface. Here, a smooth surface that contacts the trabecular bone at a few locations is modified so that a compliant foam coating allows for a significantly larger number of contacts; in essence, the implant would now have an elastically-averaged contact with the surrounding bone.

6.2.2   ELASTICALLY-AVERAGED COATINGS

As described by [10], "Elastic averaging enables improved accuracy derived from the averaging of errors over a large number of contacting surfaces". Here, the pursuit of an elastically averaged coating is driven by the potential for a large number of contacts to improve load distribution between an implant and the surrounding bone. Significant prior work has focused on applying a

porous structure to a solid substrate [28-30], yet a majority of these and similar patents are still subject to the limitations of the seam the porous coating and substrate.

Exact Constraint describes the use of a finite number of contacts to position a body in space, for example a kinematic coupling[24] seen in Figure 6.9. This is similar to a smooth implant in contact with trabecular bone, while there are more than the six contacts of the kinematic coupling, there is not adequate distribution of load and stress shielding occurs, as in Figure 6.3.
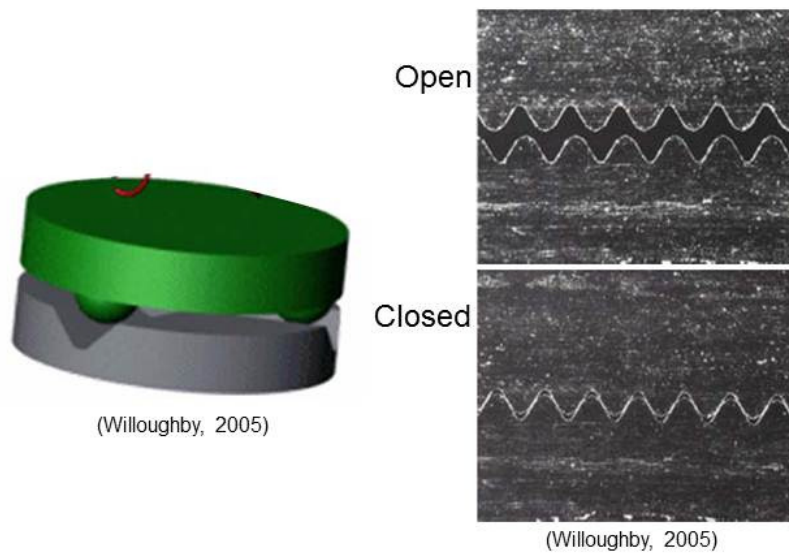
Figure 6.9: A kinematic coupling (left); Example of an elastically averaged joint [10].

An orthopaedic foam, fabricated directly into the surface of the implant to mitigate the risks of shear failure, and that has been contoured so that the stiffness of the foam varies the match the local stiffness of adjacent trabecular bone, should be able to develop essentially an "infinite" number of contacts. Thus by Wolff's Law stress shielding would be mitigated and ingrowth of bone could take place. The foam requires a variable, contoured stiffness because the size and

---

[24] For more information on kinematic couplings, the reader should visit www.kinematiccouplings.org.

shape of trabeculae in bone vary significantly, in addition to their orientation, as depicted in Chapter 2, Figure 2.6, page 49. The relative density varies with changes in the size and shape of the bone spicules, and thus variations in the modulus of the foam [9]. A simple model can be constructed to describe the elastic averaged coating hypothesis, as seen in Figure 6.10.
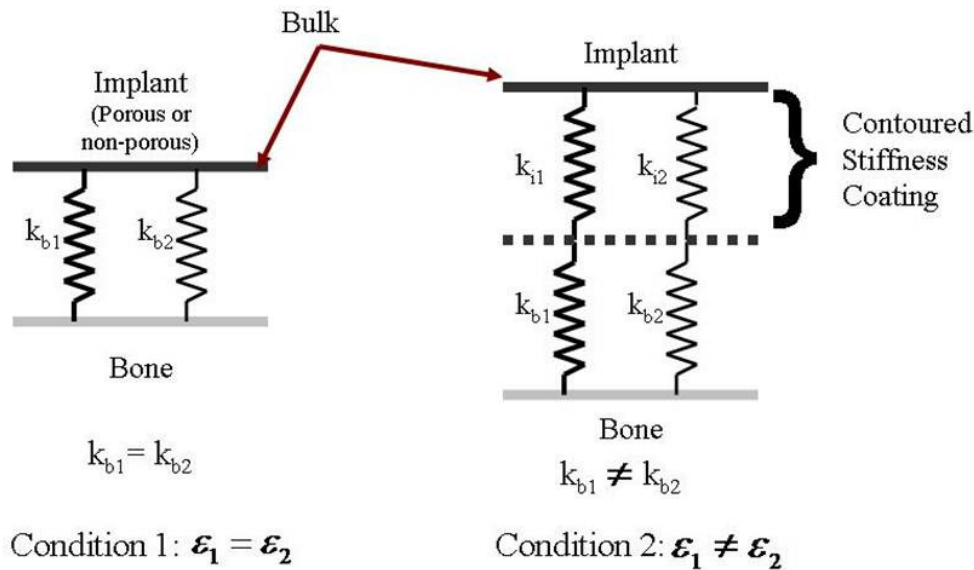
Figure 6.10: Schematic of an implant with uniform stiffness (condition 1), and an implant with a porous coating that has been contoured to match the stiffness of nearby bone.

If the modulus of an implant can be made to match that of the bone, it could more effectively stimulate bone growth and regeneration, and prevent further degeneration.

6.2.3   MECHANICS OF POROUS COATINGS

Current methods of fabricating metal foams lead to a risk of delamination failure between the foam and implant [31]. Porous coatings fabricated directly onto the surface of the implant offer a reliable method of improving implant integration; intrinsic porous coatings could lead to stronger

structural joints. A model for the interface between the coating and the bone is devised so that improved integration can be achieved with any coating.

The elastic yield stress σ^*_{el}, and young's modulus E^* of an open-cell foam are given by Equations 1 and 2, respectively. Equation 6.1 relates stress to the relative density of the foam and the young's modulus of the solid from which the foam is manufactured; Equation 6.2 shows that the modulus of the foam is the product of the foam relative density and modulus of the solid [9].

$$\sigma^*_{el} = 0.05 E_s \left(\frac{\rho^*}{\rho_s} \right)^2 \quad \textbf{Eq. 6.1}$$

$$E^* = E_s \left(\frac{\rho^*}{\rho_s} \right)^2 \quad \textbf{Eq. 6.2}$$

Under normal loading conditions, it is assumed that trabeculae will remain elastic. In the event that an adverse loading condition is experience (e.g. a fall), it would be beneficial to prevent the titanium foam from yielding, and thus a safety factor of 1.5 is used to determine the desired elastic yield strength of the titanium foam. Table 6.2 provides the mechanical properties of trabecular bone, with an assumed relative density of 25% [9]. The predicted elastic modulus can be used to optimize the material properties of the implant before use.

Table 6.2: Material properties of 25% dense trabecular bone.		
Parameter	**Value**	**Symbol**
Trabeculae solid modulus	18 GPa	E_s
Relative density	0.25	(ρ^*/ρ_s)
Elastic yield stress	56 MPa	σ^*_{el}
Elastic modulus	1.13 GPa	E^*

The first step in analyzing the material behavior of a porous foam coating is to determine whether the foam is *open-celled* or *closed-celled*. From observing Figure 6.11, the size, shape, and number of edges and vertices is very irregular, and the foam is open-celled. It is assumed that most cells in the foam have faces with five edges [9]; a detailed statistical study of the number of edges possessed by each face would be required to accurately determine the average number of edges per face, n_{bar} [9].
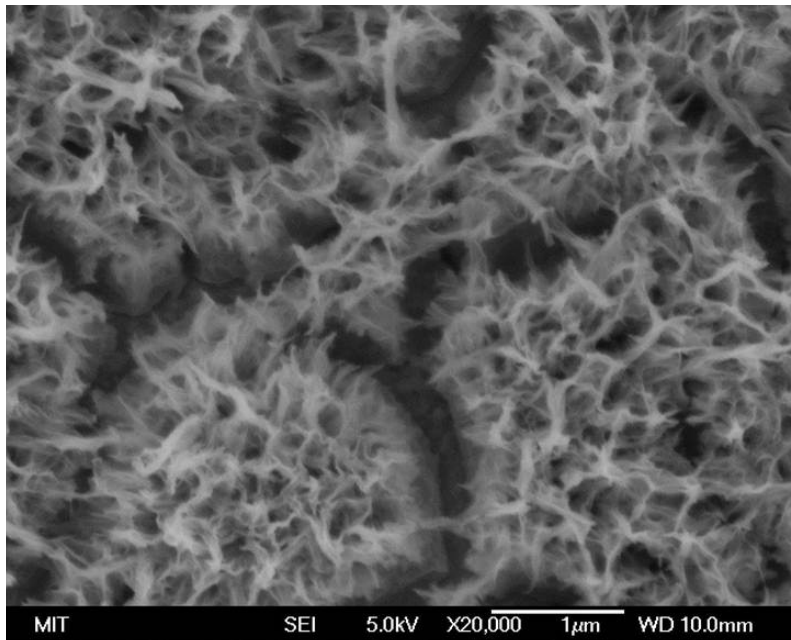
Figure 6.11: SEM image of the etched titanium coupon seen in Figure 6.8.**Figure 6.8:** Images of polished (left) and etched (right) Ti6Al4V coupons.

Edge connectivity Z_e is assumed to be 4, and Z_f assumed to be 3, as this is a foam [9]; cell shape is approximated as a tetrakaidecahedron, with f=14, and thus n_{bar}=5.4. The ratio of average strut length to thickness, from Figure 3, is approximated as 3:2, giving a t/l ratio of 0.66. Equation 6.3 gives the relationship between relative density and the aspect ratio of the struts, and Table 6.3 summarizes the properties of the NaOH-etched Titanium foam.

$$\frac{\rho^*}{\rho_s} = \left(\frac{t}{l}\right)^2 \quad \textbf{Eq. 6.3}$$

Table 6.3: Properties of the etched titanium foam.

Parameter	Value	Symbol
Edge connectivity	4	Z_e
Face connectivity	3	Z_f
Avg. sides per face	5.4	$\bar{n}$
Ti6Al4V Modulus	110 GPa	E_s
Strut aspect ratio	3:2	t/l
Relative density	0.44	(ρ^*/ρ_s)
Foam elastic modulus	21.3 GPa	E^*

These feature sizes are of sub-micron order, however the porous nature of the coating, combined with the natural osteogenicity of titanium, would allow for penetration of osteoblast cannaliculae as well as other materials essential for bone mineralization. The required relative density of the implant porous coating can now be calculated using Equations 6.2 and 6.3, and equating the elastic moduli of the trabecular bone and titanium foam. Equation 6.4 gives the required strut aspect ratio as a function of the elastic modulus of solid bone E_b, titanium E_t, and the relative density of trabecular bone (ρ^*/ρ_s).

$$E_b^* = E_b \left(\frac{\rho^*}{\rho_s}\right)^2 = E_b \left(\frac{t}{l}\right)^4$$

$$E_b^* = E_t^*$$

$$E_b \left(\frac{\rho^*}{\rho_s}\right)_b^2 = E_t \left(\frac{t}{l}\right)_t^4$$

$$\left(\frac{t}{l}\right)_t = \sqrt[4]{\frac{E_b}{E_t}\left(\frac{\rho^*}{\rho_s}\right)_b^2} \quad \textbf{Eq. 6.4}$$

The titanium foams have a microstructure which is composed of features similar in shape to regular hexagonal prisms, and as such it is assumed that the size of the pores is on the order of strut length. Given a titanium modulus of 110 GPa, and a solid bone modulus of 18 GPa, the struts in the titanium foam should have a length of between 5 and 10 microns, and a thickness of between 1.6 and 3.2 microns. This will lead to osteogenic titanium foam which would support adequate integration of the implant. Table 6.4 summarizes the calculation of optimal strut aspect ratio for the titanium foam. Once the optimal foam modulus is found, it can be combined with knowledge of the manufacturing process to enable fabrication of a contoured-foam implant. Use of a non-destructive testing can be used to verify the resulting foam material properties.

Table 6.4: Material properties of Ti6Al4V foam coating.		
Parameter	**Value**	**Symbol**
Bone Elastic Modulus	18 GPa	E_b
Bone relative density	0.25	(ρ^*/ρ_s)
Titanium solid modulus	110 GPa	E_t
Ti strut aspect ratio	0.32	n/a
Required pore size	5-10 μm	d
Strut thickness range	1.6-3.2 μm	T

Relative density of bone varies (k_1). Stiffness of implant vs. stiffness of cortical bone ($k_{b1}=k_{i1}$). Use differences in stiffness to drive fabrication. Elastic averaging: contour implant to match underlying bone. Significant over-constraint with compliant structures [10]. Increase number of

implant/trabeculae contacts. Potential to decrease stress-shielding. Can lead to improved osseo-integration

6.2.4 MICRO-INDENTATION TESTS

Micro-indentation tests[25] utilized a Vickers tip, with testing parameters listed in Table 6.5[32]. Force and displacement were measured and multiple trials were averaged to obtain an estimate for the stiffness of the nano-scale coating.

Table 6.5: Nano-indentation testing parameters.	
Paramater	**Value/Units**
Contact load	1 N
F_{max}	2 N
Pause	10 s
$V_{approach}$	60 μm/min
Loading	30 s
Unloading	30 s
Indenter	Vickers V-H-66

The stiffness of cancellous bone is predicted to be between 2-7 GPa, based on variations in spicule width and length. The predicted stiffness of the porous titanium coating is 21 GPa, as derived in Table 6.3. The modulus of the nano-scale foam was measured to be 912 GPa, a result that is almost an order of magnitude higher than the modulus of the solid. It is postulated that this resulted from surface energy effects due to the small length scale of the foam, and further work is

---

[25] Performed in Prof. Franz Ulm's lab in the Department of Civil and Environmental Engineering at MIT [32].

required to calibrate the indenter based on the material properties of the solid from which the foam is made and to achieve a more accurate measurement of foam modulus [33]. Figure 6.12 shows a schematic of the test set-up and a plot of force vs. displacement for a single test.
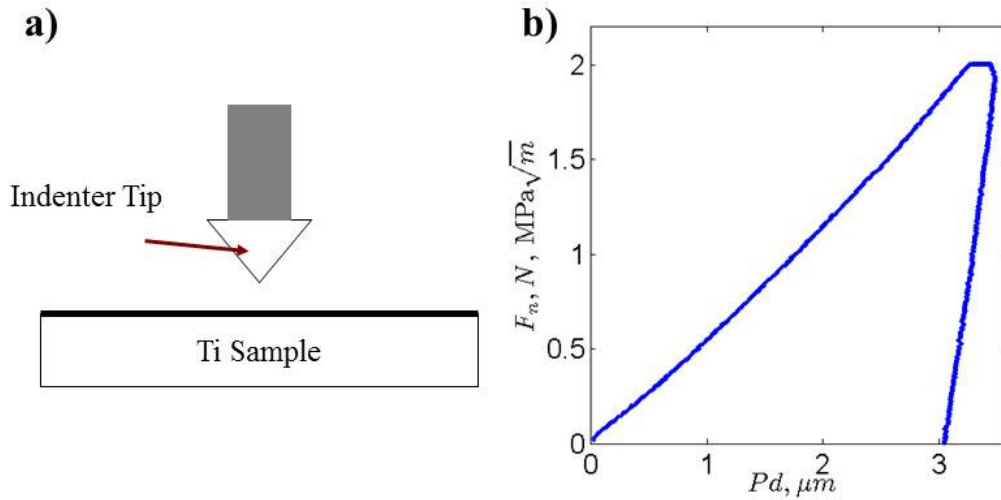
Figure 6.12: (a) schematic of the micro-indentation test set-up; (b) Plot of force (F_n) vs. penetration depth (Pd) for a single test.

6.2.5   CELL CULTURE

The etched and non-etched coupons from Figure 6.8 were plated with mouse mouse calvaria-derived preosteoblastic cells (MC3T3-E1; ATCC CRL-2593) and cultured in alpha minimum essential medium (Invitrogen Corp., Grand Island, NY), supplemented with 10% fetal bovine serum (Invitrogen) and 1% antibiotics (comprising penicillin and streptomycin; Invitrogen). The medium was changed every other day, and the cultures were incubated at 37 °C in a humidified atmosphere containing 5% CO_2. Growth was assessed after 2 days. Cells grew well on the porous coating and can be seen in Figure 6.13. Unfortunately, after fixation most of the cells released from surface so a better method of visualization needs to be used, most likely involving sputtering and imaging with an SEM.
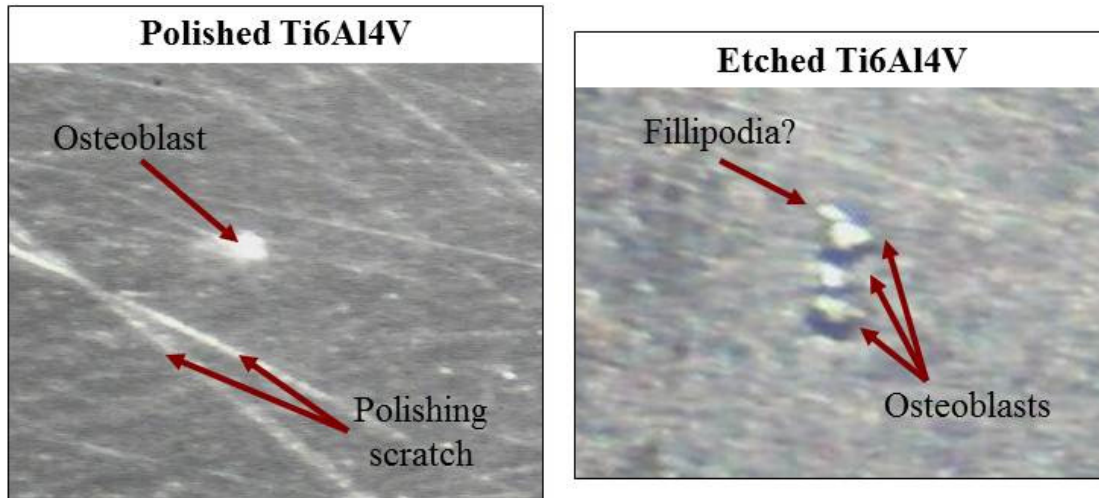
Figure 6.13: Images, taken with a dissecting microscope, of osteoblasts grown on polished and etched titanium coupons.

The intent of further work will be to demonstrate that delamination risk has been mitigated, while retaining the benefits of existing porous coatings technology. The method of testing the modulus of the nano-scale coating will be adjusted according to [33] to better calibrate the indenter. Also, additional wet lab work will focus on biological assays to measure differentiation and proliferation of cells on etched and anodized coatings. These results are very preliminary, but have laid the foundation for further investigation.

6.3   IMPLANT LUBRICATION

Lubrication is the key to life, for it enables sliding motion, and this section focuses on applications of porous coatings to improve lubrication of prosthetic joints, which are often used to replace synovial joints. Figure 6.14 shows examples of synovial joints, which are lubricated by synovial fluid (SF), which is a water-based lubricant produced by the synovial membrane surrounding the articular capsule. When a prostheses replaces a diseased or damaged synovial

joint, the articular capsule is usually preserved and the prosthesis becomes bathed in synovial fluid. As discussed in previous chapters, wear of the joint components leads to significant morbidity; if improvements to lubrication in a prosthetic joint can be achieved, there is the potential to lessen the rate of wear of joint components, leadings to increased joint lifetimes and improved outcomes.
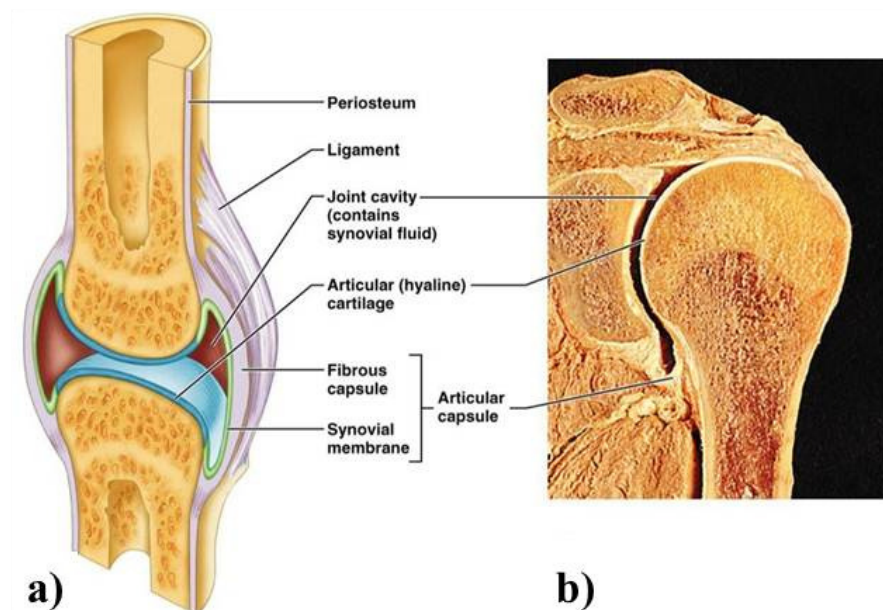
Figure 6.14: (a) schematic of a synovial joint; (b) cross-section of the gleno-humeral (shoulder) joint, showing the thin layer of hyaline cartilage and the articular capsule[26].

Porous coatings are unique in that when the coating is fabricated from a material that is non-wetting or only slightly wetting (like smooth titanium), the resulting porous surface is usually far more wetting, as will be shown. This is important because the coating can be used to stabilize a water-based lubricant at the surface of the implant [34, 35]. Joints already have a lubricant present; SF is 98% water and the other 2% are proteins like albumin and lubricin. Thus, a

---

[26]Image source: http://classconnection.s3.amazonaws.com/990/flashcards/769990/jpg/picture51318462971093.jpg. Accessed: 12/31/2012

wetting surface will encapsulate SF, and prevent "squeeze out" when two surfaces are brought into close contact, as often occurs in prosthetic joints. To lubricate a prosthetic joint with a porous coating, only a single fluid can be encapsulated as risks associated with a pre-impregnated fluid leaking out are too high [34, 35].

There are two principle types of lubrication regimes present in synovial joints, illustrated by the Stribeck Curve in Figure 6.15. When an individual is at rest, their joints settle, much like a journal bearing, and when they start moving boundary layer lubrication is present; in the native joint, this is dominated by the surface chemistry of articular cartilage.
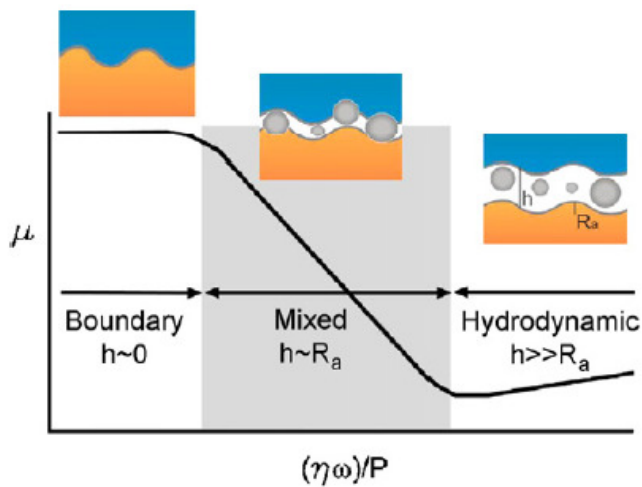
Figure 6.15: Stribeck curve showing types of lubrication present in synovial joints [36].

Boundary lubrication has been found to be the dominant factor leading to wear of artificial joint bearing components [36]. As motion continues, hydrodyanimc forces increase, leading to formation of a hydrodynamic lubrication regime and separation of the joint components by a fluid gap. The dynamics of synovial joint lubrication are made even more complicated by the

fact that the lubricant, synovial fluid, is shear-thinning: As the shear rate increases, the viscosity will decrease [37, 38]

Figure 6.16 shows sketches of collagen fiber orientation. Cancellous bone, which supports vertically-oriented collagen fibers, can be seen near the bottom of Figure 6.16a. At the hydrophobic surface, the fibers are oriented in the nominal direction of greatest stress (horizontal). Figure 6.16b shows how longer collagen fibers orient themselves near underlying bone, and the surface. Lubrication and SF flow during joint motion is incredibly complex [36, 39-41], and simple models are used here to demonstrate potential improvements.
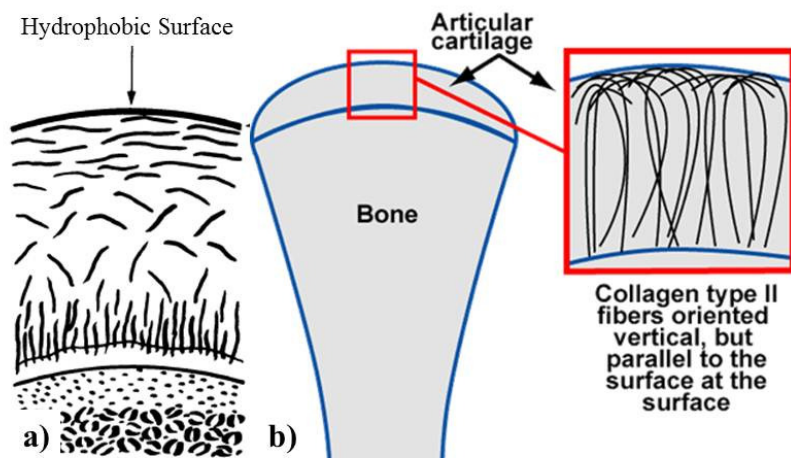
Figure 6.16: (a) sketch of collagen fibers in articular cartilage adjacent to bone [42], and (b) across the cartilage layer, oriented in line with the nominal direction of maximum stress.

The lubrication of cartilaginous joints initially begins as hydrostatic and hydrodynamic, during motion. When motion stops the joint settles and fluid eventually gets squeezed out of the contact patch; cartilage is different from metal in that it is deformable and permeable to SF. Boundary lubrication then becomes the dominant mode of lubrication as fluid support decreases and the fluid is squeezed out. There are also significant molecular forces that help support compressive

loads in the synovial joint, like electrostatic repulsion of Glycosaminoglycans embedded in the extracellular matric of articular cartilage [39, 40]. Porous coatings could be used to create an "artificial cartilage" through fluid encapsulation. Shear-thinning synovial fluid, which is water based, could then create self-induced shear thinning flows patterns similar to core flow [43]. Local decrease in friction could lead to formation of a single-fluid core flow, where the outer layers of the fluid are encapsulated and shear-thin, while the core of the flow remains at a higher viscosity.

Improvements to lubricity through the use of two similar nano-engineered hydrophilic coatings are evaluated using principles of tribology and rheology. It is hypothesized that by modifying the surface chemistry of a material to improve wettability, the surface will encapsulate synovial fluid, leading to the presence of more mixed or elasto-hydrodynamic lubrication regimes. Increases in hydrophilicity of the surface could also support adsorption of normal SF proteins, and prevent adsorption of denatured proteins; the latter has been shown to have significant negative effects on lubricity [44, 45].

Adsorption of native proteins, which are hydrophilic, is driven by Van der Waals forces; native proteins will also form a thicker film because their hydrophilic moieties remain more hydrated by the SF than would those of denatured, hydrophobic proteins [44]. Improvements to lubrication of implant surfaces would lead to decreased wear, resulting in increased implant lifetime and improved patient outcomes. Elastohydrodynamic (fluid film) lubrication is optimal, as boundary layer lubrication can lead to significant wear [46]. Mixed lubrication has slightly better wear characteristics than boundary layer lubrication, but is still non-optimal [47, 48].

Lubrication is key to the success of everything from high-performance precision machines to prosthetic joints; the most common total joint replacements occur at the hip and the knee [49]. The combination of current limitations to prosthesis lifetime, an increasingly aging population, and the fact that more patients are receiving joint replacements at a younger age, necessitate investigation of improvements to joint performance on all fronts [50-53]. Current thrusts in joint research are focused in the fields of materials science and materials selection, mechanical component design, and improving the lubricity of the prosthesis' components when bathed in synovial fluid (SF). Commonly used orthopaedic alloys include Cobalt-Chrome (CoCr), Stainless Steel, Titanium, and Cross-Linked Ultra-High Molecular Weight Poly-Ethylene (UHMWPE) [53].

Implant lubrication is achieved using synovial fluid, an ultrafiltrate of blood plasma containing proteins and other small molecules which affect the normal lubrication regimes [44, 53, 54]. Denaturation of synovial fluid proteins, primarily albumin, has been attributed to friction and heat generated at the metal/polymer interface [55]. In bovine synovial fluid, Bovine Serum Albumin (BSA) is the most abundant protein [45, 56]; it is also, by convention, the most common lubricant used for tribological testing of orthopaedic materials. Denatured albumin preferentially adsorbs onto hydrophobic surfaces and forms a compact, passivating layer that increases sliding friction leading to increased shear stress and greater wear [44, 45]. It has also been shown that glycoproteins present in SF adsorb onto the hydrophobic polymer component by way of their hydrophobic backbone, presenting their hydrophilic side chains to form a hydrated boundary layer on the surface of the polymer. As such, due to the wide range of proteins found in

SF, and the variability in surface chemistryIt should be noted, however, that increasing friction doesn't necessarily lead to increased wear rates [44].

Fluorescence microscopy and gel electrophoresis have been used to investigate the ability of glycoproteins to adsorb onto UHMWPE and alumina in the presence of other synovial fluid proteins [45]. This, combined with other studies, led us to believe that the wide range of proteins present in SF, including albumin, glycoproteins, proteoglycans, and glycosaminoglycans (GAGs), should be included in any tribo-rheological characterization of nano-engineered coatings. Using SF would ensure that results accurately predict the behavior of the surfaces in relation to in-vivo lubrication. Models of normal articulating joint lubrication suggest that a lubricating gel is formed from thickly concentrated hyaluronic acid molecules, which acts as a boundary lubricant preventing cartilage-to-cartilage contact very briefly during gait cycles [57]. In a prosthesis, a similar boundary layer is formed from normal and denatured proteins. If a polymer bearing insert is used, however, as in a total knee replacement, because polymers are not good conductors of thermal energy this can result in heating and micro-melting at any points of contact where increased friction is observed due to denatured protein adsorption. This results in further increases to the rate of protein denaturing, and could suggest one mechanism leading to increased wear of the hydrophobic surface of the polymer.

6.3.1   FLOW OVER TEXTURED SURFACES

Figure 6.17 shows a schematic of the proposed flow profile; by adding a porous encapsulating surface to the system, the no-slip boundary condition is eliminated at the lower boundary and the fluid encapsulation ensures that only hydrophilic native proteins adsorb onto the surface. This is

analogous to the way in which water is used to create core flows in the transport of viscous heavy oils in the petroleum industry [43].
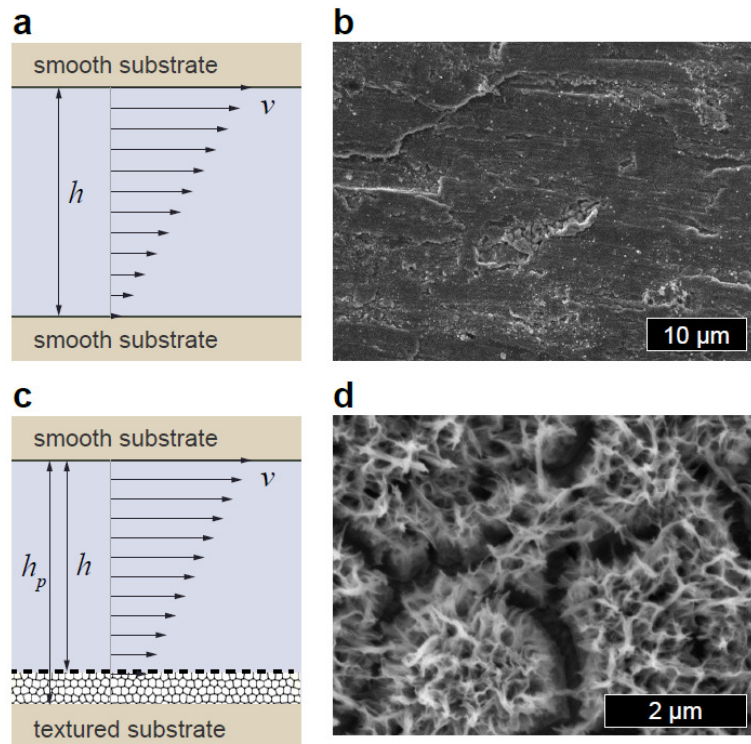
Figure 6.17: Schematic of lubrication between two surfaces (left), and SEM image of the surface (right) for (a) standard polished metal surface and (b) etched surface showing nano-scale pores for SF encapsulation.

Grade 5 titanium alloy (Ti6Al4V) is used as the primary material for tribo-rheological tests. While cobalt chrome alloys are generally used for the metallic component paired with the polymer bearing, their high cost made them unattractive for the current experiments; also, the surface treatment processes have been proven to work in titanium, and remain to be proven in Cobalt Chrome.
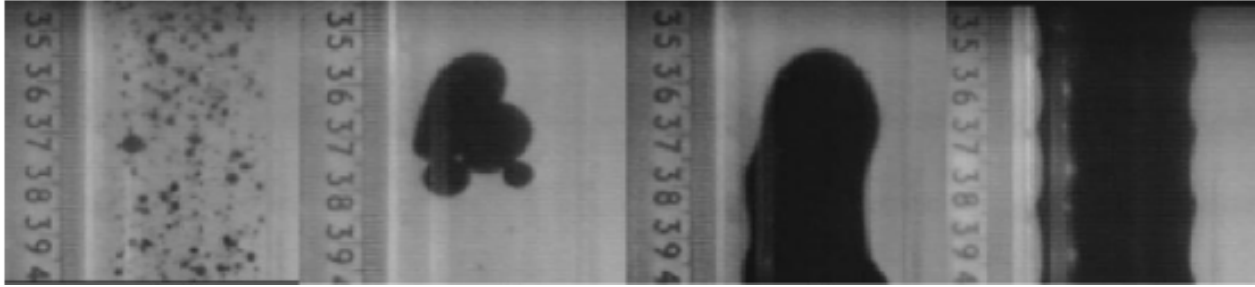
Figure 6.18: Visualizing the formation of oil core flows in the laboratory [43]

Starting with observations of fluid drainage in micro-textured surfaces [58], a model for lubrication with nano- and micro-textured surfaces can be postulated with an effective fluid viscosity $\eta_{eff}=\alpha\eta$. The factor α is a function of the porosity, defined by $\alpha \sim 1 + h^2/d^2$, where h is often taken to be the length, and d the diameter, of the spicules making up the porous structure. The effective viscosity of a fluid flowing through the nanotexture would be larger than the normal viscosity of the fluid; for an equivalent gap height *H*; however, the coating changes the couette flow boundary conditions at the interface between the free flow v_f and that through the porous medium v_p, through fluid encapsulation [58]. In a lubricated system with one smooth surface and one textured surface, there are three boundary conditions: 1) the no-slip condition at the bottom of the porous coating ($v_p = 0$), 2) the equal-stress condition at the boundary between the porous and free flows ($\eta_{eff}\, dv_p/dy = \eta\, dv_f/dy$), and 3) the no-slip condition at the smooth contact ($v_f = \Omega$), but there is no free surface as in previous analyses [58].

Core flows are demonstrative of the flow conditions present; a low viscosity fluid (water) is used to transport a high viscosity fluid (crude oil). The need for a single-fluid core flow system becomes apparent when considering the risks associated with having an implant that has been impregnated with a non-renewable fluid. . Here, a textured coating allows for the use of a single

fluid to achieve a modified boundary condition between essentially two fluids (defined by their viscosities): in the core flow case they are oil and water, in this case the two "fluids" are the free flow and that flowing through the porous coating [43], which necessitates the use of a shear-thinning lubricant like synovial fluid.

The second boundary condition is significantly modified when shear-thinning lubricants, like synovial fluid or serum albumin, are used. An equation for shear-dependence of viscosity was given by Kavehpour [59] to be

$$\eta(\dot{\gamma_R}) = \frac{T}{2\pi R^3 \dot{\gamma}_R}\left(3 + \frac{d\ln\left(\frac{T}{2\pi R^3 \dot{\gamma}_R}\right)}{d\ln\dot{\gamma}_R}\right) \textbf{Eq. (6.5)}$$

From this, the equal-stress boundary condition can be modified as $\alpha\eta(\dot{\gamma_R})\,dv_p/dy = \eta(\dot{\gamma_R})\,dv_f/dy$. Now, because the shear in the fluid just at the interface is equal, the viscosity of the shear-dependent fluid will be equal to that of the fluid in the gap, and the viscosity term can be eliminated. This yields Equation 6.6, which relates the porosity to a ratio of the gradient of velocity in the porous flow and the flow in the gap:

$$\alpha = \frac{dv_f/dy}{dv_p/dy} \textbf{Eq. (6.6)}$$

The effective viscosity of the fluid in the porous medium is greater than the viscosity of the fluid in the free flow. By definition, both α and in turn the velocity gradient ratio given in Equation 6.6 must be greater than 1. While this is counter to the more uniform velocity profile in crude oil found in core flows, because the single fluid we are using is shear-thinning, increased shear stress on the fluid will result in a lower viscosity. The porous coating acts to increase the effective viscosity of the boundary, inducing shear-thinning at the edge of the free-flow, and resulting in overall improved lubrication. Additionally, at these length scales capillary forces

dominate under static loads, and prevent fluid from being squeezed out from between the two surfaces.

In the case of two smooth surfaces where one is stationary and one rotating, there are two boundary conditions: 1) no-slip at the stationary plate, and 2) no-shear at the rotating plate. Because of the no-slip condition, the shear stress on the bottom plate with a fluid velocity gradient of dv_s/dy given by $\tau = \eta\, dv_s/dy$. If a shear-thinning lubricant is used, this equation becomes $\tau = \eta(\dot{\gamma})\, dv/dy$. A system using only smooth surfaces with a shear thinning fluid will have reduced friction at increased shear rates simply because of the nature of the lubricant. In order for the porous coatings to improve upon this, the shear stress induced at the porous/free flow boundary must be greater than the shear stress at the bottom smooth plate. The condition for improving lubrication with a porous coating is defined by Equation 6.7

$$\alpha\eta(\dot{\gamma_R})\, dv_p/dy = \eta(\dot{\gamma_R})\, dv_f/dy > \eta(\dot{\gamma})\, dv_s/dy \quad \textbf{Eq. (6.7)}$$

6.3.2   SYNOVIAL FLUID MODELS AND PROTEIN ADSORPTION

While Kavehpour [59] proposed a model for the shear-dependence of a fluid viscosity, there have been significant efforts to develop a model for the shear-dependency of synovial fluid. Biological fluids are inherently complex, as evidenced by the fluid behavior of organic fluids like blood, saliva, and synovial fluid [60, 61, 62]. Of these potential lubricants, we are most concerned with synovial fluid; Hron proposed a model for it's viscosity defined by $\eta = \eta_0\alpha\beta + \gamma|D|^2\alpha^{n(c)}$. In this equation, the parameters α, β, γ, and n must be determined experimentally [62], and they are also dependent on the concentrations of the various components of the synovial fluid. It is interesting to note that these can be affected by various disease states, age,

and whether an individual has a prosthetic joint. Due to this complexity, this work relies primarily on empirical measurements of synovial fluid to determine the viscosity at a given shear rate [38, 63].

6.3.3 SAMPLE PREPARATION

Samples were manufactured as 40mm diameter coupons with a 6mm central relief hole; the relief provides a place to mount the samples using a dowel pin for tribo-rheological experiments, as well as to ensure a non-zero minimum radius for fluid flow. The coupons were roughed out by laser cutting 3mm Ti6Al4V plate and 6mm UHMWPE plate [26]. These were then trued up and faced off in a lathe to ensure concentricity of the central hole with outer diameter, flatness of the surfaces, and parallelism between the top and bottom surface. The coupons were then polished to ensure smoothness using and polished using a buffing wheel.

Each coupon was placed individually in an ultrasonic bath at room temperature for 20 minutes; after cleaning they were placed in clean covered petri dishes for storage before chemical treatment. All polymer coupons were placed in individual beakers filled with De-Ionized water at room temperature, and the beakers were then placed in an ultrasonic bath at room temperature for 20 minutes. These were then placed in clean covered petri dishes for storage before experimentation. Porous coatings were then created on each sample via two surface treatment methods: an alkaline etch (etched) and alkaline-based electrochemical anodizing (anodizing). Etching consisted of placing the coupon in a solution of 29M NaOH at 80°C for 29 hours [22], and led to the formation of nano-scale pores with a characteristic size on the order of 200-300

nm as seen in Figure 6.19. Anodizing utilized a 29M H_3PO_4 solution at 80°C combined with 24V

DC applied for the duration of the 28 hour treatment [24].
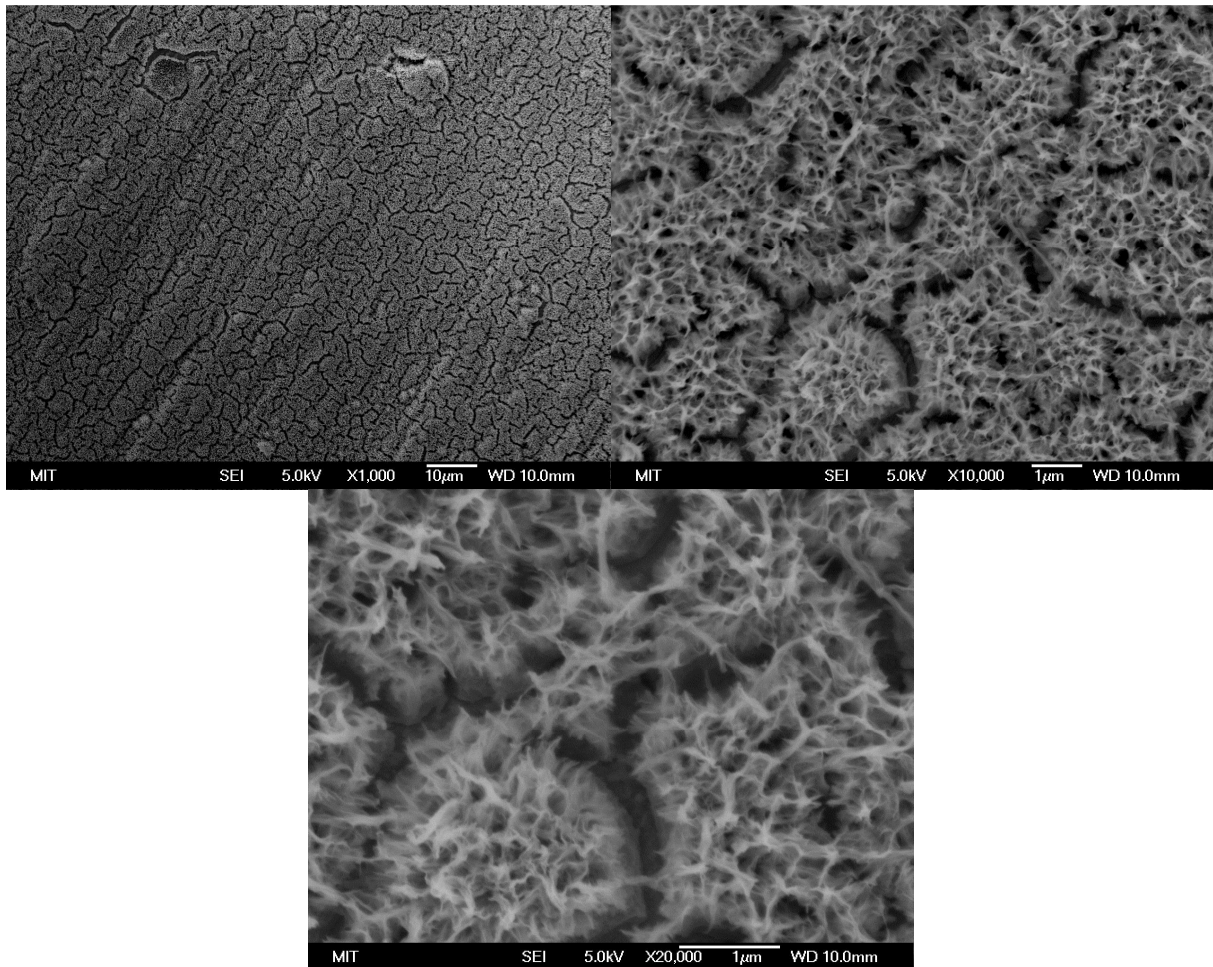
Figure 6.19: Sequence of images obtained with an SEM showing higher magnification views of

the alkaline etched samples, which resulted in a sub-micron scale porous coating
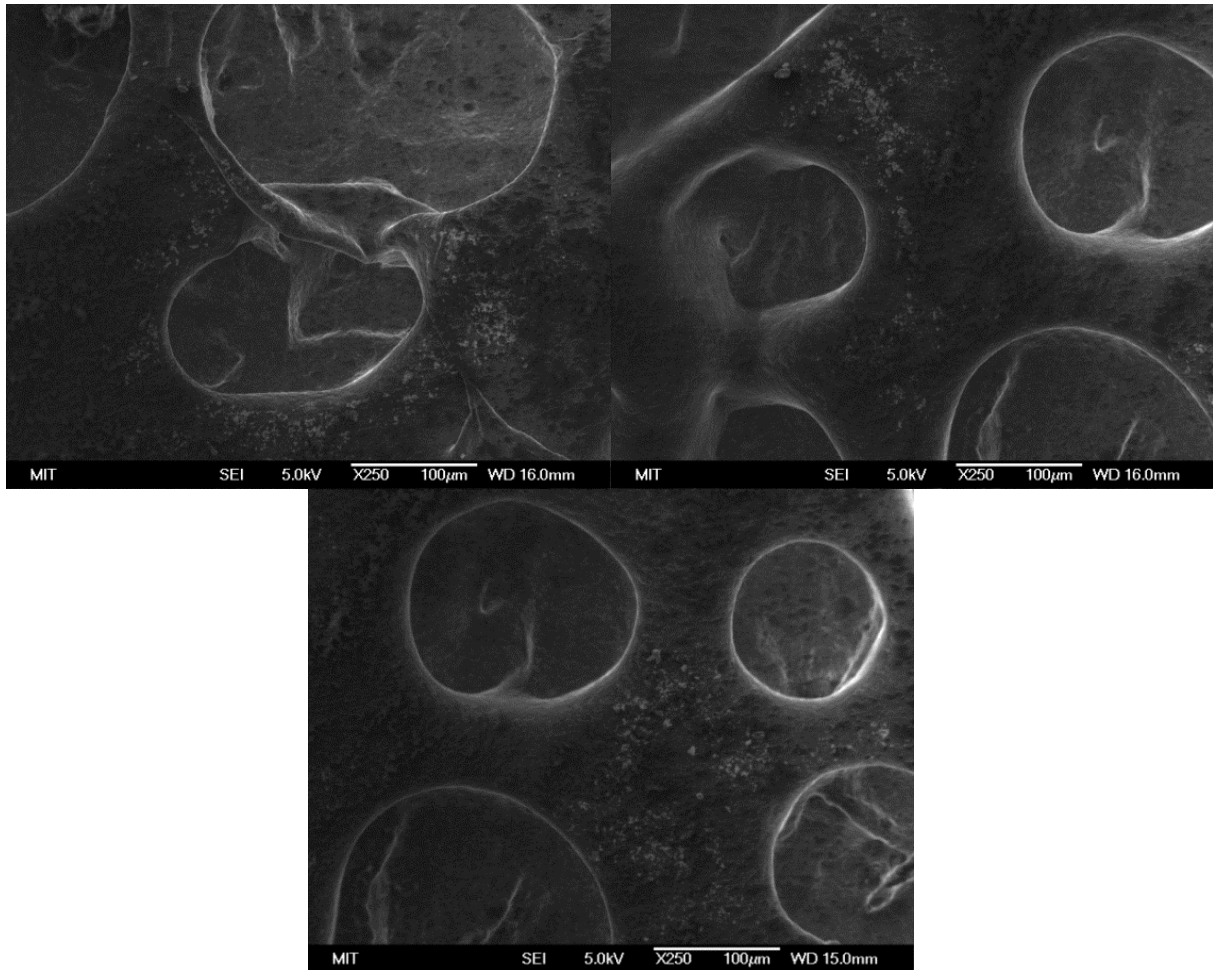
Figure 6.20: 250x zoom images of the anodized surface coating, taken with an SEM.

Surface roughness was measured for each sample (except the UHMWPE coupons) using a white-light interferometer. For the polished coupons, mean surface roughness was approximately 50 nanometers; the etched coupons had a mean surface roughness of approximately 120 nanometers, and the anodized coupons had a mean surface roughness of approximately 200 nanometers. These are summarized in Table 6.6. Figure 6.21 and Figure 6.22 show the results of white light interferometry of the smooth, anodized, and etched surfaces, including the peak-to-valley measurement (PV), RMS roughness, average roughness (RA), and the skew (RSK). The porous coatings should then, by the Wenzel equation, increase the wettability and hydrophilicity

213

of the smooth surface. Increasing the hydrophilicity of an orthopaedic metal would result in greater resistance to adsorption of denatured synovial fluids proteins, and help to maintain a low-friction surface [44].

Table 6.6: Characterization of three different surface treatments (smooth, etched, anodized).

	PV	RMS	RA	RSK
Smooth	2.913 +/-0.084	0.385 +/-0.021	0.280 +/-0.035	2.114 +/-0.583
Anodized	1.360 +/-0.075	0.074 +/-0.004	0.046 +/-0.003	-2.139 +/-0.445
Etched	0.732 +/-0.051	0.048 +/-0.003	0.038 +/-0.003	-0.805 +/-0.378
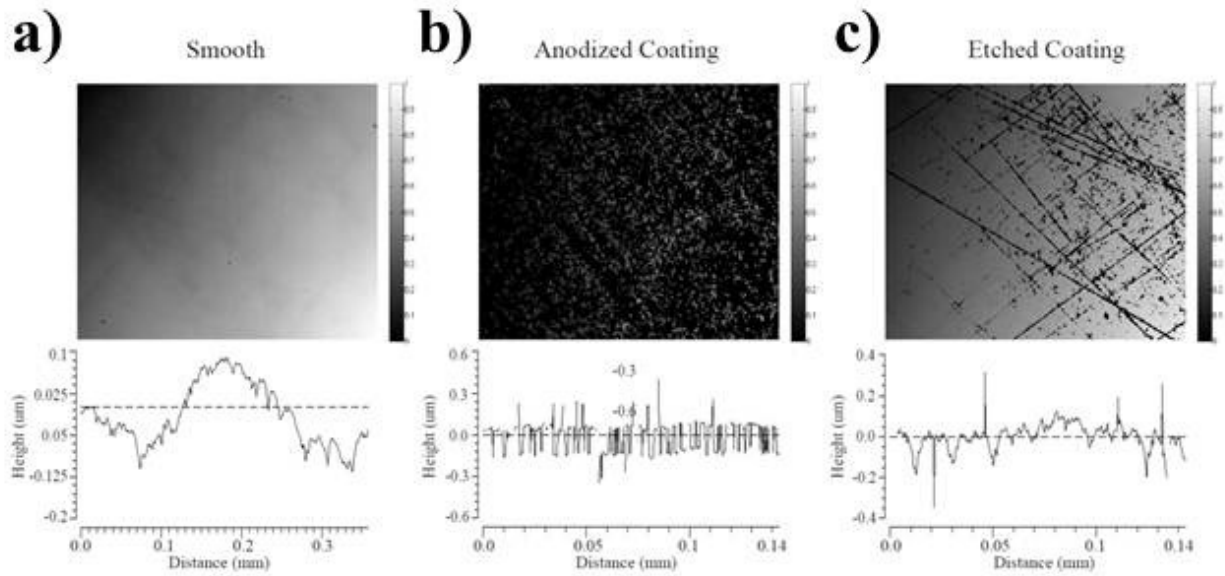
Figure 6.21: WLI measurement of roughness of (a) polished Ti6Al4V; (b) anodized coating; (c) etched coating.
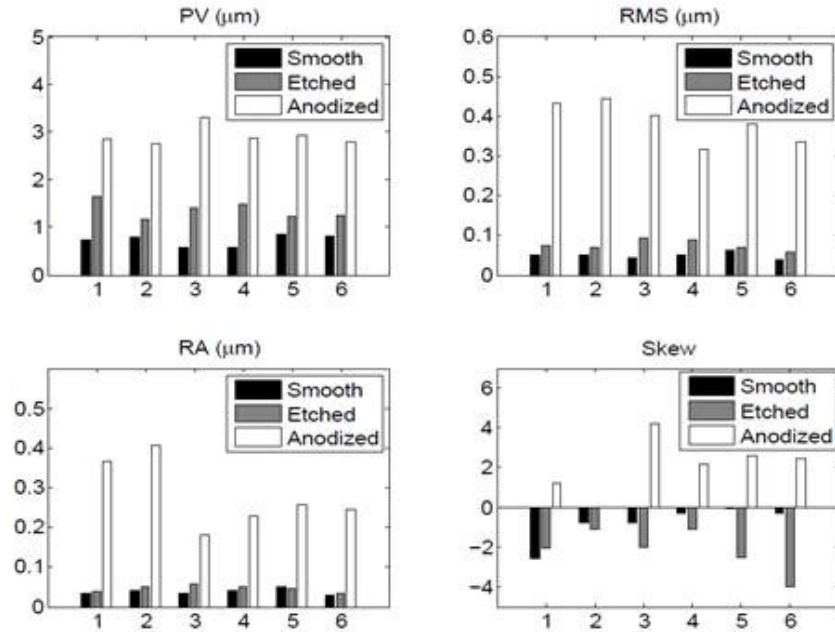
Figure 6.22: Graphical representation of the surface topology of the three tested coupons, including RMS, RA, and Skew.

It also becomes important to mention the concept of surface skewness [64, pp. 80-82], which is defined as the "ratio of the third moment of the amplitude distribution and the standard deviation σ from the mean line draw through the surface roughness measurements". Skew describes whether there are more peaks or more valleys in the surface, and a negative value implies there are more valleys than peaks. Two surfaces with equal RMS roughness can have different skew. More peaks increases the risk of asperity contact between two surfaces, while more valleys increases the space for fluid encapsulation [65]. Roughness directly affects flow in a lubricated contact, and is an important characteristic of these systems which must be considered, along with typical design considerations for sliding contact bearings [64, pp 425-444]. Flow in the lubricated contact has been described previously by [59]; from the Couette description of flow between two rotating disks, the shear rate in the fluid is given by $\dot{\gamma} = \Omega r / H$. A feedback system

in the rheometer allows for experiments to be run at either constant height, or constant normal force (stress) [59]. In this experiment a constant gap height H was used, and the resultant normal force F_N was recorded and used to calculate normal stress by $\sigma = AF_N$.

Starting with observations of fluid drainage in micro-textured surfaces [58], a model for lubrication with nanotextured surfaces can be postulated. The effective viscosity of a fluid flowing through the nanotexture would be larger than the normal viscosity of the fluid; for an equivalent gap height h, however, the coating eliminates the zero-slip condition present in normal couette flow at the solid surface, by encapsulating a fluid within its porous structure [58]. An analogous situation of oil core flows used to transport high-viscosity crude is demonstrative of the conditions present. Using the principle of reciprocity, the system is now limited to a single fluid so impregnation of the nanotexture will eliminate the no-slip boundary condition and result in lower friction [43, 65]. Additionally, at these length scales capillary forces dominate under static loading conditions and prevent fluid from being squeezed out from between the two surfaces.

6.3.4   SURFACE WETTING

Hydrophilicity of each surface was measured by tracking the advancing and retreating contact angle of a droplet using a Ramé-Hart Model 500 Advanced Goniometer with DROPimage Advance v2.4 software (Ramé-Hart, Succasunna, NJ) and deionzed water (DIW). Each sample was placed on the goniometer platform and contact angle was measured multiple times with a 6uL droplet. Contact angle images can be seen in Figure 6.23; the contact angles for each surface

are given in Table 6.7. From these measurements it can be observed that by creating a porous coating in the smooth titanium surface, its wetting characteristics can be significantly improved.

Table 6.7: Summary of contact angles on different surfaces.

Material	Advancing Contact Angle	Retreating Contact Angle
Smooth Ti	95°	75°
Anodized Ti	25°	25°
Etched Ti	45°	40°
UHMWPE	100°	50°
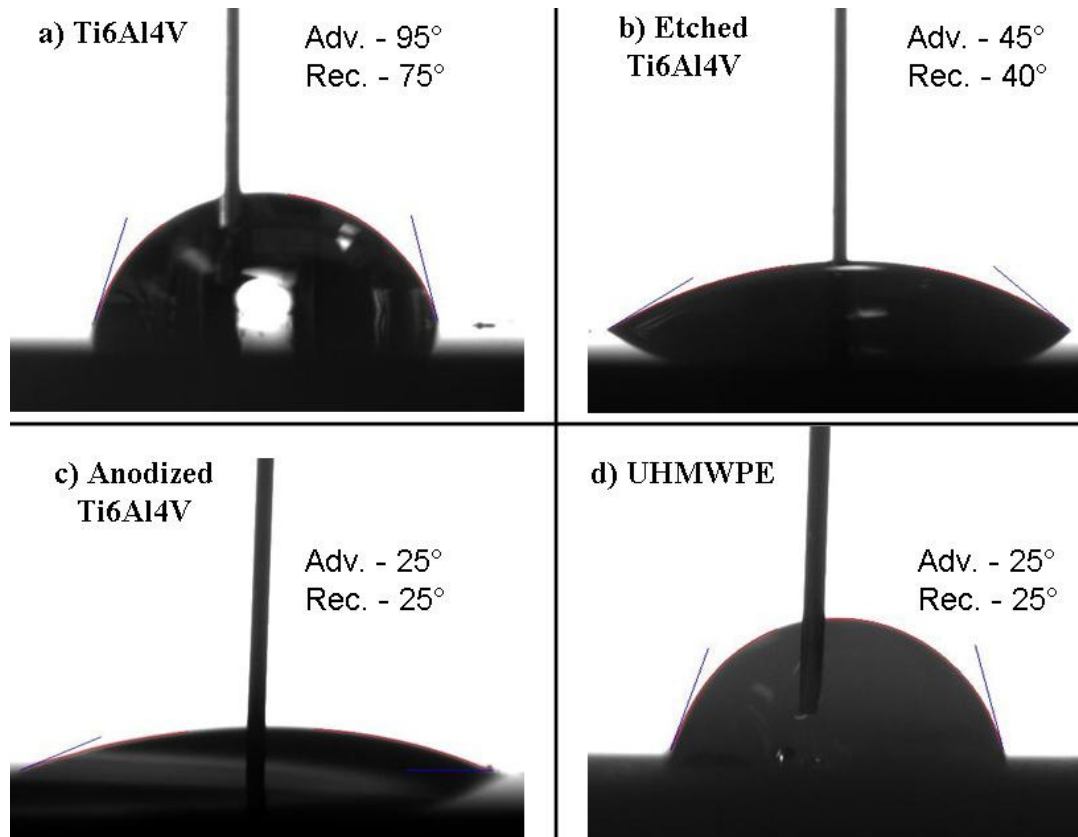
Figure 6.23: Contact angle measurements for (a) smooth Ti6Al4V; (b) etched Ti6Al4V; (c) anodized Ti6Al4V; and d) UHMWPE.

6.3.5   TRIBO-RHEOLOGY OF NANOENGINEERED SURFACES

Rheology is the study of fluid flow and viscosity, while tribology is the study of friction and wear in a lubricated contact. Tribo-rheology utilizes a rheometer to study the characteristics of a contact paring lubricated by a given fluid [59]. Typically, a Stribeck plot is used to describe a lubricated contact; it gives the measured friction coefficient versus a non-dimensional velocity termed the *stribeck number*. The stribeck number is equal to the product of viscosity and rotation velocity, divided by normal stress; linearity in the plot typically is interpreted as indicating the presence of hydrodyanimic lubrication [65, 66].
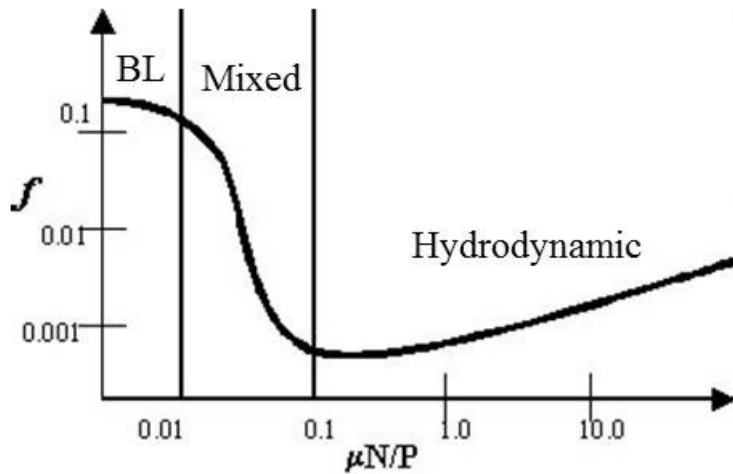
Figure 6.24: Representative Stribeck diagram (friction coefficient versus Stribeck number)[27].

Bovine Synovial Fluid (BSF, Lampire Biological Laboratories, Pipersville, PA), De-ionized water (DIW), and Silicone Oil (SO) were obtained for use in lubricating the coupons. Tribo-rheological characteristics of the system were assed in an AR-2 Rheometer (TA Instruments, New Castle, DE) using a plate-on-plate configuration. Tribological characteristics of the interface are determined based on previous methods described by [59]. Tribo-rheological testing

---

[27] Image source: http://www.stle.org/resources/lubelearn/lubrication/default.aspx

of 7 different surface configurations was performed using different fluids: deionized water (v_w = 1E-3 cSt), silicone oil (v_o, = 50E-3 cSt), and bovine synovial fluid (SF, v_s). Four experiments were used to generate Stribeck curves for a lubricated contact, wherein the lubricant fluid was compressed between two coupons: smooth-smooth, smooth-etched, smooth-anodized, and etched-anodized.

"Smooth" refers to a polished coupon that has not had any chemical surface treatment, "etched" refers to a coupon treated with alkaline etching, and "anodized" refers to a coupon treated with alkaline anodization. The same battery of tests were performed, including range of shear rates, using deionized water (a Newtonian fluid) as a lubricant to provide a baseline of comparison for the synovial fluid tests. Any coating applied to a surface in an attempt to improve lubrication must serve two purposes: 1) it must produce either an equivalent or lower coefficient of friction as conventional implant surfaces, and 2) it must encapsulate the fluid in order that lubricant (in this case, synovial fluid) is not squeezed out from between the components, in order to prevent touch-down.

Determination of the coefficient of friction for a given system consisting of a pair of surfaces and an intervening lubricant was based previous work by Kavehpour and McKinley [59] using the same AR-2 rheometer (TA instruments, New Castle, DE). Because two different surfaces need to be pre-fabricated, and different parings of coatings on surfaces are required to evaluate the full number of potential pairings, a fixture had to be constructed so that different surfaces could be rotated against one another. Taking inspiration from prior work using a wax-based mechanism to maintain alignment [59], as well as previous work by the author on fixturing and alignment for

nanomanufacturing[28], a passive alignment mechanism was designed utilizing a kinematic coupling (KC) supported by flexures[28]. This mechanism can be seen in the series of images in Figure 6.25; further publications will provide a detailed description of the work that went into designing and fabricating the passive alignment fixture, along with additional data from experiments with silicon oil and measurements of the stability of the fixture.
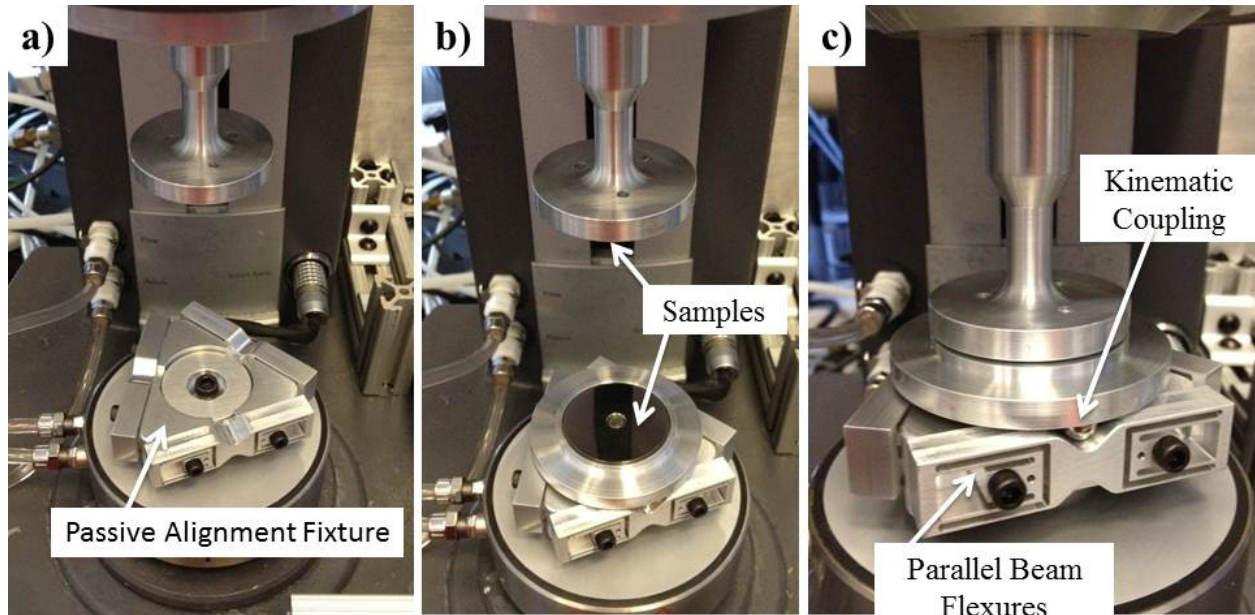
Figure 6.25: The precision passive alignment fixture designed to ensure planarity of different sample pairings during experiments on the AR-2; (a) showing the conical clamp (center) used to fix the base to the rheometer; (b) bottom sample on kinematic coupling, upper sampled fixed to the machine's rotating spindle; (c) detail view of the KC and accompanying flexural support.

Using the alignment fixture seen in Figure 6.25, multiple experiments were run on each material pairing. Shear rate was varied between 0.01 and 1000 s^{-1} for each experiment, and a constant gap height of 100 microns was used for all tests. While normally the gap height is allowed to change,

---

[28] For more information on kinematic couplings, visit: www.kinematiccouplings.org, a copy of the author's Master's thesis, "Design of Nanomanufacturing Systems", can be found here: http://dspace.mit.edu/handle/1721.1/61920.

as determined by the dynamics of the fluid, it is not known what contact between, for example, an etched coating and a smooth surface would do to the coating. Here, the fact that gap height is kept constant means that boundary-level effects at lower shear rates, like a higher coefficient of friction, are not expected to be seen on the Stribeck diagram. This also means that below a certain shear rate, what should be boundary-layer type flow is only approximated as such. Hydrodynamic lubrication is usually present at high shear-rates under steady-state conditions, so those can be studied to determine any improvements, and later further experimentation can be performed where the gap height is allowed to change as needed.

The first experiments performed involved Deionized water, which acts as a control because it is a Newtonian fluid and the expected shape of the Stribeck diagram is known [65]. Plots of shear stress versus shear rate will be presented first, and then stribeck diagrams for each situation will be shown. Figure 6.26 gives a log-plot of shear stress versus shear rate for the case of deionized water. The slope of the linear region above a shear rate of 10 should be the viscosity of water, which is 1×10^{-3}; the slope of the plot in the figure is approximately 10^{-3}, which means that the setup performs as expected.

SF is a visco-elastic non-newtonian shear-thinning fluid, so no single value for kinematic viscosity is given. Synovial fluid viscosity is dependent on shear rate, control values for SF were taken from previous studies by [63], where viscosity is given as a function of shear rate for human synovial fluid. Here, the viscosity measured in the experiment measured from 6 – 0.01 Pa-s with increasing shear rate. Also, because SF is a non-newtonian shear-thinning lubricant,

the simple couette flow model of lubrication between two plates, seen in Figure 6.17 must be modified [38].
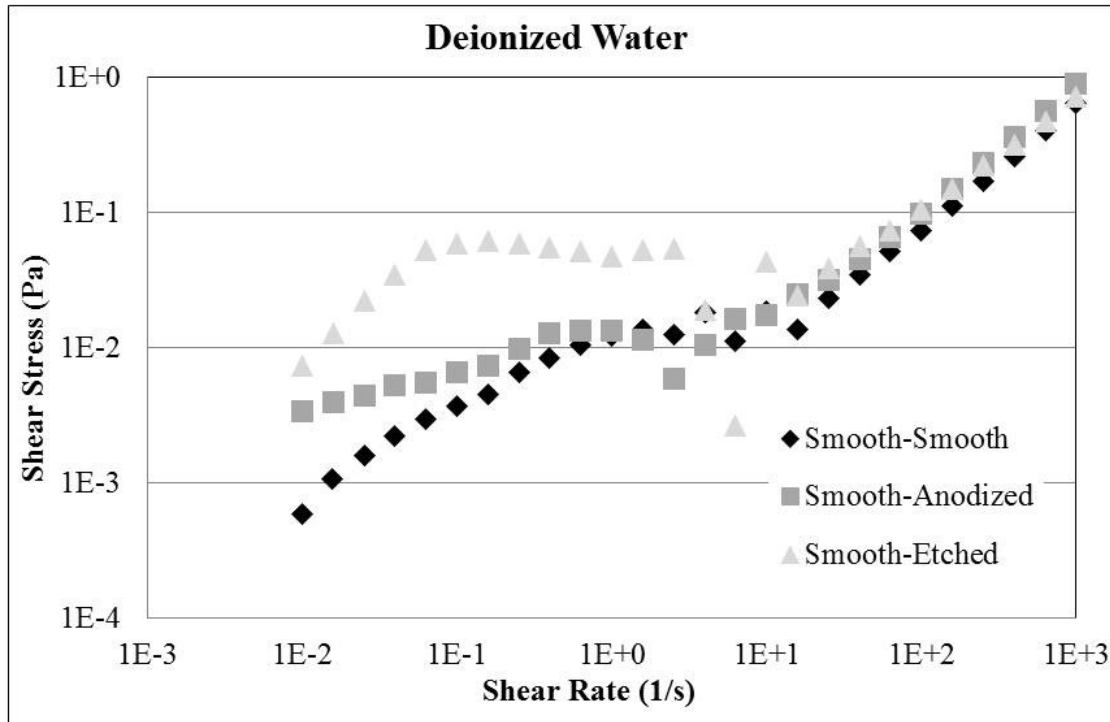
Figure 6.26: Shear stress versus shear rate for three contact pairings lubricated by DIW.

Figure 6.27 shows a log-plot of synovial fluid versus shear rate. At low shear rates (<1/s), the gap height would normally be determined by boundary layer lubrication, but because it is set to 100 µm, the shear stress is significantly reduced. Low-amplitude oscillations were observed during collection of data, and because of the present of boundary layers the surface chemistry of the smooth or coated coupon would also have an effect on the flow (whether or not it supported a stable boundary layer). At higher shear rates (above 10/s), shear-thinning of the synovial fluid is observed as the shear stress stays constant even as the shear rate increases. In the figure, the anodized coating leads to a decrease in shear stress by an average of 63%.
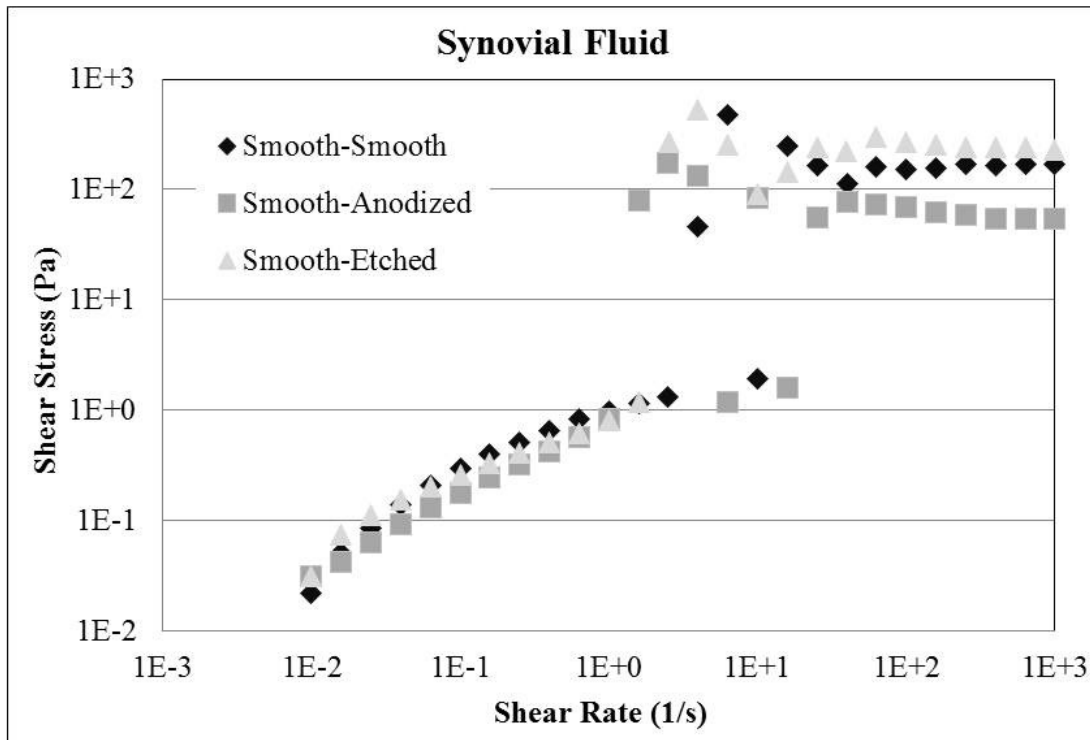
Figure 6.27: Log-log plot of shear stress vs. shear rate, illustrating the reduction in stress achieved when an anodized coating, lubricated with synovial fluid, is in contact with a smoorth surface (giving a known boundary condition for one side of the flow).

The effects of the anodized coating can be further highlighted by plotting the data from Figure 6.27 on a linear scale, as seen in Figure 6.28. The value for shear stress indicated by the final data point is given; the smooth-smooth sample pair sees a shear stress of 170 Pa, but when one is replaced by a sample which has been anodized, the shear stress drops to below around 55 Pa, a reduction of 68%.
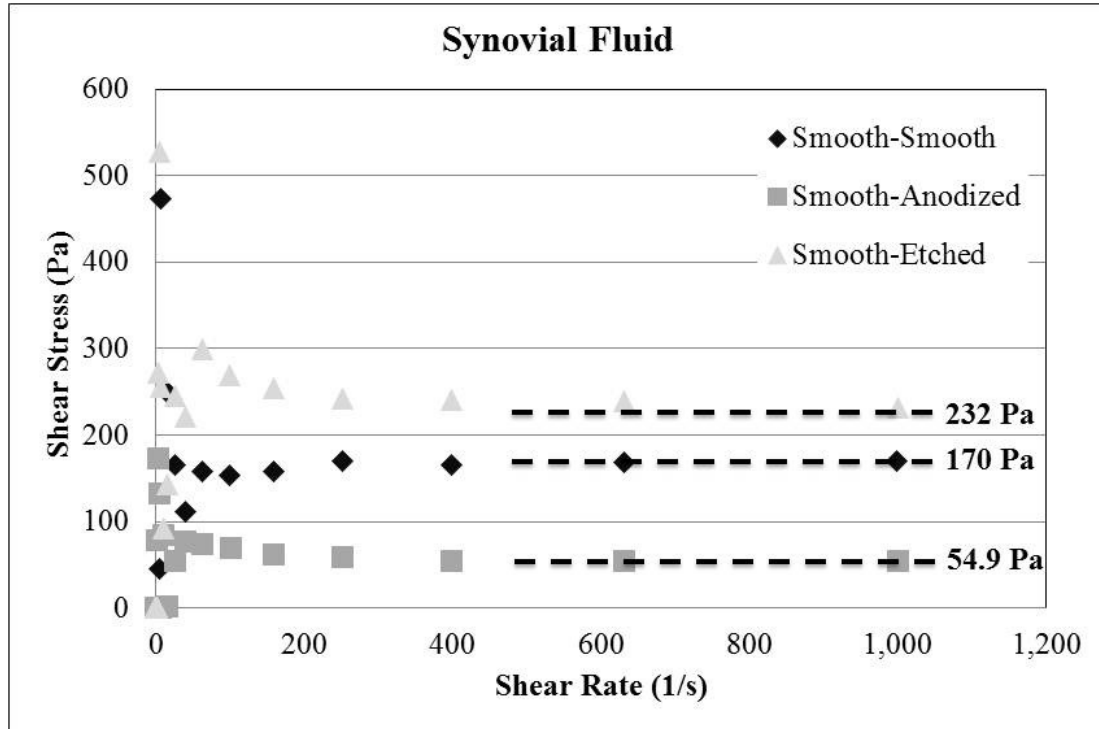
Figure 6.28: Linear plot of shear stress vs shear rate (using the same data from Figure 6.27), which better illustrates the degree of shear stress reduction

Based on observations of each experiment, spikes in shear stress and friction coefficient appeared between shear rates of 1 and 10 across lubricants and contact pairs, seen in Figure 6.26 and Figure 6.27. Currently, it is hypothesized that this is due to resonant phenomena existing with the compliant beams in the precision passive alignment mechanism used to ensure planarity between coupons. In Figure 6.29, conditions suggesting the presence of hydrodynamic lubrication (linearity) are seen more readily when synovial fluid is used, particularly when combined with the anodized coating as in (b).
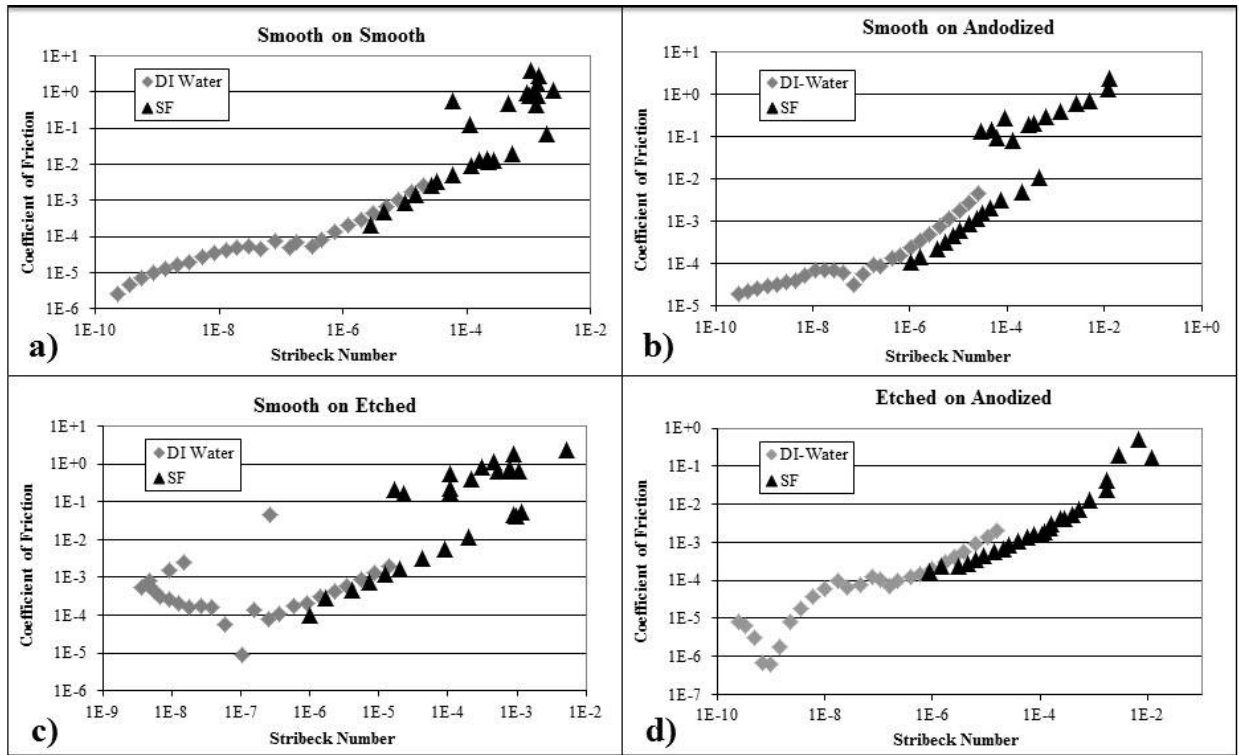
Figure 6.29: Stribeck plots for different surface coating pairs using de-ionized water and synovial fluid as lubricants, including: (a) smooth on smooth; (b) smooth on anodized; (c) smooth on etched; and etched on anodized.

Dissipation in the fluid gap can also be assessed by plotting the measured viscosity of the synovial fluid versus shear rate. Spikes in the viscosity between shear rates of 1 and 10/s are further suggestive of a resonant or other phenomena resulting from the presence of the compliant flexures. The downward slope seen in Figure 6.30 after a shear rate of 1/s is illustrative of shear-thinning, as the amount of dissipation and the anodized coating induces the greatest degree of this effect as the viscosity of the lubricant is lowest.
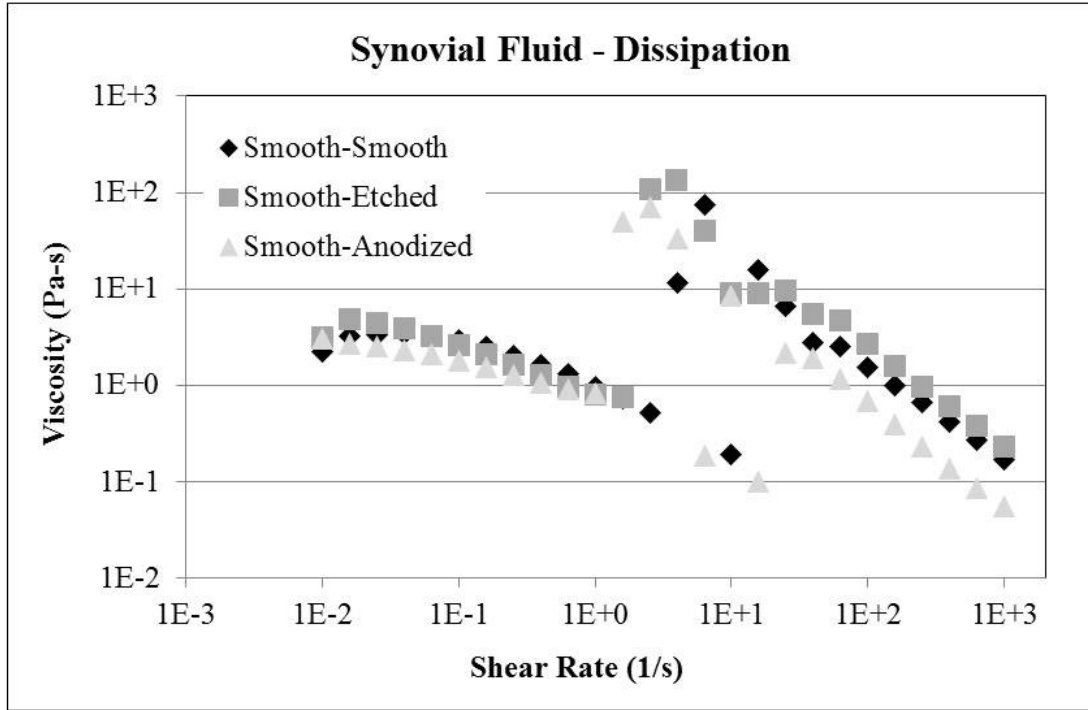
Figure 6.30: Dissipation in the synovial fluid for different lubricated contacts, including smooth on smooth, smooth on etched, and smooth on anodized coatings.

6.3.6 SLIP LENGTH

Previous experiments [67] utilized an angled platen, and glycerin and water as lubricants; Figure 6.31 shows a schematic of the micro textured coating impregnated with air used by [67]. Equation 6.8 gives an expression for slip length based on the shear stress at the top and bottom contacts, and used to estimate a slip length of $\delta = 170$ µm for the anodizing coating.

$$\left(\frac{\tau_{slip}}{\tau_{no-slip}}\right)_{couette} = \frac{1}{1+(\delta/h)} \text{ Eq. (6.8)}$$

226
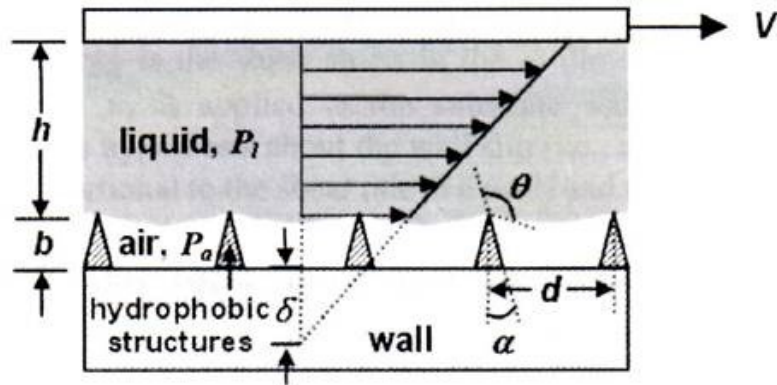
Figure 6.31: Schematic of a micro-textured surface illustrating the concept of slip length, which in the figure is labeled as δ [67].

6.4   REMARKS

The resonant phenomena mentioned previously will be a topic of further work, as damping mechanisms will be added to the alignment mechanism in Figure 6.25 and the experiments re-run. Also, cobalt chrome material will be procured and attempts will be made to use the etching and anodizing processes to create micro- or nano-scale porous coatings. The cobalt chrome coatings will then be evaluated for their potential to improve lubricity, in the same manner as those presented here were characterized. Recent work [68-70] shows that studies are already underway to evaluate the tribological characteristics of micro- and nano-textured coatings in various applications and with many different lubricants.

6.5   REFERENCES

[1] Biohexagon, Retrieval Studies – TKA. Biohexagon, Varnis 36, Greece. Online URL: http://www.biohexagon.com/main/index.php?option=com_content&view=category&layout=blog&id=39&Itemid=163. Image accessed January 9th, 2013.
[2] Hug, K. T., Henderson, R. A., Hansen, B. J., Wellman, S. S., Vail, T. P., Bolognesi, M. P., "Polished Cobalt-Chrome vs Titanium Tibial Trays in Total Knee Replacement (a Comparison using the PFC Sigma System)". The Duke Orthopaedic Journal. Available Online:

http://www.jaypeejournals.com/eJournals/ShowText.aspx?ID=2919&Type=FREE&TYP=TOP&IN=_eJournals/images/JPLOGO.gif&IID=228&isPDF=NO. Image accessed January 9th, 2013.

[3] Geetha, M., Singh, A. K., Asokamani, R., Gogia, A. K., "Ti Based Biomaterials, the Ultimate Choice for Orthopaedic Implants – A Review", Progress in Materials Science, Vol. **54**, pp. 397-425, 2009.

[4] St-Pierre, J.-P., Gauthier, M., Lefebvre, L.-P., Tabrizian, M., "Three-Dimensional Growth of Differentiating MC3T30E1 Pre-Osteoblasts on Porous Titanium Scaffolds", Biomaterials, Vol. **26**, pp. 7319-7328, 2005.

[5] Hahn, H., Palich, W., "Preliminary Evaluation of Porous Metal Surfaced Titanium for Orthopaedic Implants", Journal of Biomedical Materials Research, Vol. **4**;4, pp. 571-577, 1970.

[6] M/L Taper Hip Prosthesis, Zimmer, Inc., Warsaw, IN. Image Source: **Error! Hyperlink reference not valid.**.

[7] DJO Surgical, CLP Hip Stem. Image Source: http://www.djosurgical.com/products/hip/CLP/index.htm.

[8] Schwartz, et al., "Effect of Micrometer-Scale Roughness of Ti6Al4V Pedical Screws in Vitro and in Vivo, JBJS, November 1, 2008.

[9] Gibson, L. J., Ashby, M. F., "Cellular Solids: Structure and Properties", 2nd ed. Cambridge University Press, Cambridge, UK, 1999.

[10] Willoughby, P. J. (2005). *Elastically Averaged Precision Alignment*, PhD Thesis, MIT.

[11] Mallory, T. H., Lombari, A. V., *et al.* "Why a Taper?", J Bone Joint Surg, 2002 Nov 1; Vol. **84**(suppl 2):S81-89.

[12] Trabecular Metal coated Monoblock Acetabular component and Hip Stem, Zimmer, Inc., Warsaw, IN. Online URL: http://www.zimmer.com/en-US/hcp/hip/product/tm-primary-hip-prosthesis.jspx.

[13] Levine, B., Della Valle, C. J., Jacobs, J. J., "Applications of Porous Tantalum in Total Hip Arthroplasty", J Am Acad Orthop Surg, November 2006; **14**:646-655.

[14] Bobyn JD, Stackpool G, Toh K-K, et al. Bone ingrowth characteristics and interface mechanics of a new porous tantalum biomaterial. J Bone Joint Surg. 1999;81-B:907-914.

[15] Trabecular Metal Material, Zimmer, Inc., Warsaw, IN. Accessed 1/1/2013. Online URL: http://www.zimmer.com/z/ctl/op/global/action/1/id/9193/template/IN.

[16] Trabecular Metal Technology, Zimmer, Inc., Warsaw, IN. Accessed 1/1/2013. Online URL: http://zimmermelia.com/ctl?template=MP&op=global&action=1&id=3147.

[17] Ryan, G., Pandit, A., Apatsidis, D. P., "Fabrication Methods of Porous Metals for Use in Orthopaedic Applications", Biomaterials, Vol. 27, pp. 2651-2670, 2006.

[18] Sun, L., Berndt, C. C., Gross, K. A., Kucuk, A., "Material Fundamental and Clinical Performance of Plasma-Sprayed Hydroxyapatite Coatings: A Review", Journal of Biomedical Materials Research, 58:5, pp. 570-592, 2001.

[19] Regenerex® Porous Titanium Construct, Biomet, Inc., Warsaw, Indiana. Online URL: http://www.biomet.com/orthopedics/productDetail.cfm?category=2&product=231.

[20] Long, P. H., "Medical Devices in Orthopaedic Applications", Toxicologic Pathology, January 2008, **36**:1, pp.85-91.

[21] Habibovic, P., Barrere, F., van Blitterswijk, C. A., de Groot, K., Layrolle, P., "Biomimetic Hydroxyapatite Coating on Metal Implants", Journal of the American Ceramic Society, 85:2, pp. 517-522, 2002.

[22] Tanaka, S., Hirose, N., Tanaki, T., "Effect of the Temperature and Concentration of NaOH on the Formation of Porous TiO_2", Journal of The Electrochemical Society, **152**:2, pp. 789-794, 2005.

[23] Jonasova, L., Muller, F. A., Helebrant, A., Strnad, J., Greil, P., "Biomimetic Apatite Formation on Chemical Treated Titanum". Biomaterials, **25** (2004), pp. 1187-1194.

[24] Prakasam, H. E., *et al.*, "A New Benchmark for TiO2 Nanotube Array Growth by Anodization". J Phys Chem C, **111** (2007), pp. 7235-7241.

[25] Shah, N. J., Hong, J., Hyder, M. N., Hammond, P. T., "Tissue Engineering: Osteophilic Multilayer Coatings for Accelerated Bone Tissue Growth", Adv Mater, March 12, 2012, Vol. **24**;11, p. 1444.

[26] McMaster-Carr, Princeton, NJ. Online URL: http://www.mcmaster.com/.

[27] Mirror Finish Polishing, Kansas City, MO. Online URL: **Error! Hyperlink reference not valid.**.

[28] Zimmer patent #1: Charlebois, S. J., Gilbertson, L. N., *et al.*, "Method for attaching a porous metal layer to a metal substrate". US Patent #7,918,382.

[29] Zimmer patent #2: Devanathan, T., "Implant having a metallic porous surface". US Patent #5,571,187.

[30] Biomet patent #1: Hamman, N. M., Fleming, J., *et al.*, "Method and apparatus for forming porous metal implants". US Patent #7,635,447.

[31] Korkusuz, P., Korkusuz, F., "Hard Tissue-Biomaterial Interactions", in *Biomaterials in Orthopaedics*, edited by M. J. Yaszemski, D. J. Trantolo, K.-U. Lewandrowski, V. Hasirci, D. E. Altobelli, and D. L. Wise (Marcel Dekker, New York, NY, 2004) pp.1-6.

[32] Slocum, Jr. A. H., Adam Paxson, Agnes-Therese Akono, Eric Blough, Kripa Varanasi, "Nano-Structured Contoured Surface Coatings for Orthopaedic Implants". Presented at the Fall 2011 Meeting of the Materials Research Society, November 27th – December 2nd, 2012.

[33] Hodge, A. M., Biener, J., Hayes, J. R., Bythrow, P. M., Volkert, C. A., Hamza, A. V., "Scaling Equation for Yield Strength of Nanoporous Open-Cell Foams". Acta Materiala, Vol 55:4, February 2007, pp.1343-1349.

[34] Smith, J. D., Dhiman, R., Anand, S., Garduno, E. R., Cohen, R. E., McKinley, G. H., Varanasi, K. K., "Droplet Mobility on Lubricant-Impregnated Surfaces". *Soft Matter (Accepted)*.

[35] Anand, S., Paxson, A. T., Dhiman, R., Smith, J. D., Varanasi, K. K., "Enhanced Condensation on Lubricant-Impregnated Nanotextured Surfaces". *ACS Nano*, 2012 6 (11), pp. 10122-10129.

[36] Gleghorn, J. P., Bonassar, L. J., "Lubrication Mode Analysis of Articular Cartilage Using Stribeck Surfaces", Journal of Biomechanics, 2008, Vol. **41**, pp. 1910-1918.

[37] Sharma, V., Jaishankar, A., Wang, Y.-C., McKinley, G. H., "Rheology of Globular Proteins: Apparanet Yield Stress, High Shear Rate Viscosity and Interfacial Viscoelasticity of Bovine Serum Albumin Solutions", Soft Matter, 2011, **7**, pp. 5150-5160.

[38] Jaishankar, A., Sharma, V., McKinley, G. H., "Interfacial Viscoelasticity, Yielding and Creep Ringing of Globular Protein-Surfactant Mixtures", 2011, **7**, pp.7623-7634.

[39] Buschmann, M. D., Grodzinsky, A. J., "A Molecular Model of Proteoglycan-Associated Electrostatin Forces in Cartilage Mechanics". ASME Journal of Biomechanical Engineering, May 1995, Vol. 117; pp.179-192.

[40] Eisenberg, S. R., Grodzinsky, A. J., "Swelling of Articular Cartilage and Other Connective Tissues: Electromechanochemical Forces". Journal of Orthopaedic Research, Vol. 3:2; pp. 148-159, 1985.

[41] Schmidt, T. A., Sah. R. L., "Effect of synovial fluid on boundary lubrication of articular cartilage". Osteoarthritis and Cartilage, **15**:1, pp. 25-47, 2007.

[42] Hills, B. A., Crawford, R. W., "Normal and Prosthetic Synovial Joints are Lubricated by Surface-Active Phospholipid". The Journal of Arthroplasty, 2003, Vol. **18**, No. 4, pp. 499-505.

[43] Bannwart, A. C., Rodriguez, O. M. H., De Carvalho, C. H. M., Wang, I. S., Vara, R. M. O., "Flow Patterns in Heavy Crude Oil-Water Flow". ASME Journal of Energy Resources and Technology, **126**:3, pp. 184-189, 2004.

[44] Heuberger, M. P., Widmer, M. R., Zobeley, E., Glockshuber, R., Spencer, N. D., "Protein-mediated boundary lubrication in arthroplasty". Biomaterials, 26:1165-1173, 2005.

[45] Roba, M., Naka, M., Gautier, E., Spencer, N. D., Crockett, R.. "The Adsorption and Lubrication Behavior of Synovial Fluid Proteins and Glycoproteins on the Bearing-Surface Materials of Hip Replacements". Biomaterials, **30**:2072-2078, 2009.

[46] Meng, Q., Gao, L., Liu, F., Yang, P., Fisher, J., Jin, Z., "Contact mechanics and elastohydrodynamic lubrication in a novel metal-on-metal hip implant with an aspherical bearing surface". Journal of Biomechanics, **43**:5, pp. 849-857, March 2010.

[47] Jalali-Vahid, D., Jagatia, M., Jin, Z. M., Dowson, D., "Prediction of Lubricating Film Thickness in UHMWPE Hip Joint Replacements", J Biomech, 2001, **34**(2):261-6.

[48] Liu, F., Jin, Z., Roberts, P., Grigoris, P., "Effect of Bearing Geometry and Structure Support on Transient Elastohydrodynamic Lubrication of Metal-on-Metal Hip Implants". Journal of Biomechanics, **40**: 1340-1349, 2007.

[49] Kurtz, S., Mowat, F., Ong, K., Chan, N., Lau, E., Halpern, M., "Prevalence of Primary and Revision Total Hip and Knee Arthroplasty in the United States from 1990 Through 2002". Journal of Bone and Joint Surgery, July 2005, Vol. **87A**:7, pp. 1487-1496.

[50] Kurtz, S., Ong, K., Lau, E., Mowat, F., Halpern, M., "Projections of Primary and Revision Hip and Knee Arthroplasty in the United States from 2005 to 2030". Journal of Bone and Joint Surgery, April 2007, Vol. **89A**:4, pp. 780-785.

[51] Diduch, D. R., Insall, J. N., Scott, W. N., Scuderi, G. R., Font-Rodriguez, D., "Total Knee Replacement in Young, Active patients. Long-Term Follow-up and Functional Outcome". Journal of Bone and Joint Surgery, April 1997, Vol. 79**A**:4, pp. 575-582.

[52] Shanbhag, A., Rubash, H. E., Jacobs, J. J., Eds., "Joint Replacement and Bone Resorption: Pathology, Biomaterials and Clinical Practice", 1st Ed. (2005), CRC Press, Taylor and Franics Group.

[53] Revel, P. A., Ed., "Joint Replacement Technology", (2008), Woodhead Publishing, Ltd., Cambridge, UK.

[54] Pinchuk, L. S., Nikolaev, V. I., Tsvetkova, E. A., Goldade, V. A., "Tribology and Biophysics of Artificial Joints", 1st Ed. (2006), Briscoe, B. J. (Ed.), Elsevier, New York, NY.

[55] Mishina, H., Kojima, M., "Changes in Human Serum Albumin on Arthroplasty Frictional Surfaces". Wear, **256**:655-663, 2008.

[56] He, X. M., Carter, D. C., "Atomic-Structure and Chemistry of Human Serum-Albumin". Nature 2003;425(6383):163-5.

[57] Tandon, P. N., Bong, N. H., Kushwaha, K., "A New Model for Synovial Joint Lubrication". International Journal of Bio-Medical Computing, **35**:2, 125-140, 1994.

[58] Seiwert, J., Maleki, M., Clanet, C., Quere, D., "Drainage on a Rough Surface". EPL, **94**:16002, 2011.

[59] Kavehpour, H. P.., McKinley, G. H., "Triborheometry from Gap-Dependent Rheology to Tribology", Trib Lett, **17**:2, pp. 327-336, 2004.

[60] Anand, M., Rajagopal, K. R., "A Shear-Thinning Viscoelastic Fluid Model for Describing the Flow of Blood", International Journal of Cardiovascular Medicine and Science", 2004, Vol. **4**;2, pp. 59-68.

[61] Roberts, G. P., Barnes, H. A., Carew, P., "Modelling the Flow Behaviour of Very Shear-Thinning Liquids", Chemical Engineering Science, 2001, Vol. **56**, pp. 5617-5623.

[62] Hron, J., Malek, J., Pustejovska, P., Rajagopal, K. R., "On the Modeling of the Synovial Fluid", Advances in Tribology, Volume 2010, Article ID 104957. Onlune URL: http://www.hindawi.com/journals/at/2010/104957/.

[63] Mazzucco, D., McKinley, G., Scott, R. D., Spector, M., "Rheology of Joint Fluid in Total Knee Arthroplasty Patients", Journal of Orthopaedic Research, 2002, Vol. **20**:1157-1163.

[64] Slocum, A. H., "Precision Machine Design'" (1992), Prentice Hall, Englewood Cliffs, NJ.

[65] Hupp, S. J., Hart, D. P., "Experimental Method for Frictional Characterization of Micro-Textured Surfaces", Proceedings of the 2004 ASME/STLE International Joint Tribology Conference, Long Beach, CA, October 24-27, 2004.

[66] Dowson, D., "Elastohydrodynamic Lubrication: An Introduction and a Review of Theoretical Studies". Proc. Inst. Mech. Eng., 1965-66, Vol. 180, Part 3B, pp. 7-16.

[67] Coi, C.-W., Kim, C.-J., "Large Slip of Aqueous Liquid Flow over a Nanoengineered Superhydrophobic Surface". PRL **96**, 066001-4, 2006.

[68] Jiang, S. Y., Xie, H. J., "Tribological Behaviour of Plasma-Spray TiO2 Coating against Metallic Bearing Materials Under Oil Lubrication". Journal of Engineering Tribology, **225**:128-138, March 2011.

[69] Luo, Y., Ge, S., Zhang, D., Wang, Q., Liu, H., "Fretting Wear of Carburized Titanium Alloy Against ZrO2 under Serum Lubrication". Tribology International, **44**:11, pp. 1471-1475, October, 2011.

[70] Zhou, G., Ding, H., Zhang, Y., Liu, A., Lin, Y., Zhu, Y., "Fretting Wear Study on Micro-Arc Oxidation TiO2 Coating on TC4 Titanium Alloys in Simulated Body Fluid". Tribology Letters, **40**:3, pp. 319-326, 2010.

This page intentionally left blank

CHAPTER

7

MENS ET MANUS

"Don't judge each day by the harvest you reap, but by the seeds you plant" – Robert Stevenson

7.1   CONTRIBUTIONS OF THIS THESIS

The primary contribution of this thesis is demonstrating a method of synthesizing a prosthetic rolling contact knee joint based on a four-bar linkage mechanism. This could lead to an improved knee brace, and in the future potentially a rolling contact replacement knee joint. Further, the method of synthesizing cam surfaces presented in Chapter 5 can be applied to other mechanisms to eliminate the use of a linkage and instead utilize a rolling contact joint. This joint can be seen in Figure 7.1a, and the durability testing machine in Figure 7.1b.

Second, as described in Chapter 6, it is demonstrated that micro-textured coatings encapsulating a shear-thinning lubricant like synovial fluid can decrease shear stresses and reduce the chance of squeeze out, potentially leading to more hydrodynamic lubrication and reduced joint wear. As part of this work, a passive alignment mechanism for performing tribo-rheological studies was

developed, opening the door for further investigation of various other lubricated contacts as a result of the increased flexibility attained by the rheometer. The fixture used to run tribo-rheological experiments during this thesis can be seen in Figure 7.1d.

Thirdly, Chapter 3 of this thesis described the deterministic design of rolling contact joints for biomedical applications, and described synthesis of a testing machine for evaluating new fracture fixation technology [1]. This was used to characterize the performance of a deformable bone plate [2] and demonstrate its equivalence with existing bone plate technology. This is important in the evaluation of new medical technology because demonstrating equivalence is often required in order to make new, better medical devices available to patients. The bone plate testing machine can be seen in Figure 7.1c.
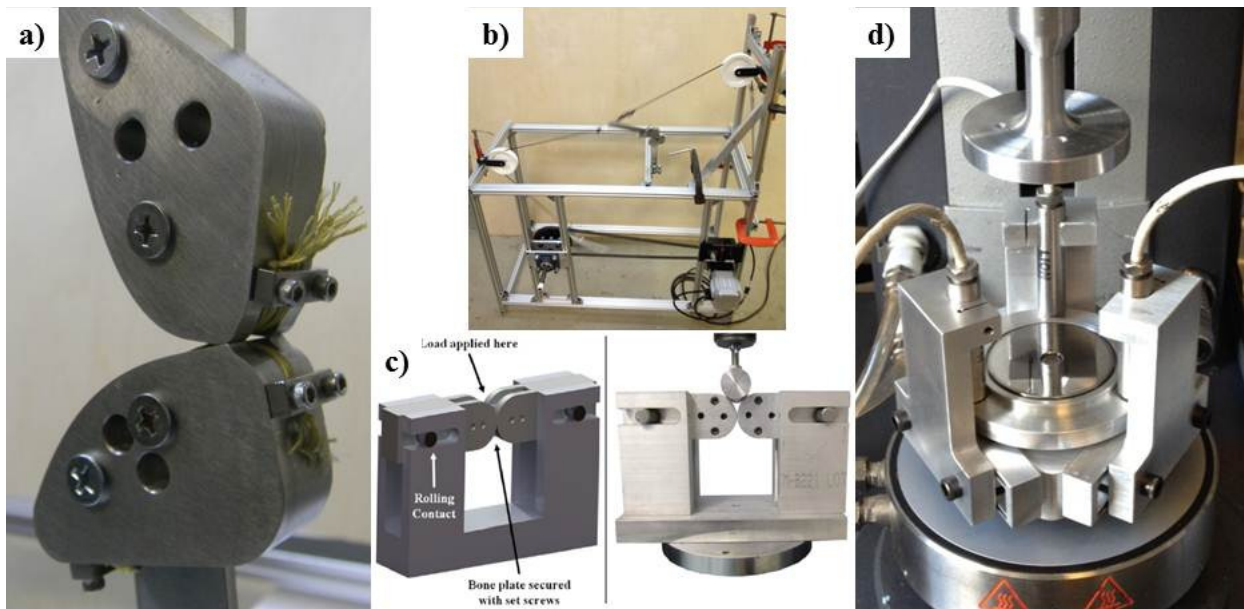

Figure 7.1: Photos of thesis contributions, including (a) rolling contact knee brace joint; (b) rolling contact joint testing to half a million cycles; (c) rolling contact joints used for evaluating new fracture fixation technology; (d) evaluation of nano-textured coatings for improving lubrication, utilizing a passive rheological alignment mechanism.

7.2 CLINICAL CONSIDERATIONS

There are a significant number of factors influencing the evaluation of diseased and damaged joints, indications for treatment, and types of treatments (brace, replacement, etc.). Here, treatment with knee braces is discussed, along with aspects of joint replacement which much be taken into consideration by patients and physician. Things like hypersensitivity reactions (allergy) to metal ions, particle disease, and infection can all cause significant morbidity and have negative impact on outcomes. This list is by no means complete; a design engineer should at the very least consult a volume on surgery of the joint for which they are designing a prosthesis. There are a number of resources for knee and hip surgery, like Insall & Scott [3], and Callaghan [4]. Technical works like those by Revell, Shanbhag, and Kurtz are also great resources, and contain comprehensive discussions of all different aspects of joint design and implantation; such volumes are essential resources for the biomedical design engineer.

7.2.1 KNEE BRACES

Osteoarthritis is one of the leading causes of morbidity in the elderly, and the prevalence of this disease increases by 60% from age 70-80 [5]. Knee braces are often given to patients with arthritis to try to prevent the progression of the disease. They are also often used by individuals who have suffered traumatic injury to the joint, like torn ligaments, or fractures that affect joint integrity, as these injuries often require significant rehabilitation and have been shown to lead to the development of early arthritis [6, 7]. Use of a knee brace can decrease the overall stress in the joint, while not causing a significant detriment to the individual's range of motion.

Stanley *et al.* showed that patients who wore a knee brace had increased range of motion in joints subjected to ACL reconstruction, as use of the brace resulted in reduced ACL loading [8]. They can also lead to decreased pain and disability [9], and on a more abstract level use of a knee brace can improve an individual's confidence in the joint, aiding in psychological rehabilitation as well. Other uses of knee braces are to decrease post-operative pain [10]. Finally, one of the most visible uses of knee braces is in professional athletes like football players, where they are often used as prophylaxis against traumatic injury.

Figure 7.2: A conventional knee brace (left), and a rolling contact brace (right).

The dual-hinge design used in today's prostheses works to simply approximate knee motion, and any deficiency between the kinetics of the mechanical and biological joints is filtered by the

flexible fabric materials used to affix the joint to the individuals lower extremity. While approximating the joint does not appear to have a detrimental effect on usage of the brace, anecdotal evidence suggests that soreness in the joint while wearing the prosthesis is a manifestation of adverse effects associated with use of the brace. Improving the design of the joint used in the brace, such that it exactly matches the kinetics of the primary degree of freedom in the knee, could lead to improved functional support and better long-term outcomes for patients using the brace for rehabilitation.

7.2.2   METAL ION ALLERGIES

Approximately 10% of the population is hypersensitive (allergy) to metals, with a higher incidence being reported in women than in men (17% to 3%) with regards to nickel, and similar rates of 1-3% towards metals like cobalt and chromium [11]. Release of metal ions in orthopaedics is especially important to consider as the implants are often semi-permanent, and are only removed in cases of severe morbidity, for example significant metal allergy. Methods of screening are currently being investigated [12]. Chronic hypersensitivity response in a patient receiving an implant with an unknown allergy to metal ions can lead to significantly increased morbidity and premature implant failure.

Stainless steel is a commonly used material in orthopaedics. This alloy, however, can release nickel and other metal ions. Other commonly used items are cobalt-chrome and titanium. When these alloys release metal ions, the ions induce an immune response, leading to tissue inflammation and release of other factors, which all contribute to osteolysis and loss of bone near

the implant. This can require revision of the prosthesis, involving removal of the old prosthesis and replacement with an updated prosthesis.

7.2.3 ASEPTIC LOOSENING

Implant Integration is critical to the long-term success of an implant. The surface of the metallic components, used to anchor a prosthetic relative to bone, can be modified to support a porous coating and improve ingrowth of bone and thus the chances that the implant will last. Further, preventing coating delamination off of smooth implant surfaces is critical, as plasma-sprayed coatings are the current state-of-the art. Some of the most recent data from the field highlight the degree of improvement achieved with current technology [13]. These and other clinical aspects of aseptic loosening were discussed in detail in Chapter 6, Section 6.2. Additional reading on the subject of bone resorption can be found in [14].

7.2.4 INFECTION

The incidence of infection in patients receiving total joint replacement has decreased steadily since the first procedures were performed, where the rate was about 10 %, to the current rate of around 1 percent [15, pp. 350]. Also, studies have evaluated strategies for reducing risks of complications like infection in patients receiving multiple joints, but have found little difference in morbidity and mortality associated with simultaneous replacement or separate procedures [16]. Infection of the joint is a serious risk as the trauma associated with surgery can lead to osteomyelitis (a bone infection), or even life threatening sepsis.

When infection is suspected, there are several methods available which can be used to confirm the diagnosis, ranging from simple blood tests (will see elevated white cell count, or WCC), to imaging (also to exclude other pathology like a fracture), and even aspiration of joint fluid with subsequent culture [15]. In the case of revision surgery, histologic examination and culture of samples taken from the implant/bone interface is often of interest to determine if an infection was present and could have contributed to failure. Overall, infection is always a challenge for surgical patients, and can cause significant morbidity in orthopaedic patients.

7.2.5 REVISION TKA

One of the many challenges facing patients and physicians involved in revision total knee replacement is bone loss. This is often managed in the operating room by using bone grafts to replace areas of significant reabsorption, or by augmenting the structure of normal prosthesis components like those seen in Figure 7.3. In addition, significant preoperative planning is required, along with procurement of tools designed to extract the old implant components while causing minimal damage to the surrounding tissues [17]. In the figure, the label near each prosthetic joint specifies which type of biologic joint it is designed to replace. Periprosthetic osteolysis, as previously mentioned in Chapter 2, can be exacerbated by allergy to small particles released from the implant, or a lack of integration and adequate stimulation of bone near the implant.

Figure 7.3: Images of prostheses for use in revision surgery in cases of significant bone loss[29].

7.3   FURTHER WORK

Further work will include several different pursuits, such as additional tests on the prototype joint in the testing machine presented in Chapters 4 and 5, more lubrication experiments with cobalt chrome samples as discussed in Chapter 6, and clinical evaluation of the rolling contact knee brace. Additionally, more in-depth experiments will be pursued in the wet lab to evaluate the growth and proliferation of osteoblasts on the porous coatings discussed in Chapter 6.

---

[29]Image source: http://www.zimmer.com/content/pdf/en-US/MOST_Options_System_Surgical_Technique_97-5010-002-00_04_2009.pdf

Joint durability experiments will be conducted in a similar manner to previous exercises. Femoral and tibial components will be assembled again using Kevlar® string; then they will be affixed to new versions of the tabbed pieces for mounting in the testing machine, but with generous application of Loctite™ to prevent loosening of the bolts as previously occurred. Screws have also been purchased with nylon patches to further reduce the risk of loosening. Also, cycling will be stopped at least once every 24 hours for assessment of all bolted interfaces and loose bolts will be tightened and then documented. In parallel, a third iteration joint is being designed utilizing fewer bolted interfaces and will be used for clinical experiments.

Carpenter Biodur® Cobalt Chrome was purchased from Boston Centerless[30] and manufactured into coupons for placement in the rheological fixture. Dimensions of the raw stock and one of the ten coupons, with an example of a near mirror finish manufactured by MIT's Central Machine Shop, can be seen in Figure 7.4. At the time of this writing, two of the ten coupons had been processed, one etched and one anodized. Work to characterize the surfaces is underway, including contact angle measurements, white light interferometer images of the surface, and microscopic imaging of the surface.

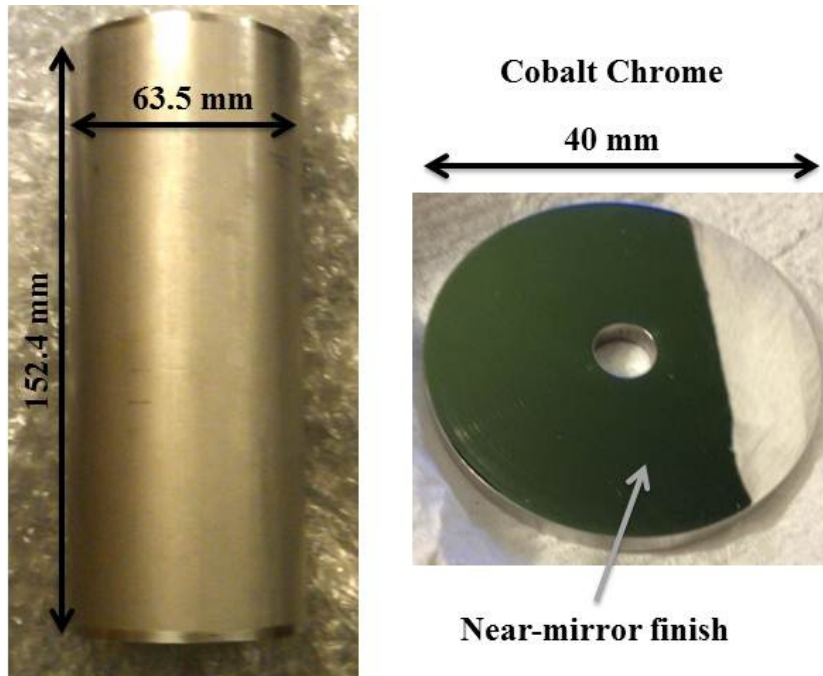[30]Boston Centerless, Woburn, MA; URL: www.bostoncenterless.com

Figure 7.4: Carpenter Biodur® Cobalt Chrome stock (left); polished coupon (right) [18].

Further work on clinically evaluating the performance of the rolling contact joint has commenced in the form of a translational research grant to compare the performance of conventional and rolling contact knee braces when used by patients both pre- and post-TKA. Outcome measures will be assessed by having the subjects perform various tasks related to Activities of Daily Living.

Finally, potentially improvements to the bone/implant interface will continue to be investigated, focusing on both the etched and anodized coatings. Tests will focus on culturing osteoblasts, as discussed in Chapter 6, and assaying them for growth and phenotype. This will be accomplished with assays for things like alkaline phosphatase activity, osteocalcin release, total protein, and calcium content [19].

7.4   REFERENCES

[1] **Slocum, Jr., A. H.,** Cervantes, T. M., Seldin, E. B., Varanasi, K. K., "Analysis and Design of Rolling-Contact Joints for Evaluating Bone Plate Performance". Medical Engineering & Physics, Vol. **34**, pp. 1009-1018, 2012.

[2] Cervantes, T. M., Slocum, Jr., A. H., Seldin, E. B., "Design and Experimental Evaluation of Adjustable Bone Plates for Mandibular Fracture Fixation", Journal of Biomechanics, Vol. **45**:1, pp. 172-178, 2012.

[3] N. W. Scott, 'Insall and Scott Surgery of the Knee', 4th Ed. (2005), Churchill Livingstone, Philadelphia, PA.

[4] Callaghan, J. J., Rosenberg, A. G., Rubash, H. E., Simonian, P. T., Wickiewicz, T. L., "The Adult Knee", 1st Ed. (2002), Lippincott Williams & Wilkins, Philadelphia, PA.

[5] Felson, D. T., et al. "The prevalence of knee osteoarthritis in the elderly. The Framingham Osteoarthritis Study". Arthritis and Rheumatism, Vol. **30**, Iss. 8, pp. 914-918, August 1987.

[6] Lohmander, L. S., Ostenberg, A., Englund, M., Roos, H., "High Prevalence of Knee Osteoarthritis, Pain, and Functional Limitations in Female Soccer Players Twelve Years after Anterior Cruciate Ligament Injury". Arthritis & Rheumatism, 2004, Vol. **50**:10, pp. 3145-3152.

[7] Chaudhari, A. M., Briant, P. L., Bevill, S. L., Koo, S., Andriacchi, T. P., "Knee Kinematics, Cartilage Morphology, and Osteoarthritis after ACL Injury". Medicine and Science in Sports and Exercise, 2008, **40**(2):215-222.

[8] Stanley, C. J., Creighton, A., Gross, M. T., Garret, W. E., "Effects of a knee extension constraint brace on lower extremity movements after ACL reconstruction". Clin Orthop Relat Res (2011) 469:1774-1780.

[9] Briggs, K. K., et al. "Improvement in Quality of Life with Use of an Unloader Knee Brace in Active Patients with OA: A Prospective Cohort Study". Journal of Knee Surgery, 2012; **25**(05): pp. 417-422.

[10] Brandsson, S., et al. "Is a knee brace advantageous after anterior cruciate ligament surgery?" Scandinavian Journal of Medicine and Science in Sports, Vol. **11**;2, pp. 110-114, April 2001.

[11] Thyssen, J. P., Menne, T., "Metal Allergy – A Review on Exposures, Penetration, Genetics, Prevalence, and Clinical Implications". Chem Res Toxicol (2010), **23** (2), pp. 309-318.

[12] Niki, Y., Matsumoto, H., et al., "Screening for Symptomatic Metal Sensitivity: A Prospective Study of 92 Patients Undergoing Total Knee Arthroplasty", Biomaterials, March 2005, Vol. **26**:9, pp. 1019-1026.

[13] Shah, N. J., Hong, J., Hyder, M. N., Hammond, P. T., "Tissue Engineering: Osteophilic Multilayer Coatings for Accelerated Bone Tissue Growth", Adv Mater, March 12, 2012, Vol. **24**;11, p. 1444.

[14] Shanbhag, A., Rubash, H. E., Jacobs, J. J., Eds., "Joint Replacement and Bone Resorption: Pathology, Biomaterials and Clinical Practice", 1st Ed. (2005), CRC Press, Taylor and Franics Group.

[15] Revel, P. A., Ed., "Joint Replacement Technology" (2008), Woodhead Publishing, Ltd., Cambridge, UK.

[16] Morrey, B. F., Adams, R. A., Ilstrup, D. M., Bryan, R. S., "Complications and mortality associated with bilateral or unilateral total knee arthroplasty". The Journal of Bone and Joint Surgery, American Volume (1987), **69**(4):484-488.

[17] Dennis, D. A., Berry, D. J., Engh, G., Fehring, T., MacDonald, S. J., Rosenberg, A. G., Scuderi, G., "Revision Total Knee Arthroplasty", Journal of the American Academy of Orthopaedic Surgeons", August 2008, Vol. **16**:8, pp. 442-454.

[18] Carpenter Technology Corporation, Inc., Reading, Pennsylvania, Online URL: http://www.cartech.com/ssalloysprod.aspx?id=2868.

[19] St-Pierre, J.-P., Gauthier, M., Lefebvre, L.-P., Tabrizian, M., "Three-Dimensional Growth of Differentiating MC3T30E1 Pre-Osteoblasts on Porous Titanium Scaffolds", Biomaterials, Vol. **26**, pp. 7319-7328, 2005.

- FIN -